Thermodynamic study of protein synthesis and of antibiotics targeting the ribosome

Emma Schenckbecher

UNIVERSITÉ DE STRASBOURG

ÉCOLE DOCTORALE DES SCIENCES DE LA VIE ET DE LA SANTE

UPR 9002 Architecture et Réactivité de l'ARN - IBMC

THÈSE présentée par :

Emma SCHENCKBECHER

soutenue le : **20 septembre 2019**

pour obtenir le grade de : **Docteur de l'université de Strasbourg**

Discipline/ Spécialité : Biophysique et biologie moléculaire

Thermodynamic study of protein synthesis and of antibiotics targeting the ribosome

THÈSE dirigée par :

Eric ENNIFAR	Directeur de recherche, Université de Strasbourg

RAPPORTEURS :

Reynald GILLET	Professeur des universités, Université de Rennes 1
Axel INNIS	Directeur de recherche, Université de Bordeaux

AUTRES MEMBRES DU JURY :

Gulnara YUSUPOVA	Directeur de recherche, Université de Strasbourg
Eva MUNOZ	PhD, AFFINImeter

Résumé

La traduction est une étape clé de l'expression des gènes et correspond au décodage de l'ARN messager en protéines. Elle se divise en 4 étapes, l'initiation, l'élongation, la terminaison et la dissociation, et a lieu chez les bactéries au niveau le ribosome, composé d'une petite et d'une grande sous-unité. Ces dernières années, de nombreuses études structurales et cinétiques ont été menées sur le ribosome, permettant des avancées spectaculaires et une meilleure compréhension de la traduction. En revanche, il existe peu d'informations thermodynamiques sur ce sujet. Pourtant, lorsqu'elles sont combinées aux données structurales, ces données permettent de mieux appréhender les interactions mises en jeu entre tous les acteurs à chaque étape du processus de synthèse protéique chez les bactéries, un mécanisme qui constitue une cible majeure des antibiotiques. L'équipe au sein de laquelle j'ai effectué ma thèse s'intéresse à différents aspects de la traduction par différentes approches biophysiques innovantes afin de caractériser les interactions d'un point de vue thermodynamique, grâce à la microcalorimétrie ITC, et cinétique, via la méthode kinITC développée au laboratoire et des puces ADN utilisant la nouvelle technologie switchSENSE.

Des travaux précédents effectués pendant la thèse de Benoit Meyer (non publiés) se sont intéressés à l'étape d'initiation de la traduction, primordiale et finement régulée, chez *Escherichia coli*. La formation du complexe d'initiation est orchestrée au niveau de la petite sous unité 30S à l'aide de différents partenaires, 3 facteurs d'initiation (IF1 à 3), l'ARNm messager et l'ARNt initiateur fMet-ARNt^{meti}. Le but de cette phase est de former un complexe 30SIC avec l'ARNt initiateur dans le site P du ribosome en phase avec le codon d'initiation porté par l'ARNm. Un tel complexe fonctionnel permet ensuite la liaison avec une sous-unité 50S pour l'entrée en phase d'élongation de la chaine protéique. Les facteurs d'initiation sont alors là pour aider à l'obtention de ce complexe, suivant une organisation séquentielle qui a notamment pu être déterminée par des études thermodynamiques.

L'étape d'initiation procaryotique disséquée, il est apparu intéressant de s'intéresser à l'initiation chez les eucaryotes. Cependant, cette dernière est bien plus complexe chez les eucaryotes et fait intervenir pas moins de 12 facteurs. C'est pourquoi, une première partie de mon projet de thèse a visé à étudier un type d'initiation non canonique faisant intervenir des IRES (*Internal Ribosome Entry Site*) viraux. Ces séquences d'ARN non codant originellement trouvée en amont d'une ORF chez les virus, permet le recrutement direct du ribosome au niveau du codon d'initiation avec un nombre réduit ou en absence de tout facteur d'initiation. Cette stratégie permet ainsi aux virus de s'approprier la machinerie cellulaire et de s'affranchir des étapes de recrutement du ribosome à la coiffe et de scanning, classiquement utilisées par les messagers cellulaires. Mon travail a consisté à étudier l'interaction de l'IRES intergénique du virus de la paralysie du criquet avec le ribosome de la levure *Saccharomyces cerevisiae*.

Déjà largement caractérisé d'un point de vue structural et biochimique, compléter ces données par des analyses thermodynamiques et cinétiques pourront permettre de mieux comprendre la liaison de cet IRES au ribosome eucaryote afin d'appréhender plus clairement comment les IRES fonctionnent, et à fortiori les virus. Les analyses ont donc été menées en utilisant en parallèle l'ITC et le switchSENSE. A noter que pour les deux approches, l'étude d'un si gros complexe macromoléculaire tel que le ribosome constitue des défis techniques non négligeables. D'une part, pour l'ITC il faut produire une très grande quantité de ribosomes et d'IRES ce qui est un facteur limitant pour effectuer plusieurs réplicas à différentes températures. D'autre part, au cours de ma thèse la technologie switchSENSE a dû être optimisée pour être capable de travailler avec une aussi grosse molécule. Les affinités obtenues pour la liaison au ribosome entier ainsi qu'aux différentes sous-unités via une approche thermodynamique ou cinétique, ont été comparées. Une comparaison des vitesses d'association et de dissociation a aussi pu être effectuée grâce au switchSENSE et kinITC. De plus, la traduction chez les procaryotes via des IRES de la même famille que celui étudié a été démontré dans une étude américaine (Colussi et al., 2015) ce qui m'a conduit à tester en parallèle l'interaction avec du ribosome procaryote par les deux méthodes.

Finalement, des contrôles, perturbant la structure de l'IRES, ont également été réalisés pour vérifier la spécificité de l'interaction. Nous avons alors montré l'interaction spécifique du 80S de *S. cerevisiae* avec l'IRES intergénique du CrPV avec une forte affinité de l'ordre de plusieurs dizaines de nM (entre 20 et 80 nM à 30 °C). En revanche, la petite sous-unité eucaryotique 40S semble avoir une affinité moins bonne, 5 à 10 fois plus faible que le ribosome entier. De manière moins surprenante, le 70S d'*E. coli* présente également une affinité plus faible, de l'ordre de centaines de nM. Les profils thermodynamiques quant à eux sont similaires indiquant que ces interactions sont dirigées par l'enthalpie (formation de laisons hydrogènes, … et changements conformationnels défavorables). Les cinétiques observées par switchSENSE et kinITC montrent des résultats très comparables validant les deux approches ainsi que les données obtenues. Au final, il semble que la fixation du ribosome entier au niveau de l'IRES intergénique du CrPV se fasse préférentiellement avec du 80S entier, plutôt que la petite sous-unité. En se replaçant dans le contexte cellulaire, un recrutement du ribosome entier directement au niveau de l'ARN viral en vue de traduction permettrait de s'affranchir de l'étape d'association des 2 sous-unités et de gagner ainsi du temps.

La seconde partie de ma thèse s'est focalisée sur l'interaction du ribosome *d'Escherichia coli* avec des antibiotiques. En effet, la lutte contre les souches résistantes aux antibiotiques actuellement utilisés, représente un problème de santé publique majeur à l'échelle mondiale. La progression constante de ces résistances rend alors incontournable la recherche de nouvelles molécules plus efficaces et spécifiques. Dans ce but, nous souhaitons étudier la liaison au ribosome bactérien de certains antibiotiques cliniquement utilisés, ainsi que de potentiels nouveaux antimicrobiens, ceci dans le but de mieux comprendre le mode d'action des antibiotiques étudiés afin de faciliter le développement de nouveaux antibiotiques et de contourner les mécanismes de résistance d'organismes pathogènes.

Mon travail s'est focalisé sur des antibiotiques ciblant le tunnel de sortie peptidique (PET) de la grande sous-unité 50S, notamment les macrolides. Cette classe historique compte aujourd'hui des dizaines de molécules regroupées en 3 générations différentes, en fonction de leurs structures et propriétés. Malheureusement, leur étude a été délaissée pendant plusieurs années en raison de leur inefficacité grandissante face aux bactéries résistantes. Mais récemment, une équipe américaine (Pr. Andrew Myers, Université de Harvard) a mis au point une approche inédite de synthèse totale, ouvrant la voie à la découverte de centaines de nouveaux macrolides. Une compréhension plus fine de l'interaction des anciens macrolides avec le ribosome s'avère primordiale pour mieux appréhender l'efficacité de ces nouvelles molécules aux propriétés antibiotiques encourageantes. L'ITC est particulièrement bien adaptée à ce projet car aucun marquage n'est requis et elle n'est pas limitée par la grande différence de taille des molécules testées. En revanche, la grande différence de taille entre les deux partenaires lors d'une interaction rend l'étude complexe. A cela s'ajoute, le problème de la très haute affinité des macrolides pour le ribosome, qui atteint la limite de sensibilité de la technique et complique une détermination précise des paramètres de l'interaction.

J'ai pu mettre au point une stratégie d'ITC par compétition sur le ribosome, permettant de déterminer plus précisément les paramètres de liaison des macrolides. L'ITC par compétition se base sur la capacité pour un ligand fort à pouvoir déplacer un ligand de plus faible affinité, appelé compétiteur, à condition qu'ils partagent un même site de fixation. Une première expérience permettant la fixation du compétiteur est directement suivie par le déplacement de ce dernier par le ligand d'intérêt (ici des macrolides). Pour notre étude, nous avons la chance de disposer de molécules possédant une région de fixation au ribosome similaire à celle des macrolides, les PrAMPs. Ils représentent une nouvelle classe intéressante d'antibiotiques produits naturellement par certains mammifères et insectes. 3 PrAMPs ont été testés (Bac 7, Metalnikowin et Pyrrhocoricin) pour sélectionner le meilleur compétiteur capable d'être déplacé par les quatre macrolides étudiés (érythromycine, azithromycine, telithromycine et josamycine). Après détermination des paramètres de liaison des PrAMPs, il est possible de définir, suite à l'expérience de déplacement, le profil thermodynamique de l'interaction des macrolides avec le ribosome ainsi que leur affinité pour ce dernier. La cinétique d'interaction, la vitesse d'association et celle de dissociation au cours de l'expérience de déplacement ont également été étudiées par kinITC.

Nous avons pu réaliser des expériences de compétition avec Bac 7 et la Pyrrhocoricin avec les 4 macrolides étudiés. En revanche, la Metalnikowin n'a pu être déplacée par aucune des 4 molécules, ce qui pourrait être expliqué par une conformation différente dans le tunnel de sortie peptidique. Au regard des données thermodynamiques, cinétiques et structurales nous nous sommes demandés si la Pyrrhocoricin pouvait être présente dans le PET en même temps qu'un des macrolides. Une analyse structurale par cryoEM a été réalisée pour répondre à cette question. Au final, des données d'interaction d'antibiotiques avec le ribosome bactérien ont été obtenues avec une approche originale et innovante.

En conclusion, mes travaux de thèse auront permis de caractériser les interactions du ribosome avec d'une part un IRES viral et d'autre part des antibiotiques, le tout avec des approches biophysiques intégrées. De plus, considérant la complexité moléculaire du ribosome, ces projets ont représenté des défis techniques permettant d'améliorer les méthodes disponibles. Outre les caractérisations plus précises et complètes des systèmes étudiés, nous avons donc pu optimiser certains de nos outils méthodologiques.

TABLE OF CONTENTS

ABBREVIATIONS

3'CITE: 3' cap-independent translation element

4E-SE: eIF4E-sensitive element

°: degree

°C: degree Celsius

%: percentage

Å: angström

aa: amino acid - amino-acyl

ABC: ATP binding cassette

AEBSF: 4-(2-aminoethyl)benzenesulfonyl fluoride hydrochloride

AKT: protein kinase B

AmpR: ampicillin resistance

AMR: antibacterial multi-resistance

ASL: anticodon stem loop

ATP: adenosine tri-phosphate

BP: base pair

BSA: bovine serum albumin

c: Wiseman coefficient

C: heat capacity

CamR: chloramphenicol resistance

CBP: cap-binding pocket

CL: clover leaf

cm: centimeter

cNLA or B: complementary nanolever A or B

Cp: calorific power

CrPV: cricket paralysis virus

cryoEM: cryo-electron microscopy

DC: decoding center

DEAE: diethylaminoethyl

DLS: dynamic light scattering

DMSO: dimethyl sulfoxide

DNA: deoxyribonucleic acid

DTT: dithiothreitol

E: energy

EC: elongation complex

EDTA: ethylenediaminetetraacetic acid

EF-G: elongation factor G

EF-Tu: elongation factor thermo unstable

EMCV: encephalomyocarditis virus

Erm: erythromycin methyltransferase

EtBr: ethidium bromure

EV-A71: enterovirus A71

FMDV: foot-and-mouth disease virus

FPLC: fast protein liquid chromatography

FT: formyltransferase

FTH: formyl-tetrahydrofolate

G: Gibbs free energy

GDP: guanosine di-phospahate

GT: glycosyltransferase

GTP: guanosine tri-phospahate

h: hour

H: enthalpy

HCV: hepatitis C virus

HEPES: 4-(2-hydroxyethyl)-1-piperazineethanesulfonic acid

HRV: human rhinovirus

IC: initiation complex

IF: initiation factor

IGR: intergenic

IRES: internal ribosome entry site

ITAF: IRES trans-acting factor

ITC: isothermal titration calorimetry

K: kelvin

Ka: constant of association

Kcal: kilo calorie

Kd: constant of dissociation

Keq: equilibrium constant

Koff: dissociation rate

Kon: association rate

L: liter

LB: luria broth medium

LC-MS-MS: liquid chromatography tandem mass spectrometry

M: molar

MALDI-TOF: Matrix Assisted Laser Desorption Ionisation - Time of Flight

MATE: multi-antimicrobial extrusion protein

Mef: macolide efflux

Met: methionine

MetRS: methionyl-tRNA-synthetase

MES: 2-(N-morpholino)ethanesulfonic acid

MFS: major facilitator superfamily

mg: milligram

min: minute

miR: microRNA

mL: milliliter

MLS_BK: macrolide lincosamide streptogramin B ketolide class

mM: millimolar

mol: mole

MOPS: 3-(N-morpholino)propanesulfonic acid

Mph: macrolide phosphotransferase

mRNA: messenger ribonucleic acid

Msr: methionine sulfoxide reductase

n: number of experiments

N: stoichiometry

nm: nanometer

nmol: nanomole

nM: nanomolar

NTP: nucleotide tri-phosphate

Nts: nucleotides

OD: optical density

ODL: odilorhabdin

ORF: open reading frame

P: pressure

PCR: polymerase chain reaction

PET: peptide exit tunnel

PEV8: porcine enterovirus 8

pH: potential hydrogen

PK: pseudoknot

PrAMP: proline-rich antimicrobial peptide

PTB: polypyrimidine tract-binding protein

PTC: peptidyltransferase centerPV : poliovrius

Q: heat

R: gas constant

RdRP: RNA-dependent RNA-polymerase

RF: release factor

RNA: ribonucleic acid

RND: resistance-nodulation-division

rNTP: ribonucleotide tri-phosphate

rpm: rotation per minute

RRF: ribosome recycling factor

rRNA: ribosomal RNA

s: second

S: entropy

S: Svedberg

S_A, S_B: streptogramins A, streptogramins B

SD: Shine-Dalgarno

SDS-PAGE: sodium dodecyl sulfate polyacrylamide gel electrophoresis

SL: stem loop

smFRET: single molecule florescence resonance energy transfer

SMR: small multidrug resistance

SV2: simian virus 2

T: temperature

TC: ternary complex

TCV: turnip crinkle virus

tRNA: transfer ribonucleic acid

U: unity

µg: microgram

µL: microliter

µM: micromolar

UTR: untranslated

V: volt

VEGF: vascular endothelial growth factor

VPg: viral protein genome-linked

VSV: vesicular stomatitis virus

W: work

WHO: world health organization

YPD: yeast extract peptone dextrose

CHAPTER I

GENERAL INTRODUCTION

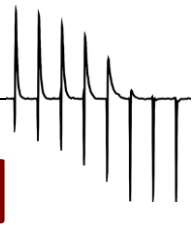

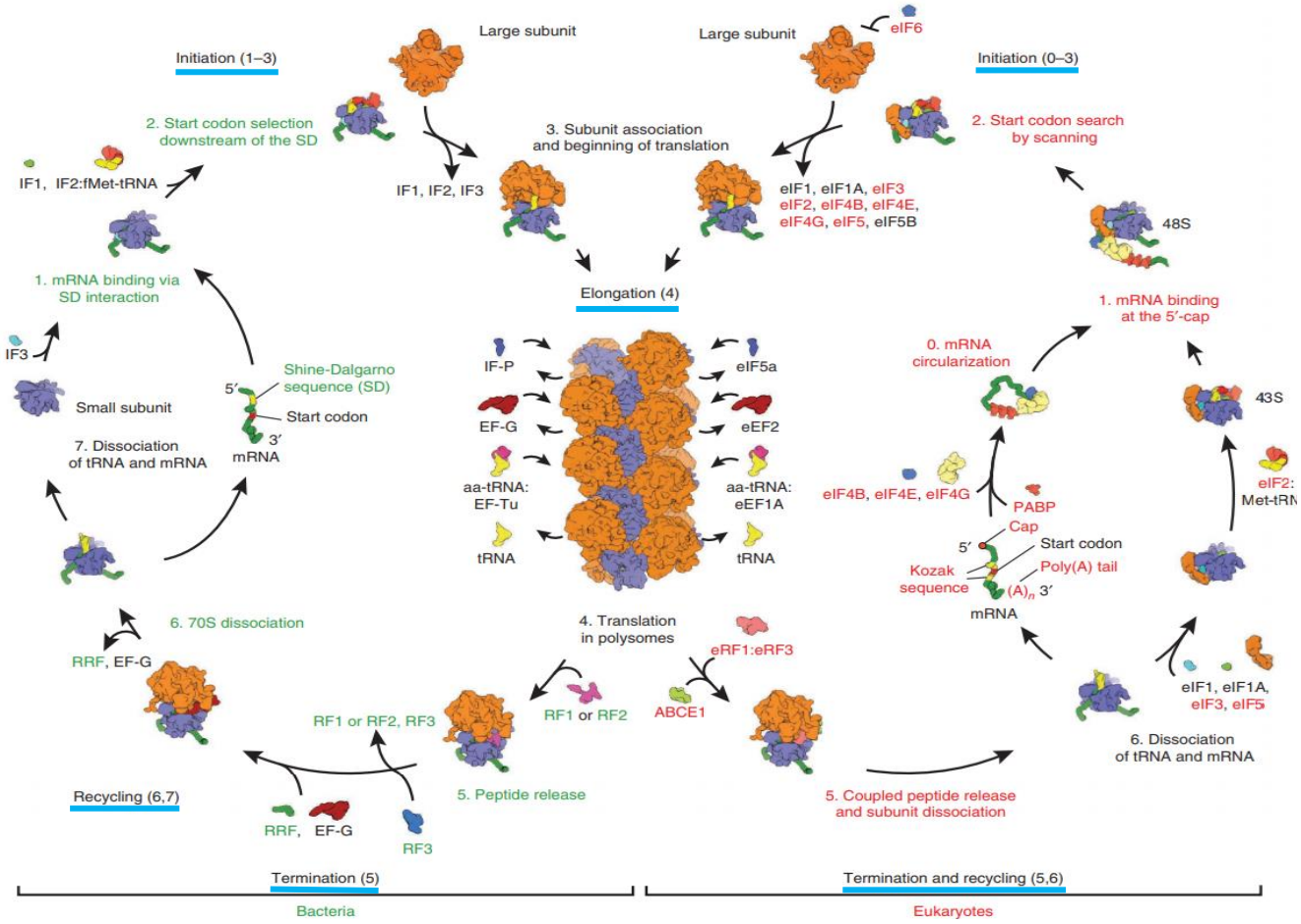

Figure 1: Major features of translation steps in bacteria and eukaryotes. From Melnikov et al., 2012.
The four steps of translation (underlined in blue) are assisted by protein factors, called initiation factors (IFs), elongation factors (EFs), termination or release factors (RFs) and ribosome recycling factors (RRFs). The lower-case letter e is added for eukaryotic factors. Bacterial and eukaryotic specificities are presented in green and in red, respectively. The common steps and homologous factors are in black.

Chapter I: General introduction

I. The ribosome, a key player in protein synthesis

1. Overview of the protein synthesis

The gene expression pathway corresponds to the decoding of the genetic information from DNA to functional proteins, which have crucial roles in biological processes (Crick, 1970). The translation of nucleotides to amino acids, based on the genetic code, requires two crucial RNA molecules: (i) an intermediate, the messenger RNA (mRNA) which carries the genetic information as triplets of nucleotides, called codons, and (ii) a translator RNA, the transfer RNA (tRNA) which correlates codons with distinct amino acids thanks to its anticodon sequence. The 3'-CCA end of tRNAs is loaded with the correct amino acid by specific enzymes, the aminoacyl-tRNA synthetases. This last step of gene expression is catalyzed by the ribosome, in which tRNAs are selected, and progress along the mRNA through tRNA sites, named A-, P- and E-sites (Ben-Shem et al., 2010; Rheinberger et al., 1981; Watson, 1964).

In all domains of life, the translation is divided into four steps (**Figure 1**) (Dever and Green, 2012; Melnikov et al., 2012; Ramakrishnan, 2002): the initiation, the elongation, the termination and the ribosome recycling. All of these steps are coordinated and tightly regulated by protein factors, called initiation, elongation, release or ribosome recycling factors.

During the canonical initiation step, the association of initiation factors, the initiator $tRNA^{Meti}$, mRNA and ribosomal subunits lead the establishment of mRNA-$tRNA^{Meti}$ interaction in the P-site thanks to codon-anticodon interaction (Kozak, 1999) (**Figure 1**, step 1-3). The initiation complex thus formed can be joined by the large subunit to constitute elongation-competent ribosome. Non-canonical initiation strategies also exist in eukaryotes, especially guided by RNA structures, to circumvent canonical initiation. One of the best examples such structures is the viral internal ribosome entry site, also called IRES, discovered in untranslated regions of viral genomes and which allow the direct recruitment of the host cell ribosome to drive viral protein synthesis.

As soon as the first elongator aa-tRNA enters in the A-site, the elongation step begins (Achenbach and Nierhaus, 2015; Dever and Green, 2012; Noller et al., 2017). Elongation is well conserved between eukaryotes and bacteria, and can be subdivided into three steps (**Figure 1**, step 4) : (i) the decoding of codons in the decoding center (DC) allowing the incorporation of the cognate aminoacyl-tRNA (aa-tRNA) in the A-site, (ii) the transpeptidation, corresponding to the formation of the peptide bond between the peptidyl-tRNA and the aa-tRNA, catalyzed by the peptidyl transferase center (PTC) and (iii) the translocation which allows the ribosome to move along the mRNA by transferring A-site and P-site tRNAs in P- and E-site, respectively.

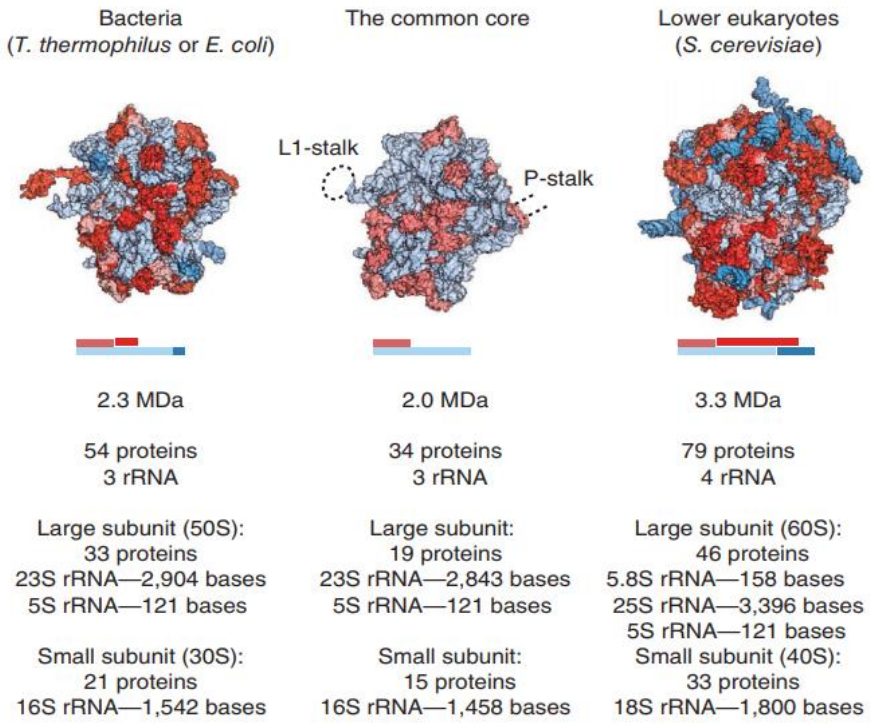

Figure 2: Composition of bacterial and eukaryotic ribosomes. From Melnikov et al., 2012.
The common core of the ribosome (light blue and red) has been implemented in the bacterial and eukaryotic ribosome structures (dark blue and red). Number of ribosomal proteins and rRNA, together with type and size of rRNA, is detailed for each subunit.

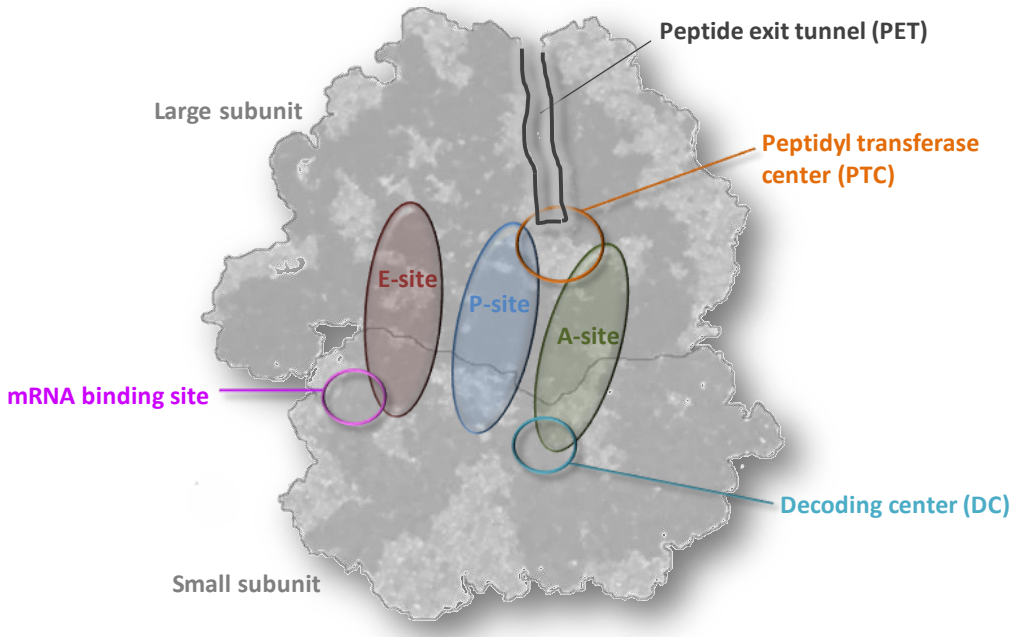

Figure 3: Essential functional sites of the ribosome.
The whole ribosome is divided in two subunits (in grey), the small one (bottom) and the large one (up). The A-, P- and E-sites are in green, blue and red, respectively. The global position of decoding center (DC) and the mRNA binding site on the small subunit are indicated in turquoise and pink, respectively. The peptide exit tunnel (PET) and the peptidyl transferase center (PTC) are indicated on the large subunit in black and orange, respectively.

Finally, the termination step occurs classically when ribosome meets a stop codon (**Figure 1**, step 5-7), which can be either UAA (“ochre”) or UAG (“amber”) or UGA (“opal”) (Korostelev, 2011; Ramakrishnan, 2002). The hydrolysis of the peptide bond between the P-site tRNA and the newly synthesized protein induces the peptide release and the dissociation of all factors. Finally, mRNA and tRNA dissociate from the small subunit and initiation factors can interact again with the small subunit to begin a new cycle of translation.

2. The ribosome, a remarkable ribonucleoprotein complex

The platform for protein synthesis is the ribosome, a massive and complex ribonucleoprotein particle with a RNA-protein ratio of 2:1. Ribosomes across all domains of life are asymmetric molecules and composed of two subunits whose names are defined by their sedimentation coefficient in Svedberg (**Figure 2**). The small subunit (30S in bacteria and 40S in eukaryotes) and the large one (50S and 60S, respectively) interact together to form the whole ribosome (70S and 80S, respectively). The small subunit is responsible for the decoding process in the DC and ensures the fidelity of the translation. The large subunit contains the PTC which catalyzes the peptide bond formation (**Figure 3**). The PTC is located at the entrance of the peptide exit tunnel (PET) in a highly conserved region of the ribosome. The three tRNA sites straddles the two subunits and have specific roles during translation (**Figure 3**). The A-site allows the arrival of aa-tRNA, the P-site is occupied by the peptidyl-tRNA, carrying the nascent peptide chain, and the E-site contains the uncharged tRNA before its exit from the ribosome. The polypeptide chain being synthesized progresses in the peptide exit tunnel (PET) before being totally exposed to the cellular environment.

Ribosomal RNAs (rRNA), localized in the center of the molecule, ensure the catalytic activities of each subunit and are recovered by proteins thanks to numerous interactions. Despite specific sets of rRNAs, proteins, extensions and interactions, bacterial and eukaryotic ribosomes share a common core (**Figure 2**). The ribosome composition can however vary between individuals, organelles or even within an individual. The bacterial small subunit is made of 21 proteins and one rRNA, the 16S, while in lower eukaryotes the 40S is constituted of 33 proteins and the 18S rRNA. The 16S or 18S rRNA is involved in the mRNA binding and the decoding process. In bacteria, as well as in eukaryotes, the small subunit is divided in three major domains: the 5’ domain called the body, the central domain known as the platform and the 3’ domain named the head (Kastner et al., 1981; Wimberly et al., 2000). The large subunit is more sophisticated with 2 rRNA (23S and 5S) and 33 proteins in bacteria compared to 46 proteins and 3 rRNA (25S, 5.8S and 5S) in lower eukaryotes. The biggest rRNA (23S or 25S) is responsible for the peptidyl transferase activity of the ribosome (Monro, 1967) and is also the main component of the PET.

A lot of interactions between rRNA and proteins are involved in the ribosome assembly. rRNA-rRNA interactions are mostly located in the center of the complex whereas protein-protein or rRNA-protein bonds are rather on the periphery (Dunkle et al., 2011). Both subunits interact through several contact points. Seven intersubunit bridges are conserved between bacteria and eukaryotes, but several bridges are between bacteria- or eukaryotic-specific elements (Ben-Shem et al., 2011; Selmer et al., 2006).

3. The translation, a target of choice for therapeutic compounds

One of the major world health problems is the increasing difficulty to fight against bacterial infections. The appearance of antibiotics, at the end of 19th century, was a huge revolution for medicine. Indeed, released from bacterial and fungal infection threat, the modern medicine era began with invasive surgeries, chemotherapies, transplantations, … Antibiotics are small inhibitory molecules which can perturb essential processes implied in cell growth and division of bacteria. Among them, the protein synthesis has become a target of choice by targeting either the ribosome or translation factors. To date, half of available drugs binds to the ribosome (Wilson, 2014). Unfortunately, the overuse of drugs in agriculture or in animal and human therapeutic treatments has enabled the selection and spread of drug-resistant bacteria (Blair et al., 2015; Brown and Wright, 2016). Recently, some antibiotic-resistant genes have even been discovered in strains of the high Arctic, which is yet one of the most secluded places on Earth (McCann et al., 2019). Thus, the pharmaceutical world has been forced to renew itself in order to find new efficient compounds.

In the past few years, translation has also become an interesting target for treatments of some human diseases, non-related to microbials. Indeed, the deregulation of protein synthesis can lead to dramatic pathologies, as cancer. Drugs targeting the human ribosome therefore appeared as an alternative strategy in anti-cancer treatments to reduce uncontrolled cell proliferation (McClary et al., 2017; Prokhorova et al., 2016). Disruption of translation also constitutes an area of study for the treatment of genetic disorders induced by nonsense mutations (Karijolich and Yu, 2014). For instance, the aminoglycoside antibiotic family, which normally targets the decoding center of bacterial ribosome, is able to promote the suppression of the premature translation termination in eukaryotic cells (Nudelman et al., 2009; Prokhorova et al., 2017). Furthermore, the IRES-mediated initiation pathway and IRES elements also emerged as potential therapeutic targets (Komar and Hatzoglou, 2015). For example in antiviral treatments, viral IRESes could be targeted to block the viral replication (Martinez-Salas et al., 2018). More recently, cellular IRESes became a promising target for anti-cancer therapies since in certain stress conditions, a subset eukaryotic mRNAs use also IRES-dependent protein synthesis (Vaklavas et al., 2015, 2017).

II. Biophysical approaches for studying interactions between the ribosome and its translational partners

1. Overview of major advances on ribosome

Due to the importance of the protein synthesis process in drug development strategies, the study of bacterial and eukaryotic translation became very attractive in the second half the 20th century. Since its discovery in 1955 by Georges Palade, a lot of breakthroughs highlighted the mechanism of action of the ribosome and associated factors during translation cycle. During the 50's and 60's, several biochemical studies led to a better understanding on the role of the ribosome in the different steps of the protein synthesis, together with the identification of all translational actors. An important discovery was the cracking of genetic code in 1966 which allows understanding the fundamentals on the correspondence between nucleotides and amino acids.

Then, a structural era began with the announcement of the first crystals of 50S in 1981 (Appelt et al., 1981) and the first diffraction pattern in 1991 (von Böhlen et al., 1991) by Pr. A. Yonath. In the same period, the first crystallographic data for the whole bacterial ribosome were also obtained (Trakhanov et al., 1989; Yusupov et al., 1991), as well as ribosome-tRNAs complexes (Yusupova et al., 1991). Those works were the firsts among numerous studies to decipher the structural complexity of the ribosome. The first high-resolution crystallographic structures appeared at the beginning of this century (Schmeing and Ramakrishnan, 2009), including the structure of the 30S by Pr. V. Ramakrishnan (Wimberly et al., 2000) and the 50S by Pr. T. Steitz (Ban et al., 2000) which earned them the Nobel prize in 2009 together with Pr. A. Yonath. Those structural bases have paved the way for several reference structures of the 70S with increasing resolutions (Schuwirth et al., 2005; Yusupov et al., 2001) and for the first translation complex (Selmer et al., 2006).

Regarding the eukaryotic ribosome, its structure was only discovered lately, with first the publication of the crystallographic structure of the yeast 80S in 2010 by Ben-Shem et al., followed few years later by the presentation of the human ribosome (Khatter et al., 2014). Finally, several dozens of ribosome complexes (bacterial or eukaryotic) with substrates, RNA or protein factors are currently available.

In parallel to crystallography, the cryo-electron microscopy emerged as a promising structural technic and the first tridimensional structure of the bacterial ribosome was obtained in the mid 90'S (Frank et al., 1995; Stark et al., 1995). The important technical advances in cryoEM allow now to reach same range of resolution than in crystallography (Bartesaghi et al., 2015; Jobe et al., 2019). More recently, new biochemical methods were also developed to analyze global and in vivo translation, as the ribosome profiling, or to decipher ribosome movements during the translation, as single-molecule approach using FRET.

Among all strategies to understand better how the ribosome works during the translation, the characterization of its interaction with all partners is fundamental. For those studies, as illustrated by the overview of major discoveries, the most preferred approaches are structural and biochemical methods. Thanks to a panel of structures of drug-bound ribosome or translation complexes, extensive underlying molecular mechanisms were established. Despite the importance of those information, thermodynamics and kinetics are also needed to provide data on the dynamic and driving forces of interactions in order to understand fully mechanisms at the atomic level.

2. Thermodynamic characterization of biological systems

A. The basics of thermodynamics

Thermodynamics is a branch of science that study heat, energy and the ability of that energy to do work. Thermodynamics became helpful in modern biology to give molecular interpretations of biological events and show how particles of life are *moved, moulded and conformed* (D'Arcy Thompson, 1917). Indeed, statistical principles of thermodynamics are relevant for systems with many particles, as in biological complexes. The thermodynamics relies on two fundamental laws: the energy is conserved (no creation or loss, only exchanges) and the entropy can only increase (universe entropy increase upon any spontaneous transformations). To understand such theories, it's important to clarify all basic notions and define a few crucial quantities (Physical Biochemistry, Van Holde, 1971).

We always speak about the thermodynamics of "a system". A system is actually a part of the universe chosen for the study and can be either open, if matter and energy are transferred, or closed, when only energy can be exchanged, or isolated, in absence of any exchange, like for the universe (**Figure 4**). The state of a system can only be defined at the equilibrium and changes in equilibrium states may be reversible or irreversible. The state of a system also depends on variables, called state variables, such as temperature, pressure and volume. In thermodynamics, functions of state variables are called state functions and define the equilibrium state of thermodynamic systems.

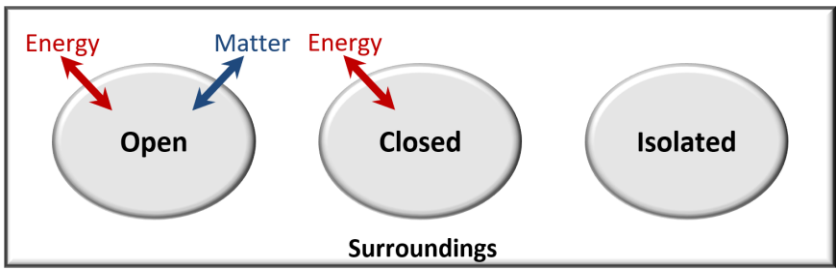

Figure 4: Schematic representation of the system diversity.
In an open system energy and matter can be exchanged with the surroundings while in a closed system, only energy can be exchanged. In an isolated system, like the universe nothing is exchanged.
In a system of interactions, the energy (E) is seen as the capacity to do work or produce heat.

The heat (Q) corresponds to the energy transferred into or out of a system, following a temperature change. Any other exchange of energy between a system and its surroundings corresponds to the work (W). The system possesses an internal energy (E), which is a function of state that involved translational, rotational and vibrational energies of the molecules, but also the energy of chemical bonds and nonbonding interactions between molecules. If we consider additional volume and external pressure exerted on the system, we do not speak about internal energy anymore but about enthalpy ($H = E + PV$). The change in enthalpy (ΔH) corresponds to the energy released or absorbed by a system for the reaction to happen. The heat absorbed by a process at constant pressure measures ΔH, while at constant volume it measures ΔE. However, as in biological systems, P is constant and V changes are still small, the heat exchanged corresponds to the enthalpy variation in all calorimetry experiments ($\Delta H = \Delta E$). Furthermore, the enthalpy increase by degree of temperature increase is defined by the heat capacity (C in $kcal.K^{-1}$). In other words, it is the amount of energy needed to raise the temperature by 1 °C; and the molar heat capacity (Cp in $kcal.mol^{-1}.K^{-1}$) is more precisely for one mole of a substance.

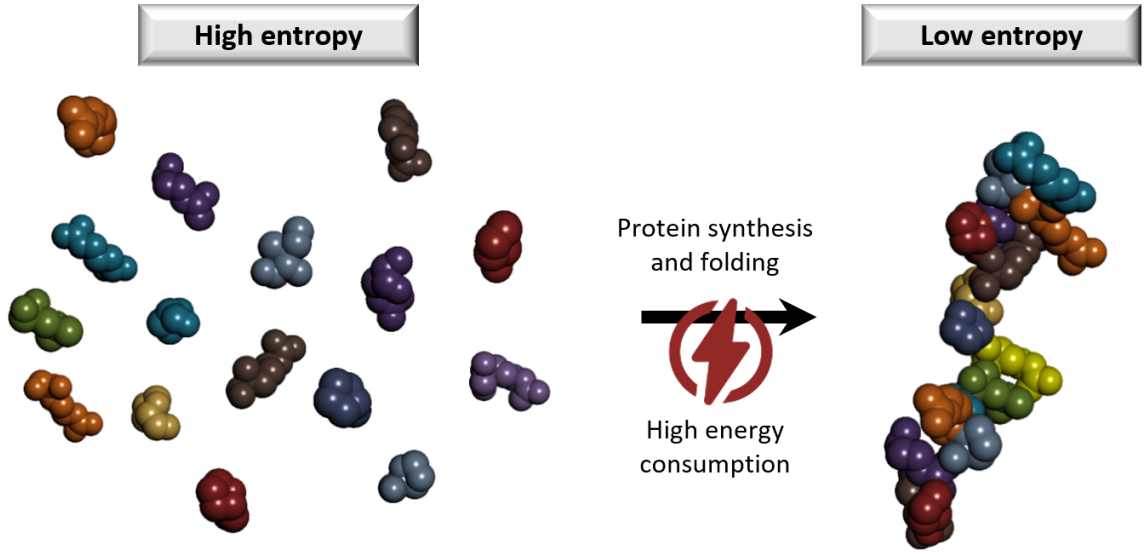

Figure 5: Concept of entropy illustrated with protein synthesis.
The assembly of dispersed amino acids (on the left) into structured proteins (on the right) decrease the entropy by decreasing the disorder of the cell. But as compensation, the high consumption of energy, to attach and fold all aa together, favors the increase of disorder and allow the following of the 2nd thermodynamic law.

One of the determinants of the equilibrium of a system with many particles is the randomness of the system or the number of ways in which the particles may be distributed (**Figure 5**). To describe this measure of the disorder, the last essential concept, without which modern thermodynamics would not exist, is the entropy (S). A negative change in the entropy (ΔS) means a decrease of the disorder. According to the 2nd thermodynamic law, a spontaneous process must correspond to an increase of the total entropy of the universe ($\Delta S_{universe} = \Delta S_{system} + \Delta S_{surroundings}$).

Indeed, the propensity of entropy to increase drives systems to reach equilibrium state, which is the most stable but the less ordered one. The energy, provided to decrease the entropy of a given system, increases the total entropy of the universe. At constant E and V, an isolated system will be at equilibrium only when the entropy reaches a maximum. As biochemistry works at constant T and P and the entropy cannot be directly used, a new function of state was defined, the Gibbs free energy. Gibbs and von Helmholtz established a strong relation with the temperature at a constant P, saying that the Gibbs free energy is the difference between heat energy and entropic energy (G = H - TS) (**Figure 6**).

Gibbs free energy represents the free energy of the system and is the most important state function of a system. Its variation (ΔG) measures the amount of energy that is available to do useful work and informs us about the spontaneity of a process. (It should be noted that in biology, ΔG is normally defined as ΔG' but we usually use ΔG). A system will always spontaneously evolve to a lower energy state. When ΔG < 0, the reaction is spontaneous and qualified as exergonic while for a ΔG > 0 the reaction is endergonic, *i.e.* non-spontaneous. The ΔG is also linked to equilibria constant of a reaction through the law of mass action ΔG = -RT * Ln Keq, where Keq is the association constant at the equilibrium, also called Ka. The opposite term Kd is the dissociation constant (Ka = 1 / Kd) which is usually used to define the affinity of an interaction system. The lower the Kd, the higher the affinity.

A last relationship allows to correlate the affinity variation of an interaction system with the temperature, to the change in temperature (T) given the standard ΔH, this is the Van't Hoff relationship. To simplify, affinity increases with decreasing temperature.

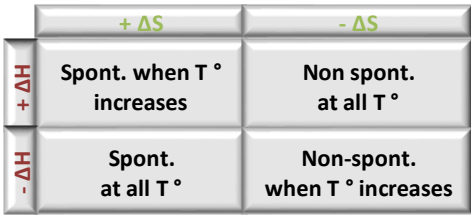

Figure 6: Relation between Gibbs free energy and temperature.
Spontaneity (spontaneous: Spont. and non-spontaneous: Non spont.) of reactions, represented by the Gibbs free energy variation, is related to the evolution temperature (T°) or not.

B. Thermodynamics and life

Energy is needed for all biological processes that allow a cell to survive: synthesize and fold macromolecules (as the formation and functional folding of proteins from amino acids in **Figure 5**), maintain its highly organized structures, ensure intra- and extracellular molecule concentrations, do mechanical work (as muscle contraction) and realize all the underlying chemical reactions.

The living constantly seeks to create order in a world that is tending towards more and more disorder. A living cell is a low-entropy system, because equilibrium and life are not compatible. In biological systems, entropy forces are dominated by reactions that on one hand create order, but on the other hand consume a lot of energy, leading to the distance of the equilibrium state (**Figure 5**).

Consequently, a cell is an open system that always maintains a nonequilibrium state by permanent exchanges with its environment to follow the 2nd law of thermodynamic. The surroundings entropy is increased and its ΔS must be positive and greater than the one of the cell. The energy is stored in bonds, transferred between atoms and molecules to find stable forms and released to the environment to do work.

Some biological reactions require energy to happen because of their non-spontaneity nature. Thus, the energetic coupling with exergonic reaction is a very convenient strategy to get energy, as long as they have a common intermediate and a global negative ΔG. For instance, he protein synthesis by the ribosome is a perfect illustration of this concept, since the correct assembly of amino acids into protein, which corresponds to a disorder decrease, requires energy provided by ATP hydrolysis (**Figure 5**).

C. Microcalorimetry and Isothermal Titration Calorimetry

Calorimetry is the method of choice to study thermodynamics. It is the science to study heat exchanges in chemical processes and physical events. More precisely, the microcalorimetry is applied to reactions of biomolecules following interaction and conformational changes. To perform such studies, the isothermal titration calorimetry (ITC) is the gold standard method which allows the characterization of interaction between molecules in a single experiment and without any label. All binding parameters can be determined: the stoichiometry N, the enthalpy variation ΔH (cal.mol^{-1}), the entropy variation ΔS (cal.mol^{-1}.K^{-1}), the Gibbs free energy variation ΔG (cal.K^{-1}.mol^{-1}) and the affinity constant Kd (mol.L^{-1}). It is a useful tool in candidate selection, clarification of action mechanisms, specificity evaluation and of course in drug development.

a. ITC device

The microcalorimeter is a very sensitive device able to detect temperature changes during gradual titration. Since ΔH is equal to the heat absorbed or released by the system (because P is constant), enthalpy changes is directly measured during chemical reactions. The microcalorimeter is composed of three main elements: a reference cell filled with water or buffer, a sample cell containing the molecule of interest and a syringe filled with the ligand (**Figure 7A**). Each cell is equipped by heaters, to control the temperature, and a temperature sensor is present between them. A small, constant and precise difference of temperature is maintained between the two cells. As soon as the detector senses any change of temperature in the sample cell following a binding event, heaters will compensate this heat, thus generating a peak on the thermogram (**Figure 7B**). Thus, the amount of heat exchange is directly proportional to the amount of binding. When the cells come back to being equals and the signal return to its initial position (the initial baseline), the thermodynamic equilibrium is reached. Small aliquots of ligand molecules are successively injected and the molar ratio between analytes increases until molecules in the cell are totally saturated. This is used to calculate the stoichiometry of the reaction.

Two types of heat exchanges can be observed: absorption of heat for an endothermic reaction or heat release for an exothermic reaction. For exothermic reactions, the sample cell gets warmer than the reference cell so a negative ΔH is obtained, and a downward peak is observed with our calorimeter. On the contrary, for endothermic reactions the sample cell gets colder than the reference one, so an upward peak is observed, and a positive ΔH is obtained. Following integration of all peaks by a dedicated software, a titration curve is generated, which corresponds to a sigmoid in classical one set of binding site situation (**Figure 7B**). Binding parameters of the interaction are then also automatically estimated using the fundamental relationship ΔG = - RT * Ln Ka = ΔH – TΔS. The constant of association at equilibrium is directly related to the slope of the curve (**Figure 7B**).

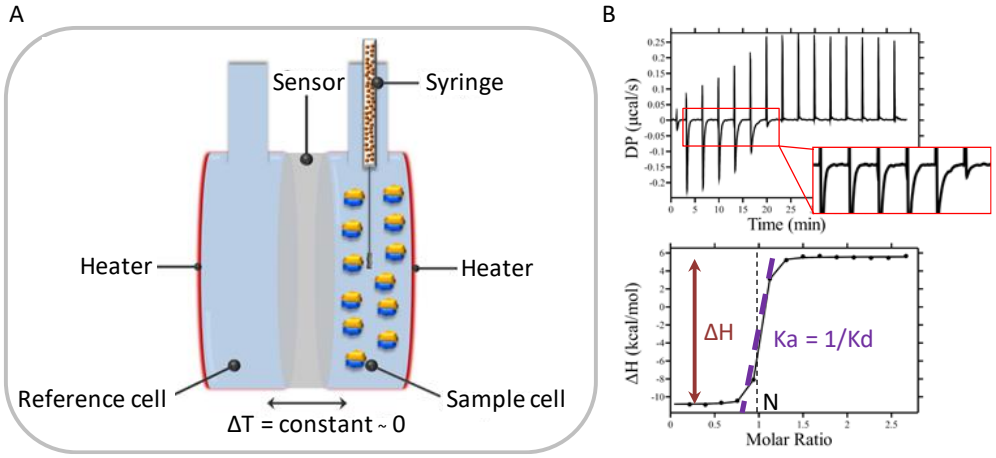

Figure 7: Composition of ITC device and interpretation of signals.
Elements of ITC are presented in (A). The sample cell and syringe are filled with analytes, ribosomes and antibiotics, respectively. An example of thermogram (up) and titration curve (bottom), obtained from integrated peaks, and from which some parameters (enthalpy variation ΔH, association constant Ka and stoichiometry N) can directly be calculated, is presented in (B).

b. Molecular interpretations

The state functions ΔH and ΔS give information about bond formation and molecular events. Indeed, the ΔH of an interaction mostly represents the difference between bonds at the initial and final states and is the result of all positive and negative influences (hydrogen bonds, electrostatic and van der Walls forces). Whereas, ΔS translates the global degree of conformational liberty upon a complex formation and the establishment of hydrophobic interactions via the destructuring of the hydration network. The thermodynamic profile, which is the combination of ΔH, ΔS and ΔG, provide information on enthalpy or entropy contributions and which forces drive the interaction. If enthalpy or entropy drive the forces in favor of the complex formation, the interaction is defined as enthalpy-driven or entropy-driven, respectively. Then, the strength of the interaction is given by the Kd and the stoichiometry indicates the number of binding sites. Interesting information can also be extracted from experiments performed at several temperatures through the change in heat capacity (ΔC_p), which is the derivative of the enthalpy variation with temperature.

This notion is extremely important in calorimetry since it relates thermodynamics and structural rearrangements. ΔC_p determination provides information about the variation of contact surface area between proteins and the solvent (Livingstone et al., 1991). A negative ΔC_p is typical of important structural rearrangements and a large reduction of contact with the solvent. It was shown that a good approximation of the number of hydrophobic aa involved into structural rearrangement can be obtained with ΔC_p (Spolar et al., 1989).

c. Experimental considerations

A successful ITC experiment relies on some critical features, such as suitable sample concentrations, strictly identical buffer composition between syringe and cell molecules, or a ΔH sufficiently different from 0 to ensure a good signal-noise ratio. The most important experimental consideration is the dialysis of each studied molecule in the same buffer. Indeed, the microcalorimeter is so sensitive that any difference between buffers can generate a buffer mismatch due to the heat of dilution of buffers. Moreover, the quality of a titration also depends on the concentration of each molecules. Indeed, ITC requires mg of biomolecules to obtain low signal-noise ratio. To improve signal intensity, concentrations can be increased almost as much as desired, depending on the studied molecule and its limits of production. For instance, with ribosome, the amount used for only one experiment can reach 15 mg, which corresponds to around 300mL of culture (this is a lot!).

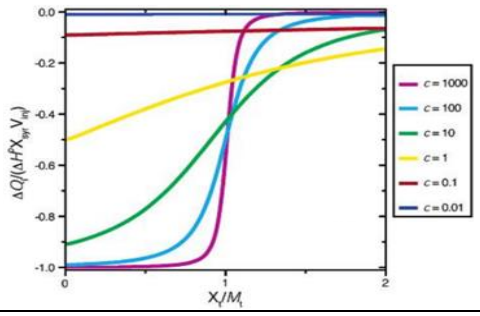

Figure 8: Influence of c value on titration curve shape. From Turnbull and Duranas, 2003.

Syringe and sample cell concentrations are estimated using the Wiseman coefficient (c = [sample in the cell] - Kd). To obtain an exploitable titration curve, the optimal c value is between 10 and 500; values between 1 and 1000 are still acceptable (**Figure 8**) (Tellinghuisen, 2005; Wiseman et al., 1989).

3. Kinetic characterization of interactions

A. Importance of kinetics in biological processes

Kinetics deals with evolution of reactions over time and provides quantitative measurements of biological binding reactions (affinity, association and dissociation constants); that is to say, how fast concentrations of reactants and products change with time.

The dissociation constant Kd is actually the result of the equilibrium between association (kon or on-rate) and dissociation (koff or off-rate) rates: Kd = koff/kon; so, for a same Kd, we can have totally different association and dissociation rates (**Figure 9**). Key factors affecting the dissociation constant are the temperature and the presence of a catalyst.

As thermodynamics alone does not allow the determination of which of association or the dissociation event is critical for the interaction (**Figure 9**), kinetic analyses are complementary. Indeed, this is the only way to have a dynamic dimension about transition states. The kinetic aspects are therefore important and allow, together with thermodynamics, to have a complete overview of a molecular interaction.

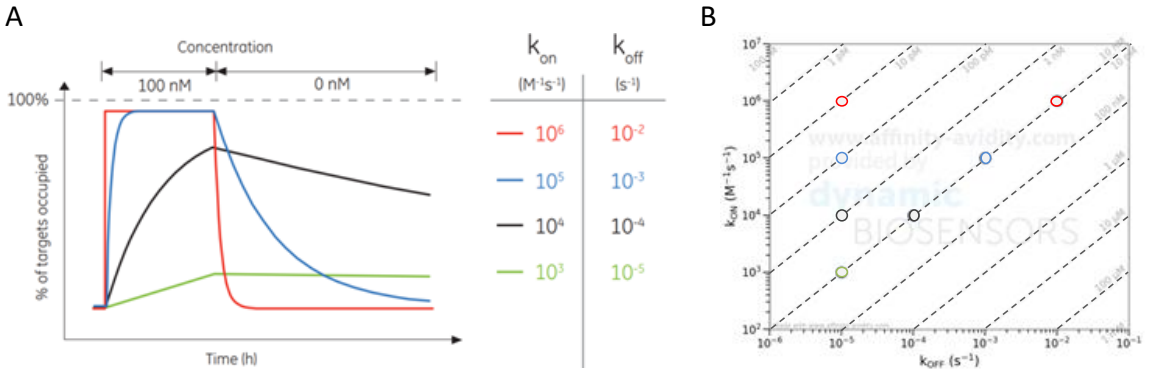

Figure 9: Influence of on- and off-rates on the affinity constant Kd.
Simulation of on- and off-rates for a same Kd of 10 nM with kinetic curves (by Markku D. Hämäläinen, GE Healthcare) in (A) or with the affinity map representation (https://affinity-avidity.com by Dynamic Biosensors) in (B).

B. kinITC, an ITC-derived approach

The potential for the ITC to provide kinetic data has been ignored for a long time. In chemistry, the relation between the measure of the heat power and kinetics has already been investigated, but not in biology. My host lab recently developed a methodology to get a complete kinetic description of biological systems using ITC data, termed kinITC (Burnouf et al., 2012; Dumas et al., 2016).

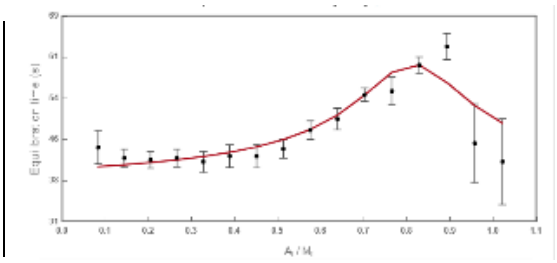

Figure 10: Equlibration time curve (ETC).
Time to return to the baseline after each injection is plotted against molar ratio of the titration experiment.

The heat exchanged during a reaction corresponds to the instant power integrated over time. Each peak in an ITC experiment is due to the heat power evolved in the measurement cell by the reaction between compounds. Importantly, it was shown that the shape of each injection peak provides kinetic information by analyzing the time required to return to the baseline after each injection, called the equilibration time (**Figure 7B**). If the resulting Equilibration Time Curve (ETC) has bell shape, it allows the determination of the off-rate (**Figure 10**).

Then, knowing Kd and koff, kon can be deduced. This new application for ITC was possible thanks to technical advances on last generation microcalorimeters (smaller cell sample volume, faster response time of the instrument) and to a collaboration between AFFINImeter and Dr. Philippe Dumas (Muñoz et al., 2019; Piñeiro et al., 2019).

C. SwitchSENSE® technology, an innovative strategy

Among all emerging techniques available for kinetic study, switchSENSE® technology appeared as very innovative in the solid-support immobilization field. By measuring analytes adsorption on a layer of actuated surface-bound fluorescent probe, this new approach can be used to investigate on binding kinetics and affinity, but also on protein hydrodynamic radius, conformational changes, or even nuclease and polymerase activity. The originality of the switchSENSE® technology lies in the DNA (cNLA) strand bearing a fluorescent dye at one extremity, attached on its opposite end to a gold-quenching surface through a sulfur linker (**Figure 11**). The complementary strand (cNLB) could be used alone or conjugated to an interaction partner.

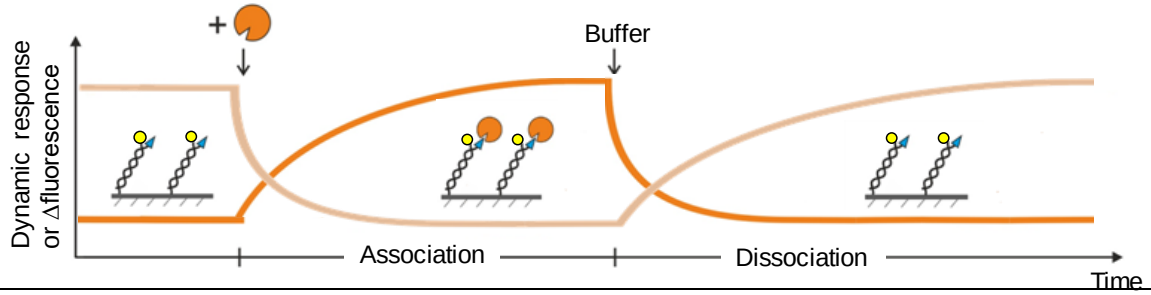

Figure 11: Principle of switchSENSE technology for kinetic analysis. Adapted from Dynamic Biosensors. The fluorochrome (in yellow) on the attached strand can be either quenched (dark orange signal) or not (light orange signal) by the conjugate (in blue). Addition of the binding molecule, corresponding to the association step, can lead to either a fluorescence increase (dark orange signal) or decrease (light orange signal). Buffer addition causes the dissociation of the complex and restore the initial fluorescence level.

Hybridization of the DNA strands generates a rigid negatively charged electro-switchable biosensor, also referred as nanolever. Two principal measurement modes are then accessible (**Figure 12**): (i) a static mode, where analyte binding is measured thanks to variation of the fluorescence intensity, and (ii) a dynamic mode where binding is detected through the change of the oscillation rate of the probe actuated by an alternative electric field. Thanks to DNA plasticity and to many biochemical tools, a wide variety of nanolevers could be adapted to the biological context of the experiment. However, this approach was not thought for large macromolecular complexes such as a ribosome. In collaboration with Dynamic Biosensors, we extended the application field of this technology to studies with ribosome complexes.

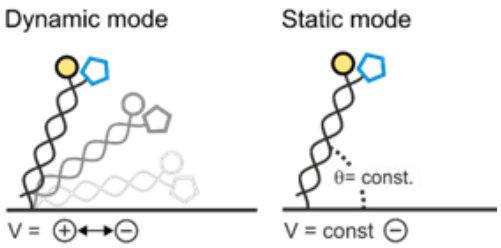

Figure 12: Different measurement modes of the switchSENSE. From Dynamic Biosensors.

III. Thesis objectives

The global vision of our team is to characterize molecular machines using biophysical approaches. Several projects focus on the translation and its inhibition in prokaryotes or eukaryotes. In this context, the aim of my PhD was to thermodynamically and/or kinetically characterize two different systems of interaction with the ribosome.

The first objective of my PhD was to study the interaction between drugs and bacterial ribosome, which is the major target of marketed therapeutic compounds. Resistant bacteria have become increasingly out of control. Thus, it's important to know how drugs exactly work and what are the resistance mechanisms in order to be able to develop new effective antimicrobials. Among the drugs of a great therapeutic interest, macrolides are one of the older class and have even been designated as a priority for drug development by the world health organization (WHO). As several structural and biochemical studies are already available, we characterized the interaction thermodynamically using Isothermal Titration Calorimetry (ITC). Although ITC is a gold standard method to investigate on binding parameters between molecules, it's not so widespread in the field of translation. To set up the strategy and to ease biological sample production, this work was done with ribosome and translational factors of the model bacteria *Escherichia coli*. Thermodynamics of antibiotic binding would provide interesting and complementary information for a better understanding of macrolide mode of action.

The second part of my PhD project was focused on the hijacking of eukaryotic translation by viruses through the IRES-mediated initiation pathway. IRESes are well-known non-coding RNA structures that can directly recruit the ribosome to initiate translation with a reduced set of initiation factors. The intergenic class of IRESes is the simplest initiation system ever characterized among all domain of life, with notably the well-known example of the IGR IRES of the cricket paralysis virus (CrPV). This group of IRESes is used since many years to better characterize several aspects of translation, whether IRES-dependent or not. It was proved to be active on a wide range of ribosomes, including yeast which is used in this work. As for the studies on antibiotics, few data about thermodynamics, or kinetics, are known for the interaction of IGR IRES with eukaryotic ribosome. Using innovative biophysical approaches, as ITC and switchSENSE, we wanted to better characterize the dynamic of IRES binding to the ribosome. In parallel, we wanted to use this system of interaction as a proof of concept for further thermodynamic and kinetic investigation on human pathogenic virus IRESes.

Combining thermodynamics and kinetics with available atomic structures will allow a better understanding of the molecular interactions and forces involved in complex formation, which are fundamental information for strategies of drug development. Altogether, my project focused on two different aspects of translation, but with similar approaches.

CHAPTER II

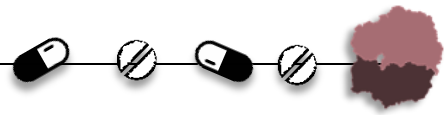

THERMODYNAMIC STUDY OF ANTIBIOTIC BINDING TO THE BACTERIAL RIBOSOME

Class	Well-known members	Origin	Inhibited step	Mode of action	Antibacterial activity and clinical use	Resistance mechanisms
Aminoglycosides*	-mycin subclass: streptomycin, neomycin, spectinomycin, hygromycin B, kasugamycin -micin subclass: gentamicin, verdamicin	*Streptomyces spp.* *Actinomyces spp.* *Micromonospora spp.*	Decoding, translocation and recycling	Bacteriocidal Bacteriostatic in some cases	Infections related to aerobic G- bacteria	
Tetracyclines	Original class: doxycycline, tetracycline Glycylcyclines*: tigecycline	*Streptomyces* spp.and semi-synthetic derivatives	A-site tRNA delivery	Bacteriostatic	Broad spectrum Infections related to urinary, respiratory and intestin tracts	
Tuberactinomycins*	Viomycin Capreomycin	*Streptomyces puniceus* *Streptomyces capreolus*	Translocation	Bacteriostatic	Anti-tuberculosis properties, especially active on *Mycobacterium tuberculosis*	
Odilorhabdins	NOSO-95 derivatives	*Xenorhabdus nematophila*	Decoding at low concentrations Translocation at high concentrations	Bacteriocidal	*Ongoiing reserach and clinical trials to come* Broad spectrum activity, including carbapenem-resistant pathogens	
Negamycins	Negamycin	*Streptomyces purpeofuscus*	Decoding and translocation	Bacteriocidal	*Never clinically approved* Broad spectrum, including resistant pathogens	
Edeines	Edeine A, edeine B	*Bacillus brevis*	Initiator tRNA binding	Bacteriostatic at low concentration Bacteriocidal at high concentration	Broad spectrum	
Streptogramins	Streptogramins A: Virginiamycin M Streptogramins B: Pristinamycin IA	*Streptomyces virginiae* *Streptomyces* spp.	Peptide bond formation Nascent chain elongation	Bacteriostatic Bacteriocidal for S_A and S_B combination	Infections related to VRSA and VRE strains	
Macrolides**	1st generation: pikromycin and erythromycin 2nd generation: azithromycin, josamycin	*Streptomyces spp.* *Actinomyces spp.* *Micromonospora spp.*	Nascent chain elongation (in a context-specific manner)	Bacteriostatic	Active on G+ bacteria and limited G- bacteria Infections affecting respiratory tract and soft-tissue infections	
Ketolides (macrolide 3rd generation)**	Telithromycin, solithromycin	Semi-synthesis from macrolides		Bacteriocidal	*Only telithromycinis clinically used* Effective against macrolide-resistant bacteria	
Lincosamides	Clindamycin, lincomycin	*Streptomyces spp. (S. lincolnensis, S. roseolus,* and *S. caelestis)*	Peptide bond formation	Bacteriostatic	Infections related to G+ bacteria and MRSA Alternative for penicillin-allergic patients	
Phenicols	Chrloramphenicol	Streptomyces venezuelae and chemical synthesis	Peptide bond formation	Bacteriostatic	Broad spectrum	
Oxazolidinones*	Linezolid, tedizolid	Chemical synthesis	Initiation (initiator tRNA and aa-tRNA positioning)	Bacteriostatic Bactericidial in some cases	Effective agasint G+ bacteria, including VRE, MRSA and PRSP Skin, pneumonia, and tuberculosis infections	
Pleuromutilins	Lefamulin Tiamulin	*Clitopilus* spp.	A-site tRNA delivery	Bacteriostatic	*Recently approved as emergent drug* Active against communinty-acquired bacterial pneumonia Veterinary medicine	
Orthosomycins	Evernimicin Avilamicyn	*Streptomyces virdochromogenes* *Micromonospora carbonacea*	Initiation complex formation and A-site tRNA delivery	-	Broad spectrum MRSA-related and VRE-related infections	
Thiopeptides	Thiostrepton, micrcoccin	Soil and marine bacteria	Factor binding	Bacteriostatic and bacteriocidal	Effective on G+ bacteria, including MRSA, and limited G- bacteria	
PrAMPs	Onc112, pyrrhocoricin Bac7, Tul1A	Insects Mammals	Nascent peptide elongation	Bacteriostatic and bacteriocidal	*Ongoing research* Active on pathogens with SbmA receptors	
Nucleoside analogs	Blasticidin S	*Streptomyces griseochromogenes*	Peptide bond formation and peptide release	Bactericidal	Broad spectrum	
Unassigned	Klebsazolicin	*Klebsiella pneumonia*	Nascent peptide elongation	-	*Ongoing research*	
	Thermorubin	*Thermoactinomyces antibioticus*	Initiator tRNA binding	-	Infections related to G+ and G- bacteria	

Abbreviations: sp.: species ; G+: Gram-positive bacteria ; G-: Gram-negative bacteria ; VRSA: vancomycin-resistant *S. aureus* ; VRE: vancomycin-resistant *Enterococcus* ; MRSA: methicillin-resistant *Staphylococcus aureus*. ; PRSP: penicillin-resistant *Streptococcus pneumoniae*

Broad spectrum: G+ and G- bacteria, and sometimes mycoplasmes, fungi and even higher eukaryotes.

Level of critically importance for the World Health Organization: *high priority, **highest priority.

Table 1: Principal features of most known ribosome-targeting antimicrobials.

Main classes of the ribosome-targeting antimicrobials (commercialized or under investigation) are listed with examples of the well-known members, the original producer micro-organisms, the affected translation step, their mode of action and their clinical use.

Chapter II: Thermodynamic study of antibiotic binding to the bacterial ribosome

I. Introduction: antibiotics inhibiting prokaryotic translation

1. Overview of major ribosome-targeting antibiotics

Most of the commercialized antibiotics target the ribosome and inhibit different steps of translation (**Figure 13**) (Arenz and Wilson, 2016; Lin et al., 2018; Wilson, 2014).

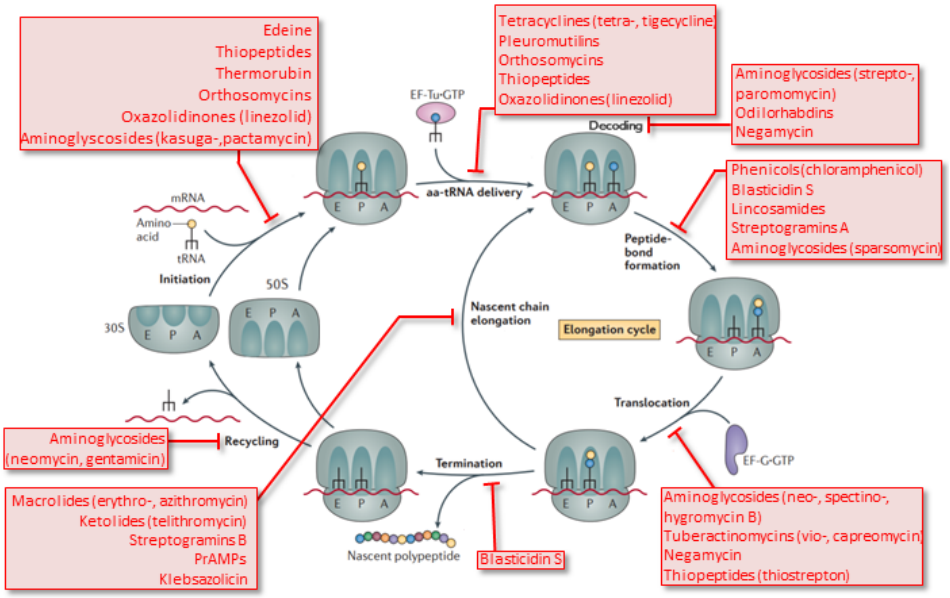

Figure 13: Translation steps affected by ribosome-targeting antibiotics. Adapted from Wilson, 2014.
Classes that affect the translation steps are indicated in red boxes. The initiation step corresponds to the formation of 70S ribosome with the mRNA and initiator tRNA well positionned in the P-site. The elongation cycle gathers several steps and represents the more targeted process of translation. The termination stage and the ribosome recycling can also be inhibited.

Only few conserved regions of the ribosome are targeted by drugs, often located in functional centers, either in the small or in the large subunit (**Figure 14**). The main features of known ribosome-targeting drug classes, such as their origin, the inhibition mechanism or the clinical use are briefly recapitulated in the **Table 1**.

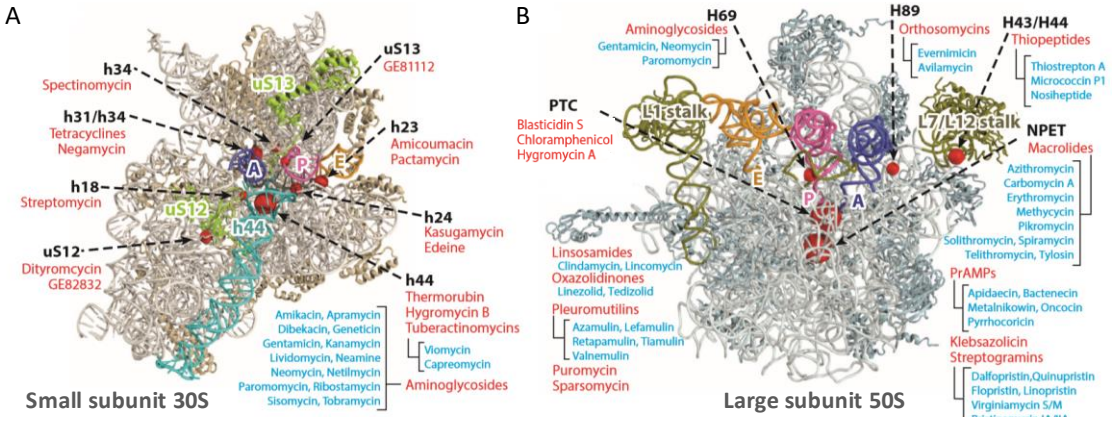

Figure 14: Binding sites of ribosome-targeting antibiotics. Adapted from Lin et al., 2018.
Binding sites of major antibiotics are represented by a red sphere on the small (A) or the large subunit (B) in complex with A- (in dark blue), P- (in pink) and E-site tRNAs (in orange). Main targeted functional sites of the ribosome are indicated by dashed black arrows.

A. 30S-targeting antibiotics

All 30S-targeting antibiotics bind to the decoding center (DC) or tRNA sites of the small subunit (**Figure 14A**) to block the initiation or the elongation steps by preventing tRNA binding or disrupting the ribosome dynamics (**Figure 13**).

a. Inhibitors of tRNA delivery and decoding

Normally, the DC drives the correct codon-anticodon interaction in the A-site. Some antibiotics inhibit this step by targeting a site at the top of h44, and more precisely two nucleotides important for the decoding event, A1492 and G530 (**Figure 15A**) (Abdi and Fredrick, 2005; Carter et al., 2000; Yoshizawa et al., 1999). A second crucial motif formed by A1492 and A1493 is also often disrupted upon DC-targeting drug binding. Indeed, those nucleotides must be flipped-out of h44 after cognate tRNA binding to induce a correct A-minor motif between the first two codon-anticodon base pairing (Ogle et al., 2001).

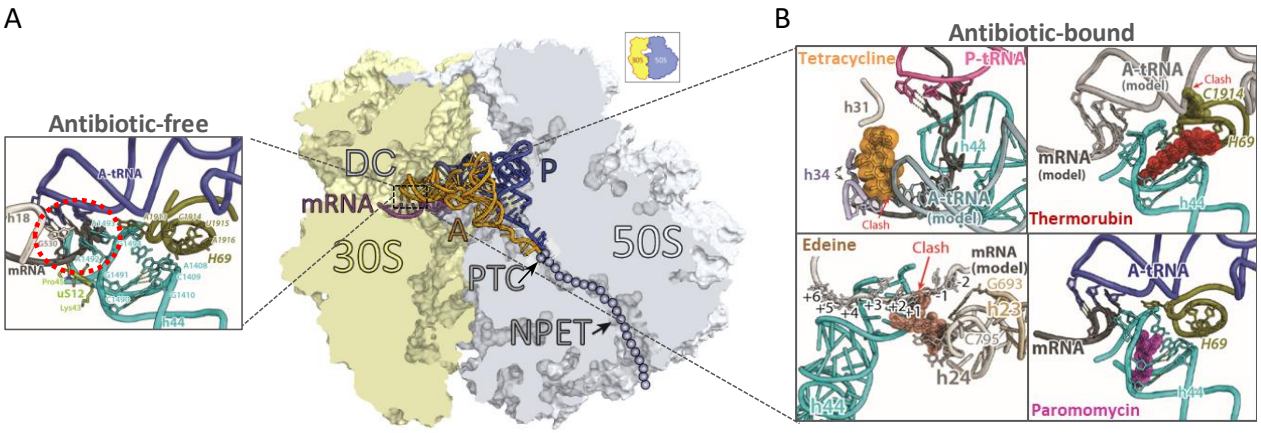

Figure 15: Molecular basis of interactions of some inhibitors of tRNA delivery and decoding processes in the decoding center of the 30 subunit.

The functional centers DC, PTC and PET are localized on the global structure of the bacterial ribosome with the 30S and 50S subunit complexed with mRNA, A- and P- site tRNAs (from Vazquez-Laslop and Mankin, 2018). (A) The molecular organization without antibiotic shows the key elements of rRNA and A-tRNA in the DC, with the three important bases G530, A1492 and A1493 in a dashed red circle (adapted from Lin et al., 2018). Detailed views of the interactions of tetracycline (PDB number: 4V9B), thermorubin (PDB number: 4V8A), edeine (PDB number: 1I95) or paromomycin (PDB number: 4V51) with the ribosome in the DC are presented in (B) (adapted from Lin et al., 2018). mRNA, A- and P- tRNAs and the helixes or residues are indicated.

The major classes of antibiotics that inhibit either tRNA delivery or codon-anticodon base pairing formation are tetracyclines and aminoglycosides. Tetracyclines inhibit aa-tRNA binding (Nguyen et al., 2014) through an overlapping binding site with the anticodon stem loop of the A-site tRNA. The broad-spectrum activity of tetracyclines is largely due to interactions with rRNA phosphate-oxygens of the backbone instead of specific rRNA bases (**Figure 15B**) (Wilson, 2014). The tigecycline, one of the latest tetracycline derivatives, has been optimized to have a better affinity for the ribosome and a more efficient antibacterial action (Jenner et al., 2013; Olson et al., 2006).

Then, most members of aminoglycosides, as streptomycin, gentamycin, paromomycin and neomycin, can induce delivery of near- and non-cognate tRNAs in the A-site. Indeed, they promote and stabilize the flipped-out conformation of A1492 and A1493 by interacting principally with h44 to increase miscoding events (**Figure 15B**) (Carter et al., 2000). Recent studies with *T. thermophilus* 70S suggested that non-cognate tRNAs are also able to stabilize this flipped-out conformation by Watson-Crick-like base pairing, independently from antibiotics, and that the high-energy consumption for maintaining this conformation results in the tRNA rejection (Demeshkina et al., 2012). Following this model, the drug binding could compensate this unfavorable interaction by local changes in h44 and H69.

Initiation steps can also be inhibited by other antibiotics. For instance, the thermorubin, which is chemically related to tetracycline, binds to the subunit interface of the 70S ribosome to inhibit tRNA delivery. Indeed, it induces rearrangements between two nucleotides of h44 and H69, involved in intersubunit bridges, leading to a clash with the incoming aa-tRNA (**Figure 15B**) (Bulkley et al., 2012). Furthermore, thermorubin also indirectly prevents the delivery of initiator tRNA in the P-site by perturbing IF1 activity. Despite its important antimicrobial activity, thermorubin is not suitable for clinical use because of its low solubility (Cavalleri et al., 1985). Finally, the peptide antibiotic edeine is also able to block fMet-tRNA^{Meti} binding by stimulating C795-G693 base pair formation that lead to a clash with mRNA (**Figure 15B**) (Pioletti et al., 2001).

b. Inhibitors of translocation and ribosome dynamics

Numerous antibiotics inhibit the translocation and, more generally, the ribosome dynamics. Negamycin and some members of the aminoglycoside family, such as hygromycin B, increases the aa-tRNA affinity for the A-site to stabilize this conformation and prevent translocation (**Figure 16A**) (Borovinskaya et al., 2008; Polikanov et al., 2014a). Other aminoglycosides affect the same processes by binding in P- and E-sites tRNA. Among them, the amicoumacin A interacts with conserved residues of the 16S rRNA in the E-site and with the mRNA phosphate backbone to anchor the mRNA in the ribosome, thus impairing translocation (**Figure 16B**) (Polikanov et al., 2014b). Few aminoglycosides, like pactamycin and kasugamycin, have an overlapping binding site with mRNA in the E-site and between P- and E-sites, respectively, leading to a disruption of the 30S initiation complex formation (**Figure 16B**) (Brodersen et al., 2000; Schuwirth et al., 2006). In the case of tetrapeptide GE81112, its binding to the P-site results in a stabilization of the anticodon-stem loop of the fMet-tRNA^{Meti} in an unusual conformation and in the reduction of 50S joining (López-Alonso et al., 2017).

The peptide-based class of tuberactinomycins are also able to prevent translocation by interfering with the global ribosome dynamics. For example, viomycin and capreomycin bind to the top of h44 at the ribosomal interface and induce the A1492-1493 flipped-out conformation, stabilizing intermediate conformation of the ribosome (**Figure 16A**) (Cornish et al., 2008; Stanley et al., 2010).

Finally, a new class of modified peptides, called odilorhabdins (ODLs), was recently discovered and exhibits encouraging broad-spectrum antibacterial activity (Pantel et al., 2018; Sarciaux et al., 2018). This innovative molecule binds to a different site of the DC that is not known for any other drug, and induces miscoding (Polikanov et al., 2018). By simultaneous interactions with 16S rRNA and the anticodon loop of aa-tRNA (**Figure 16C**), ODLs increase aa-tRNA affinity for A-site to anchor tRNA to the ribosome. A decrease accuracy of the decoding step is observed at low concentrations, while at high concentrations it also seems to hinder the tRNA translocation (Pantel et al., 2018).

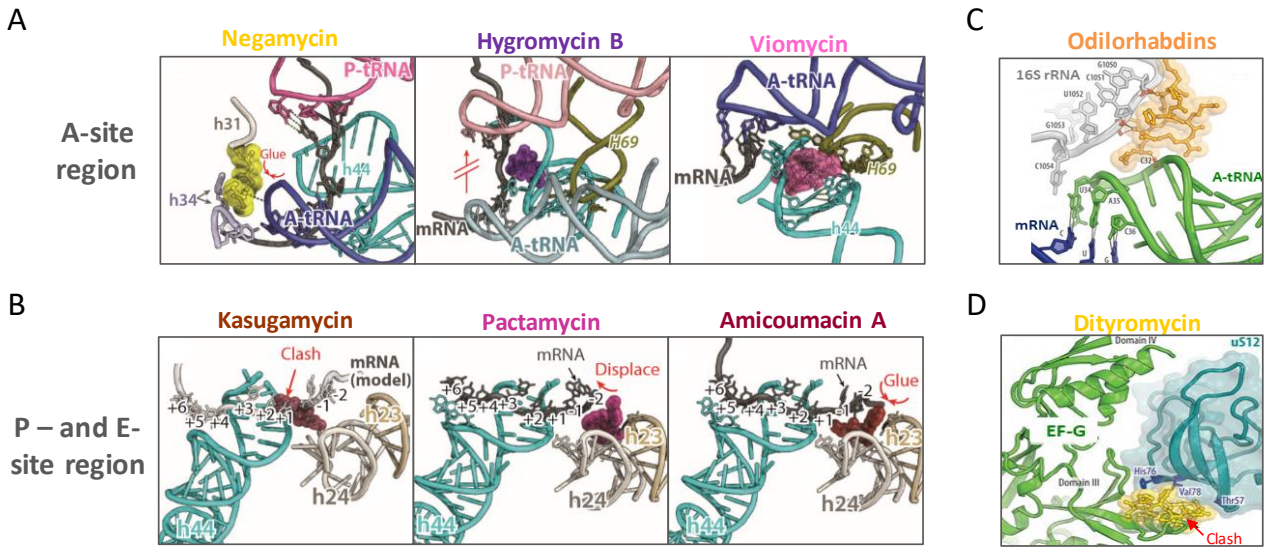

Figure 16: Molecular basis of interactions of few translocation and ribosome dynamic inhibitors in the decoding center of the 30S subunit.

Detailed views of drug interactions with the ribosome in the decoding center are presented. A-tRNA, mRNA, EF-G, 16S rRNA and their domains, helixes and residues are indicated. The effect of drug binding can be indicated in red. Negamycin (PDB number: 4W2I), hygromycin B (PDB number: 4V64) and Viomycin (PDB number: 4V7C) bind in the A-site region (A) while kasugamycin (PDB number: 2HHH), pactamycin (PDB number: 4W2H) and amicoumacin A (PDB number: 4W2F) have close binding sites in the P- and E- site regions (B) (Adapted from Lin et al., 2018). The new class of odilohabdins (C) and the dityromcine (D) present unique binding sites (adapted from Polikanov et al., 2018).

All antibiotics mentioned so far target the ribosomal RNA, but some antibiotics can bind to ribosomal proteins. For instance, the poorly characterized peptide-based dityromycin and its related compound GE82832 inhibit EF-G dependent tRNA translocation by binding to the ribosomal protein uS12 (**Figure 16D**) (Brandi et al., 2012; Bulkley et al., 2014). More precisely, when dityromycin binds to uS12 during tRNA translocation, it blocks the structural transition of EF-G from a compact to an elongated conformation (Lin et al., 2015).

B. 50S-targeting antibiotics

a. Antibiotics targeting the peptidyltransferase center

The large subunit is targeted by most of the ribosome-targeting antibiotic classes, such as macrolides, lincosamides, streptogramins, oxazolidinones, phenicols, and some aminoglycosides. Their binding site are all located in the peptidyltransferase center (PTC), either in the A- and P-sites or in the peptide exit tunnel (PET) (**Figure 17A**), to induce the inhibition of peptide-bond formation or abortion of nascent chain elongation (Nissen et al., 2000).

Among PTC-targeting antibiotics, the chloramphenicol interacts with the base C2452 of the 23S rRNA in the A-site crevice, through π-stacking interactions, leading to a steric clash with the amino acid of the incoming aa-tRNA (**Figure 17B**) (Bulkley et al., 2010; Dunkle et al., 2010; Lin et al., 2018). However, recent evidences suggest a context-specificity action which depends on the nature and identity of the amino acid (Marks et al., 2016).

Some members of other classes, such as lincosamides, aminoglycosides or oxazolidinones, bind to the A-site pocket still preventing the peptide bond formation (**Figure 17B**) (Hansen et al., 2003). The lincosamide structure consists in an unusual proline amino acid linked to a galactopyranoside sugar by a peptide bond. Lincomycin, the original member of this class, has a propyl hygric acid group in the PTC which interferes with positioning of aa-tRNA 3' end and blocks peptide bond formation (**Figure 17B**) (Polikanov et al., 2014c). Regarding the aminoglycoside sparsomycin, a fragment of its tail makes hydrophobic interactions with the A-site crevice and another region is trapped between the CCA-end of the P-site tRNA and the base A2602 (**Figure 17B**) (Hansen et al., 2003; Schmeing et al., 2005). In addition, sparsomycin stabilizes P-site tRNA to stimulate A-site tRNA translocation (Marks et al., 2016), just as the related compound blasticidin S (Svidritskiy et al., 2013).

Blasticidin S is a nucleoside analog, genetically engineered as a selection antibiotic for mammalian and bacteria cells, which competes with P-site tRNA binding to inhibit peptidyl-tRNA hydrolysis. It seems that blasticidin S enhances aa-tRNA binding to the P-site to the detriment of binding to the A-site (Svidritskiy and Korostelev, 2018). Furthermore, structures show a Watson-Crick interaction with the G2251 in the P-loop and a twist of P-site tRNA 3'end to displace the C75 nucleotide from its canonical position in the PTC (**Figure 17B**) (Svidritskiy et al., 2013).

The oxazolidinone member linezolid, has a binding site close to the one of sparsomycin in the A-site cleft (**Figure 17B**); π-stacking interactions are formed between the linezolid ring and the base U2504 while the fluorophenyl group stacks with the C2452 (Ippolito et al., 2008; Leach et al., 2007; Wilson et al., 2008). The remaining moiety is suspected to collide with the 3'end of aa-tRNA and blocking its entry. Nevertheless, despite its location in the A-site, the linezolid emerged as an inhibitor of translation initiation by perturbing the initiator P-site positioning (Leach et al., 2011).

Some antibiotic target sites also occupy regions in both A- and P-sites, as the family of streptogramins A (S_A). For example, virginiamycin M prevents A- and P- site tRNAs binding by inducing conformational changes of the A2062 and U2585 in the PTC (Chinali et al., 1984; Hansen et al., 2003). By contrast, the simplest member of this class, madumycin II, allows the A-site tRNA binding but impedes the CCA-end accommodation in the PTC. The induced structural rearrangement of U2506 and U2585 leads to the translation inhibition before the first cycle of transpeptidation (Osterman et al., 2017). The coordination of A- and P- site tRNAs can also be impeded by the binding of the promising pleuromutilin class to the PTC (Eyal et al., 2016; Dillon et al., 2019).

Moreover, a few antibiotics also bind to the interface with the small subunit For instance, gentamicin and neomycin can interact with the H69 of the large subunit to potentially impede translocation and RRF-mediated ribosome recycling (Borovinskaya et al., 2007). This interaction leads to the stabilization of an intermediate hybrid state because the movement of h44, involved in intersubunit brigde with H69, is impaired (Wang et al., 2012).

Finally, some antibiotics interfere with the binding of translation factors to the ribosome, such as thiopeptides and orthosomycins (Bagley et al., 2005; Just-Baringo et al., 2014; Mikolajka et al., 2011). Binding sites of thiopeptides, like thiostrepton, nosiheptide and micrococcin, overlap with the domain V of EF-G to inhibit translocation (Rodnina et al., 1999; Walter et al., 2012). But, they also overlap with IF2 to prevent IF2-dependent initiation complex formation (Brandi et al., 2004) and with EF-Tu to impede the aa-tRNA delivery (Gonzalez et al., 2007). They interact with the N-terminal domain of uL11 and the nucleotides A1067 and A1095 at the top of H43 and H44 helixes of the 23S rRNA, respectively (**Figure 17B**).

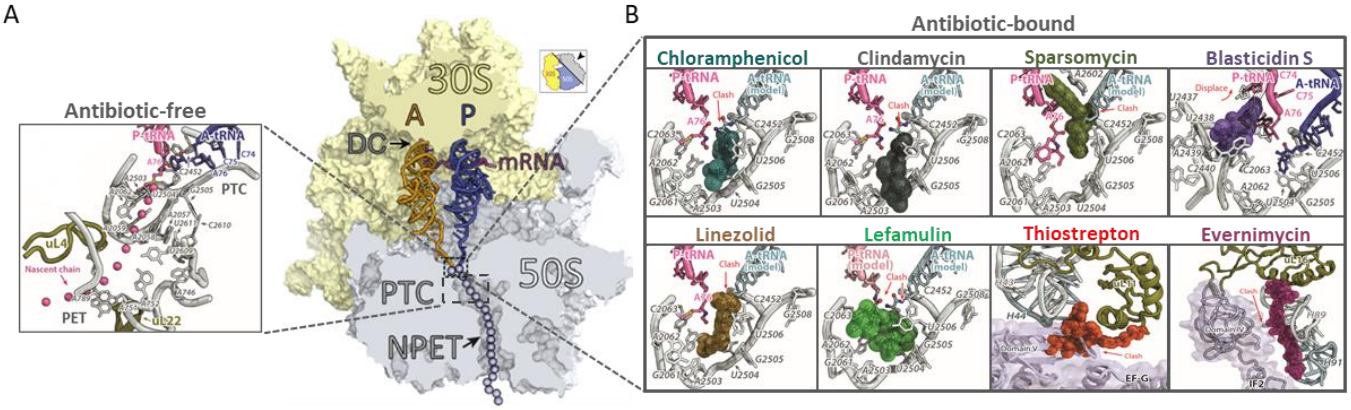

Figure 17: Molecular basis of interactions of PTC-targeting antibiotics.
The functional centers DC, PTC and PET are localized on the global structure of the bacterial ribosome with the 30S and 50S subunit complexed with mRNA, A- and P- site tRNAs (from Vazquez-Laslop and Mankin, 2018). (A) The molecular organization without antibiotic shows the key elements of the PTC and the upper PET (adapted from Lin et al., 2018). Detailed views of the interactions of chloramphenicol (PDB number: 4V7W), clindamycin (PDB number: 4V7V), sparsomycin (PDB number: 1VQ9), blasticidin S (PDB number: 4V9Q), linezolid (PDB number: 4WFA), lefamulin (PDB number: 5HL7), thiostrepton, (PDB number: 3CF5) or evernimycin (PDB number: 5KCS) with the ribosome in the PTC region are presented in (B) (adapted from Lin et al., 2018). A-tRNA, mRNA, EF-G, and their domains, helixes and residues are indicated.

The orthosomycin family, with the main representatives evernimycin and avilamycin, also highlighted a new ribosomal binding site in the minor groove of the helixes H89 and H91 of the 23S rRNA (**Figure 17B**) (Arenz et al., 2016; Krupkin et al., 2016). Their elongated conformation can also contact arginines of the uL16 that result in the inhibition of IF2-dependent complex initiation formation and of the accommodation of A-site tRNAs (Belova et al., 2001; Mikolajka et al., 2011).

b. Antibiotics targeting the peptide exit tunnel

When a protein is synthetized, a section is always in the nascent peptide exit tunnel (PET), which is one of the crucial elements of the ribosome. Mainly composed of the 23S RNA and the proteins L4, L22 and L23, the tunnel has a diameter of 10 Å to 20 Å with a length of 100 Å, and can hold up to 30-40 amino acids (Arévalo et al., 1988; Ban et al., 2000; Harms et al., 2001). The PET is directly targeted by several classes of antibiotics, such as macrolides, lincosamides, streptogramins B and the more recent macrolide-derivative class of ketolides to constitute the large MLS_BK family (Dunkle et al., 2010; Hansen et al., 2003; Schlünzen et al., 2001; Tenson et al., 2003). The lincosamides are peptidyltransferase inhibitors and directly block the transpeptidation (Spížek and Řezanka, 2017), whereas macrolides and streptogramins B inhibit the elongation process by obstructing the ribosomal exit tunnel (Dinos, 2017; Mast and Wohlleben, 2014)

Among the lincosamides members, the lincomycin and its chlorinated-derivative clindamycin also extend in the PET and interact with the same rRNA bases than macrolides, A2058 and A2059 (Matzov et al., 2017). Indeed, the lincomycin α-MTL moiety goes into the PET thanks to hydrogen bonds formed between its hydroxyl group and 23S rRNA (**Figure 17B**) (Matzov et al., 2017). The class of streptogramins B (S_B) also overlaps with macrolide binding site and are made of lactone-cyclized peptides, called depsipeptides. Type B streptogramins are usually used together with type A for a synergistic activity (**Figure 18A**) (Harms et al., 2004). Indeed, S_A induces A2062 and promotes S_B binding via stacking interactions and/or hydrogen bonds (Harms et al., 2004; Noeske et al., 2014).

Peptide-based antibiotics also constitute an important class of PET-targeting molecules. Few years ago, the class of proline-rich antimicrobial peptides appeared to obstruct the PET in the ribosome (PrAMPs). These natural peptides produced by mammals and insects adopt a specific conformation thanks to a high-proline content in order to prevent the progression of the nascent peptide. More recently, another peptide antibiotic, the klebsazolicin, was discovered as the first member of a new class produced by *Klebsiella pneumonia* (Metelev et al., 2017). It is a ribosomally-synthesized post-translationally modified peptide which is one of the most abundant family of antimicrobial agents in bacteria. The klebsazolicin binds near the PTC within the exit tunnel and overlaps with macrolide and S_B binding sites (**Figure 18A and B**). It stacks with 23S rRNA bases and form other contacts with conserved PTC nucleotides to allow blocking of the peptide elongation after only three amino acid incorporation.

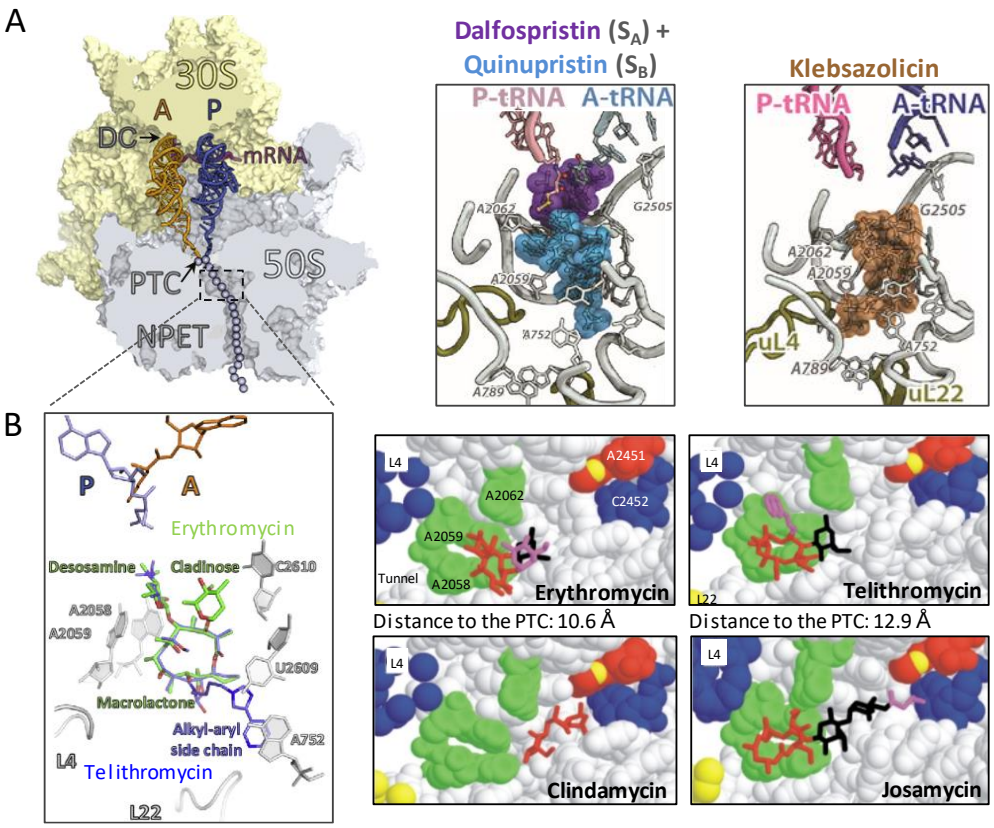

Figure 18: Molecular basis of PET-targeting antibiotic interactions with the ribosome.
The global organization of the bacterial ribosome with the 30S and 50S subunit complexed with mRNA, A- and P- site tRNAs (from Vazquez-Laslop and Mankin, 2018) is shown in (A). Localization of the functional centers DC, PTC and PET are also indicated. Detailed views of the interactions of the combination of dalfospristin and quinupristin, and klebsazolicin (PDB number: 5W4K) with the ribosome in the PET are presented in (A) (from Lin et al., 2018). The molecular details of the macrolide binding site with the visualization of key rRNA bases and macrolide-specific chemical groups are presented in (B) with the example of erythromycin (in green) and telithromycin (in blue) (adapted from Vazquez-Laslop and Mankin, 2018). Crystal structures of erythromycin, telithromycin and josamycin with *D. radiodurans* ribosome, and of the lincosamide clindamycin with *H. marismortui* ribosome indicate the localization of those drug in the PET and their distance to the PET (adapted from Tenson et al., 2003).

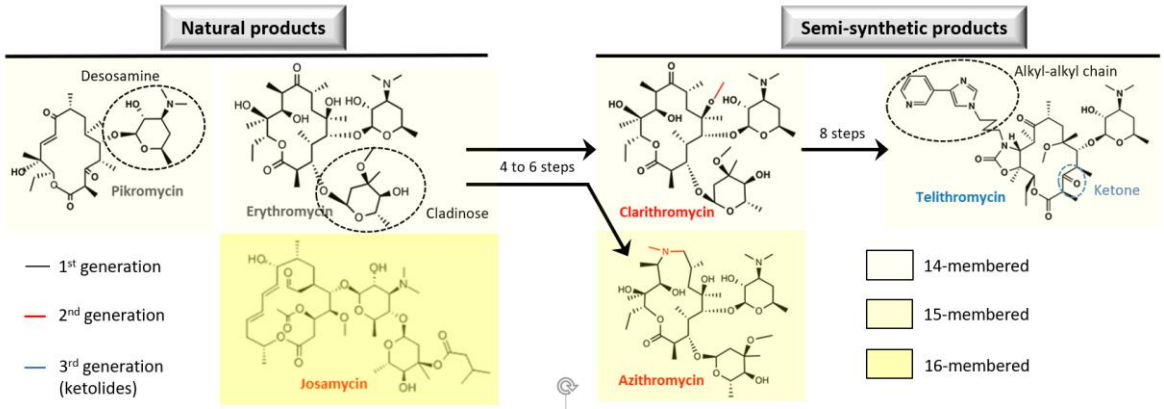

Figure 19: Chemical structures of different generations of macrolides. Adapted from Dinos, 2017 and Drugbank.
Pikromycin, erythromycin and josamycin are natural products isolated from *Streptomyces* species. The semi-synthetic products clarithromycin and azithromycin are erythromycin derivatives after 4 to 6 steps of synthesis, and the chemical difference are highlighted in red on the structures. The telithromycin is obtained from clarithromycin after 8 steps of synthesis. The three generations (1st in grey, 2nd in red and 3rd in blue) are differentiated by their pharmacological and antibacterial properties. The number of carbone atoms in the lactone ring allows the classification in groups 14-, 15- and 16-membered (gradation of yellow,). The chemical group are also showed on the macrolide structures.

2. The specific case of macrolides

A. History of antibacterial activity of macrolides

Originally, macrolides are natural fermentation products of precursors from several *Streptomyces* species and *Micromonospora* genus. Their names derive from their macrocyclic lactone ring core, whose size can vary between macrolides and which can be linked to several sugars and/or side chains (**Figure 18B and 19**). The first isolated macrolide was the pikromycin (Brodersen et al., 1953; Suhren, 1951) from *S. venezuelae*. It could not be used clinically but it consitutes the starting point for new macrolide development **(Figure 19)**.

The first macrolide available on the market was erythromycin, in the early 50's, isolated from *S. erythreus* or *Arthrobacter* species (Mcguire et al., 1952). Since then, several other members were isolated or chemically optimized from parent molecules (**Figure 19**). At the beginning, macrolide development was made to improve their pharmacological properties but over the years it became also essential to counteract the emergence of resistance mechanisms.

Macrolides can be classified according to either their chronological appearance or their number of atoms in the macrolactone ring, which can vary between 12 and 16 atoms. The first generation, like pikromycin or erythromycin, present unfavorable pharmacological properties, such as poor solubility or bioavailability, that lead to the development of a second generation of semi-synthetic compounds in the 80's and early 90's. Five derivatives of erythromycin were thus developed, among them azithromycin (Girard et al., 1987; Retsema et al., 1987) and clarithromycin (Omura et al., 1992) (**Figure 19**). Besides their better stability in acid environment, their half-life is increased, and they are also more lipophilic for a better penetration in tissues.

The third generation, also known as the ketolides, was developed to obtain a broader spectrum activity and to deal with macrolide resistance. However, efforts are still currently in progress to improve their activity and their marketing (Liang and Han, 2013). To date, the only commercially available ketolide is telithromycin, which was obtained after semi-synthesis from the clarithromycin (**Figure 19**) (Denis et al., 1999). Ketolides are named after the ketone function which replaced the cladinose in C3 position. This is the main reason for the differential activity between macrolides and ketolides. Indeed, the C3-cladinose function is bulkier than the ketone group (**Figure 19**), thus explaining why it allows less of nascent peptides passing through the tunnel compared to the ketone group. Moreover, ketolides have another structural specificity: a 11, 12 cyclic carbamate with an extended alkyl-aryl chain, which can establish additional contacts with the 23S rRNA.

B. Molecular basis of ribosome-macrolide interaction

All macrolides clog the PET to hinder progression of newly synthesized peptides as soon as they reach three to ten amino acids, subsequently inducing accumulation of peptidyl-tRNAs and arrest of bacterial translation (Otaka and Kaji, 1975; Tenson et al., 2003). The macrocyclic lactone ring is oriented on the same way in the PET regardless the macrolide identity (Bulkley et al., 2010; Dunkle et al., 2010) but the distance to the PTC differs according to each structural specificity (**Figure 18B**) (Tenson et al., 2003). Macrolides form a hydrogen bond between their desosamine hydroxyl group and the N1 atom of the A2058 nucleobase. Furthermore, some macrolides interact specifically with the base 2505 via their cladinose group (Golkar et al., 2018). The stacking of the lactone ring hydrophobic face on the 2611 and 2057 bases also allows the macrolide stabilization in the ribosome.

There are some additional contacts in the ketolide group due the heterocyclic side chain, which can be found in different positions according to the bacterial type (Berisio et al., 2003; Bulkley et al., 2010; Dunkle et al., 2010; Tu et al., 2005). For example, telithromycin forms stacking interactions with the A752-U2609 base pair (**Figure 18B**) (Lin et al., 2018), resulting in an increased affinity for the ribosome compared to erythromycin (Douthwaite, 2001). Larger macrolides with a 16-membered lactone ring, such as josamycin, can also contact the PTC via its extended tail (**Figure 18B**) (Tenson et al., 2003). This disaccharide extension at the C5 position of the ring interferes with the peptidyl-transferase reaction to prevent peptide bond formation and block the translation (Hansen et al., 2002).

C. Mode of action of macrolides

Macrolides are mostly active against Gram-positive species, as *Staphylococcus*, *Streptococcus* and *Diplococcus*, and extremely active against mycoplasmas (Bébéar et al., 1997; Doucet-Populaire et al., 1998). Only few Gram-negative bacteria, like *Neisseiria gonorrhoea* or *Haemophilus influenzae*, are sensitive to some members. Ketolides display impressive activity against Gram-positive macrolide-resistant pathogens, like *Streptococcus pneumoniae* (Farrell et al., 2015), or against respiratory tract pathogens, like *Mycoplasma pneumaonia* or the Gram-negative *Legionella* species (Hammerschlag et al., 2001).

In recent years the status of macrolides went from simple translation inhibitors to translation regulators. Their mode of action can no longer be restricted to an arrest of translation by a simple obstruction of the exit tunnel, and seems to be more context-specific (**Figure 20**) (Kannan et al., 2012; Sothiselvam et al., 2016). Indeed, the translation inhibition upon macrolide binding is dependent on the nature of the nascent polypeptide and/or the macrolide itself, that lead to the inhibition of a specific subset of proteins. Thus, a differential translation is observed between proteins that cannot be elongated in presence of a macrolide, called macrolide-sensitive proteins, and proteins capable of passing through the macrolide, called macrolide-resistant proteins (Vázquez-Laslop and Mankin, 2018).

For instance, a small proportion of proteins is still synthesized in presence 100-fold MIC of erythromycin (5-7 %), and the same concentration conditions with telithromycin allow translation of around 25 % (Kannan et al., 2012).

To explain the macrolide bypassing of proteins, two models are presented. First, the cotranslational eviction of macrolides by short peptides (**Figure 20A**) (Lovmar et al., 2006; Tenson et al., 1997) is supported by the fact that resistant proteins are produced by drug-free ribosomes (Odom et al., 1991; Starosta et al., 2010). Some oligopeptides were identified as inducing macrolide dissociation from the ribosome (Tenson et al., 1997). The second model proposes that the available space in the tunnel is sufficient for an unfolded nascent protein to pass (**Figure 20B**) (Schlunzen et al., 2001; Tu et al., 2005; Arenz et al., 2016). A small group of proteins can be translated by macrolide-bound ribosomes thanks to bypass sequences (Kannan et al., 2012).

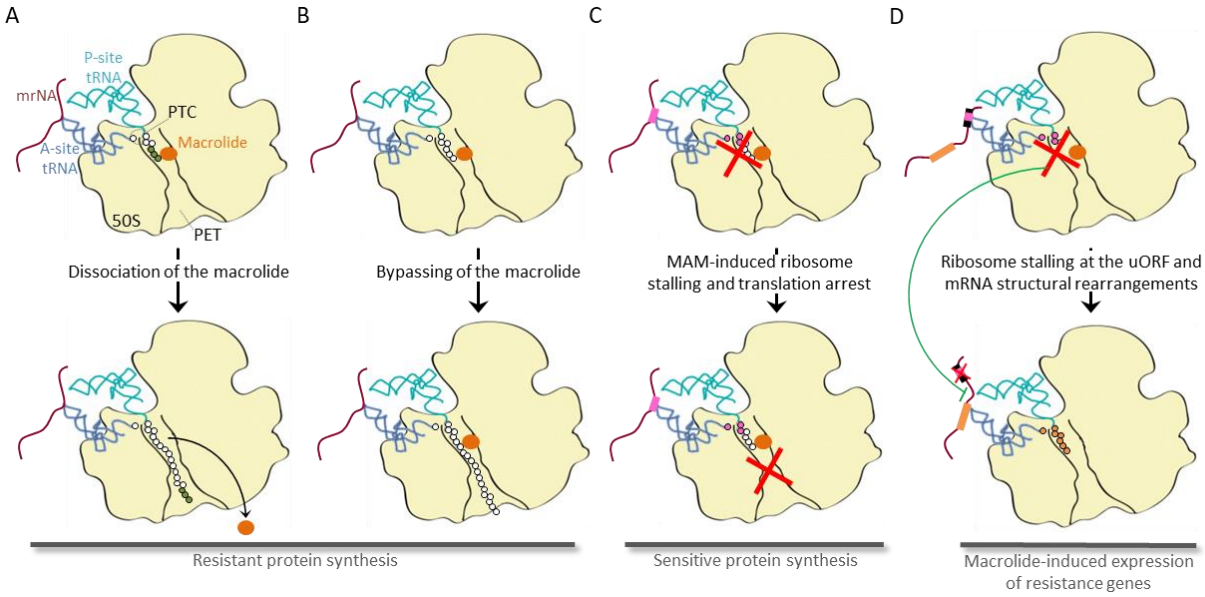

Figure 20: Mode of action of macrolides. Adapted from Kannan et al., 2012 and Vazquez-Laslop and Mankin, 2018. The macrolide (in orange) binding to the active ribosome (50S subunit in yellow), containing the mRNA (in magenta), A- (in blue) and P-site tRNAs (turquoise), has context-specific effects on the translation. The synthesis of proteins, called resistant proteins, are possible in some cases. Some oligopeptides induce the dissociation of the macrolide from its binding site (A) while some others can bypass the bound macrolide in the remaining space of the PET (B). A subset of proteins is sensitive to the macrolide presence thanks to specific MAM sequences (pink box) which block the elongation and stall the ribosome (C). Such sequences are also used in the activation of resistance gene (orange box) expression. In such cases, MAMs are present in a leader peptide (black box) upstream a repressed gene of resistance (uORF) to promote ribosome stalling; this stalled ribosome induces structural rearrangements in the mRNA to inhibit the repression and allows the translation of the resistance gene.

By contrast, a class of oligopeptides acts in synergy with macrolides to inhibit translation thanks to macrolide arrest motifs (MAMs), (**Figure 20C**) (Kannan et al., 2014; Vázquez-Laslop and Mankin, 2018). As there are no direct contacts between the MAM and the macrolide, it could be the combination of both MAM and macrolide in the PET that prevent the peptide bond formation and the elongation.

Surprisingly, those sequences were also discovered in open reading frames upstream (uORF) of certain resistance genes, whose expression is activated upon macrolide binding. Indeed, the presence of a macrolide bound to the PET leads to ribosome stalling at this MAM-containing regulatory element, called leader peptide, and the induced mRNA structural rearrangements promote the downstream gene expression (**Figure 20D**) (Ramu et al., 2009; Weisblum, 1995). In summary, translation arrest is dependent on the sequence of the leader peptide and the macrolide nature (Arenz et al., 2014; Gryczan et al., 1980; Horinouchi and Weisblum, 1980; Vazquez-Laslop et al., 2008; Vázquez-Laslop et al., 2011).

Direct macrolide-induced early stops of the translation are minor compared to arrests at those specific sequences. To highlight the real mechanisms of MAM-related arrest of translation, ribosome-profiling were used to identify precisely sites of translation stop (Davis et al., 2014; Kannan et al., 2014). The prevalent MAM contains a tripeptide R/K - X - R/K which promotes ribosome stalling, but other motifs enriched in positively-charged amino acids were also observed in context of erythromycin or telithromycin exposure.

Finally, novel less-known properties of macrolides are also envisaged, as their influence on the capacity to induce miscoding or frameshifting. These underlying mechanisms still need to be elucidated (Thompson et al., 2004; Vázquez-Laslop and Mankin, 2018).

D. Dynamics of ribosome-macrolide interactions

Dynamics of interactions between macrolides and the ribosome appeared to influence the mode of action of macrolides. Indeed, binding and dissociation kinetics allow to correlate the bactericidal or bacteriostatic activity with the macrolide structure (Svetlov et al., 2017). Other investigations also showed that all macrolides probably diffuse through the tunnel from its exit (Lovmar et al., 2009) and are all slow-binding inhibitors (Morrison and Walsh, 1988). By contrast, the dissociation rate can significantly differ between macrolides, mostly according to their structures. For instance, the additional tail of telithromycin induces a very slow dissociation from the ribosome compared to other macrolides (Di Giambattista et al., 1987; Krokidis et al., 2016). This indicates that telithromycin stays bound to the ribosome significantly longer, thus stimulating its bactericidal action (Svetlov et al., 2017). In treated cells, there is a dynamic exchange between the free and ribosome-bound forms, but when elongation has begun, macrolide would possibly be trapped in the tunnel; this trapping efficiency is dependent on nascent peptide nature and drug dissociation (Lovmar et al., 2004). The time residency of the macrolide in this drug-trapped ribosome increases when the ribosome stops at MAMs, but little is known about the kinetics of macrolide-induced ribosome arrest.

3. The promising class of proline-rich antimicrobial peptides

A. Synthesis and transport in bacteria

Proline-rich antimicrobials peptides (PrAMPs) are cationic peptides, rich in proline and arginine residues and synthetized by the innate immune system of eukaryotes in response to a bacterial invasion (Zasloff, 2002). After passing through the membrane, they inhibit intracellular processes, such as the protein synthesis (Graf and Wilson, 2019; Scocchi et al., 2011). Their non-lytic activity and their wide distribution make these molecules very attractive for new drug development strategies. Since the first PrAMP, the apidaecin, that was identified in the 80's (Casteels et al., 1989), several were discovered in arthropods (insects and crustaceans) and mammals (Agerberth et al., 1991; Cociancich et al., 1994; Gennaro et al., 1989; Stensvåg et al., 2008).

PrAMPs are produced as inactive precursors stored in granules, subsequently activated after proteolytic cleavage by elastases, contained in a different subset of granules (**Figure 21A**) (Zanetti et al., 1990). Activation of precursors is promoted by simultaneous exocytosis in the bacteria-containing extracellular space or by fusion with bacteria-containing phagosomes (Graf et al., 2017). PrAMPs can be produced through two pathways according to peptide nature. Some peptides are processed by a single-peptide activation: one mRNA codes for one polypeptide with a pre-sequence which is then cleaved; while some others require a multi-peptide activation: one mRNA contains multiple peptide coding sequences to produce a polypeptide with a pre-sequence at N-terminal extremity and pro-sequences upstream each peptide repeat (**Figure 20B**) (Casteels-Josson et al., 1993).

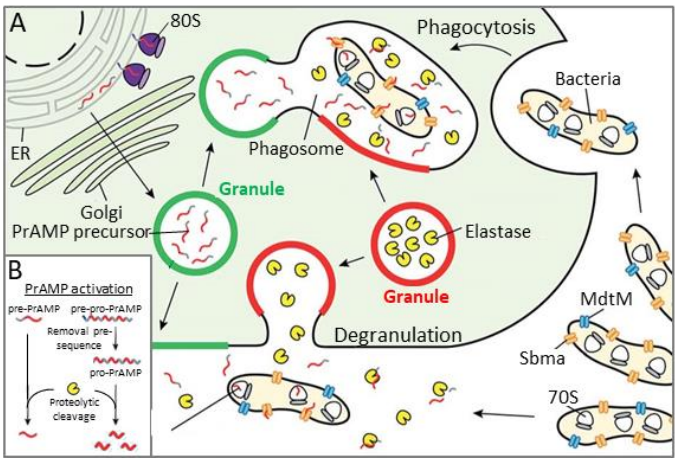

Figure 21: PrAMP synthesis and uptake. Adapted from Graf et al., 2017.
The global synthesis and action of PrAMPs are illustrated in (A). PrAMPs are synthetized as precursors by ribosomes. They are encapsidated in granules that are either fused with bacteria-containing phagosomes or delivered to extracellular medium; granules containing the proteases, elastase, undergo the same events. PrAMPs are finally imported in bacteria with SbmA or MdtM receptors. PrAMPs can be activated through two pathways (B): pre-pro-PrAMP precursors with multicopy of peptides undergo a removal of the pre-sequence followed by a proteolytic cleavage by elastases, or pre-PrAMP precursors with a single copy are only cleaved by elastase to release the mature peptide.

The uptake inside bacteria is facilitated by the SbmA transporter, a protein of the inner membrane, which is more widespread in Gram-negative bacteria compared to Gram-positive bacteria (Mattiuzzo et al., 2007). More recently, another transporter was identified, the YjiL-MdtM system (Krizsan et al., 2015). It is also an inner membrane protein mainly presents in Gram-negative bacteria. This second pathway plays an auxiliary role in the case of high peptide concentrations.

The absence of those transport systems in Gram-positive bacteria explains the weaker antibacterial activity of PrAMPs on this bacterial family. Furthermore, the import can also be favored by the peptide structure. Indeed, the mammalian PrAMP Bac7 stimulates membrane permeabilization thanks to its longer sequence (60 vs ~20 amino acids for insect PrAMPs) (Skerlavaj et al., 1990), suggesting different modes of transport and action (Podda et al., 2006).

B. Types of PrAMPs and their mode of action

Originally, PrAMPs were identified as inhibitors of the protein folding process by interaction with DnaK chaperones (Otvos et al., 2000). However, it appeared that PrAMPs were still active in DnaK-inactivated bacteria (Krizsan et al., 2014) and it was later shown that PrAMPs can actually bind to the ribosome and inhibit translation (Mardirossian et al., 2014). Despite similar mode of interaction among all PrAMPs, they can be divided into two classes according to their positioning in the tunnel and their mode of action: (i) type I PrAMPs are in the inverted orientation with respect to the nascent polypeptide chain and impede the transition to the elongation phase (**Figure 22A**) while (ii) type II PrAMPs rather block the translation termination and are in the same orientation than the emerging polypeptide (**Figure 22B**).

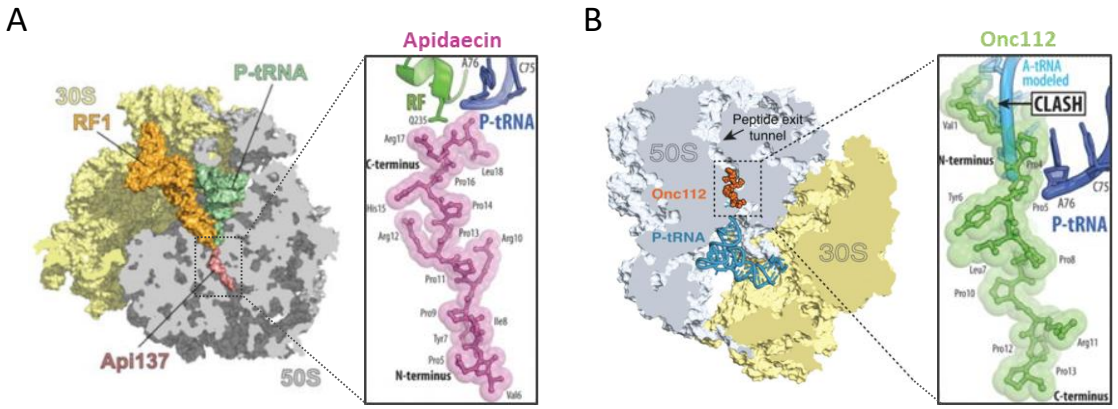

Figure 22: Localization of type I and II PrAMPs in the PET.
The binding site of the apidaecin-derivative Api137 (A; from Florin et al., 2017) and Onc112 (B; Roy et al., 2015) are shown in the full structure of the ribosome complexed with P-tRNA. RF1 is also present in the apidaecin-containing ribosome. Detailed views of their interactions in the PET are also presented with the identification of each residue (from Polikanov et al., 2018; PDB number of apidaecin: 502R; PDB number of Onc112: 4Z8C).

Type I PrAMPs are produced by insect and mammalian species (Gagnon et al., 2016). The most characterized insect PrAMPs are Oncocin and Onc 112 from the milkweed bug (Roy et al., 2015) but pyrrhocoricin from the firebeetle and metalnikowin-1 from the green shield bug are also very studied (Chernysh et al., 1996; Cociancich et al., 1994). Among mammalian PrAMPs, Bac7 from the cow is the most characterized one; but a new representant, Tur1A, recently discovered in the bottlenose dolphin, also appeared as an attractive antibacterial molecule (Mardirossian et al., 2018). By contrast, type II PrAMP family contains only insect peptides so far, and are part of the apidaecin subfamily, produced by bees, hornets and wasps. Among them, Api137, a more stable derivative of the natural apidaecin 1b from the honeybee, is the most described member (Berthold et al., 2013).

The primordial residues for the type I PrAMPs-mediated antibacterial activity are located in the A-site binding pocket, whereas in the case of type II PrAMPs, they are in contact with the PTC (**Figure 22A and B**). Type I peptides allow the entry of initiator tRNA but hinder the binding of aa-tRNA in the A-site thanks to an overlap with the CCA-end binding site. This steric clash promotes the stalling of the ribosome at the AUG codon (Graf et al., 2019). However, when a tRNA is already present in the A-site, the peptides cannot bind anymore. Considering the time window of free A-site during elongation, type I PrAMPs are ineffective on ribosomes during this step. In type II-induced inhibition, peptides cause the trapping of release factors in the ribosome. Accumulation of RF-trapped ribosomes leads to a decrease of the cellular release factors (RFs) pool which consequently induces an increase of stop codon readthrough on stalled ribosome (Florin et al., 2017). So, the trapping of RFs promotes the formation of stalled ribosomes by a dual action, either the direct trapping of RFs in the ribosome or the absence of RFs for the termination of other translating ribosomes. It has to be noted that Api137 has a low affinity for empty ribosomes in the absence of release factors (Florin et al., 2017).

C. Molecular basis of the interaction

So far, structural studies showed that PrAMPs bind to the PET in the 50S subunit thanks to polar and stacking interactions between highly positive charged residues and nucleotides of the 23S rRNA (Lin et al., 2018). Their binding sites overlap with the one of the A-site tRNA CCA-end but not with the one of the P-site tRNA (Graf et al., 2017, 2019).

Type I PrAMPs have their N-terminal end in the PTC and the C-terminal part deeper in the tunnel (**Figure 22A**). The binding site is divided into three regions: A-site binding pocket, A-site crevice and the upper part of the PET. Only N-terminal residues direct the inhibitory activity. For example, deletion of 19 of the 35 amino acids at the C-terminus of Bac7 does not abolish its activity (Benincasa et al., 2004). All PrAMPs of this class have a conserved PRP motif located in the same position with an identical conformation (**Figure 29B**). Globally, N-terminal residues establish polar contacts and stacking interactions with rRNA (**Figure 23A, B and C**). In mammalian peptides, arginine residues are largely enriched and form hydrogen bonds with the A-site binding pocket but only one stacking contact is observed between Arg2 and C2573 (Mardirossian et al., 2018; Seefeldt et al., 2016). For insect peptides, stacking interactions are more represented to facilitate the accommodation in the A-site binding pocket. In the A-site crevice, the global interaction network is similar between mammalian and insect peptides; it involves hydrogen bonds between the peptide backbone and the rRNA bases. Nevertheless, one stacking interaction is really conserved with the C2452 base; it involves the Tyr6 residue in insect peptides and the ninth residue in mammalian PrAMPs, (Tyr in Tur1A and Arg in Bac7). Finally, consistently with the minor importance of the C-terminal end, few interactions are established with the upper part of the tunnel. This is also supported by the fact that the last residues of the peptides could not be observed in structures, probably due to their lability in the tunnel (**Figure 23B and C**).

By contrast, type II PrAMPs have their C-terminal extremity in the A-site and the N-terminal end deeper in the tunnel (**Figure 22B**). Although type II PrAMPs also have an overlapping binding site with the A-site tRNA, they do not inhibit accommodation of A-site tRNAs. Indeed, their C-terminal residues are crucial for the interaction with the A-site crevice but do not reach the binding pocket (**Figure 23A**). Contrary to type I, the binding of this peptide family is principally driven by stacking interactions with PET rRNA bases (**Figure 23D**); but, they also establish polar contacts with RFs and the deacylated tRNAs (**Figure 23D**) (Florin et al., 2017). Thus, Api137 hinders the termination step by entering in the ribosomal exit tunnel after peptide release and traps the RFs in the ribosome by preventing the RF3-mediated rotation, indispensable for RF1 and RF2 release. These interactions with the RF1-bound ribosome and the P-site tRNA suggest that the Api137 activity has a narrow time window to bind, after the peptide release but before the RF1 or RF2 departure.

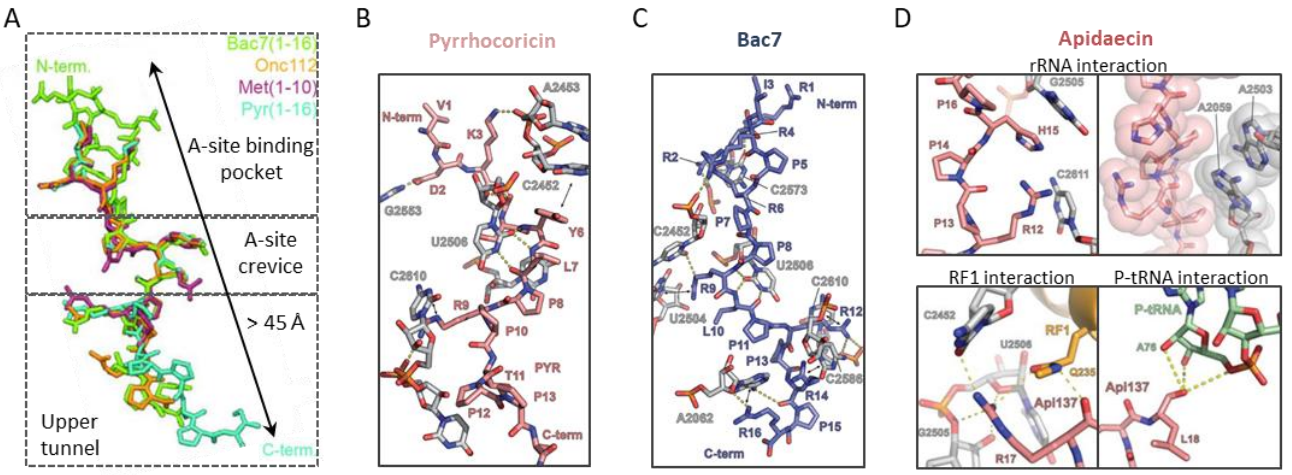

Figure 23: Molecular basis of interactions of mammal and insect PrAMPs in the PET.
Bac7 (in green), Onc112 (in orange), metalnikowin (in pink) and pyrrhocoricin (in turquoise) are superimposed in their ribosome-bound conformations with the delimitation of key sites of the PET, A-site binding pocket, A-site crevice and upper tunnel (in dashed boxes) (A; from Seefeldt et al., 2016). One example of zoomed target site of each type of PrAMPs shows the molecular details of the interactions. The insect type I PrAMP pyrrhocoricin (B) and the mammal type I PrAMP Bac7 (C) interact mainly with rRNA bases of the 23S (from Graf et al., 2017) while the type II PrAMP apidaecin (D) contacts RF1, rRNA bases from 23S rRNA and P-tRNA (from Florin et al., 2017).

4. Antibiotic resistance and therapeutic perspectives

Antibiotics revolutionized modern medicine and are an inestimable mean to fight bacterial infections, responsible for numerous diseases. Unfortunately, the widespread use of drugs helped bacteria to become resistant and more harmful through specific mechanisms (Alekshun and Levy, 2007). Drug-resistant bacteria appeared as one of the greatest threats to humanity and have been classified few years ago as a top priority by the World Health of Organization (WHO). Not to mention the incredible cost world economy, the antimicrobial resistance (AMR) issue is, above all, responsible for the death of thousands of people all over the world. In absence of improvements, the worst prediction heralds ten million deaths each year related to AMR by 2050 (Review on Antimicrobial Resistance by Jim O'Neill, 2014).

A. Overview of the mechanisms of resistance

As antibiotics were originally produced by microorganisms, resistance pathways appeared thousands of years ago (D'Costa et al., 2011) and are very diverse (Perry et al., 2014). Some bacteria are naturally resistant to certain antibiotics due to their structural properties, especially with the difference in metabolism or in the wall organization between Gram-positive and Gram-negative bacteria. In addition to their innate resistance, pathogens also acquired properties through three major ways (Brown and Wright, 2016): (i) the mobilization of resistance genes thanks to horizontal transfer from environmental and clinical sources, (ii) the mutations in antibiotic target genes (Andersson and Hughes, 2011) and (iii) the increasing of intrinsic resistance pathways, such as antibiotic-inactivating enzymes or efflux (Abraham and Chain, 1988; Fajardo et al., 2008). Among the existing resistance mechanisms (**Figure 24**), all of them have major roles in the resistance to ribosome-targeting antibiotics (Wilson, 2014; Blair et al, 2015; Lin et al, 2018).

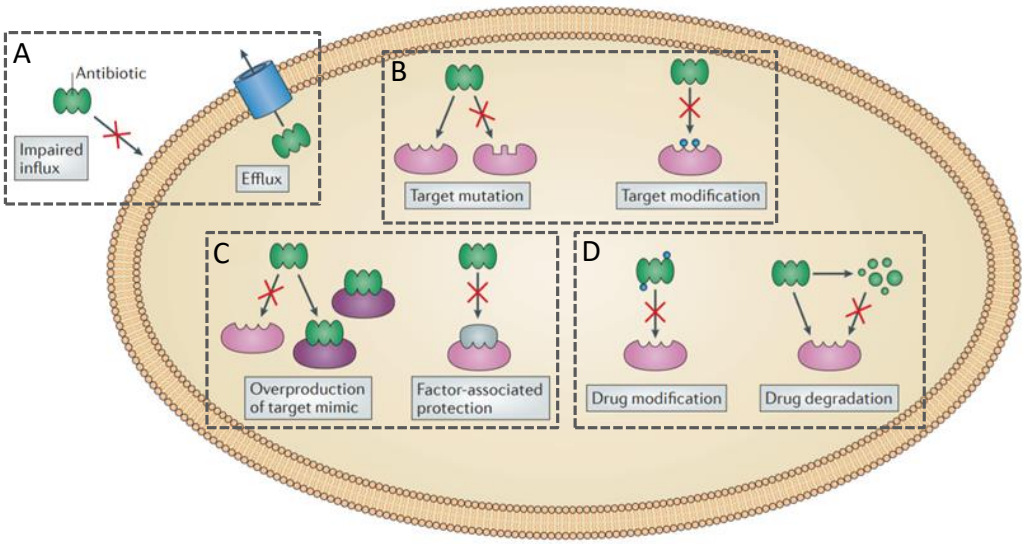

Figure 24: Mechanisms of antibacterial resistance. Adapted from Wilson, 2014.
Different mechanisms can lead to bacterial resistance. The first ones modulate membrane permeability by preventing the uptake of the drug or by enhanced efflux systems (A). The alteration of the target by mutations or modifications also hinders the drug binding (B). A trans-regulation can also be observed with target protection by cellular factors or by overproduction of target mimics (C). Finally, the drug itself can be degraded or modified (D).

a. Modulation of membrane permeability

Gram-negative bacteria and mycobacteria have natural protection against some antibiotics thanks to an impaired influx. For instance, the hydrophobic nature of macrolides prevents their penetration through the outer membrane (**Figure 24A**). In addition to structural features, the intrinsic metabolism can also contribute to the natural resistance of some bacteria. For example, anaerobic bacteria cannot realize oxidative metabolism-induced energy, thus they are innately resistant to aminoglycosides since their uptake is dependent on this pathway. Furthermore, drug-permeable bacteria are able to evacuate the drug by efflux most of the major ribosome-targeting classes of antibiotics (**Figure 24A**).

This efflux, allowing to maintain a non-toxic drug concentration in the bacteria, is mediated by pumps from five transporter families: the small multidrug resistance (SMR) family, the resistance nodulation and cell division (RND) family, the major facilitated superfamily (MFS), the ATP-binding cassette (ABC) family and the muliti-drug and toxic compound extrusion (MATE) family (Piddock, 2006). The efflux of some antibiotics can also be enhanced by outer membrane porins in Gram-negative bacteria. For instance, TolC interacts with the adaptator AcrA complexed with the transporter AcrB of the RND family to export macrolides and with the adaptator MacA complexed with the transporter MacB of the ABC family to transport chloramphenicol or tetracycline (Fitzpatrick et al., 2017; Hayashi et al., 2016). Very recently, the implication of AcrB transporter in the oxazolidinone and pleuromutilins resistance was even reported and contributes to better understanding of this RND-mediated pathway (Schuster et al., 2019).

b. Disruption of target recognition

Resistant pathogens often use modifications or mutations of the target site of antibiotics (**Figure 24B**) in order to decrease the affinity of the interaction or prevent the binding (Poehlsgaard and Douthwaite, 2005; Wilson, 2009). Mutations mainly concern the rRNA and especially conserved residues that are key elements for drug binding, such as A2058. However, as rRNA are produced from several operons, the mutations need to occur in most of these copies to be found in a large population of cellular ribosomes. Some ribosomal proteins can also be mutated. For instance, for thiopeptide antibiotic resistance, the prolines of the uL11 N-terminal domain are mutated to reduce the binding efficiency (Baumann et al., 2010). The combination of mutations on both rRNA and proteins often amplifies the resistance activity. The linezolid resistance is thus caused by the C2534U mutations associated to mutated L3 and L4 proteins in *S. aureus* (LaMarre et al., 2013).

The most frequent mechanism of modification is the methylation of rRNA by rRNA methyltransferases (Wilson, 2014). For example, methylation of the 23S nucleotide A2503 in the PTC by the Cfr methyltransferase provides resistance to a broad antibiotic spectrum, including chloramphenicols, pleuromutilins, streptogramins A, lincosamides, oxazolidinones and some macrolides (Long et al., 2006). On the contrary, a loss of methylated rRNA bases can also promote AMR. In the case of resistance to the tuberactinomycins viomycin and capreomycin, the inhibition of TlyA-mediated methylation of the 16S rRNA C1409 and the 23S C1920 is performed by resistant bacteria (Monshupanee et al., 2012).

Recognition of the target can also be impeded by a drug-induced trans-regulation via a drug sequestration caused by an overexpression of the target or of a mimic target. (**Figure 24C**) However, although this strategy has never been demonstrated *in vivo, in vitro* overexpression of a h34-mimicking motif confers resistance to the aminoglycoside spectinomycin (Thom and Prescott, 1997).

c. Alteration of the drug

The drug can be inactivated by bacterial enzyme-mediated modifications or degradations (**Figure 24D**) (Wright, 2005). Several chemical modifications are found to prevent drug binding, such as phosphorylation and acetylation which confer, among others, resistance to chloramphenicol (Mosher et al., 1995; Rajesh et al., 2013) and aminoglycosides (Dhote et al., 2008); hydroxylation, which inhibits tetracycline and tigecycline binding (Moore et al., 2005; Volkers et al., 2011); glycosylation, which contributes to macrolide resistance; and adenylation which enables resistance to lincosamides and aminoglycosides.

B. Specific resistance to MLS_BK class antibiotics

As macrolides, lincosamides, streptogramins B and ketolides (MLS_BK) share overlapping regions in the peptide exit tunnel, bacteria exhibit same resistance mechanisms.

a. Trans-acting regulation

Macrolide action can be altered by cellular proteins, which can either decrease intracellular macrolide concentration or physically displace it from the ribosome. Pumps involved in the efflux of macrolides belong to the Mef family from the major facilitator superfamily (MFS) that is mainly present in Gram-positive bacteria. Among the Mef proteins, Mef(A) and Mef(E) contribute to the efflux of 14- and 15-membered macrolides for example. Among the ABC transporter superfamily, the Msr family is a group of proteins capable of decreasing the concentration of macrolide-bound ribosomes by displacing the drug from its binding site (Sharkey et al., 2016; Wilson, 2016). Just as Mef family, Msr proteins confer resistance to 14- and 15-membered macrolides. However, the co-expression of *mef*(E) genes with the *msr*(D) family of genes confer a high-level of resistance to macrolides in *S. pneumoniae* and a synergistic activity enhance macrolide resistance in *E. coli* (Nunez-Samudio and Chesneau, 2013).

b. rRNA alteration

Gram-positive bacteria and *E. coli* became sensitive to 23S rRNA modifications leading to a high-level of resistance to MLS_BK after acquisition of resistance genes (Roberts et al., 1999). Principal modifications of the rRNA are mono- and di-methylation of the N6 position of the key A2058 nucleotide, that impedes the binding of all MLS_BK antibiotics (**Figure 25**). This reaction is performed by methyltransferase enzymes (Katz et al., 1987). As these enzymes were found to originally confer resistance to erythromycin, they were called erythromycin-resistant methylases (Erm) and are encoded by several *erm* genes. Interestingly, the Erm-mediated methylation is either inducible by the intracellular presence of macrolides (Ramu et al., 2009), or constitutive in resistant strains and thus independent of the macrolide presence (Poehlsgaard and Douthwaite, 2003). The induction of methylation occurs only after exposure to 14- and 15-membered, and not 16-membered or 14-membered-ketolides which do not contain the C3 sugar element (Dinos, 2017).

As mentioned previously (see section II.2.C), some genes of resistance are activated in presence of macrolides thanks to specific motifs (MAMs) in the leader peptide sequence. In the case of the *erm*D gene, this ribosome stalling-induced expression has been largely studied (Hue and Bechhofer, 1992; Sothiselvam et al., 2014). But, some leader peptides, as ermBL and ermCL which control *erm*B and *erm*C gene expression, respectively, do not contain MAMs and use a distinct stalling sequence to activate macrolide-resistant genes (Wilson, 2016).

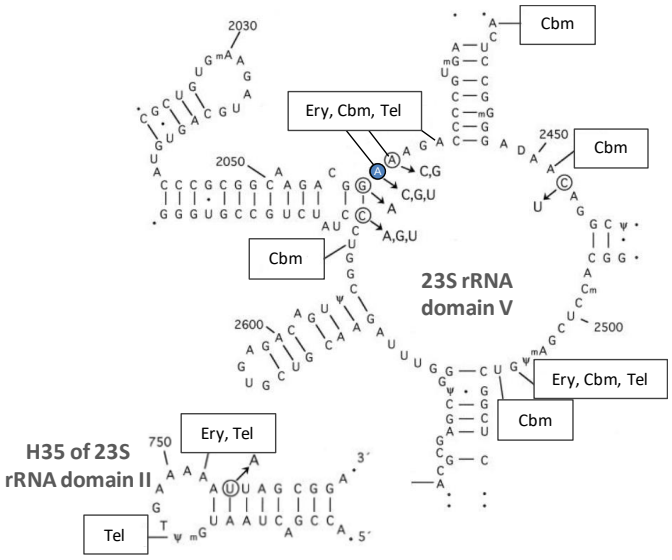

Figure 25: rRNA alteration in key domains of macrolide binding sites in 23S rRNA. Adapted from Vester and Douthwaite, 2001.
Nucleotides of the PTC are showed on secondary structure models of the domain V of the 23S rRNA and of domain II of H35. Nucleotides involved in the interaction with erythromycin (Ery), telithromycin (Tel) and carbomycin (Cbm, equivalent to josamycon) are indicated (boxes with appropriate macrolide). The circled bases indicate the principal mutations that confer drug resistance. The blue circled base (A2058) indicate the position of major mutation responsible for macrolide resistance.

Although it's less frequently than modifications, rRNA mutations of key conserved 23S rRNA nucleotides can also affect the interaction with macrolides (**Figure 25**). Again, the key A2058 nucleotide is affected and its mutation to a G provides a high-level resistance to most of the MLS_BK antibiotics (Canu et al., 2002; Vester and Douthwaite, 2001). An exception is *S. pneumoniae* for which this mutation only induces low-level of ketolide resistance (Farrell et al., 2003). Mutations at adjacent nucleotides, A2057 and A2059, have also been found in clinical strains (Fyfe et al., 2016). Other mutations affect nucleotides important for the binding of some MLS_BK drugs. For instance, the U2609C mutation in *E. coli* abolishes the interaction with the nucleotide 752, which connects domain II and V of the 23S rRNA and assists ketolide stacking interactions (Dunkle et al., 2010). This mutation results in high resistance to the ketolide telithromycin (Garza-Ramos et al., 2001). In *S. pneumoniae*, further mutations were also identified, such as deletion of A752 which confers resistance to macrolides and ketolides or C2610 and C2611U mutations (Canu et al., 2002) which render ribosomes resistant to macrolides.

Interestingly, archaeal and eukaryotic ribosomes are innately resistant to macrolides thanks to a G in the position equivalent to *E. coli* A2058 (Böttger et al., 2001). The reverse G2058A mutation in archaea enhances erythromycin binding (Tu et al., 2005). Nonetheless, the same mutation in yeast is not sufficient to restore the sensitivity to erythromycin, supporting the implication of other determinants in eukaryotic resistance (Bommakanti et al., 2008).

c. Ribosomal protein mutations

Numerous mutations in L4 and L22 proteins of *E. coli* laboratory strains or clinical isolates, such as *S. pneumoniae* (Farrell et al., 2004; Tait-Kamradt et al., 2000a) or *S. aureus* (Prunier et al., 2005), were described over the years to confer MLS_BK resistance (Franceschi et al., 2004). Mutations in a conserved sequence of *S. pneumoniae* L4 ($_{63}$KPWRQKGTGRAR$_{74}$) or in the C-terminal region of L22 (examples: G95D, A101P or G83E) induce a lower susceptibility to macrolides or ketolides (Pihlajamäki et al., 2002; Tait-Kamradt et al., 2000b). Furthermore, in *S. pneumoniae* isolates, the association of three amino acid deletion in the L22 with the A2058G increases telithromycin resistance (Faccone et al., 2005). In the case of *M. Pneumoniae* pathogens, the resistance to 14-membered macrolide conferred by the T508C mutation in L22 is combined with A2058G or A2059G mutations (Cao et al., 2010; Jensen et al., 2014). Thus, all mutations in ribosomal proteins induce rRNA structural rearrangements and indirectly impede the placement of the drug in its binding pocket (Tu et al., 2005).

d. Macrolide modifications

Several enzyme-mediated modifications of the drugs can result in structural changes preventing their binding to the ribosome (Golkar et al., 2018).

Both Gram-negative and Gram-positive bacteria, from clinical, veterinary, agricultural or environmental origins, possess macrolide phosphotransferases which are crucial enzymes for macrolide inactivation (Fyfe et al., 2016; Roberts, 2008). They have an inducible or constitutive expression and are commonly found in mobile genetic elements. The macrolide 2' phosphotransferases (Mphs) are able to transfer the γ-phosphate of NTPs to the desosamine 2'-OH group of 14-, 15-, and 16-membered ring macrolides (**Figure 26**) to inhibit their fundamental interaction with A2058 (Fong et al., 2017; Shakya and Wright, 2010).

Another class of macrolide-inactivating enzymes targets the ester bond of macrocylic lactone ring, which is the key element to close the ring of macrolides (Donadio et al., 1991). Those enzymes, called esterases, can thus revert this final step to modify the macrolide structure (**Figure 26**).

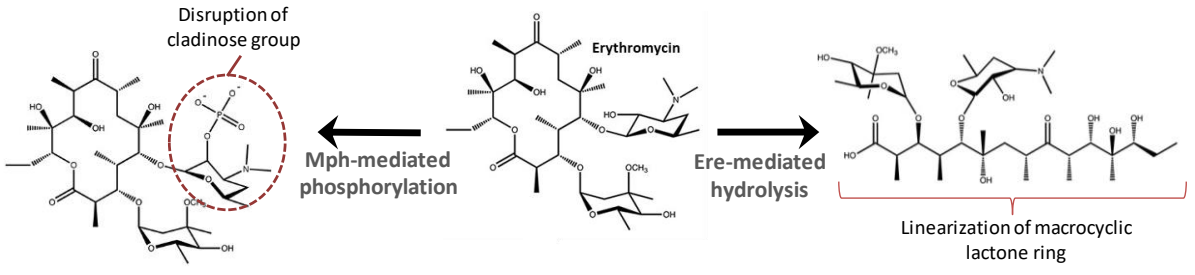

Figure 26: Enzyme-mediated modifications of macrolides. Adapted from Golkar et al., 2018.
Examples of erythromycin modification by Mph-mediated phosphorylation (left) or Ere-mediated hydrolysis (right).

Since the discovery of the first esterase, Ere(A), isolated from a *E. coli* macrolide resistant isolate (Barthélémy et al., 1984), the presence of esterase genes has been confirmed in a clinical isolate of *S. aureus* (Wondrack et al., 1996) and in environmental isolates of *Pseudomonas* species (Kim et al., 2002). Their localization on mobile elements of the genome suggests a large possibility to spread in the microbial world. Esterases display their hydrolytic inactivation activity only for 14- and 15-membered macrolides (Morar et al., 2012).

By contrast, glycosyltransferases (GTs) are less used in bacterial resistance. So far, the glycosylation of macrolides has only been reported for antibiotic producer organisms, as *Streptomyces antibioticus* which produces the oleandomycin, in a perspective of self-protection (Vilches et al., 1992). The macrolide is inactivated by an intracellular glycosyltransferase, which transfers donor sugars to macrolide acceptors, and which is reactivated by an extracellular glycosidase after secretion.

C. Evolution of drug development

The combination of the drug-resistant bacteria rise to the dearth of novel effective antimicrobials has made the drug resistance a persistent and worrying issue. Consequently, other strategies were and are still even needed to accelerate the discovery of new therapeutic agents.

a. Chemical synthesis

One alternative approach in drug development was to focus again on natural products to find others molecular scaffolds. To that purpose, optimization of ancient drugs by semi-synthesis, *i.e.* chemical modifications of natural products, was still relevant to improve pharmacological properties, such as solubility, drug uptake, affinity for the ribosome and insensitivity to modifications. Good examples of such new classes are the ketolides and the oxazolidinones. While ketolides chemically derive from macrolides, the oxazolidinones is the first fully synthetic class of ribosome-targeting antibiotics. Their unique scaffold, still overlapping with known binding site, opens a new era in synthetic drug development. Similarly, procedures for macrolide chemical synthesis were recently engineered (Seiple et al., 2016). A platform allows the fully synthetic synthesis of new macrolides by simply using a convergent assembly of chemical blocks.

Another strategy was to use hybrid antibiotics by combining classes of antibiotics with distinct target or close sites to compensate resistance mechanisms (Pokrovskaya and Baasov, 2010). For instance, because of their binding site proximity, sparsomycin and linezolid were conjugated to obtain a synergistic effect and produce chimeric drug (Franceschi and Duffy, 2006; Li et al., 2011), as well as macrolides and chloramphenicol (Svetlov et al., 2019; Wu and Su, 2001).

b. New target exploration

The lastest alternative is to find new molecules with new target sites to avoid both classical- and cross-resistance with the existing drugs and their derivatives. For example, the genomic exploration is now used to find promising candidate-encoding genes. The analysis of the human microbiome led recently to the discovery of two encouraging antibiotics, lactocillin and lugdunin (Donia et al., 2014; Zipperer et al., 2016). Furthermore, among the most naturally abundant antimicrobials synthetized by the human microbiota, a new ribosomally synthesized post-translationally modified peptides, called klebsazolicin, was identified (Donia and Fischbach, 2015; Metelev et al., 2017). Similarly, the orthosomycin class was found to bind to a unique site in the ribosome (Arenz et al., 2016). Although problems of toxicity and solubility need to be overcome, those molecules were very attractive for development of drugs with novel target sites. Pipelines for computational predictions of antibiotic cluster genes were also recently developed to support the discovery of new molecules (Alanjary et al., 2017)

Classical screening methods still allow finding of new classes of natural antibiotics. For example, the underestimated genus bacteria *Xenorhabdus* has been identified as a good source of antimicrobials agents thanks to its symbiose with soil-dwelling nematodes (Gualtieri et al., 2009), such as the new broad-spectrum class of the odilorhabdins (Pantel et al., 2018). In addition, other natural molecules were found after analysis of innate immune system of bacteria-infected hosts, as the discovery of PrAMPs several years ago.

Finally, these computational and chemical investigations are strongly supported by the high-resolution structures of antibiotic-bound functional ribosome complexes, that provide unprecedented insights into the mechanisms of action of antibiotics and the related mechanisms of resistance.

4. Goals of the study

Numerous studies led to a better understanding of the binding to the ribosome of many classes of antibiotics, in order to highlight their exact mechanisms of action and of resistance. PET-targeting compounds, and more precisely macrolides, were at the center of my studies due to their therapeutic relevance. Among the existing structural and biochemical studies, my project is distinguished by the innovative biophysical approaches used to study antibiotic interactions with the bacterial ribosome. Only few thermodynamic data are available about drug-ribosome interactions, although they are essential for a precise and complete description of the mechanisms of action. Indeed, thermodynamically-driven drug design is crucial to determine the energetic forces driving the binding which are useful for understanding and optimizing interactions of drugs. My goal was to establish the thermodynamic profile and affinity parameters of four known macrolides among the three generations.

II. Materials and methods

1. Purification of the bacterial ribosome of *E. coli* (adapted from Fechter et al., 2009)

A. Native 70S

70S ribosome is produced in a *E. coli* MRE600 strain (glycerol stock conserved at -80 °C), in which ribonuclease activity is insignificant to avoid ribosome degradation. From an overnight pre-culture, LB medium is seeded at 0.05 $OD_{600\ nm}$ and incubated at 37 °C. Usually, 250 mL of pre-culture are used to seed a culture of 10 L. Bacterial growth is stopped at 1 $OD_{600\ nm}$, cells are harvested (20 min, 4000 rpm, 4 °C) to obtain around 2 g of bacteria/L of culture and washed in lysis buffer (20 mM Tris HCl pH 7.5; 20 mM $MgCl_2$; 200 mM NH_4Cl; 0.1 mM EDTA; 6 mM β-mercaptoethanol). After conservation at 4 °C, cells are mechanically lysed in lysis buffer complemented with 1X protease inhibitor cocktail, 10 U DNase I and 1 mM $CaCl_2$ using a *French Press* (1.6 bar of pressure). A first centrifugation (30 min, 18 200 rpm, 4°C in 50.2 Ti rotor) is done to get rid of cellular debris. Ribosomes are then pelleted by 4h centrifugation at 41 700 rpm at 4 °C. A brownish layer at the surface of the pellets is removed and they are resuspended in AE buffer (20 mM Tris HCl pH 7.5; 20 mM $MgCl_2$; 200 mM NH_4Cl; 0.1 mM EDTA; 6 mM β-mercaptoethanol).

Subsequently, ribosomes are isolated through a 30 % sucrose cushion (19 h, 31 500 rpm, 4 °C) to eliminate all remaining contaminants (mostly initiation factors still present on ribosomes). Again, a brownish layer is removed from the top of the translucent pellets to be finally resuspended in a conservation buffer (20 mM Tris HCl pH 7.5; 10 mM $MgCl_2$; 50 mM NH_4Cl; 0.1 mM EDTA; 6 mM β-mercaptoethanol). Ribosomes suspension is clarified by a final centrifugation (1 h, 18 200 rpm, 4 °C) to eliminate remaining contaminants. At the end, ribosomes are concentrated using 100 K centrifugal filter unit (Centricon, Merck Millipore) before being flash-frozen in liquid nitrogen and conserved at -80 °C. Integrity of 16S rRNA and 23S rRNA is checked on 1 % agarose gel, 0.5 µg.mL^{-1} EtBr. Finally, considering RNA composition of ribosomes, 70S concentration is obtained from $OD_{260\ nm}$ using a 1-20 diluted suspension. Several dilutions need to be done for accurate concentration and their homogenisation before measurement is crucial for repeatable results. Generally, 50 mg of purified 70S native ribosomes are obtained from 1 L of culture.

1 $OD_{260\ nm}$ = 0.06 mg.mL^{-1} = 24 nM

B. Dissociation of ribosomal subunits

50 mg of native ribosomes are dialysed in a dissociation buffer (30 mM Tris HCl pH 7.5; 1 mM $MgCl_2$; 300 mM NH_4Cl; 0.1 mM EDTA; 1.5 mM DTT) for 4 hours at 4 °C using a small 3 kDa dialysis cassette. The decrease of the magnesium concentration leads to the dissociation of the 30S and 50S subunits, which are physically separated using a 10 % - 30 % sucrose gradient (15 h, 30 000 rpm, 4 °C in SW 32 Ti rotor).

Ribosomal subunits are then collected from the top using a Gradient Fractionator (Auto Densi-Flow Labconco) connected to an AKTA FPLC system (GE Healthcare) (**Figure S1**). Purity of fractions is assessed by visualization of 16S rRNA and 23S rRNA on a 1 % agarose gel, 0.5 µg.mL^{-1} EtB (**Figure S1**)r. Pure fractions of 30S and 50S are concentrated separately and washed in a conservation buffer (20 mM Tris HCl pH 7.5; 10 mM MgCl2; 50 mM KCl; 0.1 mM EDTA; 1 mM DTT) before being flash-frozen in liquid nitrogen. Aliquots are conserved at -80 °C. As for the 70S, subunits concentrations are taken by measuring the absorbance at 260 nm.

30S: 1 $OD_{260\ nm}$ = 72 nM
50S: 1 $OD_{260\ nm}$ = 36 nM

C. 70S reconstitution (inspired from Blaha et al., 2002; Pulk et al., 2006)

50 mg of purified 70S are dialysed in a dissociation buffer (20 mM Tris-HCl pH 7.5; 1 mM $MgCl_2$; 300 mM NH_4Cl; 0.15 mM EDTA; 1.5 mM DTT) for 4 hours at 4 °C using a small 3 kDa dialysis cassette. The dissociated ribosome is then dialyzed in a reassociation buffer (20 mM Tris-HCl pH 7.5; 20 mM $MgCl_2$; 300 mM NH_4Cl; 0.150 mM EDTA; 1.5 mM DTT) and concentrated using a 100 K centrifugal filter until approximately 500 µL. Ribosomes are finally incubated 1 h at 37 °C, before being loaded on 15 % - 40 % sucrose gradients. After ultracentrifugation (15 h, 28 000 rpm, 4 °C), reassociated 70S are isolated using the Gradient Fractionator coupled to an AKTA FPLC system. Fractions are pooled and ribosome is dialysed and concentrated in ITC buffer using 100 K centrifugal filter unit. As mentioned earlier, rRNA integrity can be checked again on 1 % agarose gel, 0.5 µg.mL^{-1} EtBr. Usually from 50 mg of 70S around 7 mg of 30S and 5 mg of 50S are obtained. Aliquots are flash-frozen in liquid nitrogen and conserved at -80 °C.

D. Validation of 70S status

In vitro translation experiments were done by the previous PhD student of the team to attest the activity of 70S purified following the same protocol. Mass spectrometry analysis was done to confirm the presence of all ribosomal proteins. Furthermore, the efficiency of reassociation also seems to confirm the integrity of the 70S ribosome. DLS experiments were also done to assess the absence of aggregation.

2. Purification of bacterial initiator transfer RNA, fMet-tRNA^{Meti}

A. Isolation of tRNA^{Meti}

a. Bacterial growth

An optimized strain, generously provided by Dr. Axel Innis, was used and the purification protocol was adapted to our needs. The plasmid inside HB101 cells is pBS (pBluescript, Stratagene), a high-copy pUC plasmid that carries an Amp^R gene. LB culture media are complemented with 400 µg-mL Ampicillin for bacterial growth.

From a glycerol stock conserved at -80 °C, a pre-culture in LB-medium is done and growth is stopped after 6 to 7 hours at 37 °C. An aliquot of the pre-culture is used to seed an overnight culture. Usually, 4 to 8 L of cultures are done from a 50 mL aliquot of 100 mL pre-culture. Cells are harvested (25 min, 4 000 rpm, 4 °C) and washed in a buffer (50 mM Tris HCl pH 7.2; 150 mM NaCl) to obtain approximately 5 g of cells-L of culture.

b. Phenol-chloroform extraction

Each pellet of 5g is resuspended in 20 mL of lysis buffer (20 mM Tris HCl pH 7; 20 mM magnesium acetate) and ½ volumes of phenol-chloroform 5:1 (homemade) is added. Tubes are agitated 1 h at 4 °C. The time during which the agitation takes place is important for the final yield. After a centrifugation of 45 min at 4000 rpm at 4 °C, the first supernatant is conserved and 20 mL of lysis buffer are added on the phenolic phase. The suspension is quickly vortexed, centrifuged again (45 min, 4 000 rpm, 4 °C) and the second supernatant is also recovered. A mix of phenol-chloroform 1:1 (homemade) is added on the both supernatants and vortexed quickly. After centrifugation (45 min, 4 000 rpm, 4 °C), supernatants are pooled.

Then, a step of DNA precipitation is done by mixing 0.15 volume of sodium acetate 3M pH 5 and ¼ volumes of isopropanol. After centrifugation (1 h, 4 000 rpm, 4 °C), a precipitation of tRNAs is done on the supernatant. 1 volume is added and the whole thing is incubated overnight at 4 °C. tRNAs are pelleted (1 h, 5 000 rpm, 4 °C) and resuspended in 10 mL of 200 mM Tris –Acetate pH 9 in order to deacylate all tRNAs; and incubated 1 h at 37 °C. An ethanol precipitation is performed by adding 1-5 volumes of 3 M NH_4OAc pH 5.2 and 2.5 volumes of absolute cold ethanol, followed by 1 h incubation at -20 °C. After centrifugation (30 min, 5 000 rpm, 4 °C), the pellet is washed by cold 70 % ethanol. A last centrifugation (30 min, 5 000 rpm, 4 °C) is done before pellet being dried and resuspended in few mL of 10 mM NH_4OAc pH 5.2. $OD_{260\,nm}$ is taken and tRNAs is kept at -20 °C.

1 $OD_{260\,nm}$ = 40 $ng.\mu L^{-1}$ for RNA
$MW_{tRNAMeti}$ = 25 056 $g.mol^{-1}$

c. Chromatographic columns

For the first step of purification, extracted tRNAs are injected on a Q sepharose column (16 mL) and eluted using increasing NaCl concentration (150 mL gradient from 40 to 80 % of 1 M NaCl in 20 mM HEPES pH 7.0). A saturated and large peak is detected in the middle of the gradients, and fractions are kept for isopropanol precipitation (addition of 1 volume followed by 3 h of incubation at 4 °C). After centrifugation (1 h, 5 000 rpm, 4 °C), pellet is resuspended in few mL of milliQ H_2O. A second step of purification is done with a phenyl sepharose column (25 mL), equilibrated in buffer A (50 mM KPO_4 pH 7.0; 1.7 M $(NH_4)_2SO_4$). tRNAs elution will be directly correlated to their hydrophobicity degree, very hydrophobic tNRAs interacting strongly with phenyl sepharose matrix. A gradient of 5 to 35 % of B on 170 mL is done by mixing buffer A and buffer B (20 mM MOPS pH 8.0). To avoid deacylation after elution, 500 µL of 1 M sodium acetate pH 5.0 is added to each 5 mL fractions.

Then, main peak fractions are concentrated in 50 K centrifugal filter unit. At this step, most of contaminants tRNAs is eliminated.

d. Selection of $tRNA^{Meti}$

Once tRNAs are concentrated, a step of amino acylation and formylation of $tRNA^{Meti}$ is necessary to discriminate the initiator $tRNA^{Meti}$ from the elongation one. This part is achieved using *E. coli MRE 600* S100 fraction, which contains the whole set of tRNA synthetases. S100 fraction, available in our laboratory, is obtained from supernatant obtained after pelleting ribosomes.

A 1.1 mL mix of aminoacylation-formylation is realized:
- 110 mM HEPES pH 7
- 22 mM $MgCl_2$
- 327 mM KCl
- 4.5 mM ATP
- 0.09 $mg.mL^{-1}$ Methionine
- 1.8 mM FTH*
- 1.8 $mg.mL^{-1}$ S100
- ~100 nmol tRNA

The mix is incubated 45 min to 1 h at 37 °C.

*Formation of 10-Formyltetrahydrofolate (FTH):
A solution of folinic acid is prepared at a concentration of 6 mM from powder. HCl is added to reach a pH of 1.5 (45 µL of 1 M for 1 mL and control with pH paper) and β-mercaptoethanol is also incorporated for a final concentration of 100 mM. At this stage, formation of 5,10-Methenyltetrahydrofolate occurs at room temperature and can be visualized by following $OD_{350\ nm}$. This reaction takes between 3 to 4 h to reach saturation. The product is conserved at -20 °C. The substrate of the formyl transferase, 10-Formyltetrahydrofolate, is finally obtained after mixing 5,10-Methenyltetrahydrofolate with a buffer of pH > 7.0.

A new phenol-chloroform extraction needs to be done to isolate tRNAs. After adding 1 V of a mix of phenol-chloroform 1:1 (homemade) and vortexing, the suspension is centrifuged (15 min, 4 500 rpm, 4 °C). 1 V of chloroform is then added to the aqueous phase and, after vortexing, is again centrifuged (15 min, 4 500 rpm, 4 °C). An ethanol precipitation is realized by adding 0.2 volumes of 3 M NH_4OAc pH 5.2 and 2.5 V of absolute cold ethanol, followed by 1 h incubation at -20 °C. After centrifugation (30 min, 5 000 rpm, 4 °C), the pellet is washed by cold 70 % ethanol. A last centrifugation (30 min, 5 000 rpm, 4 °C) is done before pellet are dried and resuspended in few mL of buffer A (phenyl sepharose purification buffer).

$OD_{260\ nm}$ is taken and tRNAs is either kept at -20 °C or directly injected again on the phenyl sepharose column, following exactly the same conditions than for the first run of purification (see previous subsection 2.A.c.).

Fractions of the main peak are concentrated and dialysed against 5 mM NH_4OAC pH 5.2 in 50 K centrifugal filter unit, before being flash-frozen in liquid nitrogen and conserved at – 20 °C. At this step, the purity of fMet-$tRNA^{Meti}$ is acceptable (**Figure S2**), but if a very high purity is needed a third run on phenyl sepharose can be done (see section 2.B. below).

B. Obtention of highly pure fMet-$tRNA^{Meti}$ (adapted from L. Filonava thesis)

Highly pure fMet-$tRNA^{Meti}$ is obtained either from commercial lyophilized $tRNA^{Meti}$ or from homemade purified $tRNA^{Meti}$. Aminoacylation and formylation are done simultaneously to increase purification yield.

A 1 mL mix is realized:
- 1X final ion mix (300 mM Imidazole pH 7.6; 100 mM magnesium acetate; 1 M KCl)
- 5 mM ATP
- 0.5 mM 10-FTH
- 0.15 $\mu g.mL^{-1}$ BSA
- 2 $mg.mL^{-1}$ $tRNA^{Meti}$
- 9 $\mu g.mL^{-1}$ Methionine
- 0.175 $\mu g.mL^{-1}$ FT (purified in the lab); 200 times pre-dilution of the stock in a specific buffer (20 mM Tris-HCl pH 7.5; 4 $mg.mL^{-1}$ BSA; 10 mM β-mercaptoethanol)
- 1.3 $\mu g.mL^{-1}$ MetRS (purified in the lab); 400 times pre-dilution of the stock in the same dilution buffer than FT

The mix is divided in 250 µL aliquots and incubated 45 min at 37 °C.

An ethanol precipitation is done by incubating at -80 °C for 20 min each aliquot with a mix containing 81 mM potassium acetate pH 5.2, 194 mM NaCl and 2.4 volumes of absolute cold ethanol. After centrifugation (30 min, 14 000 rpm, 4 °C), the pellet is extensively dried and resuspended in a buffer (160 mM KAc pH 5.2; 795 mM NaCl; 4.5 mM β-mercaptoethanol) before a new centrifugation (30 min, 14 000 rpm, 4 °C). 3 volumes of absolute cold ethanol are then added to the supernatant and incubated at -80 °C overnight. fMet-$tRNA^{Meti}$ is pelleted (30 min, 14 000 rpm, 4 °C) and resuspended in 50 µL of 5 mM sodium acetate pH 5.2.

For the purification, the phenyl sepharose is used in the exact same conditions as established previously (see previous subsection c.). Before flash-freezing, concentration of fMet-$tRNA^{meti}$ is calculated by considering the $OD_{260\ nm}$.

C. Validation of $tRNA^{Meti}$ identity

During the optimization of $tRNA^{Meti}$ purification, several verifications were done for tRNA purity, integrity and identity (**Figure S2**) using different approaches (denaturing acrylamide gel, amino acylation and mass spectrometry).

a. Radioactive amino acylation

Presence and purity of $tRNA^{Meti}$ can be checked by attachment of ^{14}C-Methionine.

An aminoacylation mix of 50 µL is prepared:
- 1 X PM buffer (100 mM Tris HCl pH 7.5; 30 mM KCl; 10 mM $MgCl_2$) from a 5 X stock
- 2 mM ATP
- 1.6 $mg.mL^{-1}$ S100
- 1 µL ^{14}C-Methionine

10 µL of diluted sample containing $tRNA^{Meti}$ are then added to the mix. Usually, 3 dilutions are done and a control with total tRNA of E. coli is used as reference.

After an incubation of 10 min at 37 °C, the reaction is stopped by addition of 1 mL of cold TCA and the whole thing is incubated 5 to 10 min in ice. Free ^{14}C-Methionine is eliminated by filtration, using filters on which charged $tRNA^{Meti}$ are retained. Each sample is added on filters, previously washed by TCA. After 3 TCA washes, filters are dried 10 min and put in vials with glittering liquid.

b. Mass spectrometry

After the first purification, $tRNA^{Meti}$ was digested by RNase T1 and analyzed by MALDI-TOF at the mass spectrometry platform. Predicted fragments were compared to the spectrum obtained for the purified tRNA to validate $tRNA^{Meti}$ identity (**Figure S2 A and B**).

3. mRNA purification

The mRNA used here is the mRNA sodB (56 nts) with a strong S-D sequence (Duval et al., 2013; Geissmann and Touati, 2004): 5' GGA AAU UAA UAA UAA AGG AGA GUA GCA **AUG** GGC ACG UCC GUC AGA GAA AAU AAA A 3'.

DNA template for mRNA production by T7 transcription is obtained by hybridization with 2 oligonucleotides chemically synthesized by IDT. DNA hybrid is made by serial incubations of 5 min at 90 °C, 5 min at 0 °C and 20 min 54 °C.

For 1 mL mix of transcription:
- 1 X T7 buffer (400 mM Tris Hcl pH 8.0; 150 mM $MgCl_2$; 500 mM NaCl)
- 0.005 $U.µL^{-1}$ pyrophosphatase
- 1.5 mM spermidine
- 0.15 $mg.mL^{-1}$ BSA
- 50 mM DTT
- 4 mM rNTPs
- 0.025 % Triton X-100
- 15 to 20 µg of DNA template
- 20 µL of homemade T7 RNA polymerase

The mix is incubated 3 h at 37 °C. After 1 h of transcription 10 µL of RNA polymerase is added. Transcripts are then purified by phenol-chloroform extraction and ethanol precipitation. 1 V of phenol-chloroform (Roti®P-C-I, Roth) is added and sample is centrifuged 5 min at 6 000 g after a vigorously vortexing. The aqueous phase is kept and 1 V of chloroform-isoamylic alcohol (25:1) is added and again after vortexing, sample is centrifuged. This step is repeated once, and the supernatant is finally mixed with 2.5 V of cold absolute ethanol and 1-10 of 3M sodium acetate. Precipitation is done at -80 °C at least 30 min. After pelleting RNA (30 min, 6 000 g, 4 °C), a wash with cold 70 % ethanol is done without resuspending the pellet. Finally, the pellet is resuspended in mQ water, before being washed in water and concentrated using 50 K centrifugal filter unit.

Transcripts are purified using a 10 % denaturing large acrylamide gel containing 8 M urea. The RNA is mixed with 1 V of urea blue and after heating 5 min at 95 °C, the sample is deposited in an unique well. The mRNA of interest is then visualized by UV shadowing and the band of interest is excised. A passive elution is achieved overnight in a buffer containing 10 mM Tris HCl pH 7.5, 200 mM NaCl and 0.5 mM EDTA. Finally, mRNA is purified on a DNAPac PA100 column (Dionex), equilibrated in buffer A (20 mM MES pH 6.5; 4 M Urea). mRNA is eluted by a 40 mL gradient of 120 to 260 mM $NaClO_4$ using a mix of buffer A and B (20 mM MES pH 6.5; 4 M urea; 400 mM $NaClO_4$). Fractions are checked on a 10 % denaturing large acrylamide gel, before being pooled, washed and concentrated in water. Samples are kept in -20 °C.

4. Purification of translation factors

A. Initiation factors (adapted from Milon et al., 2007)

Initiation factors are purified considering their physico-chemical properties, without any tag. IF1, IF2 and IF3 are synthetized from genes *infA*, *infB* and *infC*, respectively, using the strain *E. coli K12 UT5600*. Strains for the purification of each initiation factor are available in the laboratory. It contains two plasmids: one pCI857, kanamycin-resistant, coding for the thermosensible repressor CI, and a second pPLC2883, Ampicillin-resistant, carrying a gene coding for one of the initiation factors under the dependence of the lambda pL promotor controlled by CI repressor. Thus, the expression is induced by an increase of the temperature during the growth.

Growth and lysis steps are identical for the three factors. An overnight pre-culture, from a glycerol stock conserved at -80 °C, was grown at 30 °C and used to seed LB-medim complemented by 60 $\mu g.mL^{-1}$ of Ampicillin and 25 $\mu g.mL^{-1}$ of kanamycin. Usually, 500 mL of pre-culture are done for a 12 L culture. As soon as $OD_{600\,nm}$ reaches 0.8 to 1, the temperature is increased from 30 °C to 42 °C for 30 min to inactive CI repressor and to induce expression. Bacteria are then placed at 37 °C for 1h30 to boost expression yields, before being harvested (20 min, 4 000 rpm, 4 °C) and washed in lysis buffer (10 mM Tris HCl pH 7.7; 60 mM NH_4Cl; 5 mM MgAc; 6 mM β-mercaptoethanol). Generally, we obtain 5.5 g of cells-L of culture.

Cells are directly lysed using a *French Press* (1.6 bar of pressure) in lysis buffer complemented by 1X protease inhibitor cocktail, $mg.mL^{-1}$ DNase I and 1 mM $CaCl_2$. Cellular debris are eliminated by centrifugation (1 h, 10 000 g, 4 °C) and NH_4Cl powder are added to the supernatant to a final concentration of 1 M in order to dissociate initiation factors still attached to ribosomes. After ultracentrifugation (16 h, 35 000 rpm, 4 °C in 50.2 Ti rotor), supernatant can be used for purification steps. For IF1 and IF3, the same protocol is followed, whereas IF2 purification is specific. During my PhD, I did not need to purify IF1 since stocks from the previous PhD student were still available in the lab.

a. Chromatographic steps for IF3 purification

Supernatant is diluted in 9 V of buffer A without NH_4Cl (20 mM Tris HCl pH 7.1; 1 mM EDTA; 10 % glycerol; 6 mM β-mercaptoethanol), before being loaded on a homemade-packed phosphocellulose column (60 mL, GE Healthcare), previously equilibrated in buffer A (20 mM Tris HCl pH 7.1; 100 mM NH_4Cl; 1 mM EDTA; 10 % glycerol; 6 mM β-mercaptoethanol). When $OD_{280\ nm}$ is stable again, elution is done on 350 mL by a salt gradient from 0.1 to 0.7 M of NH_4Cl, using a mix between buffer A and B (buffer A with 700 mM NH_4Cl). After identification of the fractions of interest by SDS-PAGE, eluate is dialyzed overnight against denaturation buffer C (20 mM Tris HCl pH 7.1; 50 mM NH_4Cl; 1 mM EDTA; 10 % glycerol; 6 M urea; 6 mM β-mercaptoethanol). Dialysate is then reinjected on the phosphocellulose column, previously equilibrated with buffer C. Elution is done on 350 mL by a salt gradient from 0.05 to 0.7 M of NH_4Cl, using a mix between buffer C and D (buffer C with 700 mM NH_4Cl). Again, IFs-containing fractions are selected using SDS-PAGE and pooled, before a dialysis against renaturation buffer E (20 mM Tris HCl pH 7.1; 200 mM NH_4Cl; 0.1 mM EDTA; 10 % glycerol; 1 mM DTT). At this step, IFs are quite pure. Dialysate is concentrated with centrifugal filter unit 10 K and injected on Superdex^{TM} 75 10-300 GL (GE Healthcare), previously equilibrated in buffer E. Pure fractions, checked on SDS-PAGE are pooled and concentrated with centrifugal filter unit. Aliquots (for ITC) are done, before being flash-frozen and conserved at -80 °C. Usually 15 mg of IF3 are obtained for 1 L of culture.

IF3: $1\ OD_{280\ nm} = 4.6\ mg.mL^{-1}$
$MW_{IF3} = 20\ 560\ g.mol^{-1}$

b. Chromatographic steps for IF2 purification

Supernatant is diluted in 9 volumes of buffer A without NH_4Cl, before being loaded on a homemade-packed phosphocellulose column, previously equilibrated in buffer A (20 mM Tris HCl pH 7.1; 100 mM NH_4Cl; 1 mM EDTA; 10 % glycerol; 6 mM β-mercaptoethanol). When $OD_{280\ nm}$ is stable again, elution is done on 600 mL by a salt gradient from 0.1 to 0.6 M of NH_4Cl, using a mix between buffer A and B (buffer A with 700 mM NH_4Cl).

After determination of interest fractions by SDS-PAGE, eluate is dialyzed overnight against buffer F (20 mM Tris HCl pH 7.9; 100 mM NH_4Cl; 1 mM EDTA; 10 % glycerol; 6 mM β-mercaptoethanol) to change the pH.

Dialysate is then injected on a homemade-packed DEAE-sepharose Fast Flow column (25 mL, GE Healthcare), previously equilibrated with buffer F. Elution is done on 150 mL by a salt gradient from 0.05 to 0.6 M of NH_4Cl, using a mix between buffer F and G (buffer F with 600 mM NH_4Cl). As at this step, the three IF2 isoforms are already quite pure; flowing steps allow to isolate the alpha isoform, which is the one used in our experiments. After SDS-PAGE, fractions of interest are pooled and dialyzed against buffer MonoQ A (20 mM Tris HCl pH 7.9; 100 mM NaCl; 1 mM EDTA; 10 % glycerol; 6 mM β-mercaptoethanol) to remove excess of NH_4Cl. Dialysate is loaded on MonoQ 5-50 GL column (GE Healthcare), previously equilibrated with buffer MonoQ A. Isoforms are separated with a 0.17 to 0.5 M of NaCl gradient on 40 mL, by mixing buffer MonoQ A and MonoQ B (buffer MonoQ A with 600 mM NaCl). Pure fractions of IF2α are selected after SDS-PAGE, concentrated with 50 K centrifugal filter unit and washed in buffer E. As for IF1 and IF3 aliquots are done before being flash-frozen and conserved at -80 °C. Usually, we obtain 8.5 mg of IF2-L of culture.

1 $OD_{280\ nm}$ = 3.5 $mg.mL^{-1}$
$MW_{IF2\alpha}$= 97 350 $g.mol^{-1}$

B. Elongation factor, EF-Tu

EF-Tu is purified using a C-terminal histidine-tag. pET-24b (+) plasmids, which carries the appropriate gene (*tufB*) and Kan^R gene, are available in the laboratory and were generously gifted by Attilio Fabbretti. *E. coli* BL21 Rosetta 2 (Cam^R) were transformed with each plasmid and a colony on LB-agar plate, complemented with 34 $\mu g.mL^{-1}$ of Chloramphenicol and 30 $\mu g.mL^{-1}$ of Kanamycin, was used to prepare a glycerol stock conserved at -80 °C. IPTG induction system allows protein expression thanks to LacO repressor encoded by plasmids.

From a pre-culture grown at 37 °C in LB medium, complemented with 34 $\mu g.mL^{-1}$ of Chloramphenicol and 30 $\mu g.mL^{-1}$ of Kanamycin, a culture is seeded at 0.05 $OD_{600\ nm}$ until it reaches $OD_{600\ nm}$ 0.7 to 0.8. Expression is then induced by 1 mM IPTG and after 3h of overexpression at 37 °C, bacteria are harvested, washed in lysis buffer (20 mM Tris HCl pH 7.5; 200 mM NaCl; 10 mM $MgCl_2$; 10 mM Imidazole pH 7.6; 5 % glycerol; 10 mM β-mercaptoethanol) and conserved at 4 °C. Usually, we get 2.5 g of cells-L of culture. Cells are lysed mechanically using a *French Press* (1.6 bar of pressure) in lysis buffer complemented with 1X protease inhibitor cocktail, $mg.mL^{-1}$ DNase I and 1 mM $CaCl_2$. Cellular debris are eliminated by ultracentrifugation (1h, 45 000 rpm, 4 °C).

Supernatant is injected on HiFliQ Ni-NTA FPLC column (1 mL, Clinisciences), previously equilibrated with lysis buffer. As soon as $OD_{280\ nm}$ is stable, a high-salt wash (500 mM NaCl in lysis buffer) is done to remove possible contaminants. EF-Tu is eluted by increasing Imidazole concentration to 200 mM in one step. After checking EF-Tu purity on SDS-PAGE, it appears that EF-Tu is almost pure at this step. Yet, a second step of purification allows improving its purity. Pooled fractions are diluted in buffer A (50 mM Tris HCl pH 7.5; 50 mM NaCl; 5 mM MgCl2; 7 mM β-mercaptoethanol) complemented with 50 µM of GDP and injected on a homemade-packed Source Q column (7.8 mL, GE Healthcare). EF-Tu is eluted using a 30 mL gradient of 4 to 100 % of buffer B (buffer A with 500 mM NaCl). After SDS-PAGE, pure fractions are pooled, concentrated in 10 K centrifugal filter unit and washed in conservation buffer (50 mM Tris HCl pH 7.5; 50 mM KCl; 10 mM MgCl2; 50 µM GDP; 5 mM β-mercaptoethanol). Finally, the protein is diluted in ½ volumes of 100 % glycerol and conserved at -20 °C.

1 $OD_{280\ nm}$ = 2.1 $mg.mL^{-1}$
$MW_{EF\text{-}Tu}$ = 43 284 $g.mol^{-1}$

5. Formation and purification of ternary complex (TC), EF-Tu-GTP - Gly-$tRNA^{Gly}$ (adapted from Rodnina and Wintermeyer, 1995)

The formation of the TC consists in the exchange of GDP on EF-Tu by GTP and loading of the dedicated aminoacid on the aa-$tRNA^{aa}$. Here, we use $tRNA^{Gly}$, which is available in the laboratory.

A 1.2 mL mix is realized:
- 1 X PM buffer (100 mM Tris HCl pH 7.5; 30 mM KCl; 10 mM $MgCl_2$) from a 5 X stock
- 2 mM ATP
- 2 mM phosphoenolpyruvate
- 0.15 $mg.mL^{-1}$ phosphoenolpyruvate kinase
- 0.4 $mg.mL^{-1}$ S100
- 200 µM GTP
- 200 µM glycine
- 2 µM EF-Tu-GDP
- 16.8 OD_{260nm} $tRNA^{Gly}$ (pure at 16 %)

The mix is incubated 45 min at 37 °C.

The mix is then concentrated until 250 µL, using Microcon-30 K centrifugal filter unit. The complex is injected on Superdex™ 200 Increase 10-300 GL (GE Healthcare) which allows discrimination of the TC from tRNA and EF-tu alone. Fractions of the complex peak are pooled and concentrated using 30 K centrifugal filter unit until 100 µL approximately. The complex is always directly used for ITC or formation of translation complexes.

6. Formation of translation complexes, 70SIC and 70SEC (adapted from Belardinelli et al., 2016; Goyal et al., 2015)

All partners of initiation complexes (reassociated 70S or reactivated 30S and 50S, IFs, fMet-tRNAt^{Meti} and mRNA) are dialyzed against ITC buffer using centrifugal filter unit.

300 µL of 30SIC and 70SIC complexes are formed by mixing 1.5 fold excess of IFs and fMet-tRNAt^{Meti} , 2-fold excess of mRNA and 2.5 mM of GTP, and incubated 1h at 37 °C. Then 1.5-fold excess of 50S is added to 30SIC to form a 70SIC complex. 70SEC formation is achieved by mixing 70SIC (from reassociated 70S) and TC. Complexes are purified through 1.1 M sucrose cushion in ITC buffer and centrifuged 3h, 108 000 rpm, 4 °C (rotor S145-AT in Sorval Discovery M150SE Hitachi ultracentrifuge). The pellets are then resuspended in ITC buffer before performing ITC experiments.

7. Preparation of ITC experiment (Schenckbecher et al., 2019, **Annex 1**)

A. Sample preparation

Ribosomes are dialyzed against ITC buffer using 4 mL centrifugal filter unit. Generally, 15 to 20 mL are used for the wash for an initial aliquot of 1 mL or less. Regarding peptides and antibiotics, powders are dissolved directly in ITC buffer when solubility allows it. Erythromycin, azithromycin and telithromycin were solubilized in ITC buffer whereas josamycin was solubilized in 100 % DMSO at a high concentration and then diluted in ITC buffer. In such case, the final percentage of DMSO is determined and the same amount is added in the 70s sample in the cell. Since concentrations must be very accurate, diluted solutions prepared for the sample cell and for the syringe are checked by absorbance measurements before running experiment; except for the antibiotics for which concentrations cannot be verified after powder dilution in ITC buffer. Ribosome concentration is obtained by measuring OD_{260nm} of twentieth dilution and for peptides, OD are taken at 277 nm.

$\varepsilon_{pyrrhocoricin}$ = 2 980 $M^{-1}.cm^{-1}$
$\varepsilon_{metalnikowin}$ = 1 490 $M^{-1}.cm^{-1}$

B. Classic experiment

As ribosomes are always placed in the sample cell, a minimum of 280 µL is needed at the desired concentration. Concentrations are usually between 8 and 15 µM for an experiment with peptides and increased at 15 to 22 µM for antibiotics. Ligands must be in 70 µL at the desired concentration, which is generally 10 times higher than cell concentration. For antibiotics, this ratio is even increased to 15-20 times higher. Size and number of injections depend on the concentrations, type of ligands and intensity of heat release. For most situations, 19 injections of 2 µL are performed during a titration.

All measurements were realized on PEAQ ITC (Malvern) and processed with PEAQ-ITC analysis software. For kinITC analysis, Affinimeter software was used.

C. Competition using incremental ITC

Incremental ITC consists in serial of classic ITC experiments and is applied to competition experiments, which are based on the use of a weak and strong binder for a same binding site. In our case, PrAMPs present a weaker affinity for the PET than macrolides. Ribosomes-PrAMPs complexes are formed in a first ITC experiment, and then kept in the sample during the syringe cleaning and subsequent loading with a macrolide. In order to take into account ribosome dilution following the first ITC experiment, a concentration >15µM of ribosome is needed. PrAMPs are 10 times more concentrated and injection size can be reduced to 1 or 1.5 µL. Regarding macrolides, concentration is about 15 times higher than diluted ribosomes and 2 µL injections are used. For this second ITC, which concretely corresponds to displacement of the peptide by a macrolide, time between injections must to be significantly increased to at least 800 s, compared to 200 s in traditional cases.

8. Detection of peptide in 70S ribosomes

A. Pull-down of 70S-pyrrhocoricin complexes

A strain of *E. coli* producing a tagged ribosome was generously given by the lab of Pr. Reynald Gillet. A 6-His tag is located on the rpsB gene coding for the 30S ribosomal protein S2 and a Streptag on the rpsT gene coding for 30S ribosomal protein S20. The tagged-70S was purified following exactly the same protocol than for the purification of the native 70S. From 70S-pyrrhocoricin-ITC formed complexes, an affinity purification using Nickel beads (Ni Sepharose High Performance, GE Healthcare) was performed. Ribosomes were pelleted by a 2 h centrifugation at 41 000 rpm at 4 °C (rotor in Sorval Discovery M150SE Hitachi ultracentrifuge) and resuspended in 300 µL of lysis buffer (20 mM Tris HCl pH 7.5; 10 mM $MgCl_2$; 150 mM KCl; 30 mM NH_4Cl; 1X protease inhibitor cocktail). Then, 50 µL of beads are added to the solutions. After 1 h of agitation at 4 °C, 3 washes with lysis buffer were done. Ribosomes were eluted in 400 µL of lysis buffer complemented with 150 mM of Imidazole before being dialyzed against lysis buffer overnight at 4 °C. Finally, concentration of ribosomes in dialysates is determined at OD_{260nm}. 10 µg of sample are used for LC-MS-MS analysis. At each steps, presence and integrity of ribosomes were checked on 1 % agarose gel, 0.5 $\mu g.mL^{-1}$ EtBr.

B. CryoEM

For data collection, 3 µl of the ITC-formed 70S-pyr-telithromycin complex, with a concentration of 120 nM, was applied to 400 mesh holey carbon Quantifoil 2-2 grids (Quantifoil Micro Tools, Jena, Germany), blotted with filter paper from both sides for 2 seconds in the temperature- and humidity-controlled Vitrobot apparatus Mark IV (FEI, Eindhoven, Netherlands, T = 4°C, humidity 100%, Blot Force 5, Blot waiting time 30'') and vitrified in liquid ethane pre-cooled by liquid nitrogen. Data were collected on the spherical aberration (Cs) corrected Talos™ Arctica™ instrument (ThermoFisher Scientific) operating at 200 kV acceleration voltage and at a nominal underfocus of Δz = -0.8 to -4.5 µm using the second-generation back-thinned direct electron detector CMOS (Falcon III) 4096 x 4096 camera and automated data collection with EPU softwares (FEI, Eindhoven, Netherlands). The microscope was carefully aligned as well as the Cs corrector. The Falcon III camera was calibrated at nominal magnification of 92,000 X resulting in 1.612Å pixel size at the specimen level. Camera was set up to collect 40 frames with a total electron dose of 21 ē-Å2 (or 0.545 ē-Å2 per frame). For image processing a framework with integrated several software package (SCIPION, de la Rosa-Trevin, J.M. et al., 2016) has been used to obtain the 3D reconstruction of the *E. coli* 70S potentially in complex with pyrrhocoricin and/or telithromycin

III. Results and discussion

Characterization of drug binding to their target is crucial to investigate on antibiotic resistance mechanisms. Most of such studies are done using structural, biochemical or sometimes kinetic approaches. Although underestimated in academic research, thermodynamics is largely used by pharmaceuticals industries for the development and selection of new compounds. In our group, we decided to address this study of macrolide characterization using ITC microcalorimetry. All the experiments are listed in the **Annex 3**.

The detection of small molecules on the ribosome can be very tedious due to low heat exchange, noise, aspecificity, undetectable affinities, … Before selecting which antibiotics are the most "ITC-friendly", I screened different classes of antibiotics such as tetracycline, chloramphenicol, aminoglycosides, linezolid and MLS_BK. As expected, some thermograms were difficult to interpret mostly because of non-specificity and low heat exchanges. Macrolides and related compounds appeared to be the most suited for our approach, and among the most interesting ones in the fight against multiresistant bacteria. I chose to work with 4 well-known macrolides, erythromycin, azithromycin, telithromycin and josamycin, from different generations and/or with different structures (**Table 2**).

	Erythromycin	Azithromycin	Telithromycin	Josamycin
Generation	1st	2nd	3rd	2nd
Atoms number in the cycle	14	15	14	16
Structure	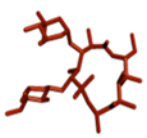		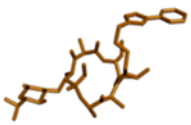	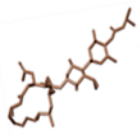

Table 2: Principal features of the macrolides of interest.

1. ITC limitations for the study of direct macrolide binding to the ribosome

The interaction between the 70S of *E. coli* and macrolides were investigated at several temperatures: 15, 20, 25, 30 and 35 °C. With ribosome concentrations ranging from 8 to 12 µM, no significant heat exchange, apart the residual heat of dilution, was detected during ITC experiments. Consequently, ribosome concentration was increased to a minimum of 15 µM to see a direct interaction between a macrolide and the 70S ribosome. Though signals intensities are in the lower limit of detection of the microcalorimeter (thermograms in **Figure 27**), we were able to detect exothermic signals for all 4 macrolides at high temperatures, such as 30 or 35 °C. ΔH are very low for the four macrolides, between -0.1 and -6 $kcal.mol^{-1}$. In addition, the ΔH of josamycin, is more negative than the others (**Figure 27**) which could be due to additional bonds with rRNA thanks to its extended tail (**Figure 18B, 19** and **Table 2)**.

The ΔH of telithromycin is the lowest but its binding was also detected at 15 °C with an endothermic reaction (**Figure 27C**). Because of the high c value (c>1000) in these experiments, ΔH should be correctly estimated; but, considering the very low signal/noise ratio, its determination can be entailed by significant errors. Slight manual adjustments of the baseline are required to improve the fit of the titration curve. Nonetheless, given that the smaller the surface area, the larger the error, the introduced ambiguity cannot be ignored (**Figure 27A and B**). Taken together, these experiments show that the binding of these 4 macrolides to the 70S ribosome is mostly entropy-driven, with a weak positive contribution of enthalpy at physiological temperature (**Figure 27D**). This means that the increased disorder provides most of the free energy for the complex formation.

Moreover, all thermograms display a similar profile of a very tight affinity binding, with an initial and a final plateau and at best only one single point in the slope (**Figure 27A**). This lack of experimental points in the slope of titration curves leads to inaccurate determination of the Kd. This issue was expected since the interaction between macrolides and ribosome presents Kd lower than 10 nM, which is approximately the sensitivity limit of the ITC device. As for ΔH determination, automatic data processing leads significant biais in the Kd determination with errors bigger than the Kd itself (**Figure 27A**). Besides, manual adjustments introduce too many uncertainties in the affinity parameters evaluation. (**Figure 27B**).

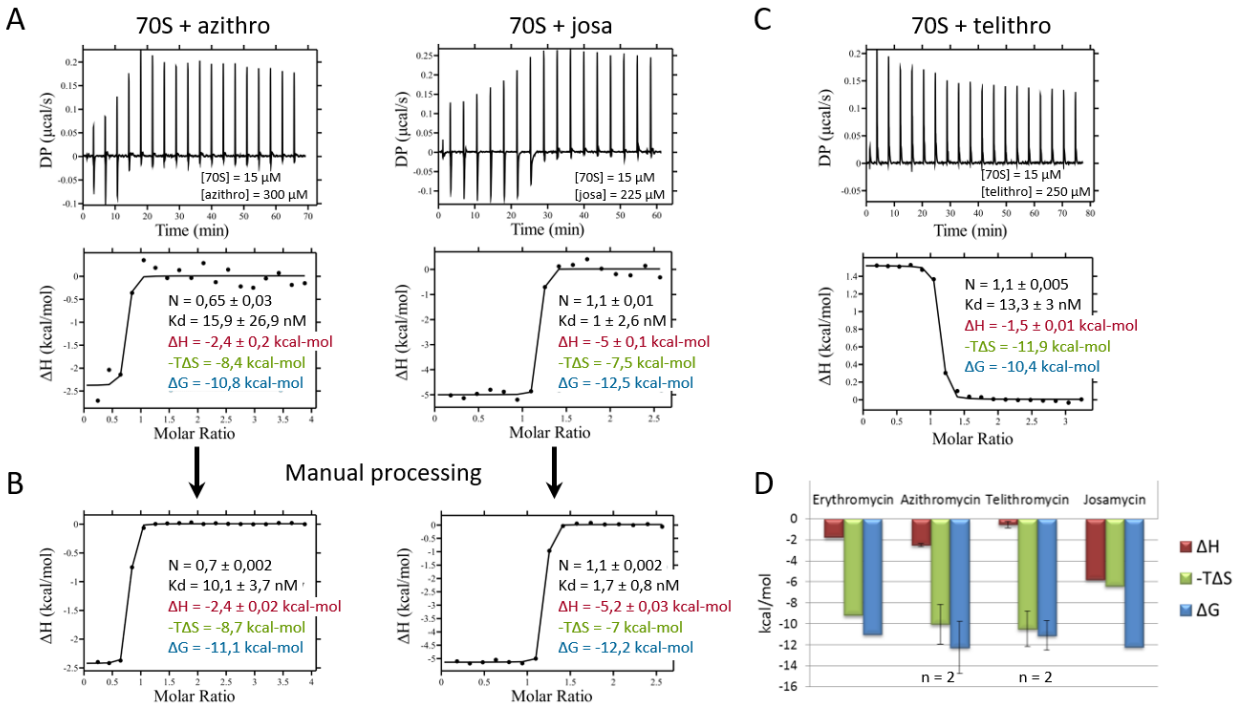

Figure 27: Features of macrolides binding to 70S by direct ITC.
Examples of ITC data for 70S titrations by azithromycin (azithro) and josamycin (josa) at 30 °C before (A) and after processing (B); and for telithromycin (telithro) binding to 70S ribosome at 15 °C (C). Thermodynamic profiles obtained for the 4 studied macrolides at 30 °C are presented in (D). Number of replicates (n) is indicted below the histogram bars. Detailed data are listed in **Table S2 of Annex 3**.

Finally, global sensitivity problems are inextricably linked to signal intensities and high affinities. The issue for heat detection emphasizes the difficulty to have access to the Kd. Indeed, in the macrolide case high concentrations of ribosomes are needed to detect a signal, but given that the Kd is very low, c > 12 000 instead of 1 < c > 1000 (**Figure 8**). In these conditions, the characterization of macrolide binding is technically impossible, that's why a strategy of competition was considered.

2. Principle of ITC competition experiments

Competition experiments are well-known approaches in ITC to obtain affinities of very weak or very strong binders (Velazquez Campoy and Freire, 2006; Zhang and Zhang, 1998). Among available strategies, we chose to displace a weak binder with macrolides acting as a very tight binder. From an experimental point of view, two successive ITC experiments are performed (**Figure 28**). In the first one, 70S is titrated by the weak competitor and binding parameters are accurately determined. Macrolide is then injected on the formed complex for a displacement experiment. After considering the Kd and ΔH of the competitor, the analysis software determines the affinity and thermodynamic parameters of the macrolide binding. These parameters being directly related to the values obtained for the weak ligand, it is crucial to obtain reliable data for the latter.

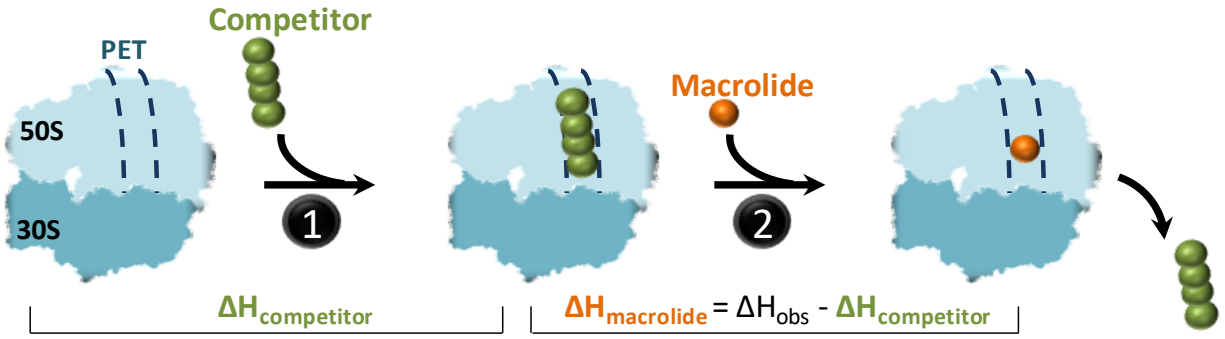

Figure 28: Strategy of competition using incremental ITC.
In a first experiment, binding parameters of the weak competitor are determined (1). Then the syringe is refilled with a macrolide for the second titration, during which competitor displacement should occur (2). Competitor must have the same binding region, a different ΔH and a weaker affinity for the ribosome.

To apply this strategy to my system of study, the selected compound should have 3 important features: (i) the same binding site or region than macrolides, (ii) a weaker affinity for the ribosome than macrolides and (iii) a different mode of binding. Among all the molecules that bind to the ribosome, natural proline-rich antimicrobial peptides recently appeared as potential interesting antibiotics by binding to sites similar to those of macrolides (Seefeldt et al., 2016). PrAMPs were therefore tested as potential weak competitors for macrolide binding.

3. Investigation on binding parameters of PrAMPs

A. Superimpositions of PrAMPs and macrolides in the peptide tunnel

Several PrAMPs have been described since the past few years. Structures of three well-known peptides (Bac7, metalnikowin and pyrrhocoricin) in complex with 70S of *Thermus thermophilus* are available (Seefeldt et al., 2016; Gagnon et al., 2016). These three PrAMPs were superimposed with macrolides to visualize and confirm the overlapping binding site in the peptide exit tunnel (**Figure 29**).

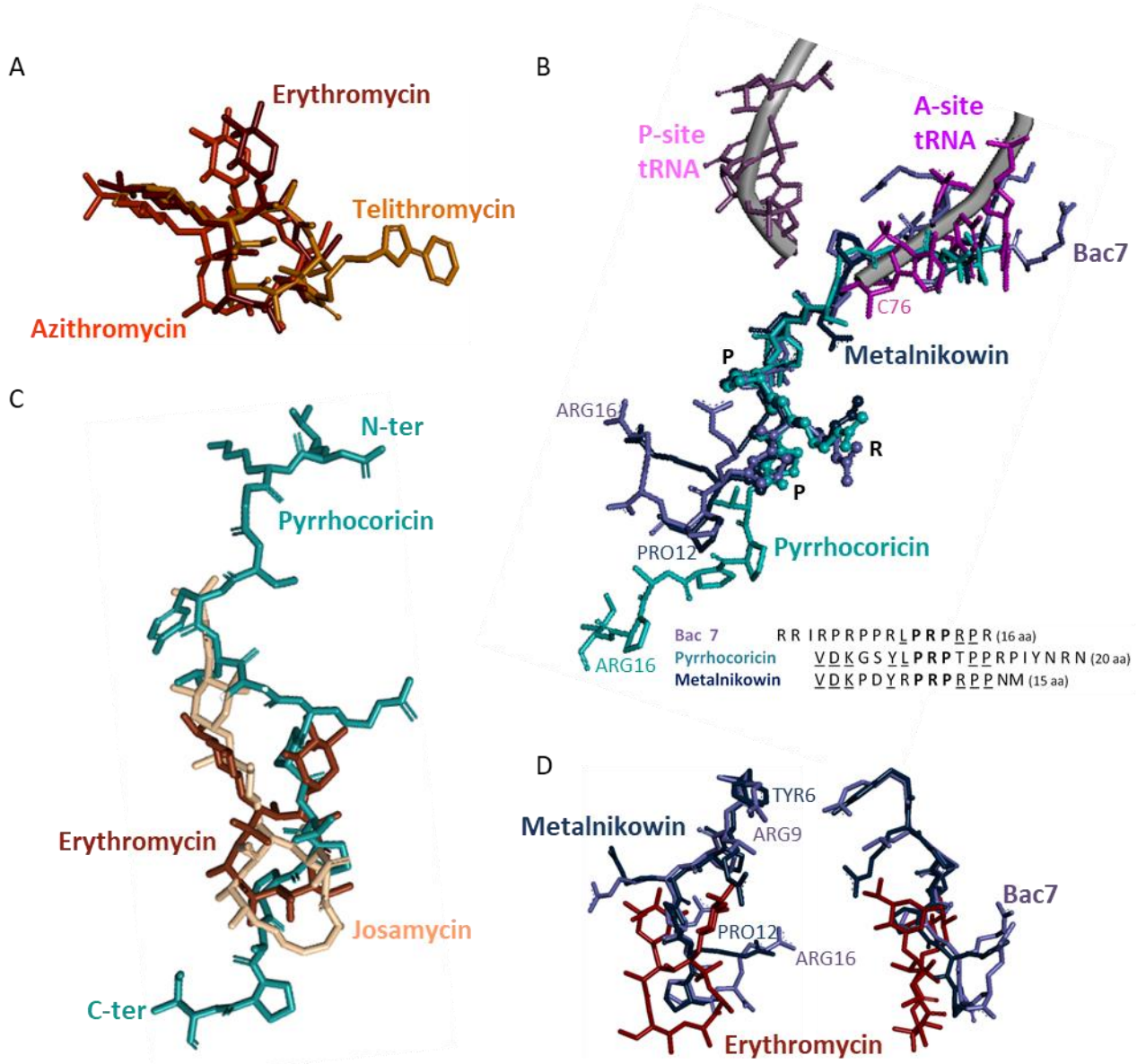

Figure 29: Superimpositions of PrAMPs with macrolides in their ribosome-bound conformations. Erythromycin (in dark orange), azithromycin (in orange) and telithromycin (in light orange) structures are superimposed in (A). Superimposition of Bac7 (in mauve), pyrrhocoricin (in turquoise blue) and metalnikowin (in dark blue) with A-site (in pink) and P-site tRNA (in violet) and sequences comparison are presented in (B). PRP motif (in bold) is showed by « Ball and stick » representation in the structures. Overlay of pyrrhocoricin with erythromycin and josamycin (beige) show the overlap region in the PET (C). Views with 2 different orientations of steric clashes between erythromycin and Bac7 or metalnikowin are showed in (D). (PDB numbers: erythromycin *Th. Thermophilus* 70S 4V7X; azithromycin *Th. Thermophilus* 70S 4V7Y; telithromycin *Th. Thermophilus* 70S 4V7Z; josamycin *D. radiodurans* 70S 2O44; Bac7 *Th. Thermophilus* 70S 5F8K; pyrrhocoricin *Th. Thermophilus* 70S 5FDV; metalnikowin *Th. Thermophilus* 70S 5HCP).

The macrolides overlap very well each other, just like the 3 PrAMPs (**Figure 29A and B**). Clearly, parts of peptides overlap with macrolides in the PET (**Figure 29C**). With Bac7 and metalnikowin, the overlay is on a very small part of molecules, but this should be sufficient to induce steric hindrance and a competition for binding (**Figure 29D**). As mentioned previously, thermodynamics and kinetics are just as important as structures to have a global view of the mode of binding of molecules and consequences on structural rearrangements. ITC experiments at different temperatures were performed to characterize interactions of the three PrAMPs (Bac7, pyrrhocoricin and metalnikowin) with the *E. coli* ribosome.

B. Binding parameters of PrAMPs

Interactions were studied at several temperatures, 15, 20, 25, 30 and 35 °C to evaluate the impact of the temperature on the binding, and the importance of structural rearrangements. As ribosomes are complex macromolecular machines, state and homogeneity can slightly differ between samples. That's why several experiments were realized to obtain the more accurate parameters.

Thermodynamic profiles have been determined for each of the three peptides to indicate driving forces of the interaction (**Figure 30**). For the three PrAMPs, entropy variation is unfavorable for the binding and interaction is enthalpy-driven (ΔH < -TΔS), contrary to macrolides (**Figure 30A**). This difference in binding profile is key for using PrAMPs as macrolide competitors. Enthalpy is directly related to the number of bonds formed, the number and type of residues. Here, pyrrhocoricin, which is 20 aa-long, displays a more negative ΔH than metlanikowin, which is only 15 aa-long, and Bac7 is intermediate. In other words, binding of Pyrrhocoricin releases much more heat than metalnikowin. Due to the heat capacity change, enthalpy evolves with temperature. Here, ΔH decreases when temperature increases, which is in line with an expected negative heat capacity change (ΔCp). This negative ΔCp reflects a significant conformational change upon PrAMP-ribosome interaction (**Figure 30B**). In the end, as the mode of binding is quite opposite to the one of macrolides, the PrAMPs meet the second condition to be efficient competitor.

A

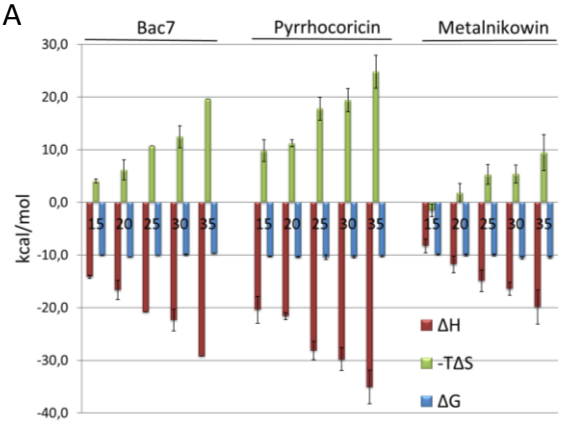

B

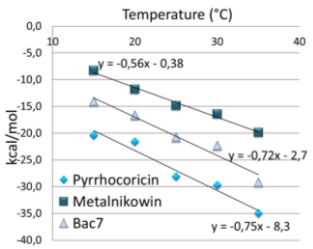

C

T (°C)	15	20	25	30	35
Bac7	2	2	1	8	1
Pyrrhocoricin	4	4	4	29	3
Metalnikowin	2	2	4	6	3

Figure 30: Thermodynamics of PrAMP interaction with 70S ribosome.
Profiles of the 3 PrAMPS with ΔH, -TΔS and ΔG are presented from several experiments at different temperatures in (A) and the number of replicates is presented in (C). ΔCp could be calculated from average ΔH at each temperature (B). The ΔCp corresponds to the slope of each straight line. Detailed data are listed in **Table S1 of Annex 3**.

Subsequently, the ITC experiments also show that affinity of each of the three PrAMPs for the ribosome is weaker than for macrolides (**Figure 31**). Yet, Kd are still in the tens nanomolar range (**Figure 31A**). Globally, affinities seem to slightly increase with temperature augmentation that agrees with thermodynamic law (**Figure 31A**). But after looking at standard deviations, it appears that differences between temperatures are not significant. Regardless the temperature, affinities are between 10 and 65 nM for Bac7, pyrrhocoricin and metalnikowin (**Figure 5A**). There is just one exception for Bac7 at 35 °C with an affinity around 140 nM, but nothing can really be concluded from one experiment (**Figure 31C**). In the end, the PrAMPs Bac7, pyrrhocoricin and metalnikowin can be considered as "weak" competitors of macrolides for displacement experiments.

C. Kinetics of PrAMP-ribosome interaction

From ITC experiments with PrAMPs and ribosomes, thermodynamic and affinity binding parameters were obtained. However, as mentioned in the general introduction, affinity and rate constants can also be obtained from ITC experiments since several years now. Indeed, my team discovered that kinetic information can be extracted from the equilibration time curve (ETC) of peak thermograms. A collaboration with AFFINImeter led to the development of an analysis software, which gives the thermodynamic and kinetic parameters for an interaction. First, it was interesting to compare Kd obtained with PEAQ-ITC Analysis or Affinimeter softwares. Several experiments were submitted to kinITC analysis, but only some of them could be used for kinetic purposes (**Figure 31B**). Indeed, it is not possible to derive kinetic data from all ITC experiments, especially in cases of very fast on- or off-rates, or for high-range c values. Processed data from a same thermogram are similar but variations are yet observed (**Figure 31B**), due to differences in baseline corrections. Since these corrections have consequences on the integration area and the shape of the titration curves, differences in parameters are inevitably detected. Despite this, binding affinities are still in the same tens of nanomolar range.

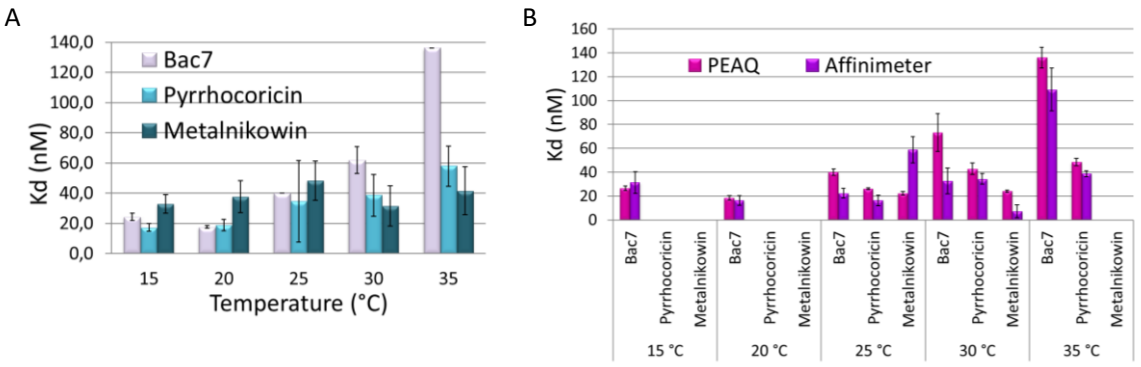

Figure 31: Affinities of PrAMPs for 70S ribosome at different temperatures.
PrAMP affinities from ITC experiments processed with PEAQ analysis software are presented for several temperatures (A). Using Affinimeter, kinetics information could be extracted for some experiments and Kd obtained by the 2 softwares were compared (B). Errors bars correspond to standard deviations between experiments in (A) and to errors of fit for one experiment in (B). Detailed data are listed in **Table S1 of Annex 3**.

Then, kon and koff obtained by those treatments can give us a tendency about the global dynamic of interaction (**Figure 32**), but the absence of experimental replicates and reproducibility cause troubles in interpretations. Nevertheless, reasonably good data could be obtained for Bac7, pyrrhocoricin and metalnikowin at 25 and 30 °C (**Figure 32A**). The three PrAMP have the same range of association (around 10^5 $M^{-1}.s^{-1}$) and dissociation (around 10^{-3} s^{-1}) rates, regardless the temperature. An exception is observed for metalnikowin at 25 °C with an off-rate higher than other PrAMPs (close to 10^{-2} s^{-1}). To confirm this observation, three experiments were processed for each temperature and lead to similar results (**Figure 32B**). Metalnikowin seems to behave distinctly between 25 and 30 °C, but it would have been interesting to obtain kinetics for other temperatures. For Bac7, one experiment could be processed for the five temperatures 15, 20, 25, 30 and 35 °C (**Figure 32C**). Nevertheless, even though we cannot conclude after one experiment, it seems that at 35 °C the weak affinity (**Figure 31B**) is due to a faster dissociation rate (around 10^{-2} s^{-1}) compared to lower temperatures; events of dissociation happen more frequently. Moreover, it tends to confirm that the koff is the limiting factor and drives the Kd since the on-rate is comparable. However, more experiments are needed to rigorously interpret those data

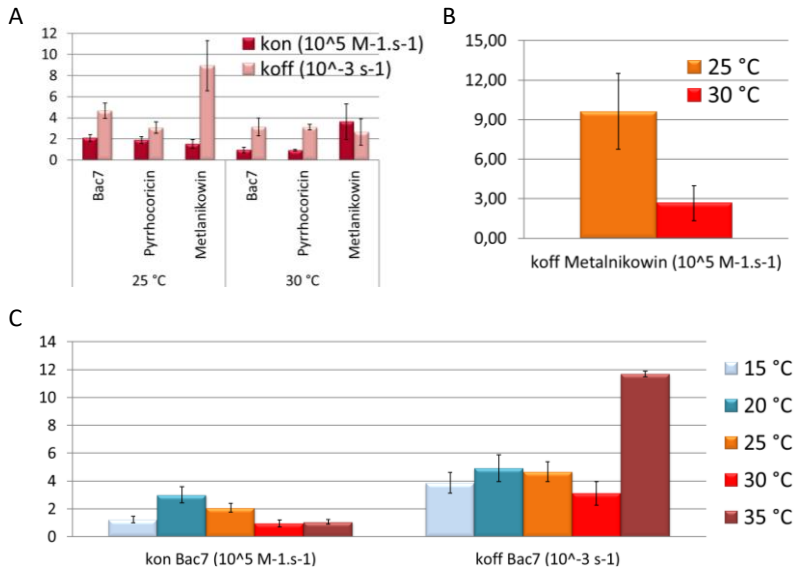

Figure 32: Kinetics of PrAMPs-70S interactions.
On- and off rates of PrAMPS, after data processing with Affinimeter analysis software, are presented for 25 and 30 °C in (A). Off-rates of metalnikowin from processing of 3 experiments at 25 °C and 30°C, are presented in (B). Kinetics profile of Bac7 was determined from one experiment at 5 temperatures (C). Errors bars correspond to standard deviations between 3 experiments in (B) and to errors of fits for one experiment in (A) and (C).
Detailed data are listed in **Table S1 of Annex 3**.

Finally, kinITC allowed us to have an idea of the dynamic of interaction between peptides and 70S. Arrival of peptides in the binding site is quite fast (10^5 $M^{-1}.s^{-1}$ range). Regarding the PET narrowness and length of peptides, it is not surprising to observe quite slow koff (10^{-3} s^{-1} range), which means that residence time are about hundreds of seconds, that is rather long. The data suggest that PrAMPs get into the tunnel quite fastly and, when bound, they take time to dissociate from the complex, thus resulting in quite tight affinities. Knowing that macrolides present quite slow association and slow dissociation rates to the ribosome (Morrison and Walsh, 1988; (Di Giambattista et al., 1987), our results suggest that PrAMPs associate and dissociate faster than macrolides. As these kinetics parameters also seem compatible with their status of potential competitors, we can conclude that Bac7, pyrrhocoricin and metalnikowin meet all criteria to be competitors for displacement experiments.

D. Evaluation of the PrAMP behavior in competition experiments

A preliminary competition experiment was already done by the previous PhD student Benoit Meyer at 30 °C with Bac7 (generously given by Pr. Daniel Wilson). A displacement of erythromycin was observed, thus confirming the interest of this approach. I could reproduce this experiment and tested two other potential competitors, metalnikowin and pyrrhocoricin (**Figure 33**). Similarly to the displacement of Bac7 (**Figure 33A**), a clear displacement was obtained for pyrrhocoricin, (**Figure 33C**). However, it has to be noted that the automatic baseline determination by the PEAQ analysis software is not really adapted to this kind of experiment (**Figure 33C**) and will always require manual adjustments.

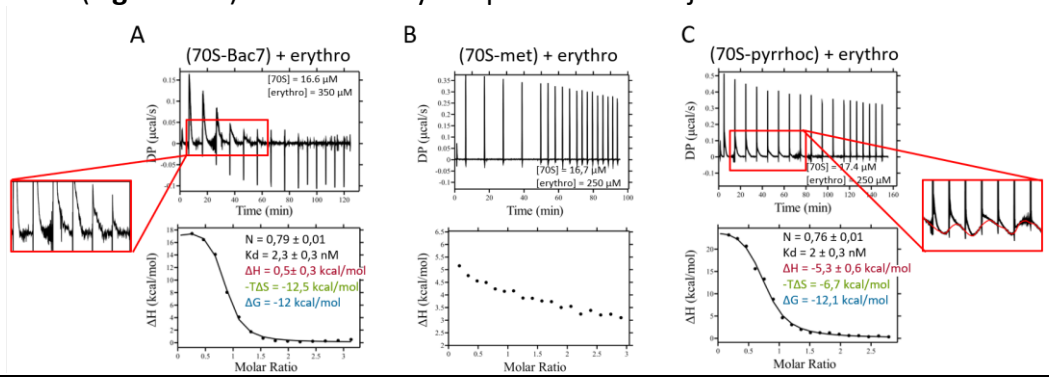

Figure 33: First trials of ITC competition using PrAMPs at 30 °C.
Erythromycin was used to try to displace Bac7 (A), metalnikowin (B) and pyrrhocoricin (C) after formation of the complex 70S-PrAMP in a 1st ITC. A zoom at the end of injection peak in (A) allows to see more precisely the time to return to the baseline while a zoom on the thermogram in (C) highlights the inaccurate baseline determination in competition experiments. Detailed data are listed in **Table S2 of Annex 3**.

Surprisingly, in the same conditions, no displacement of metalnikowin was observed by erythromycin (**Figure 33B**). As metalnikowin is very similar to Bac7 and pyrrhocoricin, this difference is quite intriguing. Even if we could not so far provide an explanation for this result, some hypothesis can be envisaged to explain this absence of signal. It could be either due to an absence of signal detection or an absence of binding. For the first case, the resultant ΔH of the displacement could be around 0 and nonvisible using ITC; but this would be surprising regarding the difference of binding enthalpy between macrolides and metalnikowin (>10 kcal.mol^{-1}). Moreover, we could hypothesize that macrolides and metalnikowin can coexist in the peptide tunnel, but that the fixation of macrolides is undetectable by ITC device in our experimental conditions. However, considering the overlapping sites between the two molecules, it would need important structural rearrangements in the target region. Furthermore, the superimpositions were done from T*. thermophilus* ribosomes so we cannot completely exclude a slight difference in the positioning of molecules in the tunnel of *E.coli* ribosome that could explain this difference of behavior. On the contrary, in the second hypothesis of no fixation of the macrolide at all, metalnikowin could also act like a resistant peptide that are able to dislodge the macrolide (**Figure 20B**) (Vázquez-Laslop and Mankin, 2018) and prevent its binding in a specific structural and/or sequence context.

In summary, we concluded that Bac7 and pyrrhocoricin could be good competitors for macrolides in ITC experiments.

4. Tests of Bac7 displacement by macrolides

A. Exploration of competition experiments

Bac7 was first used as a competitor. ITC competition experiments were done with the 4 studied macrolides (erythron-, azithro-, telithro- and josamycin) at 30 °C with 70S ribosomes of *E. coli*. I chose 30 °C as the temperature of reference for two reasons: (i) below this temperature signal-noise is weaker because $|\Delta H|$ is smaller and (ii) higher temperatures are not suitable for the ribosome in our experimental conditions (high concentration combined to high stirring speed).

Displacement ITC with the four macrolides resulted in similar thermograms that the one presented in in Figure 32A. First, the displacement event is notably slow and can take more than 5 min (**Figure 33A**); it gets slower for injections around the inflection point of the titration curve, which is typical for slow kinetics. All thermograms display endothermic reaction meaning that Bac7 dissociation combined to macrolide association results in heat absorption. However, the signal intensity is still low, and the experiment requires at least 16 µM of ribosomes.

The stoichiometry indicates that the displacement of Bac7 is quite efficient for all macrolides (**Figure 34**). Josamycin seems to displace less efficiently than the others but still with N = 0.65, while erythromycin seems to have the better displacement rate with N = 0.91. Macrolide affinities could be determined below 5 nM (**Figure 35**) with negligible error (**Figure 33A**), that is really satisfactory. These values are in agreement with values from the literature (Svetlov et al., 2017). Thermodynamic profiles are similar to those obtained by direct ITC (**Figure 37**) and the entropy-driven interaction is confirmed ($\Delta H > -T\Delta S$). However, differences between ΔH established by competition and direct ITC are quite significant, likely due to errors on antibiotics concentrations. In ITC experiments, the ΔH calculation is directly impacted by the concentration of injected molecules. The accurate concentration determination is even more important in competition experiments for two reasons: (i) the ΔH of the first binding is used to deduce the ΔH of the strong binder (**Figure 28**) and (ii) errors are cumulated in serial ITC. Unfortunately, the good estimation of Bac7 concentration is hindered by a weak solubility and the absence of aromatic residues in its sequence for absorbance evaluation.

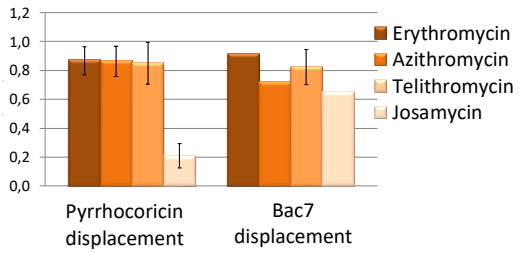

Figure 34: Displacement efficiency by macrolides for Bac7 and pyrrhocoricin at 30 °C.
Number of workable replicates at 30 °C (n) is indicated under the histogram. Detailed data are listed in **Table S2 of Annex 3**.

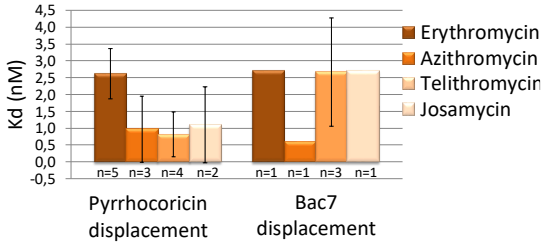

Figure 35: Affinities of macrolides for the 70S ribosome after Bac7 or pyrrhocoricin displacement at 30 °C.
Number of workable replicates at 30 °C (n) is indicated under the histogram. Detailed data are listed in **Table S2 of Annex 3**.

In the end, competitions with Bac7 allow to set up the procedure of displacement experiments. But considering the importance of accurate concentration determination, Bac7 did not appear as the more suitable peptide to use. This also explains the few exploitable competition experiments (**Figure 34 and 35**).

B. Issues with ribosomes heterogeneity

Besides the problem with Bac7 concentration, a second issue concerns the ribosome integrity in ITC conditions. For some ITC experiments, titration curves with a non-sigmoïdal shape were obtained (**Figure 36A and B**). In such cases, there is a heterogeneity of binding events with at least two types of binding. These different binding events likely correspond to binding of peptides to ribosomes in diverse states rather than two different binding sites of the peptide. Indeed, if two or more peptides could interact with one ribosome, a stoichiometry larger than one would have been expected. However, even if it's less probable, we could not totally exclude the possibility of heterogeneity in peptide population; since they are enriched in prolines, two or more peptide conformations could be adopted in solution. Interestingly, in these biphasic titrations, parameters for one of the binding sites often correspond to parameters obtained with one binding event (**Figure 36B and C**). Nevertheless, most of the time, the "abnormal" second binding event is in large minority compared to the "normal" fixation event. The frequency of those biphasic curves was reduced with the addition of glycerol to the ITC buffer.

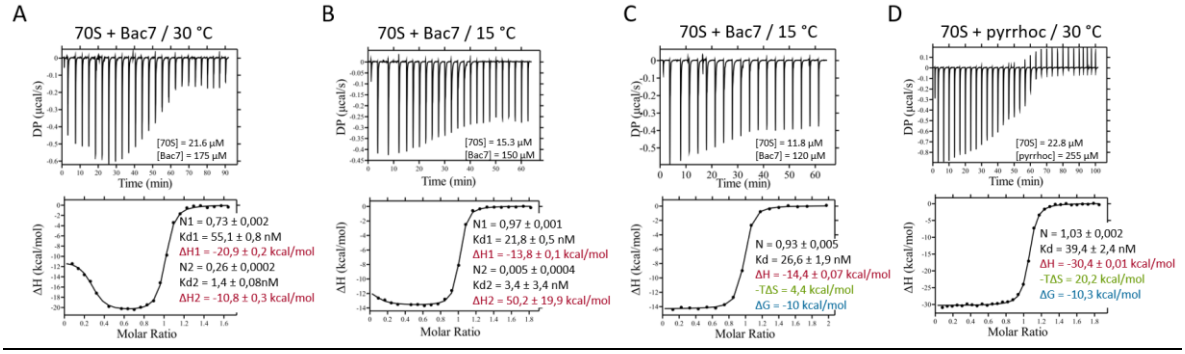

Figure 36: Examples of unusual and classic titration curves.
« Abnormal » titrations curves are presented for 30 ° C (A) and 15 °C (B), and compared to classic sigmoïd-shape curves obtained after injection of Bac7 (C) or pyrrhocoricin (pyrrhoc) (D) on 70S. Two ITC from a same stock of ribosomes and peptides at the same temperature (15 °C) are presented (C: day 0 and B: day 1).

5. Pyrrhocoricin as the best competitor for displacement by macrolides

A. Comparison of Bac7 and pyrrhocoricin displacements

Considering problems to obtain reliable results with Bac7 displacement, we used this competition strategy with the another potential PrAMP competitor, pyrrhocoricin. On the contrary to Bac7, pyrrhocoricin has two arginins residue and a good estimation of its concentration can be obtained. Pyrrhocoricin displacement was observed with the studied macrolides, after exploitable titration in the first ITC experiment (**Figure 36D**).

Data analysis shows that displacement was highly effective with erythromycin, azithromycin and telithromycin: the stoichiometry is above 0.8 for these three macrolides, indicating that more than 80 % of pyrrhocoricin was displaced (**Figure 35**). Considering the errors in antibiotics concentration and the small proportion of inactive ribosome, these results are quite satisfying. Unexpectedly, josamycin binding seems less efficient (N < 0.3) than other macrolides. Several explanations can be envisaged, like the possibility that at 30 °C the ΔH is around 0. However, it seems that its displacement capacity was better when Bac7 is bound. A difference of behaviour could be explained by the absence of a perfect overlapping of Bac7 and pyrrhocoricin near the josamycin binding site (**Figure 29C and E**). Indeed, josamycin might bind to the ribosome without any detection of the fixation and coexist with pyrrhocoricin in the PET.

Similarly to Bac7, affinities of the four macrolides for the ribosome were determined in nanomolar and subnanomolar range, between 0.3 and 3.8 nM with negligible errors (**Figure 36**). Nevertheless, several experiments were done for competition with pyrrhocoricin. Getting a reproducibility for very low Kd below the normal sensitivity limit and with standard deviation of maximum 1 nM between experiments is an encouraging progress. Globally, of the four macrolides the erythromycin seems to have the weaker affinity, with an average Kd of 2.5 nM compared to a Kd around 1 nM for josamycin, azithro- and telithromycin (**Figure 36**).

Regarding the thermodynamic profiles, the entropy-driven binding mode of interaction is the same than the one observed by direct ITC and with Bac7 displacement (**Figure 37**). Nevertheless, standard deviations are quite high in several cases. For example, for telithromycin there is a difference above 8 kcal.mol^{-1} between the minimum (-7.2 kcal.mol^{-1}) and the maximum ΔH (1.4 kcal.mol^{-1}) obtained from different experiments. As pyrrhocoricin concentration is more precisely determined than for Bac7, ΔH variations between direct and competition ITC may not be attributed solely to errors of fits or concentrations.

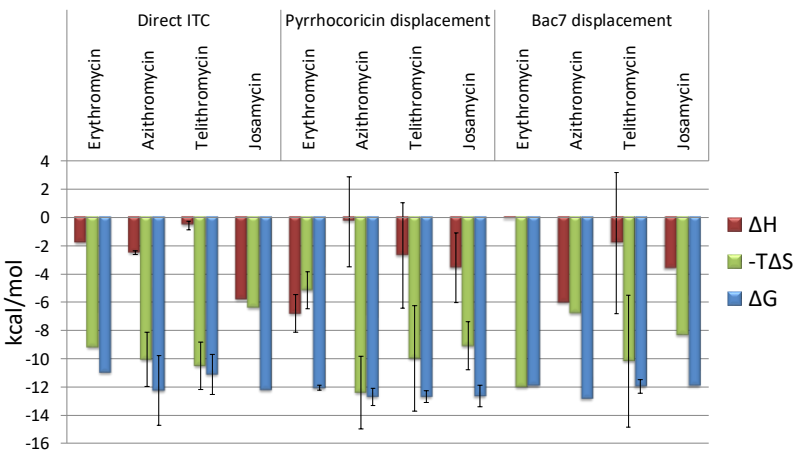

Figure 37: Thermodynamic profiles of macrolides - 70S ribosome interaction after competition experiments at 30°C. Detailed data are listed in **Table S2 of Annex 3**.

Two assumptions were made: first, the presence of other molecules could generate parasite signals and induce ΔH variations. Indeed, ribosomes are directly used from purification in their native state and even with all purification steps, tRNAs and or mRNAs can be trapped in it.

This hypothesis can be "easily" checked by dissociation and reassociation of the ribosome. The second hypothesis suggests that pyrrhocoricin could stay partially bound to the tunnel after the macrolide binding. This idea is supported by the fact that PrAMPs are longer than macrolides and interact with a larger region of the PET.

B. Control of competition parameters with reassociated ribosomes

The impact of potential contaminants molecules in the ribosome was checked using reassociated 70S (**Figure 38**).

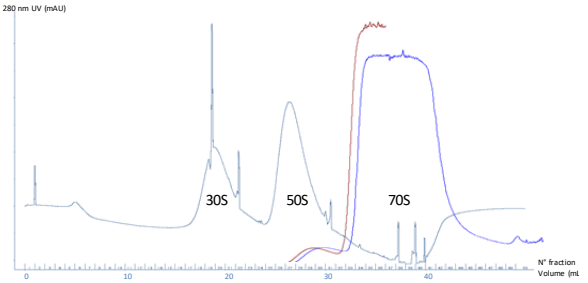

Figure 38: Validation of 70S reassociation after 15-40 % sucrose gradients.
After gradient aspiration, chromatograms of a negative control (mix of 30S and 50S), a positive control (native 70S) and reassociated 70S were superimposed to show the ribosome localization in the gradient. x-axis is to scale but for a better visualization of superimposed chromatograms, y-axis is not.

Competition experiments were realized with each of the 4 studied macrolides; displacement of pyrrhcoricin could be observed for all macrolides except josamycin. Thermodynamic profiles and affinities are very similar between native and reassociated 70S (**Figure 39**). Moreover, no difference was observed for pyrrhocoricin binding between native and reassociated 70S ribosomes either (**Figure 40**). This strongly suggests that if some contaminants tRNA are present on native ribosomes, they do not impact binding of peptides or macrolides. Consequently, data were analysed regardless of the native or reassociated state of 70S ribosomes.

Figure 39: Macrolides binding parameters after pyrrhocoricin displacement with native or reassociated 70S at 30°C.
Affinities (A) and thermodynamic profiles (B) of macrolides binding to reassociated or native ribosome. Standard deviations determined from several experiments (n) are showed.

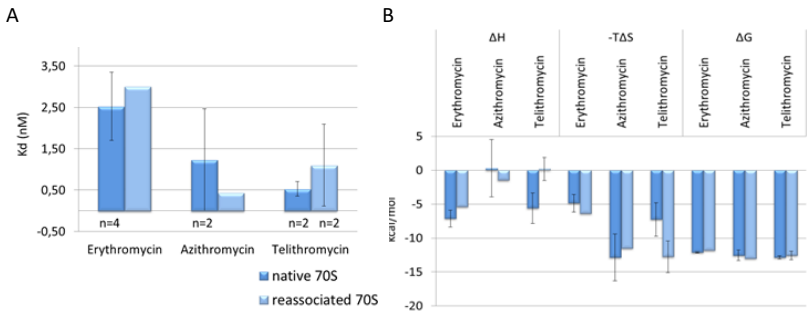

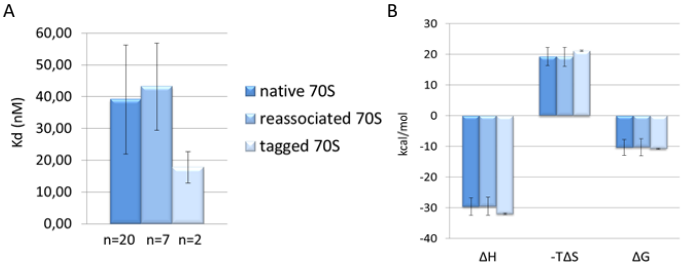

Figure 40: Comparison of pyrhhocoricin binding parameters after interaction with different 70S ribosomes at 30°C.
Affinities (A) and thermodynamic profiles (B) of pyrrhocoricin fixation to reassociated and tagged ribosome compared to native ribosome. Standard deviations determined from several experiments (n) are showed.

6. Investigation on coexistence of pyrrhocoricin and macrolides in the peptide exit tunnel

A. Attempts by pull-down of complexes and mass spectrometry analysis

To answer this question, mass spectrometry was envisaged to investigate on the presence of pyrrhocoricin in the PET after a competition experiment with macrolides. To consider this hypothesis, it is necessary to completely get rid of free peptides present in solution following an ITC experiment so that only pyrrhocoricin bound to ribosomes will be detected. Even if the ITC experiment is stopped before saturation, free peptide will be present because of equilibria. A purification of the drug-ribosome complex after ITC experiment was therefore required. A 6-His tag ribosome was used to perform ITC experiments. A first control ITC experiment was done to confirm that the tag has no effect on the interaction with pyrrhocoricin. As expected, results were very comparable with non-tagged ribosome (**Figure 40**).

In the first place, we needed to check that mass spectrometry can effectively allow the detection of Pyrrhocoricin alone. Thus, theoritical proteolytic fragments after trypsine cleavage were previsously computer-generated and the trypsic signature was determined by mass spectrometry with injection of pyrrhocoricin alone. Then, it was important to test the possibility of the detection of the pyrrhocoricin in complex with the ribosome. To do this, several conditions and controls were prepared:

(i) 70S + pyrrhocoricin complex formed by ITC to see if it's possible to detect the peptide in the ribosomal protein environment.
(ii) A control with a (70S+azithromycin) + pyrrhocoricin complex formed by ITC to check that the peptide is not detected when it is present in the sample but not bound to ribosomes.
(iii) 70S + pyrrhocoricin complex formed by ITC and purified by His-tag purification to see if the peptide can be detected after purification.

Lauriane Kuhn from the mass spectrometry platform performed 100 % methanol precipitation on those samples. It's known from previous tests that peptides do not precipitate in those conditions. Unfortunately, no peptides were identified in any of the three tested samples and only ribosomal proteins were found. This absence of detection can either be caused by a loss of the peptide before injection in the spectrophotometer or a problem in precipitation. Indeed, treatments during purification or methanol precipitation could have led to dissociation of 70S-pyrrhocoricin complexes. Pyrrhocoricin could also not be present in sufficient amounts to be detected in such conditions.

At this point, we decided to not go further with optimizations in this approach and to continue with a more reliable method to unambiguously try to visualize the different populations of ribosome after pyrrhocoricin displacement.

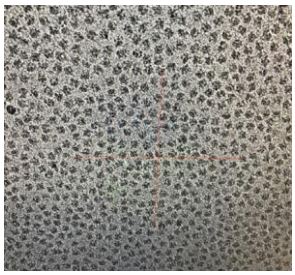

Figure 41: Homogeneity of [(70S-pyrrhocoricin) + telithromycin] complex.
Visualization of the complex using the Talos™ Arctica™ at 200 kV on 400 mesh holey carbon Quantifoil 2-2 grids.

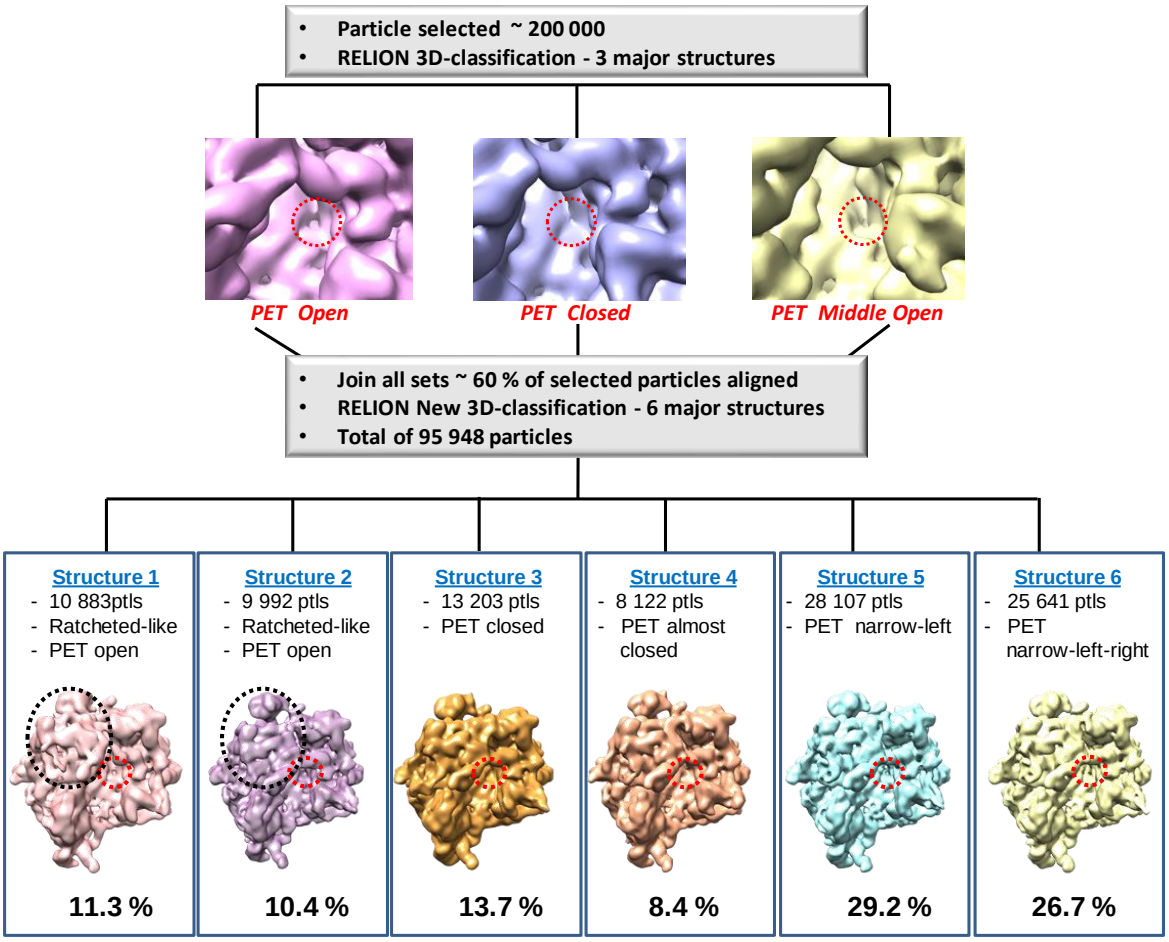

Figure 42: Structural information of [(70S-Pyrrhocoricin) + telithromycin] complex.
Around 200 thousand of particles (ptls) were selected from 40 frames using SCIPION. After particle sorting with RELION, 3 classes with different conformation of the peptide exit tunnel (PET, highlighted by a dashed red circle) for a total number of particles of around 95 thousand. Further classification lead to 6 major structures were finally obtained in different proportion, including two structures with an open conformation, two structures with a closed conformation and two structures with a middle open conformation. For the middle open PET also called narrow conformation the density can be observed either on the left of the tunnel or together on the left and right. The structures with open PET seem to present different conformational states represented by the dashed black circle.

B. Structural study using cryoEM

Images of the ITC-formed complex were collected on a Talos™ Arctica™ cryomicroscope in collaboration with Dr. Jerôme Basquin (Max Planck Institute for Biochemistry, Martinsried) (**Figure 41**). Image processing was performed Dr. Angelita Simonetti. Before particle picking, 40 frames in the stack were aligned using the Motion Correlation algorithm integrated in Scipion (Zivanov et al., 2019). Then, an average image of the whole stack was used to determine the contrast transfer function (Jonić et al., 2007) and to select semi automatically ~200 000 particles in SCIPION (Abrishami et al., 2013). Particle sorting was done by 3D classification using RELION (Scheres, 2012) leading to a 3D-class comprising 95 948 particles. Three main classes, showing structural features attributable to the *E. coli* 70S with pyrrhocoricin and/or telithromycin, are obtained and differ in the structure of the peptide exit tunnel (**Figure 42**)**.** After further 3D classification, six major classes were finally obtained. All classes were refined using RELION's 3D auto-refine and then post-processed using the procedure implemented in RELION (Scheres, 2012).

Among the six groups, the structure of the PET varies from an open conformation to a restricted and a closed conformation in different proportions. Two structures with slight variations compose each group. At this stage, structures are solved to 7.3 Å of resolution, which is not sufficient to identify what is obstructing the peptide tunnel. Nonetheless, considering its level of narrowness, some assumptions can be made. The structures 1 and 2 with an open tunnel seem to present different conformational states (called ratcheted-like), and represent 11.3 and 10.4 %, respectively, of the total particles. Thus, around one fifth of the population have a free polypeptide tunnel with apparently nothing bound in it.

The structures with a narrow PET constitute more than the half of the final population of ribosomes. Two PET conformations can be distinguished with densities in different regions of the channel. The structure 5 (29.2 % of total particles) seems to have a density on the left, which could correspond to telithromycin. This would be expected since from the competition experiment where the peptide displacement and the macrolide binding were observed with more than 70 % of efficacy. The PET of the structure 6 (26.7 % of total particles) shows a slight difference in obstruction, with densities on the left and on the right, which could potentially correspond to the presence of telithromycin and of pyrrhocoricin. However, the resolution does not allow the assignment of these densities to precise molecules.

Finally, the ribosome conformations with a clogged PET correspond to approximately one fifth of the particles. The structure 3, representing 13.7 % of the complexes, has a completely closed tunnel. The structure 4, which is less abundant with a proportion of 8.4 %, display an almost closed channel. We can hypothesize that the total obstructed channel could also correspond to ribosomes with both telithromycin and pyrrhocoricin, and that the almost closed conformation of the tunnel could suggest the presence of the pyrrhocoricin alone. But again, the resolution should be improved in order to confirm those hypotheses and to localize precisely each compound.

In these perspectives, a new processing from an increased number of realigned particles and data acquisition on the more powerful Titan Krios cryomicroscope are currently running. This would allow us to conclude about the potential coexistence of PrAMPs and macrolides in the peptide exit tunnel.

7. Test of other combinations of competition

Other combinations of competition experiments were tested, using PrAMPs, macrolides and related compounds. Inverted competition experiments, which consist in the fixation of a macrolide followed by the injection of a PrAMPs, were also done as controls. As expected in view of respective affinities, pyrrhocoricin could not interact with the 70S already occupied by erythromycin, azithromycin or telithromycin. The same inverted ITC was done with metalnikowin and erythromycin, and similarly no fixation was observed either.

The lincomycin from lincosamide class, which also bind to the PET and overlap with PrAMPs, was also studied (**Figure 43A**). Its interaction with ribosome is an endothermic reaction; its binding to the ribosome absorbs heat (**Figure 43B**). Moreover, the binding is entropy-driven (ΔH > -TΔS), showing that stacking interactions are predominant and that the desolvatation favors the conformational changes for the binding. Nevertheless, the affinity for bacterial ribosome is weaker than macrolides, with a Kd in the micromolar range (Kd ⩾ 1 µM). Knowing this, I tried to displace lincomycin with pyrrhocricin and as expected the displacement occurs (**Figure 43C**). Binding parameters of pyrrhocoricin deduced from the displacement experiment, still using the competitive fitting model, were very similar to those obtained by direct ITC (**Figure 43D and E**). This experiment allows to confirm the reproducibility and reliability of ITC competition experiments applied to other ribosome-antibiotics interactions.

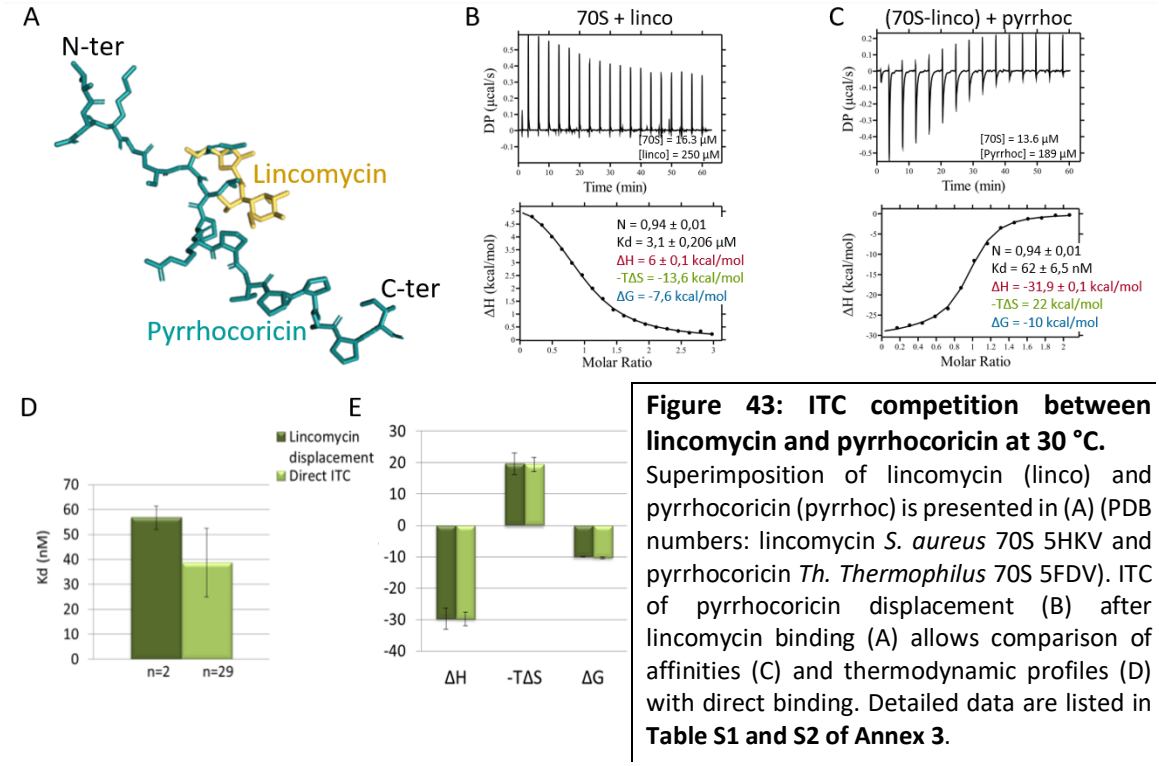

Figure 43: ITC competition between lincomycin and pyrrhocoricin at 30 °C. Superimposition of lincomycin (linco) and pyrrhocoricin (pyrrhoc) is presented in (A) (PDB numbers: lincomycin *S. aureus* 70S 5HKV and pyrrhocoricin *Th. Thermophilus* 70S 5FDV). ITC of pyrrhocoricin displacement (B) after lincomycin binding (A) allows comparison of affinities (C) and thermodynamic profiles (D) with direct binding. Detailed data are listed in **Table S1 and S2 of Annex 3**.

8. Preliminary ITC assays in translational context

All antibiotics and peptides binding experiments were performed on native or reassociated 70S. Yet, in the cell, many protein factors and RNA molecules are also present throughout the translation cycle and can interfere with antimicrobials binding. Previous studies showed that PrAMPs cannot bind to a ribosome during elongation (Graf and Wilson, 2019). Indeed, the tRNA in the A-site clashes with PrAMPs of class I at least, to which Bac7, pyrrhocoricin and metalnikowin belong to (**Figure 29B**). In this frame, we investigated on the binding of macrolides and peptides to initiation and elongation complexes.

70SIC were produced and after addition of TC complex, 70SEC complexes were purified through sucrose cushion and pyrrhocoricin binding was tested in ITC. Controls with 70SIC were also performed to compare both situations, that is to say when A-site is occupied by a tRNA or not. Thermodynamic profiles and affinities are quite similar to those obtained with "naked" ribosomes (**Figure 44**). A binding of pyrrhocoricin was observed once with 70SEC (**Figure 44A**) but with a very low stoichiometry (N = 0.26), suggesting that around only 25 % of pyrrhocoricin would have interacted with complexes. This result would match with the fact that the presence of an aa-tRNA in the A-site prevents pyrrhocoricin binding. Consequently, this could also indicate that the efficiency of elongation complex formation would be around 75 %.

Unfortunately, the controls with 70SIC were not exploitable. In a second set of experiments, ribosomes were saturated very quickly by pyrrhocoricin, with a stoichiometry around 1 either for elongation or initiation complexes (**Figure 44B, C and D**). This indicates that pyrrhocoricin bound efficiently to the ribosome and could suggest that elongation complexes were not formed correctly. Controls to assess the efficacy of translational complexes are required and need to be set up for further investigation. Finally, those experiments are at an early stage and would obviously require more time and optimizations to elaborate the whole strategy.

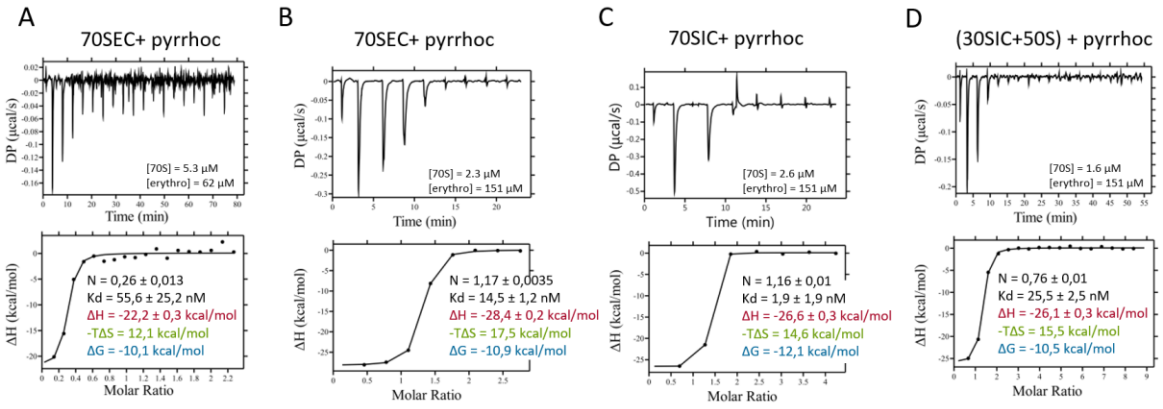

Figure 44: Investigation on pyrrhocoricin binding to translation complexes at 30 °C.
Elongation and initiation complexes were purified on sucrose cushion and pyrrhocoricin (pyrrhoc) binding to 70S was tested using ITC at 30 °C. The 2 experiments with elongation complexes (A and B) were done with different samples. Initiation complexes (C and D) and one elongation complex (B) were produced from same samples.

IV. Conclusions and perspectives

The interest of studying antibiotic interactions with the ribosome is crucial for a better understanding of how they bind to their target site, how it impacts the translational process of pathogens and how the antibiotic resistance occurs. Previous structural and biochemical studies highlighted mechanisms of action for major classes of ribosome-targeting drugs, but our knowledge is still incomplete. This is important to completely characterize the mode of action of existing antibiotics in order to decipher the associated resistance mechanisms and to develop new efficient therapeutic agents. Although thermodynamics is powerful to describe systems of interaction, it's not a widespread approach in the field of translation and ribosomes. This is partly explained by the molecular complexity of this huge molecule and the technical considerations (sensitivity, material consumption, …) for microcalorimetry studies. However, using ITC many important and complementary information could be obtained concerning the historical class of macrolides (**Conclusion figure 45**).

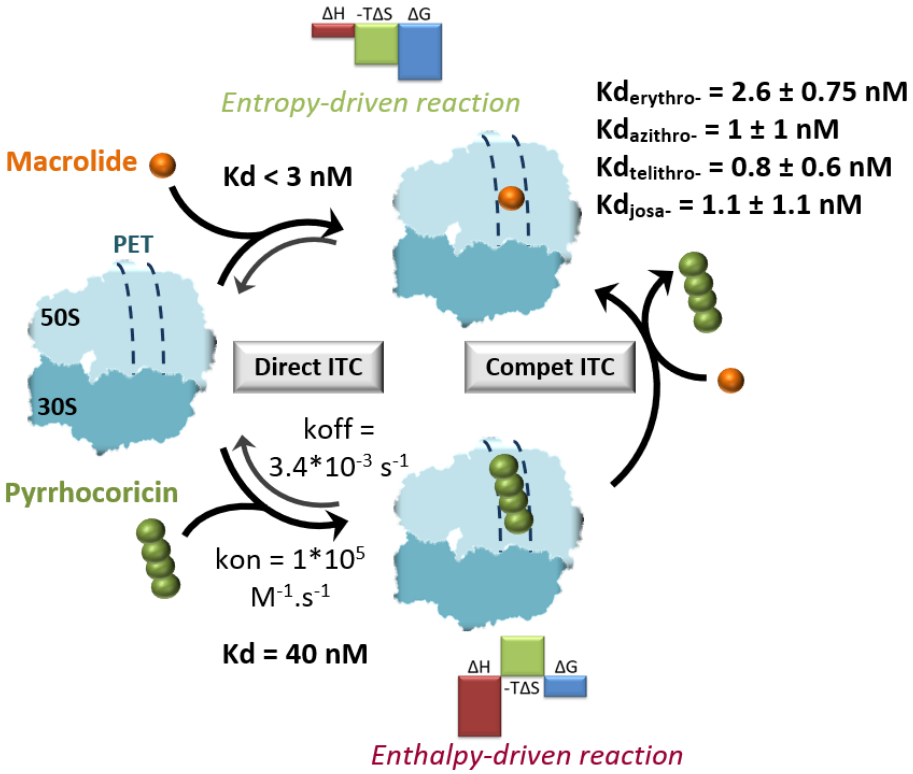

Figure 45: Graphical conclusion of the biophysical study of macrolide and PrAMP binding to the bacterial ribosome.

I focused my studies on the historical class of macrolides for which there has been a renewed interest in past few years with the discovery of new compounds with improved capabilities. Four macrolides from the three generation were used in this work (**Table 2**): erythromycin, azithromycin, josamycin and telithromycin. We were able to highlight a tight affinity of binding and an entropy-driven binding mode for macrolides (**Figure 45**). Although it is consistent with the dominance of stacking interactions, this type of binding driven by the entropy dimension is unusual for tight ligands.

Unfortunately, the tight affinity for their ribosomal target site and weak binding enthalpy appeared to be close to the sensitivity limit of ITC. That's why, an indirect approach based on competition experiments was elaborated. Displacing a "weak binder" by a "strong binder" should allow us to deduce the binding parameters of the tested macrolides.

Among the PET-targeting compounds, three antimicrobial peptides Bac7, metalnikowin and pyrrhocoricin were thermodynamically and kinetically characterized to investigate on their potential as weak competitors (**Figure 45**). New details were obtained about interaction dynamics of those promising molecules. Bac7 and pyrrhocoricin were confirmed to displace macrolides, but competition experiments led us to the conclusion that pyrrhocoricin is the best competitor for our system. Thermodynamic binding parameters and affinities were determined for the four studied macrolides (**Figure 45**), revealing Kd in the low nanomolar range or even in the sub-nanomolar range. Our ITC data are consistent with a recent study from Svetlov and collaborators who established affinities for erythromycin of 4.9 ± 0.6 nM. However, additional experiments would be necessary to reduce standard deviations of our results and minimize biais introduced by manual baseline adjustments of ITC competition experiments.

Surprisingly, despite the sequence similarity and structure of pyrrhocoricin with metalnikowin, the latter could not be displaced by any of the tested macrolides. This absence of visible metalnikowin displacement by macrolides and a possible partial displacement of pyrrhocoricin has led us to hypothesize the coexistence of PrAMPs and macrolides in the peptide channel. The combination of ITC with cryoEM should provide us with an answer and preliminary results suggest that the observed obstruction of the PET is not compatible with the presence of the peptide or the macrolide alone. Since only the conformation of the peptide in the PET from T*. thermophilus* ribosomes are known, and not from *E. coli*, it could be of interest to have structural insights into a 70S/metalnikowin complex after displacement of a macrolide. Indeed, even if the PET is highly conserved, different modifications of the rRNAs according to bacteria could be observed. In the end, those investigation on PrAMP-macrolide coexistence could be very interesting in a purpose of chimeric drug development.

Besides, using the strategy we have developed (Schenckbecher et al., 2019), the study of antibiotic interactions with the ribosome could/will be done for pathogens among the priority list of the WHO, such as the ESKAPE group (*Enterococcus faecium, Staphylococcus aureus, Klebsiella pneumoniae, Acinetobacter baumannii, Pseudomonas aeruginosa* and *Enterobacter* species). These investigations are already ongoing research in the lab and would complete the results of my studies in this global study of ribosome-targeting drugs. Indeed, in this new era of resistance and even multiresistance, it becomes crucial to characterize the mechanisms of action of antibiotics and the bacterial strategies of resistance to adapt our vision of drug discovery.

CHAPTER III

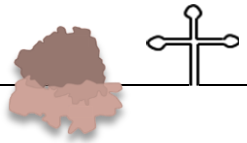

BIOPHYSICAL STUDY OF CRPV IGR IRES INTERACTION WITH YEAST RIBOSOME

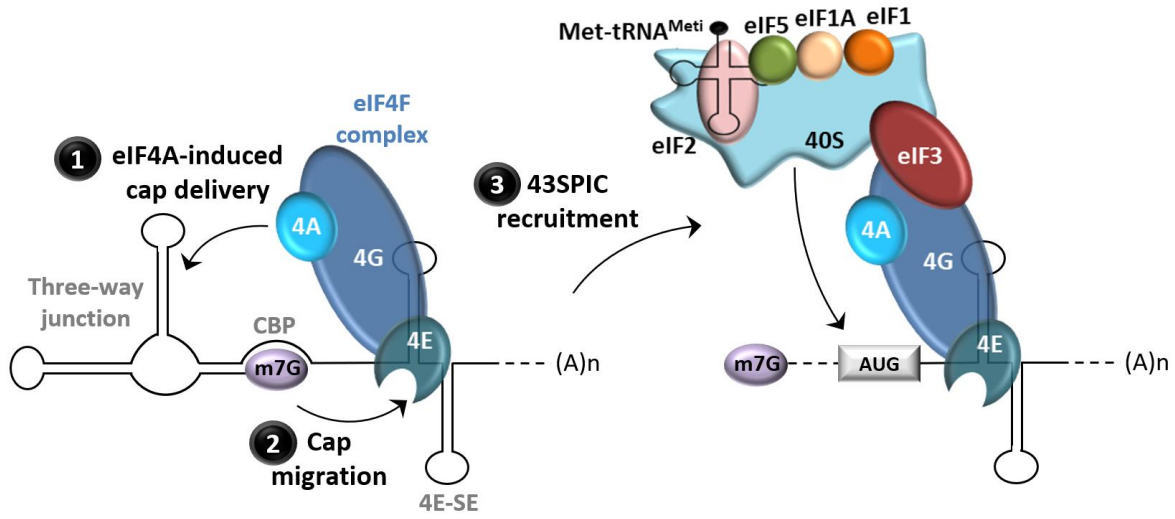

Figure 46: Ribosome tethering for H4 mRNA initiation of translation. Inspired from Martin et al., 2011.

The translation of the H4 mRNA depends on two structural motifs: the three-way junction, which binds to the m^7G cap through its cap binding pocket (CBP), and the 4E-SE element, which recruits the eIF4F complex via eIF4E. This recruitment induces structural rearrangements in the three-way junction (1) which lead to the release and transfer of the cap from the CBP to eIF4E binding pocket (2). Then, the 43S complex is recruited (3) without any scanning event.

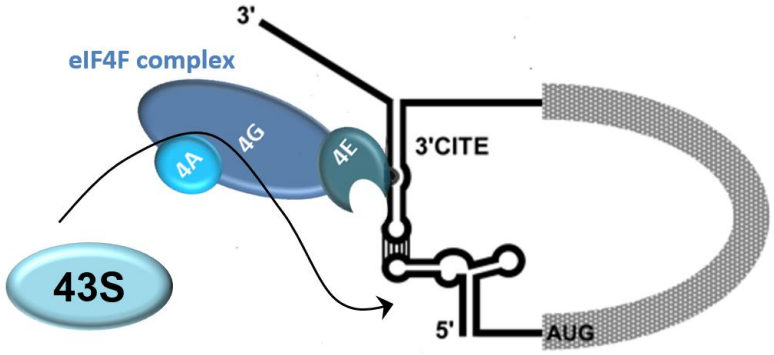

Figure 47: Alternative mechanism of translation initiation via *Tombusvirus* 3'CITE. Adapted from Nicholson et al., 2010.

The I-shape 3'CITE contacts the 5'UTR via a "kissing-loop" RNA-RNA interaction. The eIF4F complex interacts directly with the 3'CITE via eIF4E which allows the 43S complex recruitment. Subsequently, a scanning of the 5'UTR is done to reach to the AUG codon before the final 80S assembly.

Chapter III: Biophysical study of CrPV IGR IRES interaction with yeast ribosome

I. Introduction: non-coding RNA structures-guided initiation of eukaryotic translation

1. Examples of non-canonical initiation mechanisms via specific RNA elements

The canonical initiation step of eukaryotic translation corresponds to the recruitment of an initiation complex to the 5' m^7G cap of polyadenylated cellular mRNAs and is briefly summarized in the **Figure 1** of the general introduction. Though this pathway is predominant, other alternative initiation mechanisms exist in eukaryotes to translate different non-conventional mRNAs. In most cases, a diversity of mRNA structural elements is involved. They differ by their level of complexity, localization (UTR or coding region), number of eIFs required and their ribosome recruitment mode. Such structures are found in cellular eukaryotes mRNAs but also in viral genomes.

For instance, the translation of the eukaryotic H4 mRNA during the S phase of the cellular cycle is orchestrated by two specific structural motifs in the coding region (**Figure 46**) (Martin et al., 2011). One three-way helix junction, downstream the start codon, prevents eIF4E binding by sequestering the cap in a cap binding pocket (CBP) and assists the ribosome positioning on the start codon. eIF4E is then free to interact with the second structural element, a double stem-loop called 4E-SE (eIF4E sensitive element), in the middle of the coding phase, to recruit eIF4F and initiate translation. By avoiding the scanning step, the initiation rate is more efficient in the perspective of producing higher amount of H4 histone during DNA replication.

Considering that most of the viruses have neither their own translation components nor cap mRNAs essential for canonical initiation, they developed other strategies to hijack host ribosomes for their own protein synthesis (Jaafar and Kieft, 2019). Some plant viruses, as *Tombusviridae, Luteovirus* and *Umbravirus*, use a RNA structure in their 3'UTR, called 3' cap-independent translation enhancer (3'CITE), which can adopt different structures as I-, T- and Y-shape or pseudoknots (Miras et al., 2017; Nicholson and White, 2011). Those elements establish long-distance interactions with a 5'UTR stem-loop of the viral genome via kissing-loop motif to allow viral RNA circularization (**Figure 47**). This event is assisted by eIFs (eIF4E and/or eIF4G) and induces 40S recruitment (Nicholson et al., 2010). In some cases, like for the Turnip Crinkle Virus (TCV), the 60S subunit is first recruited thanks to pyrimidine-rich region in the 5'UTR, following binding of the 40S subunit (McCormack et al., 2008; Stupina et al., 2008).

Finally, to hijack the host translation machinery, animal viruses use RNA structure elements, located in 5'UTR or intergenic regions of the viral genome, called internal ribosome entry site or IRES.

2. IRES-mediated initiation of translation

A. Viral and cellular internal initiation

Since their discovery in 1988 (Jang et al., 1988; Pelletier and Sonenberg, 1988; Trono et al., 1988) in the positive RNA virus poliovirus (PV) and encephalomyocarditis virus (EMCV), a hundred of IRESes have been described (Mailliot and Martin, 2018). Up to date, most of them were identified in the same order, especially *Picornaviridae* (picornaviruses) and *Dicistroviridae* (dicistroviruses) families.

These specific RNA folds, with stem loops, bulges or pseudoknots, can be found either in untranslated regions (UTR) or intergenic regions (IGR) in order to produce viral proteins. They are capable of recruiting the translation machinery without the need of the cap and with a variable number of initiation factors (Hellen, 2009; Lozano and Martínez-Salas, 2015; Martínez-Salas et al., 2015). Some IRESes can however need auxiliary factors, called IRES trans-acting factors (ITAFs), for an efficient initiation. Thanks to multiple copies of RNA-binding domains, multimers of ITAFs can be formed to help RNA processing and protect against ribonucleases.

IRESes were also recently discovered in cellular eukaryotic mRNA, and it seems that 10 % of total mRNAs are concerned, the majority being transcription factors and growth factors (Lacerda et al., 2017; Mokrejs et al., 2010). Cellular IRESes appeared to be implied in proto-oncogen mRNA translation, which are tightly regulated, such as c-myc of cyclin D1, vascular-endothelial growth factor (VEGF) and HIF-1α. During viral infections, IRESes allow hijacking of the cellular translation machinery for a fast production of viral proteins and IRES-mediated initiation of those cellular mRNAs takes over from the canonical pathway upon cellular stress (Komar and Hatzoglou, 2011). However, mechanisms are not well known yet.

In terms of RNA structure, cellular IRESes are less complex than viral IRESes, which contain small regions with stem loops (Baird et al., 2007), but also need ITAFs for folding stabilization. Nevertheless, cellular IRESes are less translationally efficient than viral IRESes and they still remain controversial (Shatsky et al., 2010).

B. Deregulation of host translation machinery

Viruses hijack the host translational machinery to favor the synthesis of viral proteins in detrimental to host proteins. In this frame, some viral proteins inhibit the host translation process by targeting initiation factors.

a. Disruption of eIF4F formation

Viruses developed strategies to block the formation of the cap binding complex eIF4F which binds to the mRNA to allow its circularization via interaction with poly A binding proteins (PABP) and the recruitment by the 43S initiation complex (43S IC) (**Figure 1**, stage 0 in eukaryotic part and **Figure 48**).

eIF4F is composed of three subunits, eIF4A, eIF4E and eIF4G; in humans, isoforms eIF4B and H can also be found. Inactivation of the complex can be done through different mechanisms, such as proteolytic cleavage of eIF4G or sequestration eIF4E (Bushell and Sarnow, 2002). The strategy of eIF4G cleavage is found in the case of poliovirus infections. The viral 2A protease cleaves the protein in two fragments (**Figure 48A**): the C-ter part which binds to eIF3 of the 43S IC and eIF4A, and the N-ter part implied into interactions with eIF4E and PABP (Etchison et al., 1982; Lamphear et al., 1993). The 43S IC can still bind to the C-ter part of eIF4G via eIF3 and be recruited for viral translation.

Along with vesicle stomatitis virus (VSV) and EMCV, polioviruses are also able to prevent formation of a functional eIF4 complex by eIF4E sequestration. eIF4E is normally regulated in cells by inhibitory proteins, called 4E-BPs. Non-phosphorylated 4E-BPs can interact strongly with eIF4E contrary to the phosphorylated forms. During viral infections, 4E-BP dephosphorylation is activated and eIF4E cannot be integrated in the eIF4F complex anymore (**Figure 48B**).

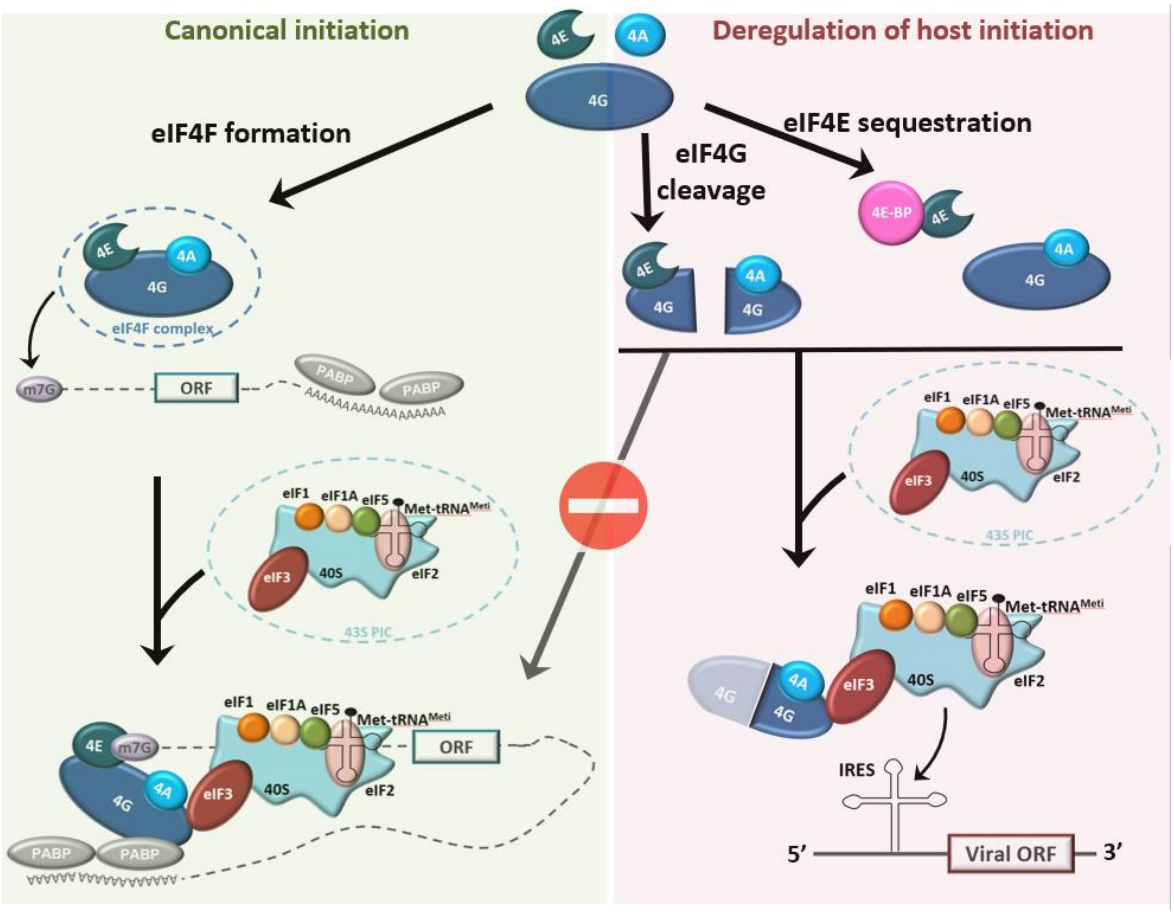

Figure 48: Example of viral strategies to disrupt host eIF4F complex formation.
Upon a viral infection, the eIF4F complex formation is abolished. Instead of classical recruitment to the m^7G cap for the canonical initiation pathway (green box on the left), the virus disrupts the eIF4F formation by either eIF4G cleavage or eIF4E sequestration, in order to deregulate host initiation and favor IRES-mediated viral translation (red box on the right). In this case, the eIF4G complexed with eIF4A cannot interact anymore with capped cellular mRNAs but can still bind to the 43SPIC via eIF3. Then, this alternative initiation complex is recognized by viral IRESes.

b. Inhibition of ternary complex formation by eIF2 inactivation

Another target to disrupt the host translation is eIF2, which is one component of the ternary complex together with initiator tRNA and GTP (Carrasco et al., 2018). eIF2 is a crucial factor for the transport of Met-tRNA^{Meti} to the 40S subunit and *in fine* for the formation of the 43S complex (**Figure 1**, 43S formation in eukaryotic part). It is composed of three subunits α, β and γ. Stimulation of eIF2α phosphorylation leads to its inactivation and a decrease in available translational complex. Among cellular kinases involved in eIF2α phosphorylation in mammals, PKR is activated upon viral infections by recognition of double-stranded viral RNA being replicated (Amici et al., 2015; McInerney et al., 2005). The kinases PERK and GCN2 are also stimulated when a cell is infected by VSV or alphaviruses (Connor and Lyles, 2005; Fros and Pijlman, 2016; Ventoso et al., 2006).

C. Structural and functional features of viral IRESes

The role of viral IRESes is to recruit the ribosome on the mRNA in a cap-independent manner (Johnson et al., 2017). This non-canonical initiation pathway requires a reduced number of eIFs and, as mentioned previously, may be also assisted by IRES trans-acting factors or ITAFs to stabilize IRES-ribosome interaction (Flather and Semler, 2015; Lee et al., 2017; Martínez-Salas et al., 2015). Those host proteins are recruited by the viral metabolism to promote the IRES-mediated initiation by stabilizing IRES-ribosome interactions or even by contributing to conformational changes in the case of the hepatitis C virus (*Hepacivirus*, HCV) (Niepmann, 2013). According to their structure and factor requirements, IRESes are divided into 4 classes (**Figure 49**): type I to IV (Filbin and Kieft, 2009; Jaafar and Kieft, 2019; Mailliot and Martin, 2018). The number of necessary initiation factors decreases as IRES structures become more complex (**Figure 49**).

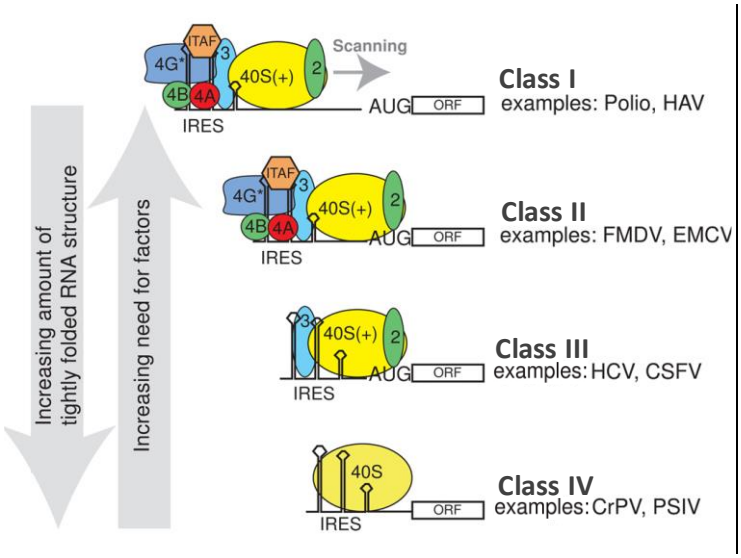

Figure 49: Classification of IRESes according to their structure complexity and level of eIFs dependence. Adapted from Filbin and Kieft, 2009.
The required initiation factors are detailed in each case, as well as the need of ITAFs or not. Well-known members of each class are also indicated.

a. Class I IRESes

Class I IRESes are found in picornaviruses family, and especially in the enterovirus genus, like in Enterovirus A71 (EV-A71), Human Rhino Virus 2 (HRV) or PV. As the PV IRES is the most characterized, molecular basis of class I are based on this IRES. It corresponds to a segment of 743 nucleotides localized in 5'UTR and organized in six structural domains (I to VI) (**Figure 50**). All structural motifs found in those domains are important for its structure but also for its function through interactions with ITAFs. The minimal IRES fragment extends from domains II to VI. The first 100 nucleotides of the PV IRES constitute the domain I, which adopts a cloverleaf structure (CL) useful for the replication of positive and negative viral RNA strands (Andino et al., 1990, 1993). This CL segment contains a C-rich motif, just as the domain IV, and is implied in interactions with a viral replication trans-acting factor, PBC2 (Sweeney et al., 2014; Toyoda et al., 2007). The apical loop of domain IV is also involved in long-distance interactions via a GNRA loop motif (Malnou et al., 2002), while the domain V is responsible for the ITAFs-modulated interaction with eIF4G and eIF4A (King et al., 2010). Between domains V and VI, a pyrimidine-rich tract is present and is required for binding to polypyrimidine tract binding (PTB) proteins, important in the modulation of eIF4G binding (Kafasla et al., 2010). As far as the translation mechanism itself is concerned, the ribosome is recruited upstream of the coding region and a classical scanning occurs in order to reach the start codon. The ribosome entry site corresponds to an upstream AUG codon, located between the nucleotides 586 and 588, and the initiation begins at the real start AUG codon in position 743 (Lozano and Martínez-Salas, 2015; Pilipenko et al., 1992). Usually class I IRESes require all eIFs except the cap-binding factor eIF4E. The absence of eIF4E requirement is induced by the host translation deregulation after perturbation of eIF4F formation upon eIF4G cleavage by the viral protease $2A^{Pro}$ (Gradi et al., 1998; Lamphear et al., 1995).

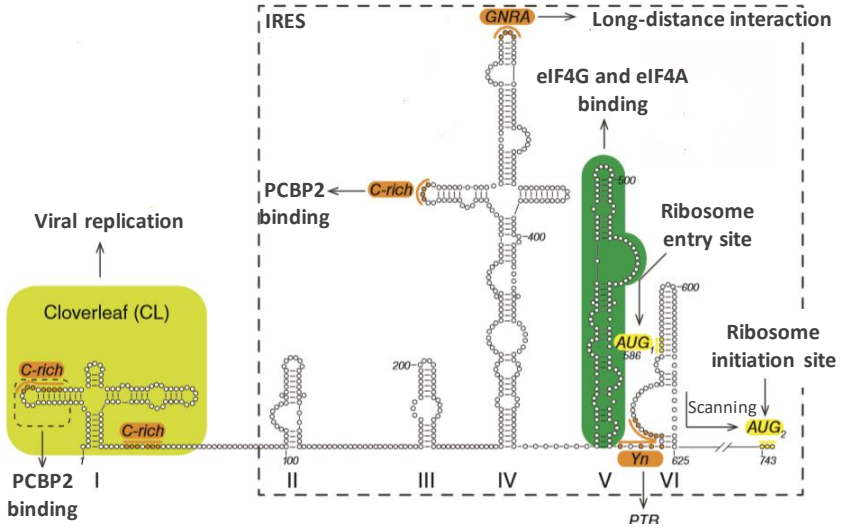

Figure 50: Structural features of the class I IRES of PV. Adapted from Mailliot and Martin, 2017.
The 5'UTR of the PV has a secondary structure divided in six domains (I to VI). The domain I (in light green) corresponds to a cloverleaf structure (CL), which is involved in the viral replication and in PBC2 binding thanks via one stem loop. The minimal IRES sequence is defined by domain II to VI (dashed box) with diverse stem loops. The domain V (in dark green) is implied in the binding of eIF4G and 4A for the eIF4F recruitment, while the domain VI contains the first AUG codon (highlighted in yellow) for ribosome binding. A second AUG codon (in yellow) allows the translation initiation after ribosome scanning. Some regions indicated in orange are implied in the binding of ITAFs or long-distance contacts.

b. Class II IRESes

IRESes from class II are also found in the picornavirus family, mostly in *Cardiovirus* and *Aphtovirus* genera. Two very similar members of each genus were mostly studied, the EMCV and the foot and mouth disease virus (FMDV). Smaller than class I IRESes, they contain a sequence of approximately 440 nucleotides organized in five domains, I to V (**Figure 51**) (Lozano et al., 2016). The minimal IRES segment contains the domains II to V. Similarly to class I IRESes, domain I is involved in viral replication, while domain II assists intrinsic IRES activity through a pyrimidine tract for PTB proteins recruitment (Andreev et al., 2007; Gao et al., 2016; Jang et al., 1990). Domain III contains GNRA motif, also crucial for IRES activity, but its exact function remains unclear (López de Quinto and Martínez-Salas, 1997). However, as class I, a C-rich loop motif has been identified to be potentially implied in long-distance interactions (Fernández-Miragall et al., 2006). Domain IV, which folds in a Y-shape (Hoffman and Palmenberg, 1995), contacts eIF4G (Imai et al., 2016; Kolupaeva et al., 1998). Finally, domain V interacts with PTB proteins, eIF4B and other RNA binding proteins *via* a pyrimidine-tract (Kafasla et al., 2009; López de Quinto et al., 2001). Although direct recruitment on the AUG codon occurs, different mechanisms between EMCV and FMDV are observed and both use two in-frame AUG start codons. While for the EMCV IRES only the second AUG is used, in the case of FMDV, the initiation can start from both AUG codons (Jackson, 2005; López de Quinto and Martínez-Salas, 1999). Initiation requires all eIFs except the cap-binding eIF4E factor because of the inhibition of eIF4F formation after eIF4G cleavage by the viral protease $3C^{Pro}$ in the case of FMDV or eIF4E sequestration for EMCV (Gingras et al., 1996; Mosenkis et al., 1985).

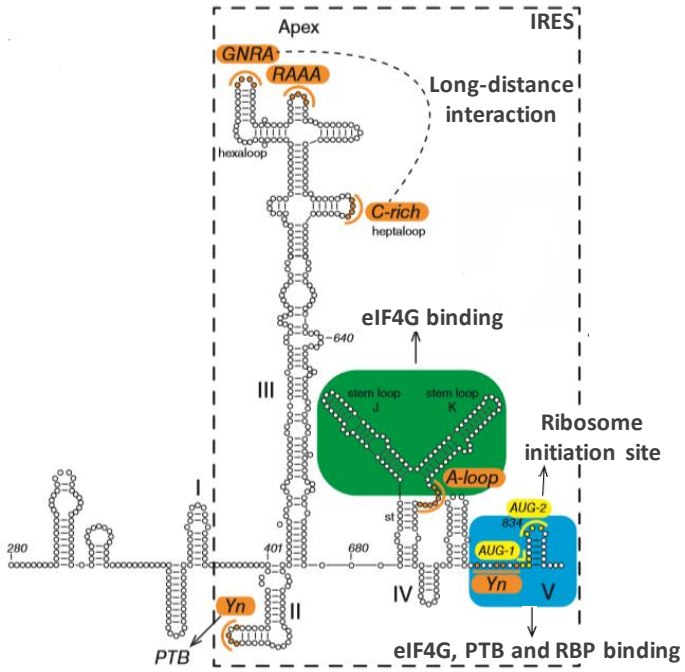

Figure 51: Structural features of the EMCV IRES of class II. Adapted from Mailliot and Martin, 2017.
The 5'UTR of the PV has a secondary structure divided in five domains (I to V). The minimal IRES (dashed box) sequence corresponds to domains II to V. The domain IV contains two stem loops (in dark green) involved in eIF4G binding. The domain V (in blue) contains the two AUG codons (highlighted in yellow) and interacts also with eIF4G. Some regions indicated in orange are implied in the binding of ITAFs, RNA binding proteins or long-distance contacts.

c. Class III IRESes

Some class III IRESes were identified in picornaviruses, like porcine enterovirus 8 (PEV8) or simian virus 2 (SV2), but they are essentially found in the *Flaviviridae* family to which HCV or dengue virus (DENV) belong to (Belsham, 2009). Considering that the class III characterization was almost only done from studies on HCV IRES, this class of structured and flexible RNA segments is also called HCV-like IRESes (**Figure 52**). The HCV IRES constitutes two of the four domains of the HCV 5'UTR (II and III). Domain II, involved in viral replication, possesses a long L-shaped hairpin with two subdomains IIa and IIB which correspond to a bulge and an E motif internal loop associated to the apical hairpin, respectively (Lukavsky et al., 2003). Domain III, linked to the II by the stem of nine base pairs S1, is subdivided into six subdomains from a to f. IIIa, b and c fold together to form a four-way helix-junctions, as well as the IIIe and f, whereas IIId is a three-way helix junction and IIIb is the apical-loop; pseudoknot structure is observed between the region S2 and the IIIa-c fold. The domain I is the target of the microRNA miR-122, which stimulates viral replication (Jopling et al., 2005; Sagan et al., 2015), and the domain IV, absent in other HCV-like viruses (Khawaja et al., 2015), is directly involved in translation since it contains a hairpin with the AUG codon in its bulge. Domains II to IV fold independently. In the end, class III IRESes are more sophisticated and flexible RNA segments than previous classes, requires less factors (only eIF2, 3 and 5) and as they do not need cap-binding factors, a direct recruitment on the AUG codon is observed (Pestova et al., 1996).

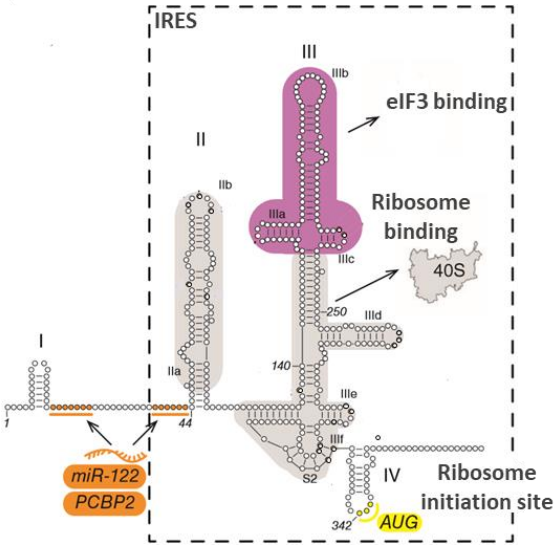

Figure 52: Structural features of the HCV IRES of class III. Adapted from Mailliot and Martin, 2017.
The 5'UTR of the HCV has a secondary structure divided in four domains (I to IV). The minimal IRES sequence (dashed box) corresponds to domains II to IV. The domain II and several subdomains of the domain III (c to f) are implied in the 40S recruitment (in grey). The subdomains a and b (in pink) are responsible for eIF3 binding. The domain IV contains the AUG codon (highlighted in yellow) to initiate the translation. The regions indicated in orange interact with ITAFs or miRNAs.

d. Class IV IRESes

Contrary to the others located in 5'UTR, class IV IRESes are in intergenic regions (IGR), and are thus called IGR IRESes. To date, they were only observed in dicistroviruses, like Plautia stali intestine virus (PSIV) or Cricket paralysis virus (CrPV), whose IRESes are the most well-known and extensively studied (Hertz and Thompson, 2011; Sasaki and Nakashima, 1999; Wilson et al., 2000).

Class IV IRES have the smallest sequence among overall IRESes, with approximately 200 nucleotides, but they contain the most compact and structured structures with several pseudoknots and long-distance contacts (**Figure 55**). Given their level of complexity, initiation does not require neither eIFs, nor classic initiation codon and initiator tRNA (Pestova and Hellen, 2003; Pestova et al., 2004).

This class of IRES allow viruses to be independent from host translation components. It represents the simplest initiation pathway and probably the most ubiquitous considering its universal activity in all domain of life: in insects, rabbits, humans, yeasts (Thompson et al., 2001) and, more surprisingly, also in bacteria but likely with a different mechanism (Colussi et al., 2015).

3. Special case of the intergenic IRES of Cricket Paralysis Virus

A. Generalities about the CrPV

a. A model for the dicistrovirus family

Dicistroviruses are small RNA viruses that infect arthropods such as bees, shrimps or crickets. Among its three genera (*Aparavirus, Triatovirus* and *Cripavirus*), 15 species of viruses have been identified (**Figure 53**). Of the four cripaviruses species, the Cricket Paralysis Virus (CrPV) has the widest diversity of hosts (24 in total) from different orders : Lepidoptera (butterflies), Diptera (flies, mosquitoes, …), Hemiptera (shield bugs, aphids, …), Orthoptera (crickets, grasshoppers and locusts) and Hymenoptera (bees, wasps, ants, …) (Bonning and Miller, 2010). Thanks to this large host range and the ease of use in insect cell culture (Scotti et al., 1996), CrPV has become a reference for viruses of the same family and genus.

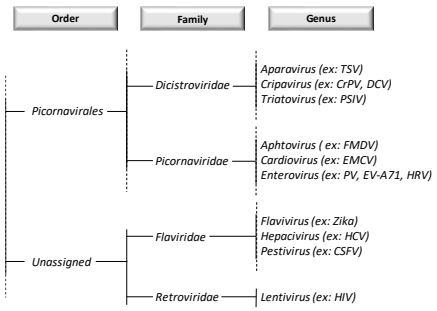

Figure 53: Phylogenetic classification of the dicistrovirus family. Adapted from Mailliot and Martin, 2017.
This phylogenetic virus classification with orders, families and genus (based on the ICTV taxonomy) presents main representants of viral IRES-mediated initiation of translation.

b. A war between host and viral gene expression

During viral infection, the goal of the virus is to produce its viral proteins to form new infectious virions. Dicistroviruses genome is a linear, monopartite and positive single-stranded RNA with two open reading frames ORF1 and ORF2 (Bonning and Miller, 2010; Woo et al., 2011) (**Figure 54**). ORF1 and ORF2 each encode a polyprotein containing precursors for non-structural and structural proteins, respectively.

Polyproteins of dicistroviruses are separated in three regions P1, P2 and P3. P1 corresponds to the four virion proteins, VP1 to 4, of the ORF2. The combination of P2 plus P3 corresponds to the ORF1. P2 is divided into three proteins: 2A, 2B and 2C-helicase. Moreover, at the N-terminal extremity of P2, a viral suppressor of silencing (SS) is encoded by the CrPV. P3 encodes four proteins: 3A, 3B, 3C-protease and 3D-RNA-dependant RNA polymerase or 3D-RdRP. In the 3B region, one or more copies of the coding sequence of the genome-linked viral protein (VPg) are also found. VPg binds to the 5' end of viral genome for a protective role in viral particles.

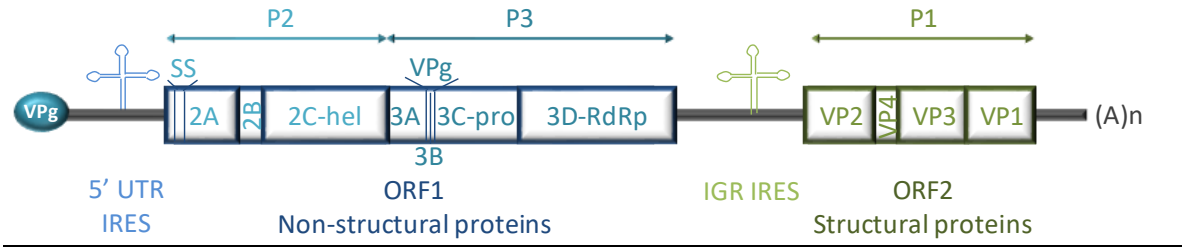

Figure 54: Genomic organization of the CrPV. (Inspired from Bonning and Miller, 2010)
The viral genome of dicistroviruses is divided in two ORFs whose each expression is IRES-dependent. The ORF1 (in blue) downstream the 5' UTR IRES, encodes the non-structural proteins from two polyproteins P2 and P3. P2 contains the proteins 2A, 2B, 2C-helicase (2C-hel) and the silencing suppressor element (SS) specific of DCV and CrPV.P3 contains the proteins 3A, 3B, 3C-protease (3C-pro), 3D-RNA-dependent RNA polymerase (3D-RdRp) and repetitions of the genome-linked protein (VPg) which binds to the viral 5' UTR. The ORF2 (in green) downstream the intergenic IRES (IGR IRES), encodes the structural proteins. The viral protein VP1 to VP4 are produced in the P1 polyprotein. Individual proteins are obtained after proteolytic cleavage of the three polyproteins.

The correct expression of dicistrovirus ORFs is controlled by two IRESes: one in the 5' UTR for ORF1 and a second in the intergenic region for ORF2. In CrPV, while the IGR IRES is very well characterized, the $IRES_{5'UTR}$ was less described until recently with its classification as a type III IRES (Gross et al., 2017). Furthermore, a difference in IRES regulation during the viral cycle was observed (Khong et al., 2016). Indeed, the $IRES_{5'UTR}$ is constitutively expressed whereas the IGR IRES is only activated in late phase of infection. Molecular mechanisms of this differential use are not yet established, but two assumptions were made: activation by viral protein(s) produced during early phase or inhibition by cellular protein(s) in early stages of infection. It's also possible that the host translational machinery, after potential modifications by viral proteins, is more suited to accomodate this IRES.

In addition, to express its viral proteins, the virus needs to take control of the host translational metabolism. The CrPV has two key strategies: in early stage of infection, it triggers the dissociation of eIF4G and eIF4E to alter eIF4F formation, and, later during viral gene expression, eIF2α is phosphorylated preventing the formation of 43S IC (Garrey et al., 2010). As a result, less cellular mRNAs are recruited and more free ribosomal subunits are available, a good combination to improve translation rate of viral proteins.

B. Molecular basis of CrPV IGR IRES-mediated initiation

a. Structural features of CrPV IGR IRES

The CrPV IGR IRES is one of the most characterized representative of type IV IRES (Hertz and Thompson, 2011; Wilson et al., 2000) (**Figure 55**). It contains three domains and three pseudoknots (PK) (**Figure 55A and D**). Domain 1 contains the PKII, domain 2 comprises the PKIII and domain 3 is composed of the PKI and a A-rich Variable Region Loop (VRL) enriched in A (Costantino and Kieft, 2005; Schüler et al., 2006). Furthermore, domain 3 is a type I domain containing a simple helix upstream PKI. However, in some other dicistroviruses like Taura Syndrome Virus (TSV), type II domains are also observed with an additional stem loop SLIII and a longer L1.1 region (Nakashima and Uchiumi, 2009). All the three PK folds independently, suggesting a high flexibility of the IRES (Jan and Sarnow, 2002).

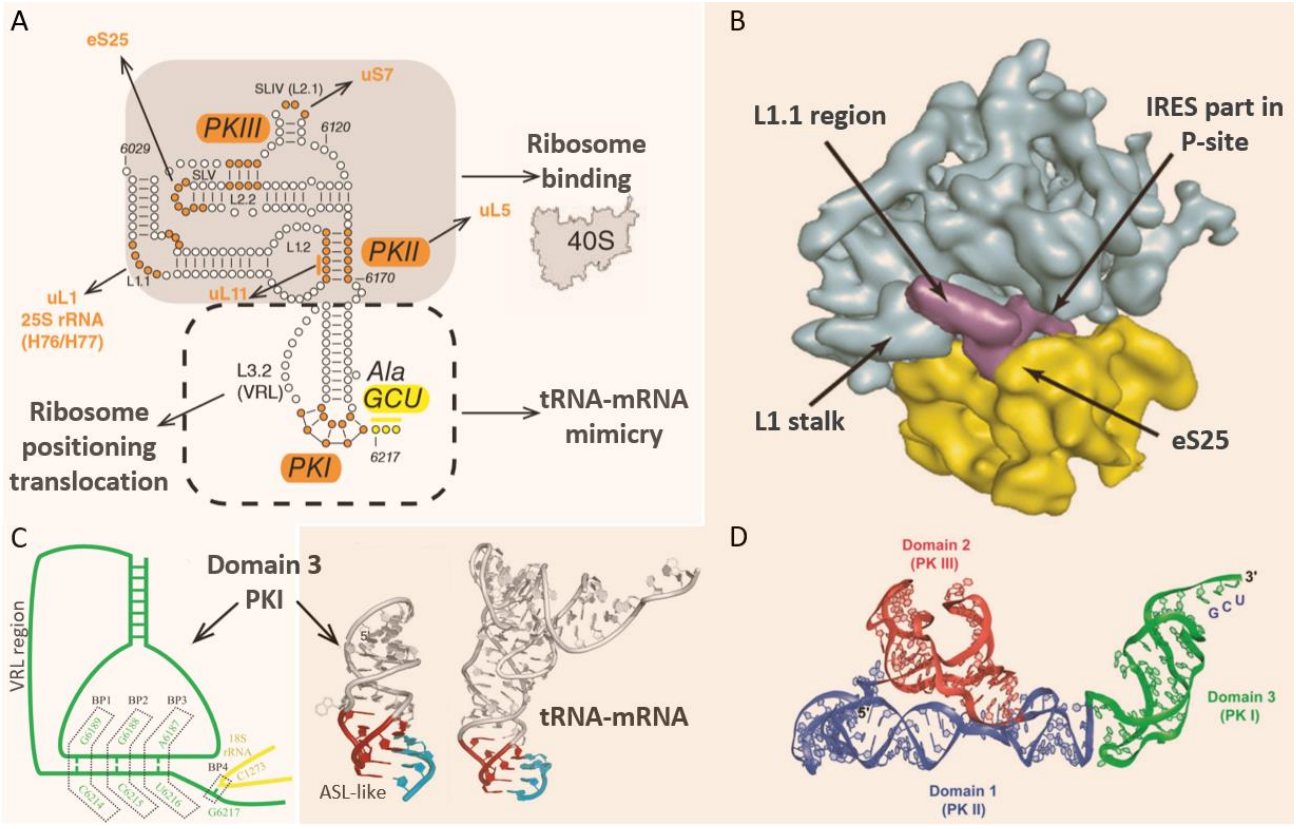

Figure 55: Structural features of the IGR IRES of CrPV, a model for class IV IRESes.
The overall position of the IRES (in violet) is in between the 40S (in yellow) and the 60S (in blue) subunits and important elements for the IRES-ribosome interaction are indicated by arrows in (B) (from Kieft, 2008). The intergenic IRES of the CrPV is composed of three domains with three pseudoknots (PKI to PKIII, highlighted in orange) visible on the secondary (from Mailliot and Martin, 2017) structure in (A) and the tertiary (from Brierley et al., 2008) structure in (D). The domain 1 and 2 (in grey) contain the PKII and PKIII, respectively, that are responsible for the ribosome binding, and the specific nucleotides involved in interactions are indicated in orange. The domain 3 (in the dashed box) contains the PKI which mimics the tRNA-mRNA interaction with the anticodon stem loop-like motif (ASL-like), whose 2D and 3D structures are detailed in (C) (from Murray et al., 2016; Kieft, 2008). The domain 3 also possesses the initiation GCU codon (highlighted in yellow) and the variable loop region (VRL), required for the folding the ASL-like motif and for the ribosomal translocation.

Contrary to domain 3, domains 1 and 2 are essential for binding to the ribosome through interactions between two stem loops (SLIV and SLV), the loop L1.1 and ribosomal proteins from the small and large subunits (Costantino et al., 2008; Fernández et al., 2014; Spahn et al., 2004). In domain 2, the SLIV and SLV interact with uS7 and eS25, respectively, whereas PKII from domain 1 contacts uL5 and L1.1 binds to uL1 as well as the 25S rRNA (Landry et al., 2009). Domain 3 is implied in the binding to A-site by mimicking the structure codon-anticodon thanks to the anticodon stem loop-like motif (ASL-like) adopted by PKI (**Figure 55C**). Mutational studies showed the importance of the three-dimensional structures of the three PK in translational activity. In addition, although the activity is less dependent on the sequence, some highly conserved residues in SL1 are critical for initiation (Jan and Sarnow, 2002).

b. Mechanism of ribosome recruitment

40S is recruited via an interaction with domains 1 and 2 of CrPV IRES and PKI is accommodated in the A-site. Then, the 60S subunit joins the 40S-IRES complex to form an elongation-competent 80S-IRES complex, in which the IRES is inserted in the subunit interface (**Figure 55B**) (Kieft, 2008). During canonical initiation, the 40S head dynamics is important to correctly accommodate the initiator tRNA in the P-site (Aylett et al., 2015; Llácer et al., 2015). But with CrPV IRES, restricted flexibility of the head is observed due to insertion of SLIV and V in the cleft between the 40S head and body. This conformation favors the binding of PKI in the decoding center (Fernández et al., 2014). Correct base pairing is essential for the tRNA-mRNA mimicry and Watson-Crick base pairs are involved to mimic the similar DC conformation with tRNA (**Figure 55C**). Besides the three classical one, an additional base pair, called BP4, was observed between the first translated nucleotide (G6217) and a base of the 18S rRNA (C1273), which normally contacts the anticodon nucleotide BP3 (Murray et al., 2016). Interestingly, this G base is conserved among all dicistroviruses (except PSIV) suggesting an essential role in the frame selection. However, relation between PKI positioning and frame selection needs further investigation. Furthermore, mRNA-like and tRNA-like fragments are connected by the VRL region (**Figure 55A, C and D**). This variable loop is a structural key element for the initiation, whose length and sequence influence the correct folding of PKI in the A-site (Ren et al., 2014; Ruehle et al., 2015).

After 60S joining, 80S-CrPV IGR IRES pre-translocated complexes appeared to exist as two states of intersubunit rotation, similar to prokaryotic ribosome: a non-rotated and a rotated state (**Figure 56A**) (Fernández et al., 2014). Those conformations obtained after peptidyl transfer, but before translocation, depends on the atypical orientation of L1 stalk from the 40S subunit, and are comparable to those observed in prokaryotes (**Figure 56B**). The movement of L1 stalk is coordinated to the rotation of the small subunit by the L1.1 part from domain 1 of IRES This non-conventional ordering, involving contacts between L1 stalk and eL36, has also been observed in GTPase-ligand binding and activation in canonical translation, whether in bacteria or in eukaryotes (Agrawal et al., 2000; Gomez-Lorenzo et al., 2000).

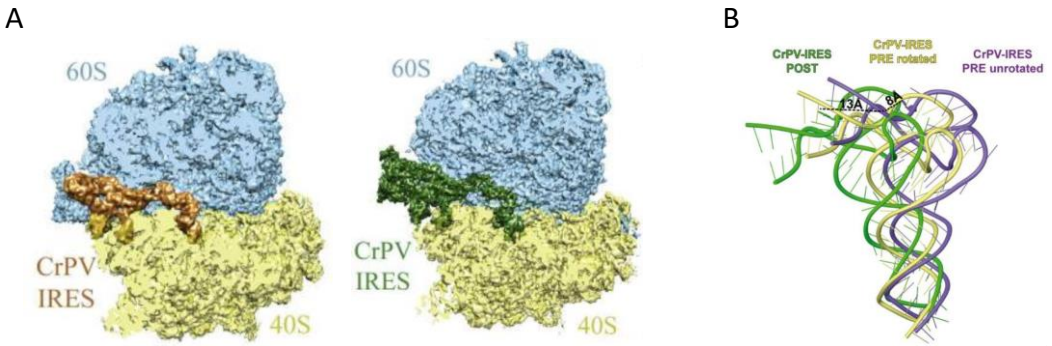

Figure 56: Ribosome rotation and L1 stalk displacement upon IRES binding.
After 60S (in blue) joining to the 40S (in yellow) bound to the CrPV IRES (in orange or in green depending on the ribosome state). Pre-translocated complexes exist as two rotated states (A) depending on the rotation of the 30S head (from Fernandez et al., 2014). Upon the IRES binding, the L1 stalk is displaced between pre- and post-translocated (in green) states, and between rotated (in yellow) and unrotated (in violet) pre-translocated complexes (B) (from Muhs et al., 2015).

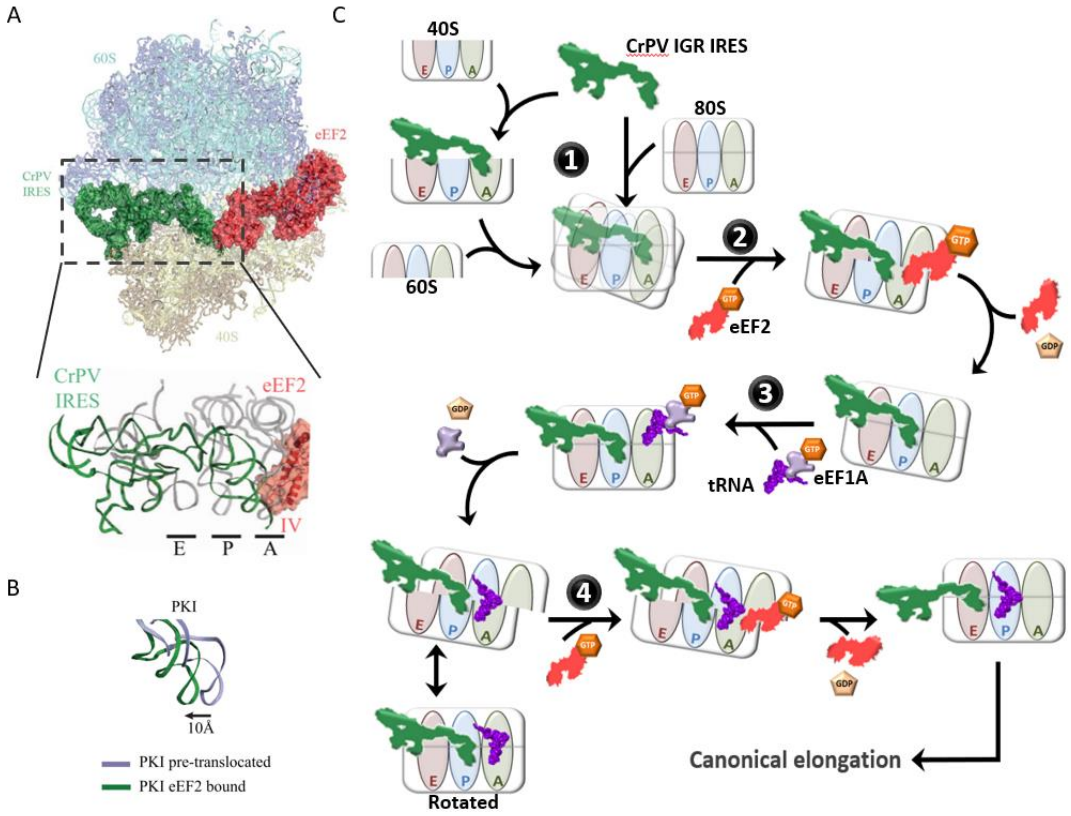

Figure 57: eEF2-mediated translocation of CrPV IGR IRES.
The structure of 80S ribosome (40S in yellow and 60S in blue) in complex with the IRES CrPV (in green) and eEF2 (in red), with a detailed view of their positioning in the different tRNA A-, P- and E-sites is presented in A (from Murray et al., 2016). The PKI is shifted in eEF2-bound ribosome compared to pre-translocated complexes (in grey) (B; from Murray et al., 2016). The overall mechanism of translocation mediated by eEF2 is depicted in C (inspired by Pisareva et al., 2018). First, the IRES binds to the 40S subunit or the whole 80S ribosome with PKI in the A-site (1). Before eEF2 binding, an alternative canonical non-rotated/rotated state is observed thanks to 40S head rotation. Upon eEF2-GTP fixation (2), a first pseudo-translocation event leads to a hybrid A-P conformation. GTP hydrolysis and eEF2 release induce the placement of PKI in the E-site to allow binding of the ternary complex aa-tRNA-eEF1A in the free-A-site (3). GTP hydrolysis and eEF1A release promote a second translocation event, with again a hybrid conformation. The binding of eEF2-GTP (4) blocks the ribosome in the non-rotated state. After eEF2 release associated with GTP hydrolysis, the final conformation with E-site PKI and P-site tRNA is obtained to enter in elongation step.

Among kinetic studies on the CrPV IGR IRES-mediated translation, one of them showed that a whole 80S can also be directly recruited by the IRES (**Figure 57C**) (Bugaud et al., 2017; Jang and Jan, 2010; Petrov et al., 2016). This is supported by the fact that eIF1, eIF1A and eIF3 are able to partially inhibit the 60S joining step (Pestova et al., 2004). The direct recruitment of 80S ribosomes could circumvent this negative regulation pathway. Based on kinetics, the proposed model presents a preferential sequential binding to the IRES rather than a direct recruitment of 80S (Petrov et al., 2016). Indeed, in presence of entire 80S and individual subunits (40S and 60S), the binding of 40S to the IRES, subsequently joined by the 60S seems predominant. This would be supported by a slower 80S association to the IRES, but the overall kinetics of this interaction needs further investigation (Petrov et al., 2016). In the end, the overall initiation rates are dictated by rate-limiting recruitment of 40S or 80S.

c. tRNA incorporation and eEF2 translocation

Peptide elongation begins with arrival of the first elongator tRNA, which is recruited via a ternary complex formed with eEF1A and GTP, like in canonical translation. It was recently shown that the continuous presence of eEF2 was necessary (**Figure 57**) for the irreversible step that finalizes initiation: the efficient incorporation of the tRNA in complex with eEF1A and GTP (Abeyrathne et al., 2016). Thus, eEF2 catalyzes a first translocation in the complex 80S-IRES is required to free the A-site and induces transfer PKI into the P-site (**Figure 57C**) (Murray et al., 2016). The correct positioning of initiation GCU codon in A-site to let the Alacyl-tRNA^{Ala} enter, assisted by eEF1A and eEF2, is possible thanks to the VRL flexibility of the IRES (Au and Jan, 2012; Au et al., 2015). Then, a second event of translocation occurs, in order to move PKI and A-site tRNA towards E- and P-site, respectively (Pisareva et al., 2018) (**Figure 57C**). eEF2 seems to facilitate the binding of the tRNA rather than stabilizing it on the ribosome (Petrov et al., 2016).

Unstable translocated 80S-IRES intermediate states suggest the existence of a slow but spontaneous back translocation event (Pestova and Hellen, 2003; Fernandez et al., 2014; Muhs et al., 2015; Petrov et al., 2016; Bugaud et al., 2017). Forward and back-translocation can be favored by the incomplete tRNA mimicry of the IRES. Moreover, this incomplete mimicry combined with the high dynamic of 80S-IRES complexes has implication in the ambiguity of tRNA frame selection. Besides the importance of BP4 interaction, kinetics of tRNA arrival has also a crucial role in 0 or +1 frame selection and initiation efficiency. +1 frame initiation is less efficient than 0 frame, but in both cases slow tRNA selection is observed compared to a non-limiting fast translocation event (Petrov et al., 2016).

Finally, after tRNAs selection and the first peptide bond formation, the elongation goes on following classical scheme to produce viral proteins.

d. eEF2-related structural rearrangements

eEF2-mediated translocation can be dissected into pre- and post-translocation states (Abeyrathne et al., 2016; Murray et al., 2016). A complex with CrPV IRES, 80S and eEF2 complexed with the non-hydrolyzable GTP analog GDPCP was studied to identify structural rearrangements upon eEF2 binding. When eEF2 binds, the ASL-like region of PKI appeared to be pushed 10° away in a position between A- and P-sites of the 40S, due to specific contacts with the domain IV of eEF2 (Murray et al., 2016; Muhs et al., 2015) (**Figure 57A and B**). This conformation is similar to the hybrid ap-P state, in which the ASL of the tRNA is placed between A- and P-site on the small subunit, while the peptidyl end is already in the P-site of the large subunit. Thus, eEF2 binding induces an unstable intermediate A-P conformation of PKI (Ratje et al., 2010).

The interaction between two loops at the end of domain IV and the IRES is facilitated by eEF2 which is anchored on the ribosome via domain III and V. The first loop is close to the major groove of the ASL-like segment of PKI whereas the second loop directly interacts with PKI through its H694 and H699 residues (Murray et al., 2016). As H699 is involved in the decoding interaction with BP1 and BP2, the arrival of eEF2 disrupts this bond and allows tRNA displacement in the P-site. More precisely, this conserved histidine residue of the eEF2 domain IV is post-translationnally modified in diphtamide (Schaffrath et al., 2014), that is really important to prevent canonical interactions with rRNAs and favor the stabilization of PKI in the A-site (Murray et al., 2016). In parallel, the post-translocated state reveals that domain 1 and 2 in the E-site are shifted 25 Å away compared to pre-translocation complex while PKI is in the P-site and shifted by 22 Å. The apical part of PKI, corresponding to ASL-like motif, is rotated from 50 ° (Muhs et al., 2015).

Regarding the second translocation event, recent studies also showed that the 40S head swivelling is important to transfer PKI in the E-site (Pisareva et al., 2018). Structures reveal a late stage intermediate of eEF2-mediated translocation thanks to slow movements of CrPV IGR IRES between tRNA sites (Petrov et al., 2016; Zhang et al., 2016). In the non-rotated ribosome with a double translocated IRES, PKI mimics the acceptor stem of an E-site tRNA and the aminoacyl-tRNA is shifted in the P-site tRNA with a mechanism similar to HCV IRES of class III (Pisareva et al., 2018). PKI and the aminoacyl-tRNA are in intermediate P-E and A-P conformations, respectively, while the eEF2 domain IV is maintained in the A-site thanks to swivel of 40S head. Upon eEF2 departure, the 40S head back-swivelling allows to complete the transfer of aminoacyl-tRNA to its final position in the P-site and PKI is then disassembled to adopt its E-site tRNA acceptor stem-like motif (Pisareva et al., 2018).

Following back-swivelling, PKII and PKIII fold in a less compact conformation compared to the single translocated state (Muhs et al., 2015), and PKI-eS25 interaction is modified from the pre-translocated state (Schüler et al., 20006) to stabilize the IRES conformation in the E-site.

The presence of eEF2 induces a 40S additional rotation of ~3° compared to complexes without eEF2 (Murray et al., 2016), such as in canonical translocation (Brilot et al., 2013). eEF2 domain III and V interact with uS12 and uL11, respectively, to anchor the factor to the ribosome (Ban et al., 2014), which then lead to ribosome head rotation and L1 displacement. In summary, studies on the dynamics of pre- and post-translocated complexes highlighted numerous molecular details of the CrPV IGR IRES-mediated initiation.

4. Goals of the study

Many studies were undertaken in order to understand the molecular mechanism of CrPV IRES binding, either from a structural or a functional point of view. Extensive data were obtained to better understand the conformational changes upon IRES binding, the ribosome recruitment pathway and translocation events. A model was recently proposed with a sequential initiation pathway, binding of 40S and then joining of 60S, predominant over a direct recruitment of the whole 80S ribosome. Furthermore, evidence showed a possible initiation of translation by IGR IRES in bacteria, but potentially with a different mode of binding. As CrPV IGR IRES-mediated initiation is dynamic and a kinetically controlled process, the goal of my work was to use innovative biophysical strategies (switchSENSE and ITC) in order to collect thermodynamics and kinetics data with the perspective of a better understanding of the molecular mechanisms involved into ribsosome-CrPV IGR IRES interaction. Furthermore, the methodological developments, done in collaboration with Dr. Guillaume Bec of our laboratory and Dynamic Biosensors GmbH, intend to establish a proof of concept for the study of IRES binding using the switchSENSE technology before studying ribosome interactions with IRESes from human pathogenic viruses.

II. Materials and methods

1. Purification of the *S. cerevisiae* ribosome

A. Native 80S

80S purification is based on the protocol published by Ben Shem et al., 2011 (Ben-Shem et al., 2011). The JD1370 strain, elaborated by Pr. Dinman's lab, is used. A first pre-culture of 3 mL YPD is done from a glycerol stock conserved at -80 °C or from a YPD agar plate, and incubated at least 10 h at 30 °C. Then a larger pre-culture of 250 mL is seeded with the 3 mL overnight at 30 °C. The culture is seeded between 0.05 and 0.1 $OD_{600\ nm}$. Yeast growth is stopped at 1.4 OD_{600nm} and cells are harvested (20 min, 4 000 rpm, 4 °C). Pellets are then washed in buffer M (30 mM Hepes KOH pH 7.5; 50 mM KCl; 10 mM $MgCl_2$; 8.5 % Mannitol; 10 mM β-mercaptoethanol; 0.5 m M EDTA) 1 to 3 times and around 1.2 g of yeast-L of culture are obtained. The cells are mixed with glass beads (0.45 to 0.5 mm of diameter) in a lysis cocktail (buffer M complemented with 0.56 mg-mL Sodium Heparine; 1.2 mM AEBSF; 1X protease inhibitor cocktail; 0.1 U-µL RNasin). 13.9 g of beads are used for 4.5 g of cells in 10 mL of lysis buffer. Yeasts are then lysed by manual shaking at a frequency of 3 Hz during 5 min with 1 min incubation in ice after each minute. Cellular debris and beads are eliminated by a centrifugation of 18 min at 25 000 g at 4 °C (rotor Type 50.2 Ti in Beckman Coulter ultracentrifuge). From now, all following treatments are done with aliquots of 1 mL in 1.5 mL Eppendorf tubes.

Proteins are precipitated by incubation with 4.5 % PEG in ice for 5 min and a centrifugation of 5 min at 20 000 g at 4 °C. KCl concentration of the supernatant is adjusted to 130 mM. After an incubation of 5 min on ice, PEG concentration is increased up to 8 %. The mix is incubated at least 10 min on ice and ribosomes are pelleted using a centrifugation of 5 min at 17600 g at 4 °C. Ribosomes are resuspended in a M2 (buffer M complemented with 0.57 mg-mL Sodium Heparine; 100 mM KCl; 1X protease inhibitor cocktail) buffer and loaded on 15 - 30 % sucrose gradients (15h, 18 000 rpm, 4 °C, rotor SW32 Ti in Beckman Coulter ultracentrifuge). Gradients are collected with a Gradient Fractionator coupled to an AKTA FPLC system (**Figure S3A**). As for the 70S ribosome, integrity of 18S rRNA and 25S rRNA is assessed on 1 % agarose gel, 0.5 $\mu g.mL^{-1}$ EtBr (**Figure S3A**). Ribosomes are finally concentrated and washed in ITC buffer (50 mM Sodium Cacodylate pH 7; 7 mM $MgCl_2$; 30 mM KCl; 70 mM NH_4Cl; 1 mM DTT; 5 % glycerol) using 100 K centrifugal filter unit, before being used directly for experiments or being flash-frozen and conserved at – 80 °C. Considering RNA composition, 80S concentration is taken at $OD_{260\ nm}$ from 1-20 diluted suspension.

$\varepsilon_{80S} = 5.10^7\ M^{-1}.cm^{-1}$

B. Dissociation and reconstitution of 80S ribosome

80S ribosomes should be dissociated for better analysis, whether for ITC or switchSENSE experiments. At the beginning, dissociation was done on the isolated 80S after sucrose gradients, which was diluted in a dissociation buffer (30 mM Hepes KOH pH 7.5; 500 mM KCl; 2 mM $MgCl_2$; 2 mM DTT; 0.1 m M EDTA). Increasing KCl concentration and decreasing magnesium ions lead to the dissociation of ribosomal subunits. Dissociated ribosomes were loaded on 10 – 30 % sucrose gradients (15h, 19 000 rpm, 4 °C) and gradients are collected with a Gradient Fractionator coupled to an AKTA FPLC system (**Figure S3B**). After optimizations, native 80S obtained after PEG precipitation (see previous section) is directly resuspended in the dissociation buffer and then loaded on 5 - 20 % sucrose gradients (8h, 28 000 rpm, 4 °C). Quality of the separation and rRNA integrity are checked by analysis of 16S rRNA and 23S rRNA on 1 % agarose gel, 0.5 µg.mL^{-1} EtBr (**Figure S3B**). To reconstitute the whole 80S ribosome, subunits are simply pooled, dialyzed in ITC buffer and concentrated using 100 K centrifugal filter unit. In the case of subunits purification, 40S fractions and 60S fractions are pooled separately, also dialyzed in ITC buffer and concentrated using 100 K centrifugal filter unit. Aliquots are either flash-frozen and kept at – 80 °C or used directly for experiments.

$\varepsilon_{40S} = 2.10^7\ M^{-1}.cm^{-1}$
$\varepsilon_{60S} = 4.10^7\ M^{-1}.cm^{-1}$

C. Adapted purification protocol

Some steps of the previous protocol were not satisfying for a large-scale purification of the 80S, so an optimized procedure was established. Growth and cells recuperation are unchanged. Lysis step is done using French Press (pressure at 2.2 bar) with the same conditions of lysis buffer. Cellular debris are then eliminated by an ultracentrifugation (30 min, 18 200 rpm, 4 °C) and supernatant is taken for proteins PEG precipitation. In a cold beaker 30 % PEG is slowly added under agitation (using magnetic bar) to reach 4.5 % and 20 min of homogenization is done. Proteins are precipitated by a centrifugation of 10 min at 50 000g at 4 °C (rotor JA-12 Ti in Beckman Avanti J-25 ultracentrifuge) in Nalgene Centrifuge Ware tubes (Thermo Scientific). Following the same method, 30 % PEG is added to the supernatant to reach a concentration of 8.5 % for ribosome precipitation. Ribosomes are finally pelleted by a 20 min centrifugation at 50 000 g at 4 °C and resuspended in M2 buffer being deposited on 15 % - 30 % sucrose gradients (as in original protocol). Following steps and 80S dissociation were also unchanged.

2. Production of the CrPV IGR IRES

ITC - T7 promotor were introduced upstream the DNA sequence of IGR CrPV IRES, long of 222 nucleotides, by PCR. The 3 oligonucleotides designed for DNA production were:

5' IRES CGTAATACGACTCACTATAGGCAAAAATGTGATCTTGCTTGTAAATACAATTTTGAGAGG
3' IRES GTTTTTGGCGTCTTCGGTATCTTGAAATGTAGCAGGTAAATTTCTTAGGTTTTTCGACTA
IRES Middle TTTCTTAGGTTTTTCGACTACCTAATCTGAAAAACCGCAGAGAGGGCTTCCTGGATAT
TGTGGGGCTGCCACTAGGCATCCTGGAACGTAAAGCTAAATAGCTAACCTAAATACAAAAATAGCAC
TACTTGTAATTTATTAACCTCTCAAAATTGTATTTAC

SwitchSense - The sequence that will hybridize to the attached DNA strand of the electroswitchable DNA chip has been introduced at the 3'end of the IGR CrPV IRES DNA sequence by PCR. This construct is amplified using 2 oligonucleotides complementary to the ends of the DNA sequence of the IRES:

T7-CrPV2 CAACAAATATTAATACGACTCACTATAGGCAAAAATGTGATCTTGCTTG
RevcNLB96-CrPV2 TAGTCGTAAGCTGATATGGCTGATTAGTCGGAAGCATCGAACGCTGATTAGTT
ACAGTACCTCCGAGAGCAAGTAGGGCACCCTGTAGTTCCTGATGTTTTTGGCGTCTTCGGTATCTTG

PCR products are washed with milliQ water using 50 K Microcon Centrifugal Filters (Merck Millipore), before being used for T7 transcription.

For 1 mL mix of transcription:
- 1 X T7 buffer
- 0.005 $U.\mu L^{-1}$ pyrophosphatase
- 1.5 mM spermidine
- 0.15 $mg.mL^{-1}$ BSA
- 50 mM DTT
- 4 mM rNTPs
- 0.025 % Triton X-100
- 15 to 20 µg of PCR products
- 20 µL of homemade T7 RNA polymerase

The mix is incubated 3 h at 37 °C. After 1 h of transcription 10 µL of T7 RNA is added.

Transcripts are purified by phenol-chloroform extraction and ethanol precipitation.1 V of phenol-chloroform (Roti®P-C-I, Roth) is added and sample is centrifuged 5 min at 6 000 g after a vigorously vortexing. The aqueous phase is kept and 1 V of chloroform-isoamylic alcohol (25:1) is added and sample is centrifuged again after vortexing. This step is repeated one time and the supernatant is finally mixed with 2.5 V of cold absolute ethanol and 1-10 of 3M sodium acetate. Precipitation is realized at -80 °C at least 30 min. After pelleting RNA (30 min, 6 000 g, 4 °C), a wash with cold 70 % ethanol is done without resuspending the pellet.

Finally, the pellet is resuspended in mQ water, before being washed in water and concentrated using 50 K centrifugal filter unit. At the end, transcripts are checked on a 8 % denaturing acrylamide gel, recovered by a phenol-chloroform extraction and resuspended in milliQ water. A final purification step on gel-filtration column did not improve the IRES purity. Finally, IRES is concentrated using 50 K centrifugal filter unit and concentration is determined by measuring OD_{260nm} of tenth dilution.

$MW_{CrPV\ IRG\ IRES}$ = 77 816 g.mol^{-1} $MW_{cnLB\text{-}IRES}$ = 109 500 g.mol^{-1}

3. Hybridization of IRES with @PK

For control experiments, 2 oligos were designed to disrupt the structure of pseudoknots 2 and 3 of the IRES. IRES and the anti-PK are mixed (1:1 or 1:2) and incubated 5 min at 60 °C. Hybridization is checked using native 8 % acrylamide gel with 5 mM MgCl2 and without EDTA (**Figure 66B**).
Anti PKII (@PKII): 5' CCG CAG AGA GGG CTT CCT GG 3'
Anti PKIII (@PKIII): 5' GGG GCT GCC ACT AGG CAT CC 3'

4. Preparation of ITC experiment

Ribosomes and the IRES need to be rigorously in the same buffer. Thus, after thawing, samples are dialyzed against ITC buffer using 4 mL centrifugal filter unit. For a starting volume of 1 L or less, 15 to 20 mL of buffer are used for a complete buffer exchange. Concentrations of both sample solutions are carefully checked before running experiment. A solution of 285 µL of ribosomes is prepared for the cell and of 70 µL of IRES for the syringe. Ribosome concentration is obtained by measuring OD_{260nm} of twentieth dilution and IRES concentration is obtained by measuring OD_{260nm} of tenth dilution. Most of the time, 8 to 14 µM of ribosomes are titrated by a solution of IRES ten times more concentrated. Size and number of injections depend on the concentrations, type of ligands and intensity of heat release. Usually, 19 injections of 2 µL are used for a titration. Measurements were realized on ITC200 and PEAQ ITC (Malvern).

5. Preparation of switchSENSE experiment (Schenckbecher et al., in press, **Annex 2**)

switchSENSE experiments are run on the DRX 2400 instrument (Dynamic Biosensor). Before being loaded in the *switchCONTROL* software, a program is made using the *switchBUILD* software to design the experiment: measurement mode, concentration and nature of analytes, time of association-dissociation, flow rate, temperature, channel and electrode number…. CrPV IGR IRES – cNL-B96 is hybridized on the microfluidic chip MPC-96-2-Y1-S (Dynamic Biosensors). Different concentrations of yeast 80S are then injected onto the IRES attached to the biochip in order to derive kinetic data. Usually, 3 serial dilutions from 1 to 500 nM are used. Data are analyzed using the *switchANALYSIS* software.

III. Results and discussion

IRESes are a well-known family of non-coding RNA, that have attracted the attention of researchers in the translation field because of their property of bypassing canonical initiation. Among them, the CrPV intergenic IRES has been very studied in the past few years and has become a model of study for type IV IRESes (Hertz and Thompson, 2011). Through structural and biochemical works, its mechanism of action was highlighted. Some information about the dynamics of binding are also available (Petrov et al., 2016) but nothing about thermodynamics. Using innovative technologies, such as kinITC and switchSENSE, we could provide both thermodynamic and kinetic data in order to get an original view of the mechanism of ribosome recruitment by the IRES. This work also intends to cross-validate the new methodologies used here. All the experiments are listed in the **Annex 3**.

1. Interaction of yeast ribosomes with CrPV IGR IRES

A. Binding of IRES to native and reassociated 80S

Yeast ribosomes were used here to study the interaction with the CrPV IGR IRES since it would have been too difficult to get enough sample from original hosts. Besides the fact that yeasts are suitable for large-scale production, the CrPV IGR IRES activity was already confirmed with yeast ribosome (Thompson et al. 2001).

a. Thermodynamic and kinetic information from ITC processing

Firstly, those results were obtained using reassociated 80S because the native ribosome leads to weak stoichiometries (**Figure 58A**). According to the literature (Ben-Shem et al., 2011), a stress protein, Stm1, is trapped in the mRNA canal preventing binding of the IRES. Thus, reassociation of the 80S likely disrupts Stm1 binding and high stoichiometries are restored for the IRES-80S binding (**Figure 58B**). IRES binding to the ribosome releases large amounts of heat and is extremely exothermic (**Figure 58**). The thermodynamic profile shows an enthalpy-driven binding mode (ΔH < -TΔS) (**Figure 59A**), meaning a weak contribution of the global degree of conformational liberty for the binding. However, a highly negative ΔCp suggests that important structural rearrangements occur following binding (**Figure 59B**).

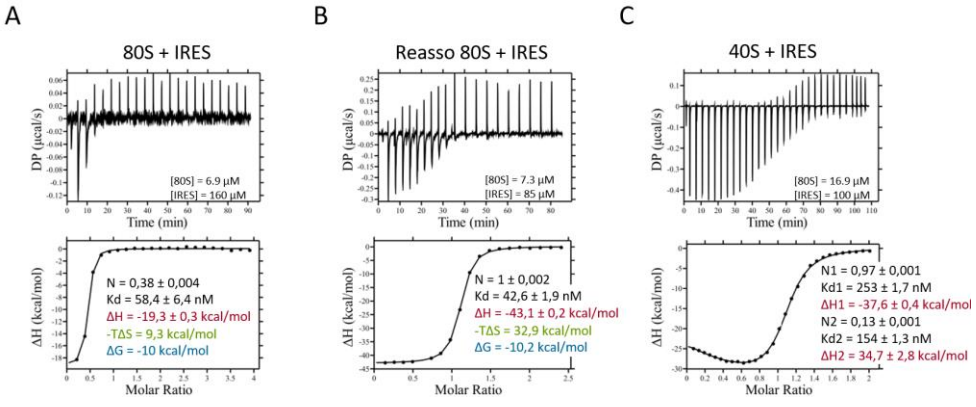

Figure 58: Examples of yeast ribosome titrations by CrPV IGR IRES at 30 °C.
Titrations and binding parameters are shown for native 80S (A), reassociated (B) and 40S (C).

Affinities of the IRES for 80S ribosome are in the range of tens of nanomolar (**Figure 60**). The best affinities are obtained at 25 and 30 °C with average Kd of around 50 nM (**Figure 60,** pink bars). Interestingly, our data suggest that the interaction does not follow Van't Hoff's relationship. Van't Hoff relationship says that the affinity improves when temperature decreases, that is to say that the Kd diminishes together with the temperature. In this system, at low temperatures (15 and 20 °C), affinities are lower than at higher temperatures, with Kd around 75 nM (**Figure 60,** pink bars). Since the 80S-IRES interaction is highly dependent on the IRES structure, at low temperatures the IRES could not fold correctly for an optimal binding. Indeed, few energy could be required to accommodate the IRES in the ribosome and at low temperatures movements are not sufficient to reach this transient state.

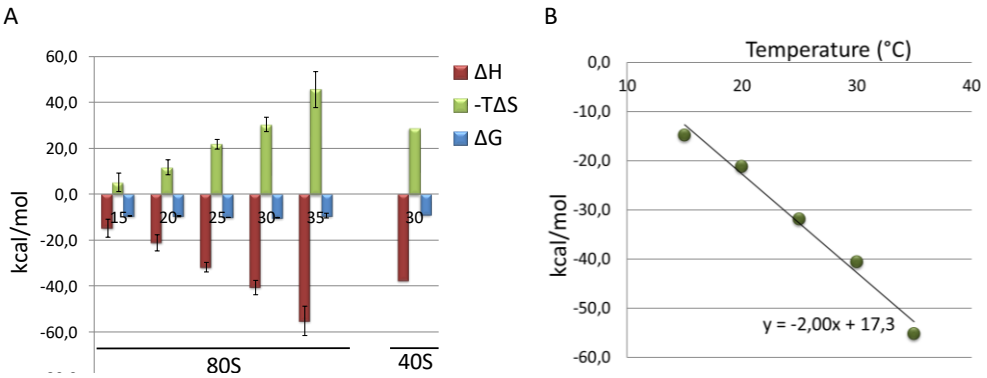

Figure 59: Thermodynamics of IRES interaction with yeast ribosome.
Profiles of IRES binding, with ΔH, -TΔS and ΔG, are presented from several experiments at different temperatures for 80S and 40S. ΔCp could be calculated for 80S ribosome from average ΔH at each temperature (B). Number of replicates is indicated in Figure 3. Detailed data are listed in **Table S3 of Annex 3**.

ITC raw data were also processed with the kinITC approach using the Affinimeter software in order to extract kinetic data (**Figure 61**). As expected, affinities obtained are similar to those obtained with PEAQ-ITC Analysis software (**Figure 60**, violet bars). kon obtained from kinITC is in the range of 10^5 $M^{-1}.s^{-1}$ which is rather fast for a such structured RNA. koff is quite slow, in the range of 10^{-3} s^{-1}, which is not surprising given the complexity of structural constraints in the interaction. However, as few experiments were exploitable for kinITC-processing, switchSENSE experiments were favored for kinetic analysis.

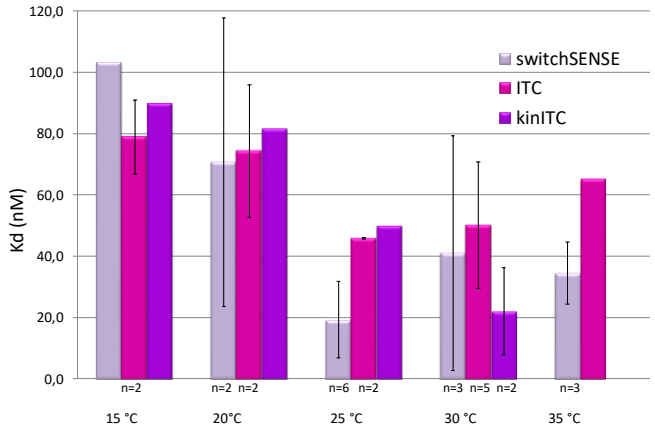

Figure 60: Affinities of IRES for 80S ribosome.
Comparison of Kd determination at several temperatures between the 3 approaches, switchSENSE, ITC (PEAQ processing) and kinITC (Affinimiter processing).
Number of replicates (n) is indicated under the bars.
Detailed data are listed in **Table S3 of Annex 3**.

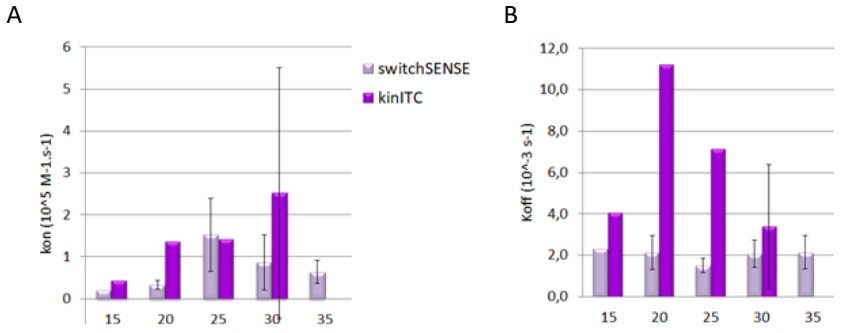

Figure 61: Kinetics of IRES - 80S interaction.
On- (A) and off- (B) rates of PrAMPS determined by switchSENSE method or by kinITC (Affinimeter processing) are presented at several temperatures. Number of replicates are the same than in Figure 59. Detailed data are listed in **Table S3 of Annex 3**.

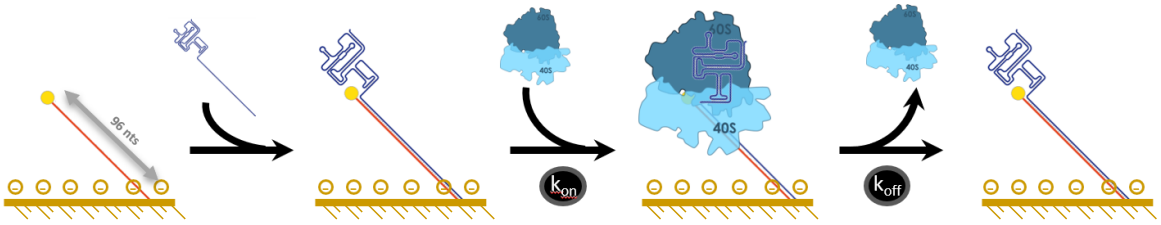

Figure 62: switchSENSE strategy for IRES - ribosome interaction study.
A DNA strand of 96 nucleotides (red) is conjugated with a fluorochrome (yellow) at one extremity and attached to the gold chip. A positive electrical field is continuously applied to maintain the negatively charged strand far from the gold surface. First the IRES-cNLB (blue) is hybridized to the fixed strand and then 80S ribosome (40S in blue and 60S in red) is added for kon determination. Ribosome dissociates (koff) after addition of a continuous flow of buffer.

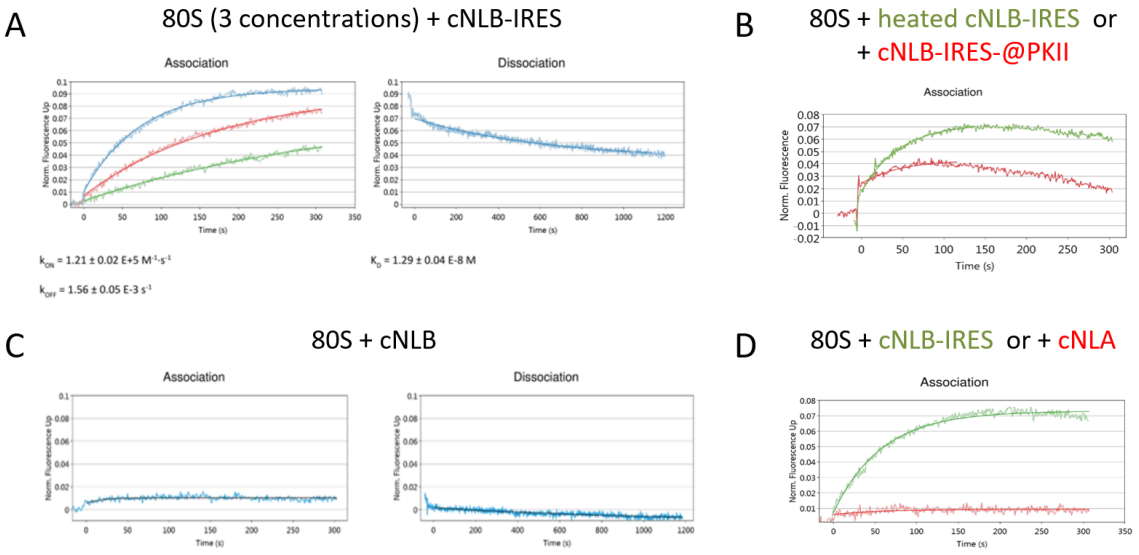

Figure 63: 80S binding in switchSENSE experiments at 25 °C.
Fits of binding of 80S to the IRES are presented in (A) after titrations by 3 increasing concentrations of 80S. Control of binding specificity was also tested. Binding of heated IRES mixed (red curve) or not (green curve) with @PKII is presented in (B). Absence of binding to DNA strands, cNLB (C) and cNLA (D) was also checked. Detailed data are listed in **Table S4 of Annex 3**.

b. Kinetic characterization using switchSENSE technology

Rate constants were determined using the switchSENSE approach in the static mode. A key benefit of the switchSENSE over kinITC is the very low amount of ribosome sample required for each experiment (at least 20 times less). To perform our analysis, IRES was added to the extremity of the complementary strand (cNLB), which hybridizes the DNA strand attached to the chip (**Figure 62A**). In the first place, the length of nanolevers were doubled compared to classical strands, to reach 96 nts and avoid steric clashes between ribosome-bound strands in the chip surface.

Kinetics of the interaction can be measured thanks to the fluorescence variation of the fluorescent dye at the free extremity of the attached DNA. Indeed, fluorescence increases following the ribosome binding (**Figure 63**), likely because the ribosome moves the dye away from the gold surface. Association rates were always obtained from 3 concentrations of 80S, whereas dissociation rates were obtained only for the last concentration (**Figure 63A**).

Affinities (**Figure 60**, mauve bars), on- and off- rates (**Figure 61**) were compared to ITC-processed data at different temperatures. Kd are very similar to those from ITC at each tested temperature, and weak affinities are also observed at low temperatures . By contrast, kinetic rates of IRES binding to the ribosome seem quite different, especially the off-rate which appears to be faster with kinITC than with the switchSENSE. However, the model in kinITC could be too simple for the IRES-ribosome interaction study. Whereas in switchSENSE the immobilization on a surface and the presence of a fluorophore could influence the binding. As mentioned before, only one or two experiments were processed with kinITC, so further experiments could be useful to confirm or infirm this tendency.

Despite this, affinity and rates are very similar between kinetic- and thermodynamic-derived data, which is really satisfactory for such technically different methods. In the end, the combination of the three methods (ITC, kinITC and switchSENSE) allows to validate both data and new approaches for this system of interaction. But, with the absence of information about the experimental temperature for their study and the use of totally different approaches could be important elements to justify those differences.

In the end, though some clarification could be required, we were able to establish a complete kinetic and thermodynamic profile of the CrPV IGR IRES binding to yeast ribosome.

B. Difference of interaction with the IRES between 40S and 80S

Binding of IRES to the 40S subunit was also studied in order to compare binding features with 80S ribosome. Nonetheless, few experiments have been done considering the experimental difficulty to obtain the 40S in high amounts. The experiments performed at 30 °C suggest that thermodynamic profiles of 80S and 40S are similar (**Figure 59A**), whereas affinities seem really different, around 100-200 nM for 40S compared to 20-40 nM for 80S (**Figure 64A**).

Moreover, the affinities for the 40S obtained from the three methods, ITC, kinITC and switchSENSE, vary quite significantly. Indeed, the better affinity, obtained with the switchSENSE, is around 100 nM while in ITC the average Kd is the double. The biggest change is observed for the Kd from kinITC which is about 500 nM. Yet, all Kd are still in the same range of the hundreds of nanomolar and the global tendency that 40S has a weaker affinity for the IRES than the 80S is kept. Moreover, more experiments could be useful to reduce standard deviations and variations between the different approaches.

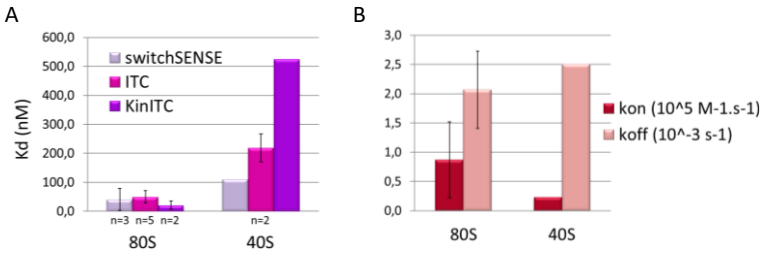

Figure 64: IRES affinities for 40S or 80S and rate constants at 30 °C.
Affinities of IRES for 40S and 80S obtained from 3 different approaches at 30 °C (A). On- and off-rates determined from switchSENSE experiments at 30 °C are presented in (B) for 40S and 80S. Number of replicates (n) are indicated. Detailed data are listed in **Table S3 and S4 of Annex 3**.

In accordance with the difference of Kd, the association and dissociation rates are also quite different between 40S and 80S (**Figure 64B and 65**). Indeed, switchSENSE experiments suggest that 40S has a lower kon and a higher koff than 80S, which means that 40S would associate more slowly and dissociates faster than 80S. These data should be however repeated and confirmed to reduce the standard deviations that are still rather high (Figure 7B). In summary, from the affinity data, the IRES seems to interact preferentially with the 80S ribosome over the 40S small subunit to initiate translation of the ORF2.

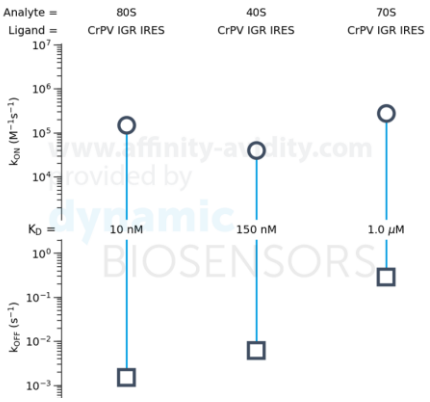

Figure 65: Affinity and rate constants for IRES interaction with bacterial or eukaryotic ribosomes from switchSENSE experiments at 25 °C.
The affinitymap has been generated using Dynamic Biosensors services (https://affinity-avidity.com) with a logarithm scale.
Detailed data are listed in **Table S4 of Annex 3**.

Our model is not really consistent with previous studies that used smFRET or gel shift assays for their analysis (Jan and Sarnow, 2002; Petrov et al., 2016). Those works suggest a better affinity of the IRES for the 40S compared to 80S (**Table 3**). Furthermore, the model of Petrov and collaborators proposed that IRES preferably binds 40S over 80S based on a slower association speed of 80S compared to 40S.

Validation of our IRES-ribosome interaction model would require acquisition of more replicates as well as translational activity test for purified 80S and 40S.

	Kinetic constants	switchSENSE (average of 3 experiments at 30 °C)	smFRET (Petrov et al., 2016)	Gel shift assay (Jan and Sarnow, 2002)
80S	kon (10^5 $M^{-1}.s^{-1}$)	0.9	> 0.3	X
	koff (10^{-3} s^{-1})	2.1	slow	X
	Kd (nM)	41	X	X
40S	kon (10^5 $M^{-1}.s^{-1}$)	0.2	0.7	X
	koff (10^{-3} s^{-1})	2.5	2.1	X
	Kd (nM)	111	26	24

Table 3: Kinetic parameters of IRES binding to yeast ribosome obtained from different methods.

2. Specificity of IRES binding to ribosomes

The specificity of IRES binding to 80S ribosome was also tested by disrupting its structure. Our strategy was to hybridize DNA oligonucleotides targeting IRES pseudoknots (anti-PK) in order to disrupt their correct folding (**Figure 66**). Two oligonucleotides were designed to hybridize to PKII or PKIII (**Figure 66A**), and hybridization was checked on native acrylamide gel (**Figure 66B**). Binding of each combination of disrupted IRES (IRES + anti-PKII or IRES + anti-PKIII) was first tested by ITC experiments. No interaction was observed in both cases (**Figure 67**).

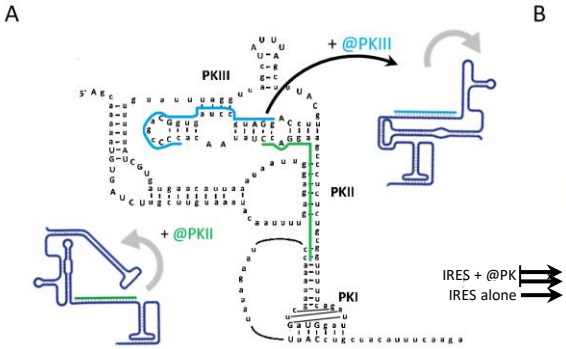

Figure 66: Disruption of CrPV IGR IRES structure.
Localization of anti-oligos hybridization (anti-PKII (@PKII) in green and anti-PKIII (@PKIII) in blue) and structural rearrangements are indicated on the IRES secondary structure (adapted from Landry et al., 2009) (A). Hybridization is validated by migration of mix IRES+@PK, pre-incubated 5 min at 60 °C, compared to IRES alone in an 8% acrylamide gel (B).

The specificity of the interaction was also investigated with the swithchSENSE. Similarly to ITC experiments, no binding was observed for the IRES bound to anti-PKII DNA oligo. (**Figure 63B**). Additional controls were done with IRES heated at 60 °C (hybridization conditions), without IRES on the cNLB strand and with only cNLA strand attached to the surface. As expected, IRES incubated at 60 °C bind normally to ribosome whereas no binding to DNA strands was observed (**Figure 63B, C and D**). Thus, these data confirmed the structure-dependent binding of CrPV IGR IRES to ribosome (Jan and Sarnow, 2002).

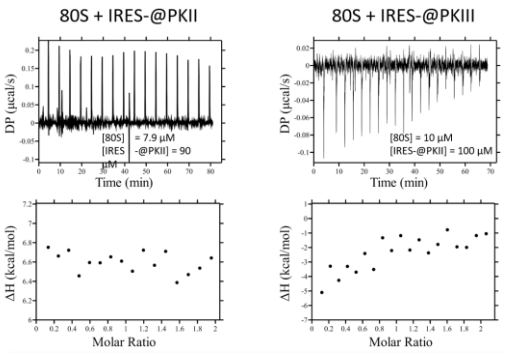

Figure 67: Inhibition of IRES binding to 80S by structure disruption.
After hybridization 5 min at 60 °C of IRES and anti-PKII (@PKII) or anti-PKIII (@PKIII), ITC experiment were performed at 30 °C.

3. IRES binding to bacterial ribosome

Colussi and collaborators published a work showing that IRES-mediated translation was possible in bacteria with intergenic IRESes, like CrPV IGR IRES (Colussi et., 2015). That's why, we decided to investigate on the thermodynamics and kinetics of this interaction using ITC and switchSENSE approaches. Experiments were performed with native *E. coli* ribosome available in our lab. We observed that the binding is highly exothermic. The thermodynamic profile is similar to the one observed for 80S binding to the IRES (**Figure 68A and 69**), with an enthalpy-driven interaction (ΔH < -TΔS). Affinity of the IRES is weaker for 70S than for 80S and 40S, mostly due to a very fast koff (**Figure 65**). Remarkably, disruption of the IRES 3D-fold, using same DNA oligonucleotides targeting pseudoknots, do not prevent 70S binding, either with ITC (**Figure 68B and C**) or switchSENSE (**Figure 70A and B**). In both cases, data could hardly be fitted with a simple model, contrary to 80S binding to IRES. Furthermore, switchSENSE experiments suggest that 70S can bind to naked DNA strands of the chip (**Figure 70C**).

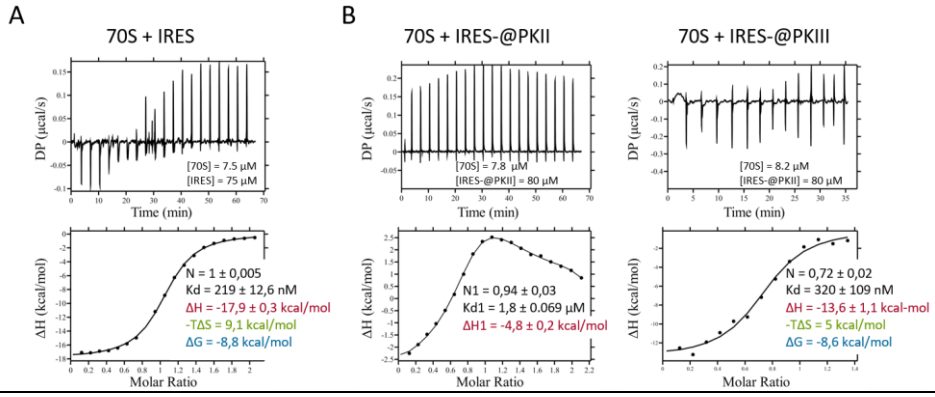

Figure 68: IRES binding to 70S ribosome at 15 °C.
70S binding was observed at in ITC 15 °C either for IRES alone or for hybrid IRES-anti-PK (@PK) obtained by pre-incubation 5 min at 60 °C. Detailed data are listed in **Table S3 of Annex 3**.

Altogether, these data suggest that the CrPV IGR IRES-70S interaction is less structure-specific compared to 80S ribosome. Fast on- and off-rates (**Figure 65 and 70**) are also supporting this weak interaction: the ribosome binds and dissociates in a distributive way. We know from structures of 70S-PSIV IGR IRES (Colussi et al., 2015; Zhu et al., 2011) that domains 1 (containing PKII) and 2 (containing PKIII) have different locations in 70S compared to equivalent 80S complexes. This structural particularity might explain the difference in behaviors with regard to IRES binding. Finally, those results are in agreement with the hypothesis of transient, less specific and weak interaction between viral IRES and bacterial ribosome proposed by Colussi and collaborators.

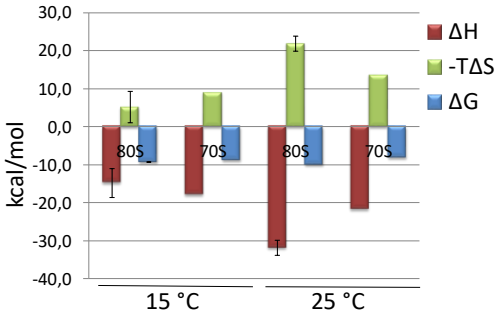

Figure 69: Comparison of IRES binding parameters to 70S or 80S ribosome.
Profiles of IRES binding to 80S and 70S, with ΔH, -TΔS and ΔG, are presented from experiments at 15 or 25 °C. For 70S, only one experiment for each temperature was performed**.** Detailed data are listed in **Table S3 of Annex 3**.

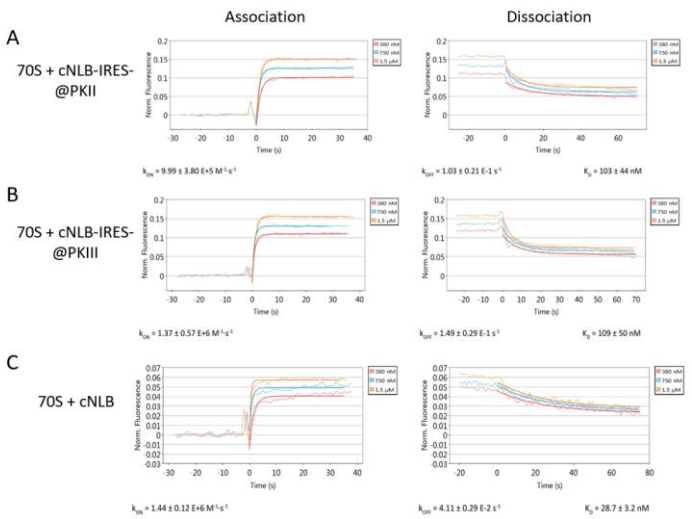

Figure 70: Non-specific binding of 70S on nucleic sequences at 25 °C.
70S binding to the cNLB-IRES was tested with different control constructions: hybrids with anti-PK, @PKII (A) and @PKIII (B), and the DNA nanolever without the IRES (C).

4. Problems of ribosome integrity and degradation

As mentioned in previous sections, limited ITC and switchSENSE experiments were performed. This was mostly due to problems with 80S integrity which was a serious obstacle for the IRES-ribosome interaction study. Gel analysis of 80S revealed smears or cleavage of rRNA (**Figure 71**), suggesting that ribosome is tainted either by denaturation or cleavage, that is to say global degradation. Interestingly, non-dissociated ribosome is less sensitive to degradation, compared to dissociated one (**Figure 71A**). More strikingly, dissociated but non separated ribosomes are not degraded, even after storage at 4 °C several days (**Figure 71B**). All the material of dissociation experiment was cleaned in case of RNase contamination and all solutions were carefully prepared and filtered. After all those changes and adaptations of the protocol (see part II.1.C), the full ribosome could be again purified in acceptable amounts and without degradation. Nevertheless, subunit separation still leads to degradation (**Figure 71C**). The most confusing part is that same materials and buffers are used for dissociation of 80S provided by RiboStruct and for *E. coli* 70S, and no such problems were observed. So, we hypothesized that RNAse could be present from the lysis stages and resist to RNAsin treatment. Investigations to produce again functional reassociated ribosomes are still ongoing in the laboratory.

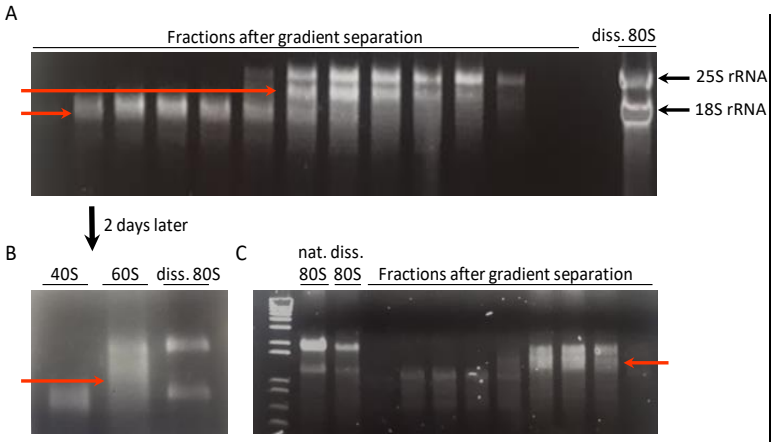

Figure 71: rRNA integrity evaluation.
18S and 25S rRNA (indicated by the black arrows) are checked on 1 % agarose gel. Dissociated ribosome (diss.80S) before and after gradients separation prepared following the original protocol are presented in (A). 40S and 60S fractions were pooled separately and concentrated, before being analyzed again 2 days later (B). The same evaluation of rRNA was done after 80S purification following the adapted protocol (C). Degradation features (other bands, smires, ...) are indicated by red arrows.

IV. Conclusions and perspectives

Our studies of the interaction between the ribosome and the intergenic IRES of the cricket paralysis virus CrPV were aimed at better characterizing this interaction by providing thermodynamic and kinetic data. In addition, our goal was also to use this well-characterized system as a proof of concept for the development of novel biophysical approaches.

By comparison with results derived from other approaches, different Kd were observed for the IRES interaction with 80S or 40S ribosomes from diverse methods. In case of gel shift assays, the obtained Kd is observed at non-equilibrium reaction and is thus less relevant. Then for FRET and swithchSENSE, we have some biais, with the immobilization of the IRES on a surface or the presence of fluorophore, which could influence the RNA whole conformation of molecules. Conformational differences could also be an explanation for such differences.

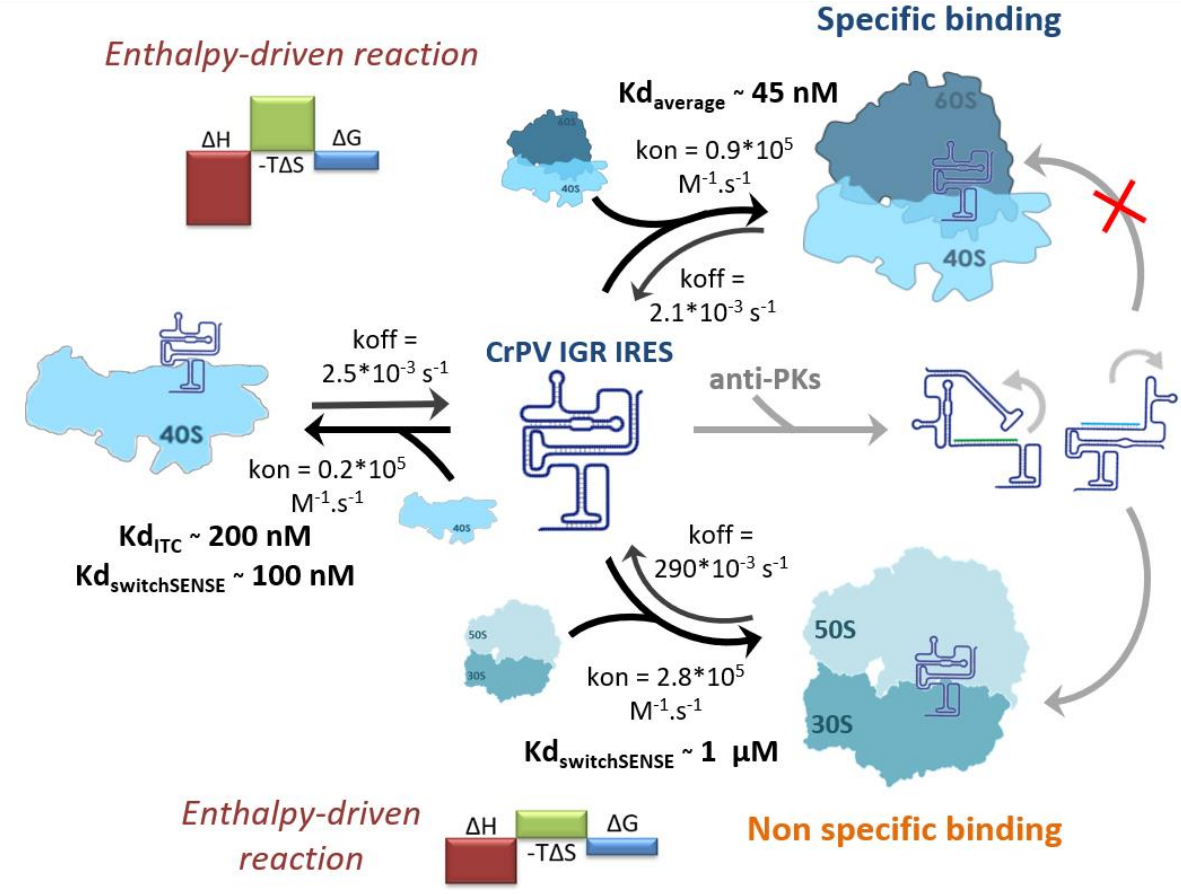

Figure 72: Graphical conclusion of the biophysical study of CrPV IGR IRES binding to ribosome.

Both ITC and switchSENSE experiments yield similar results and a complete profile of IRES binding with yeast or bacterial ribosomes (**Conclusion figure 72**). The CrPV IGR IRES binding is a highly enthalpy-driven reaction for both ribosomes. While the thermodynamic profiles are similar, affinities and rate constants are quite different, however. Our model suggests a better affinity of the IRES for the 80S compared to 40S, thanks to faster association and slower dissociation. In the case of bacterial ribosome, the affinity for the IRES is largely weaker due to very fast dissociation, and the lack of structural dependency for the binding suggests a non-specific interaction. Thus, the bacterial translation mediated by IGR IRES highlighted by Colussi and collaborators (Colussi et al., 2015) would be the result of a distributive binding of the ribosome. This supports the idea of a different mechanism compared to eukaryotes. This model should be confirmed by replicates and functionality test of the yeast ribosome.

In addition, to go further in the characterization of CrPV IGR IRES mechanism of action, it could be interesting to integrate the eEF2 factor essential for the transition to the elongation phase. Indeed, serial experiments with different combinations of IRES and eEF2 binding in switchSENSE or ITC could provide additional thermodynamic and kinetic information about eEF2-dependent translocation event.

In summary, the possibility to study huge complexes, including long-structured RNA and yeast ribosome, by ITC and especially with switchSENSE was confirmed (Schenckbecher et al., 2019). The switchSENSE analysis was a real technical challenge and led to a broadening of application fields of this technology and to new developments by Dynamic Biosensors. Our combinatorial approach to obtain kinetic and thermodynamic parameters for an interaction between RNA and ribosomes can be used as a proof of concept for studying other IRESes from human pathogenic viruses, as those of Dengue our Zika viruses (Song et al., 2019).

CHAPTER IV

GENERAL CONCLUSION

Chapter IV: General conclusion

Our original approach for studying ribosome interactions with some of its partners was quite challenging but we were able to overcome technical limitations to obtain thermodynamic and/or kinetic information.

ITC is a powerful tool to characterize simple systems of interactions. Our lab aims at extending the use of this approach to complex biological machineries, such as HIV-1 reverse transcriptase (Bec et al., 2013), and to extend the application field to the characterization of biological processes. Besides the characterization of processes in our studies was only possible because all reactions were always spontaneous, with negative ΔG.

Furthermore, methodological developments allow the use of ITC to kinetic data. Indeed, kinITC became very useful to complete thermodynamic information with a dynamic point of view of the studied interaction. Few experiments were reasonably exploitable but kinITC showed its efficiency for kinetics analysis from ITC data.

SwitchSENSE technology is also a promising tool for kinetic studies of various interactions between macromolecules, from RNA to proteins and macromolecular complexes, like polymerases or antibodies and now ribosomes. Moreover, it could become very useful in screening experiments. Indeed, ongoing methodological developments with our team could allow the coupling of switchSENSE with mass spectrometry to identify partners of interactions of RNA or proteins from a cell extract.

Finally, combination of thermodynamics, kinetics and structural studies intends to provide a complete profile of interactions. Their use showed their importance to clarify steps of mechanisms, such as the pathway of ribosome recruitment by the CrPV IGR IRES, or to complement structural data with the dissection of binding events, like for the binding of macrolides and PrAMPs to the ribosome. My projects also allow to elaborate or optimize methodologies in the lab to study the thermodynamics of interactions of complex biomolecular machines, as well as their dynamics and structures. It will be useful for further investigation on ribosome-targeting antibiotics, IRES- mediated initiation and more generally on translation in bacteria and eukaryotes.

ANNEXES

ANNEX 1

Book chapter "ITC Studies of Ribosome-Antibiotics Interactions" published in Methods in Molecular Biology, Microcalorimetry of Biological Molecules

Chapter 7

ITC Studies of Ribosome/Antibiotics Interactions

Emma Schenckbecher, Benoît Meyer, and Eric Ennifar

Abstract

The fight against multiresistant bacteria responsible for nosocomial diseases has recently been classified as an absolute priority by the World Health Organization. For some organisms, priority status has even been assessed as critical, as almost all currently available antibiotics are now inefficient against these "superbacteria." Ribosome is a major target of several antibiotics, and extensive biochemical and structural studies led to a better understanding of the mechanism of action of drugs targeting translation (Blair et al., Nat Rev Microbiol 13:42–51, 2015; Lin et al., Annu Rev Biochem 87:451–478, 2018; Wilson, Nat Rev Microbiol 12:35–48, 2014; Yonath, Annu Rev Biochem 74:649–79, 2005). However, our knowledge regarding thermodynamic data of compounds targeting the ribosome, which are yet essential for a complete understanding of translation inhibition mechanisms by drugs, is still very poor.

In this chapter we describe the use of ITC microcalorimetry to investigate the binding of bacterial ribosome to two antibiotics targeting the peptide tunnel: macrolides and proline-rich antimicrobial peptides (PrAMPs). This strategy yields reliable and artifact-free binding parameters for antibiotics and provides an original view on ribosome/antibiotics interactions.

Key words Ribosome, Antibiotics, Antimicrobial peptide, Macrolide, Competition, ITC

1 Introduction

The translation machinery and the ribosome have always been a target of choice for drug development. Ribosome interactions with antibiotics have been the focus of numerous studies, and several biochemical and structural works highlighted their inhibition mechanism [1, 2]. Several classes and generations of antibiotics have been developed to overcome the problem of multidrug-resistant bacteria [3, 4]. However, bacteria resistance is rapidly spreading, and the development of new antibiotics exploiting new inhibition mechanism dramatically dropped in the past 20 years. Consequently, there is a clear need of understanding more precisely how antibiotics affect the ribosome in order to elaborate new drugs and to escape bacterial resistance.

Thermodynamic data, when combined with already available biochemical and structural works, are extremely valuable for the

Eric Ennifar (ed.), *Microcalorimetry of Biological Molecules: Methods and Protocols*, Methods in Molecular Biology, vol. 1964, https://doi.org/10.1007/978-1-4939-9179-2_7,

development of new drugs, effective against multiresistant bacteria. Microcalorimetry (ITC) is the method of choice to provide a complete thermodynamic profile and affinity parameter of an interaction [5] and provide an original view on the mechanism of fixation of antibiotics. Yet, the study of antibiotics binding to the ribosome by ITC remains very challenging due to two main limiting steps: (1) the low signal amplitude that is observed in such interactions and (2) the very tight affinities of some compounds for the ribosome. The first issue is due to the low heat exchange (ΔH is close to zero) following antibiotic binding to the ribosome. In a classical ITC experiment, the signal amplitude can be improved by increasing concentrations of reagents in the cell and in the syringe. However, the concentration cannot be significantly increased in the case of the 70S ribosome which is already extremely concentrated in ITC experiments (~37.5 mg/mL for 15 μM 70S in the cell, which corresponds to 10.7 mg of ribosome per experiment). Regarding the second limiting step, the tight affinity of some antibiotics, such as macrolides, for the ribosome (K_d close to 1 nM or lower, $K_a \geq 10^9\ M^{-1}$) induces a c-value ($c = K_a \times M_{cell} \times n$, where n is the number of sites and M_{cell} the concentration of reagent in the cell) [6] which is out of range for ITC measurement [7] (Fig. 1). Because of the weak signal mentioned in the first limiting step, reduction of the M_{cell} concentration (which would reduce the c-value) cannot be envisaged in this situation. Consequently, a competition strategy has been considered [8, 9].

Macrolides are a historical class of antibiotics targeting the peptide exit tunnel (PET) of the 50S subunit of bacterial ribosome, with a very tight affinity (less than 10 nM) [10, 11]. Natural antimicrobial peptides (PrAMPS) also target the PET on the ribosome and were used as competitors in this study since they present a weaker affinity for the ribosome (above 10 nM) [12]. By combining classic and competition ITC experiments for macrolide antibiotics and antimicrobial peptides, we can establish the complete thermodynamic profile for several antibiotics (Fig. 2).

2 Materials

2.1 Instrument and Accessories

1. MicroCal PEAQ-ITC Software (Microcal-Malvern Panalytical, Malvern, UK).
2. MicroCal PEAQ-ITC Analysis Software for ITC data or equivalent software, such as AFFINImeter [13] (www.affinimeter.com, *see* **Note 1**).
3. NanoDrop ND-1000 Spectrophotometer (Thermo Fisher Scientific, Waltham, MA, USA) or equivalent.
4. Refrigerated centrifuge equipped with a rotor adapted for 15 mL centrifuge tubes.

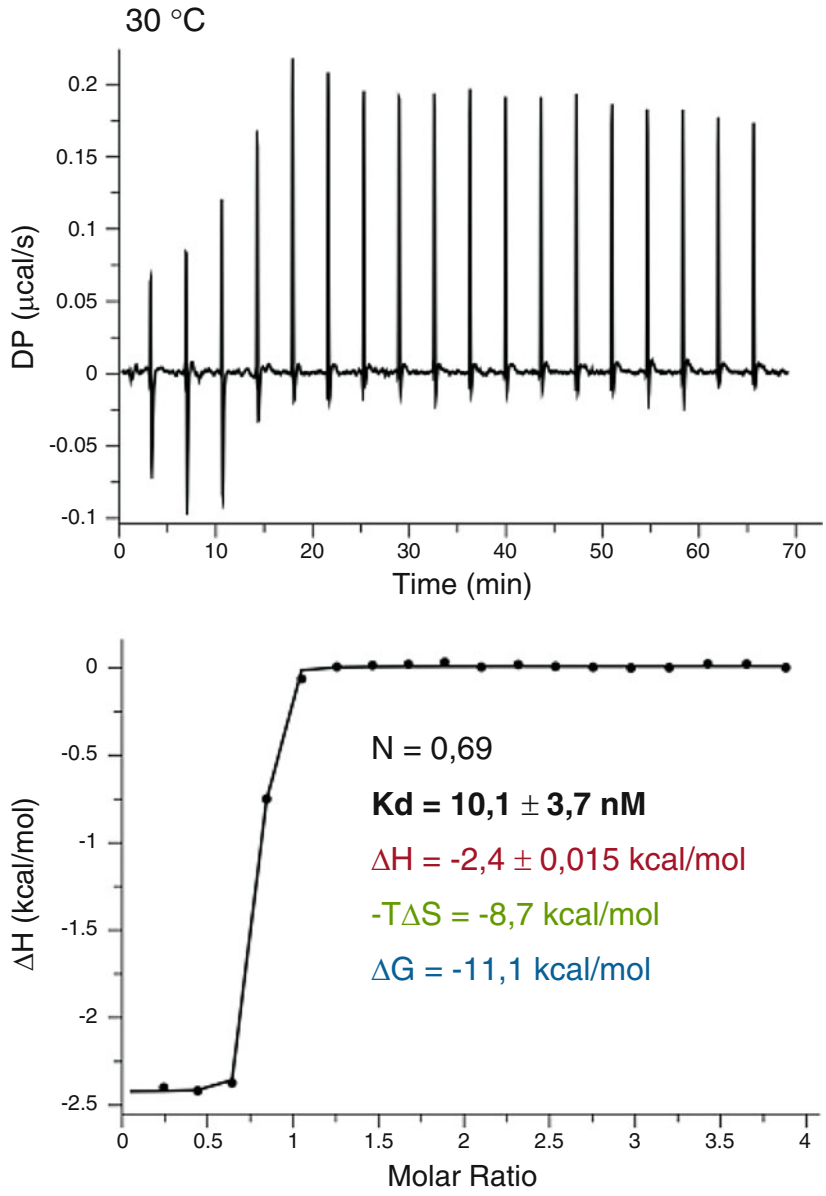

Fig. 1 Example of direct titration of 70S ribosome with azithromycin macrolide antibiotic at 30 °C. 2 µL aliquots of azithromycin 300 µM were injected in 70S ribosome (15 µM). K_d cannot be accurately determined from this experiment due to the high *c*-value. In addition, ΔH is also likely entailed with errors since the signal amplitude is low compared to the noise level (mostly due here to ribosome dilution). It is however clear from this experiment that the macrolide binding is mostly entropy-driven

5. High-precision balance.
6. Glass Hamilton loading syringes for PEAQ-ITC (Hamilton Company, Reno, NV, USA).
7. 2% Hellmanex™ detergent solution (Hellma Analytics, Müllheim, Germany) or equivalent.

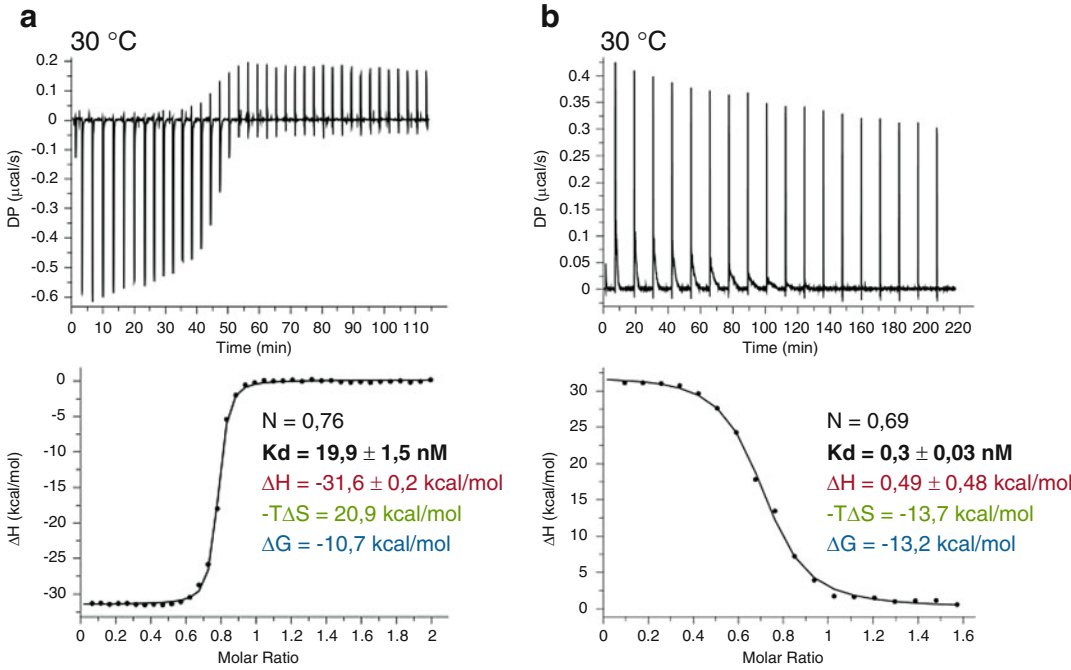

Fig. 2 Example of titration of 70S ribosome with azithromycin macrolide in a competition ITC experiment at 30 °C. (**a**) Binding of the peptide competitor to the ribosome (38 injections of 1 µL pyrrhocoricin PrAMP at 200 µM; 20 µM 70S ribosome in the cell). Binding is highly exothermic (enthalpy-driven) and generates a good signal. (**b**) The displacement was done by 18 injections of 2 µL aliquots of azithromycin 135 µM into the 70S/pyrrhocoricin complex (16.6 µM after the dilution due to the previous experiment)

8. Ultrapure and RNAse-free water.
9. Methanol, anhydrous, 99.8%.

2.2 Ribosome Preparation

1. 70S *E. coli* ribosome (MRE600 strain), flash-frozen in liquid nitrogen and stored at −80 °C in 20 mM Tris–HCl pH 7.5; 10 mM $MgCl_2$; 50 mM NH_4Cl; 0.1 mM EDTA; 6 mM β-mercaptoethanol.
2. 1× ITC buffer 50 mM MOPS pH 7.5; 7 mM $MgCl_2$; 30 M KCl; 70 mM NH_4Cl; 1 mM DTT; 5% glycerol.
3. Amicon Ultra-4 centrifugal filter unit 100,000 MWCO (Millipore, Billerica, MA, USA).

2.3 Antibiotic and Peptide Preparation

1. Macrolide antibiotic (azithromycin), powder. Stored at −20 °C.
2. Peptide PrAMP (pyrrhocoricin, sequence VDKGSYLPRPTPPRPIYNRN), powder. Stored at 4 °C. Used as a weak competitor for macrolide.
3. 1× ITC buffer 50 mM MOPS pH 7.5; 7 mM $MgCl_2$; 30 M KCl; 70 mM NH_4Cl; 1 mM DTT; 5% glycerol.

3 Methods

3.1 Ribosome and Antibiotic/Peptide Preparation for ITC Experiment

1. 70S ribosome is unfrozen slowly on ice and dialyzed against 1× ITC buffer using an Amicon Ultra-4 concentrator by 6 successive centrifugations of 40 min at 7500 × *g* at 4°C.
2. After the last dialysis, the 70S ribosome is concentrated until a maximum volume of 500 μL (lower volumes can lead to 70S aggregates), and the sample is removed from the Amicon.
3. The Amicon membrane is washed with 1× ITC buffer to recover as much as possible of the 70S sample.
4. Concentration of 70S is obtained at 260 nm using a NanoDrop spectrophotometer. Three 20th dilutions of the stock solution are performed to precisely determine the 70S concentration. 1 UA(260nm) = 24 nM of 70S.
5. Concentrated stocks of antibiotics or peptides (between 0.5 and 5 mM) are prepared in 1× ITC buffer and stored at −20 °C or 4 °C.

3.2 Designing the ITC Experiment

3.2.1 Experimental Considerations

Usually, concentration of the sample cell ranges from 5 to 100 μM. The ligand in the syringe is between 10 and 20 times more concentrated than in the sample cell (and even higher in the case of low *c*-value experiments [14]). These conditions will ensure that the sample cell becomes saturated by the end of the titration experiment. The instrument's theoretical operating range is 2–80 °C, but most experiments on biological samples are done between 5 and 37 °C. However, most interactions are characterized by a temperature dependence of the ΔH due to the heat capacity change of the event: $\Delta C_p = (\delta \Delta H / \delta T)$ (*see* **Note 2**). In the case of ribosome/antibiotics interaction, it is advisable to work at low (15 °C) or high temperature (30–35 °C) to have a significant signal.

A critical point to obtain high-quality ITC results is that both reagents in the syringe and in the cell must be rigorously in the same buffer. Buffer mismatch will generate noise and might complicate or screw up the experiment (*see* **Note 3**).

3.2.2 Classic ITC Experiment Parameters

The syringe can inject a total of ~40 μL of ligand, and the cell volume is ~200 μL in the MicroCal PEAQ-ITC instrument. Typical injections are between 0.5 and 2 μL, depending on the characteristics of the interaction and of the experiment (affinity, enthalpy, sample concentration). Volume for the first injection is set at 0.4 μL; this first injection is generally discarded during analysis (*see* **Note 4**). Duration of injections should be set in order to get an injection speed of 0.5 μL/s. The time between injections is set at 150 s per default. If the return to the baseline is slow, which is an indicator of slow kinetics, it should be increased (up to 250–300 s,

or even longer) [13, 15]. The stirring speed is set at 750 rpm per default (*see* **Note 5**). The reference power can be set at 5 μcal/s.

In the present example, ribosome concentrations range from 10 to 20 μM. Solutions containing peptides and antibiotics are 10–20 times more concentrated than ribosome.

3.2.3 Displacement ITC Experiment Parameters

The first experiment is a classic ITC experiment (*see* previous subsection), but the sample cell should be set at the higher range of ribosome concentration to anticipate dilution following injection of the weak ligand. In our case, the ribosome concentration is 17–20 μM. For the second experiment, the antibiotic in the syringe is 10–15 times more concentrated than the ribosome, considering ribosome concentration at the end of the first ITC. The stirring speed and the reference power are unchanged. In a displacement experiment, the return to the baseline is usually very slow and depends on the K_{off} of the competitor. Consequently, the time between each injection is set between 500 and 800 s (even longer time might be necessary in some situations).

3.3 Performing the ITC Experiment

1. In the MicroCal PEAQ-ITC Software, select the 19 injections mode.
2. Before starting an experiment, clean the cell and the syringe extensively using 2% Hellmanex detergent and ultrapure water using the program "Wash" for Cell and Syringe and the "Clean" button to run it.
3. The temperature is set at 30 °C; samples are preincubated at the same temperature.
4. In the acquisition software, enter cell and syringe concentrations, set the temperature experiment (30 °C), the reference power (5 μcal/s), the initial delay (60 s), the stirring speed (750 rpm), the number and volume of injections, and finally the time between injections (250 s).
5. 70 μL of ligand solution (antibiotics or peptides) is prepared in a 200 μL microcentrifuge tube, and the ligand is loaded into the syringe automatically by pressing "Load." If a bubble is present in the syringe, click on "Plunger down" and "Load" again.
6. Fill the cell with 285 μL of ribosomes with the dedicated Hamilton syringe, very gently in order to avoid formation of bubbles in the cell. Remove the excess of sample at the top of the cell.
7. Place the pipette into in the cell.
8. Click "Start"; a window appears to select the file location and the title of your experiment.
9. The instrument starts equilibration for about 10 min.

10. In a classical ITC experiment, clean the instrument (*see* Subheading 3.3, **step 2**) at the end of the experiment, and go to Subheading 3.4.
11. For a displacement experiment, the ribosome/competitor complex is kept in the cell, and only the syringe is cleaned.
12. The antibiotic with a tight affinity (macrolide in this example) is loaded in the syringe.
13. The ribosome concentration is corrected according to the volume of peptide injected during the first experiment. The exact concentration can be found in the first ITC file: open this file with the PEAQ-ITC Analysis Software; in the tab "Presentation," sub-tab "Injection table," all details for each injection with number, volume, and concentration of cell can be found.
14. The time between injections is set at 600 s.
15. Start the experiment by clicking on "Start" and enter the name of the experiment.
16. At the end of the experiment, clean extensively the syringe and the cell (*see* Subheading 3.3, **step 2**).

3.4 ITC Data Analysis

ITC data analysis using the MicroCal PEAQ-ITC Analysis Software will be described here. When the experiment is finished, either click on "Analyse" button or start the software independently and open the file. The program automatically displays the raw ITC plot window and the integrated heat in the "Overview" tab of the menu Tables.

1. The program can automatically analyze whether binding is observed or not; if an interaction is detected, a titration curve based on the raw data baseline determined by the software is generated.
2. The baseline can be adjusted in the "Adjust baseline" tab and by modifying the boundaries of the integrated peak area and manually displacing baseline points (*see* **Note 6**).
3. All experiment features and thermodynamic parameters (with estimated errors) N, ΔH, $-T\Delta S$, ΔG, and K_d are presented on the right of the window.
4. In the "Adjust fit" tab, concentrations of the cell and the syringe can also be adjusted, if needed (might be dangerous! Know what you're doing...).
5. When data processing is done, a figure can be obtained in the "Presentation" tab, "Final figure" sub-tab, showing the raw data and the titration curve. Thermodynamic data can be inserted on the plot by checking the box "Show results."
6. Baseline correction can be obtained on the figure by selecting "Substract Baseline" and "Substract offset."

7. Several graphic features (color of point and line, line thickness, etc.) can also be changed in "Options."
8. Finally, the figure can be exported in different formats (.bmp, .jpg, .gif, .png, .tif), and the processed ITC file is saved as APJ file by clicking on the disk icon, next to the menu tab.

3.5 Fitting Models

A limited number of models are available for fitting in PEAQ-Analysis (*see* **Note 7**). For ribosome/macrolides or peptides interaction, two models are used: "one set of sites" and the competition model.

3.5.1 One Set of Sites Model

In the "Overview" tab, a pull-down menu for fitting model is available with a list of available models. The model "one set of sites" is the default model, and it is appropriate for ribosome binding to macrolides and PrAMPs (Figs. 1 and 2a).

3.5.2 Competition-Binding Model

1. The competitive model is used with the "one set of sites" fit for a displacement experiment.
2. If the competition-binding model is not activated, parameters provided correspond to those for the displacement experiment plus the binding of the second ligand, antibiotics (macrolides in our example).
3. The competitive model is available in the "Adjust Fit" tab, by selecting "Use Competitive Model."
4. For the competition-binding model, ΔH and K_d of the interaction of the weak competitor with the ribosome must be filled in. The stoichiometry is set at 1 per default. "Strong" is automatically selected for the Unknown Binder.
5. Select the "Fit" button to obtain thermodynamic parameters taking into account the displacement experiment. Data corresponding to the second binding event are obtained (in our case of macrolides binding) (Fig. 2b).

4 Notes

1. AFFINImeter (www.affinimeter.com) provides kinetic data using the *kinITC* strategy in addition to thermodynamic parameters [13, 15].
2. Care should be taken in situations where no heat signal can be detected. Indeed, the lack of heat exchanged might be due to a condition where ΔH is close to zero (athermal reaction) but binding still occurs. In most interactions, the heat capacity change $\Delta C_p = \partial \Delta H / \partial T$ is negative: ΔH increases when the temperature increases and decreases at lower temperature.

3. pH difference between the ligand solution and the sample solution can generate buffer mismatch, as well as any difference in salt or glycerol concentration, buffer concentration, or additives. To minimize these differences, partners should be prepared in identical buffers.
4. This first injection might be entailed with errors due to mechanical backlash of the screw in the pipette injector, looseness in the Teflon tip in the syringe, and dilution during the equilibration step before beginning the experiment.
5. The stirring speed is set at 750 rpm using syringe with a twisted paddle (vs 1000 rpm with syringe from the previous generation). Reduction of the stirring speed improves baseline stability but might introduce artifacts due to insufficient mixing.
6. It is important to first define the area of the integrated peak for all peaks and only after displace the baseline points. Indeed, as soon as the boundaries of peaks are moved, all previous baseline modifications are lost.
7. More models, including a model builder, are available in the AFFINImeter software (www.affinimeter.com).

Acknowledgments

The authors would like to thank Philippe Dumas for his constant support, Stefano Marzi and Angelita Simonetti (CNRS Strasbourg), Daniel Wilson (University of Hamburg), and Anna Maria Giuliodori (University of Camerino) for fruitful discussions.

References

1. Lin J, Zhou D, Steitz TA, Polikanov YS, Gagnon MG (2018) Ribosome-targeting antibiotics: modes of action, mechanisms of resistance, and implications for drug design. Annu Rev Biochem 87:451–478
2. Yonath A (2005) Antibiotics targeting ribosomes: resistance, selectivity, synergism and cellular regulation. Annu Rev Biochem 74:649–679
3. Blair JM, Webber MA, Baylay AJ, Ogbolu DO, Piddock LJ (2015) Molecular mechanisms of antibiotic resistance. Nat Rev Microbiol 13:42–51
4. Wilson DN (2014) Ribosome-targeting antibiotics and mechanisms of bacterial resistance. Nat Rev Microbiol 12:35–48
5. Klebe G (2015) Applying thermodynamic profiling in lead finding and optimization. Nat Rev Drug Discov 14:95–110
6. Wiseman T, Williston S, Brandts JF, Lin LN (1989) Rapid measurement of binding constants and heats of binding using a new titration calorimeter. Anal Biochem 179:131–137
7. Velazquez Campoy A, Freire E (2005) ITC in the post-genomic era...? Priceless. Biophys Chem 115:115–124
8. Krainer G, Keller S (2015) Single-experiment displacement assay for quantifying high-affinity binding by isothermal titration calorimetry. Methods 76:116–123
9. Velazquez-Campoy A, Freire E (2006) Isothermal titration calorimetry to determine association constants for high-affinity ligands. Nat Protoc 1:186–191
10. Dinos GP (2017) The macrolide antibiotic renaissance. Br J Pharmacol 174:2967–2983
11. Svetlov MS, Vazquez-Laslop N, Mankin AS (2017) Kinetics of drug-ribosome interactions

defines the cidality of macrolide antibiotics. Proc Natl Acad Sci U S A 114:13673–13678

12. Graf M, Mardirossian M, Nguyen F, Seefeldt AC, Guichard G, Scocchi M, Innis CA, Wilson DN (2017) Proline-rich antimicrobial peptides targeting protein synthesis. Nat Prod Rep 34:702–711
13. Dumas P, Ennifar E, Da Veiga C, Bec G, Palau W, Di Primo C, Pineiro A, Sabin J, Munoz E, Rial J (2016) Extending ITC to Kinetics with kinITC. Methods Enzymol 567:157–180
14. Tellinghuisen J (2016) Analysis of multitemperature isothermal titration calorimetry data at very low c: Global beats van't Hoff. Anal Biochem 513:43–46
15. Burnouf D, Ennifar E, Guedich S, Puffer B, Hoffmann G, Bec G, Disdier F, Baltzinger M, Dumas P (2012) kinITC: a new method for obtaining joint thermodynamic and kinetic data by isothermal titration calorimetry. J Am Chem Soc 134:559–565

ANNEX 2

Book chapter "Biophysical studies of the 80S ribosome binding to CrPV IRES" in press for Methods in Molecular Biology

Biophysical studies of the 80S ribosome binding to CrPV IRES

Emma Schenckbecher, Guillaume Bec, Benoit Meyer and Eric Ennifar

Corresponding author: e.ennifar@unistra.fr

Université de Strasbourg, CNRS

Institut de Biologie Moléculaire et Cellulaire

15 Rue René Descartes, F-67000 Strasbourg, France

Running head: 80S ribosome/IRES interactions monitored using the switchSENSE technology

Keywords: Kinetics; switchSENSE; Ribosome; RNA; Biophysics

Summary

Translation initiation, in both eukaryotes and bacteria, requires essential elements such as mRNA, ribosome, initiator tRNA and a set of initiation factors. For each domain of life, canonical mechanisms and signals are observed to initiate protein synthesis. However, other initiation mechanism can be used, especially in viral mRNAs. Some viruses hijack cellular machinery to translate some of their mRNAs through a non-canonical initiation pathway using Internal Ribosome Entry Site (IRES), a highly structured RNAs which can directly recruit the ribosome with a restricted set of initiation factors, and in some cases even without cap and initiator tRNA. In this chapter we describe the use of biosensors relying on electroswitchable nanolevers using the switchSENSE® technology, to investigate kinetics of the intergenic (IGR) IRES of the cricket paralysis virus (CrPV) binding to 80S yeast ribosome. This study provides a proof of concept for the application of this method on large complexes.

1. Introduction

Due to its key role in the cell, translation machinery has been the subject of intense studies, especially since access to high-resolution structures has been facilitated by X-ray crystallography and electron cryomicroscopy studies. This includes studies focusing on the IRES-mediated initiation such as found in viral RNAs ***(1-3)***. A plethora of studies investigated interactions between various viral IRES (Internal Ribosomal Entry Site) and the ribosome ***(4,5)***, especially through the work on the intergenic (IGR) IRES of the cricket paralysis virus (CrPV) which is now well-characterized. Numerous approaches are available to characterize interactions between such macromolecular complexes, whether from a kinetic ***(6,7)***, structural (***8,9***) or biochemical point of view ***(10,11)***. Among all new emerging techniques, switchSENSE® technology appears as very innovative in the solid-support immobilization field ***(12-14)***. By measuring analytes adsorption on a layer of actuated surface-bound fluorescent probe, this combination of biophysical approaches can be used for several applications, as binding kinetics and affinity, protein diameter, conformational change, or even nuclease and polymerase activity.

The originality of the switchSENSE® technology lies in the DNA strand bearing a fluorescent dye at one extremity, attached on its opposite end to a gold-quenching surface. The complementary strand could be used alone or chemically coupled to an interaction partner (a protein). Hybridization of the DNA strands generates a rigid negatively-charged electro-switchable biosensor, also referred as nanolever (Fig. 1). Two principal measurement modes are accessible: 1) a static mode ("proximity sensing"), where analytes binding is measured following a change in fluorescence signal, 2) a dynamic mode ("switching mode") where binding is detected through the change of the oscillation rate of the probe actuated by an AC electric field. Thanks to DNA plasticity and to many biochemical tools, a wide variety of nanolevers could be adapted to the biological context of the experiment: size and type of DNA may vary ***(15)***, RNA motifs are usable ***(16)***, type of modified extremity (protein, cofactor, NTA, biotin...) ***(12)***, type of dye used (Cy3, Cy5 ...).

In this study we describe an original use of this technology to study kinetics binding of CrPV IGR IRES with the 80S yeast ribosome. We showed that this method, originally dedicated to smaller complexes, is also well-adapted to the study of big macromolecular complexes.

2. Materials

2.1 Instruments and accessories

1. DRX 2400 or DRX² instrument (Dynamic Biosensors).
2. Nanodrop ND-1000 spectrophotometer (Thermo Fisher) or equivalent
3. switchCONTROL, switchBUILD and switchANALYSER softwares (Dynamic Biosensors)
4. Biochip for large complexes studies (MPC-96-2-Y1-S, Dynamic Biosensors) bearing a 96-mer DNA probe (nanolever) attached at the 3' end.
5. CrPV IGR IRES – cNL-B96 RNA sequence, complementary to the 96-mer DNA probe onto the chip (*see* **Note 1**) ; conserved in miliQ H_2O at 4 °C.
6. Passivation and regeneration solutions SOL-PAS-1-5 and SOL-REG-12-1 (Dynamic Biosensors).
7. 10X Auxiliary buffer (100 mM Sodium Phosphate pH 7.0, 400 mM NaCl, 0.5% tween 20, 0.5 mM EDTA).
8. switchSENSE® buffer : 20 m M Na Cacodylate pH 7.0 ; 7 mM MgCl2, 100 mM KCl ; 0.05 % Tween 20.
9. Ultra-pure RNase-free water and ethanol absolute 99.9%.
10. 1.5 and 10 mL autosampler vials with septa caps and insets.

2.2 Ribosome preparation

1. Ribosome buffer: 50 mM Na Cacodylate pH 7.0 ; 7 mM MgCl2 ; 30 mM KCl ; 70 mM NH4Cl ; 1 mM DTT ; 5 % glycerol.
2. 80S *S. cerevisiae* ribosome purified from JD1370 strain following a protocol adapted from Ben Shem et al. ***(17)*** ; aliquots, flash-frozen in liquid nitrogen and stored at -80 °C or freshly prepared, in Ribosome buffer.
3. switchSENSE® buffer : 20 m M Na Cacodylate pH 7.0 ; 7 mM MgCl2, 100 mM KCl ; 0.05 % Tween 20.
4. Amicon ultra-15 centrifugal filter, mwco 100 kD (Merckmillipore)

3. Methods

3.1 Ribosome preparation

1. After purification and dialysis of 80S against switchSENSE® buffer with Amicon concentrator, 80S concentration has been obtained, at 260 nm using a NanoDrop spectrophotometer. Three independent twentieth dilutions of the stock solution should be performed for a precise concentration (ε_{260} = 50 000 000 $M^{-1}.cm^{-1}$).
2. Fresh or frozen aliquots are used at a minimal concentration of 2 µM in 500 µL.

3.2 Designing the switchSENSE® experiment

3.2.1 Experimental considerations

DRX 2400 instrument was not originally meant for analysis of complexes as large as ribosomes. Here, the size of the DNA probe attached to the chip has been doubled, compared to standard conditions, in order to deal with the large size of 80S ribosome. Furthermore, measurements are done in "proximity sensing mode" and not in "switching mode" (*see* **Note 2**) in order to avoid steric constrains. Unexpectedly, we observed that binding of the ribosome to the IRES RNA lead to an increase of fluorescence.

3.2.2 Experimental workflow building

1. switchBUILD software is used to design the experiment by the creation of successive programming blocks.
2. In the first block, biochip (MPC-96-2-Y1-S), channel number, buffer type (X140) and Auxiliary buffer (P40) are chosen.
3. A "Passivation" step is added as a second block (*see* **Note 3**).
4. The third block is a "Kinetics" step, where all the parameters of the experiment are defined in the "Properties" window : immobilization and measurement mode, nature of ligand (CrPV IGR IRES – cNL-B96 oligonucleotide) and its concentration (*see* **Note 4**), nature of the analyte (yeast ribosomes), predicted interaction kinetic data (K_d, k_{on} and k_{off}), analyte concentration, association/dissociation time and flow rate (*see* **Note 5**), temperature, electrode number (one of the six available in each channel). Optional features need to be defined for association and dissociation. Check the regeneration step after each concentration for the association part, and chose the

dissociation event only at the last concentration (*see* **Note 6**). Finally it is better to add a blank-run block (for baseline correction), where the analyte is replaced with 1X Reaction buffer alone.

5. A last "Standby" block is used at the end of the experiment (*see* **Note 7**).

6. The switchBUILD program is saved the file of interest.

3.3 Performing the switchSENSE experiment

1. In the "Kinetics" block of the switchBUILD program, the "Autosampler" window is opened to see the concentrations, volumes and dispositions of vials in the device (*see* **Note 5**). In our example, 3 concentrations have been tested (100, 33 and 11 nM in 300 µL) at a flow of 50 µL.min^{-1} after an hybridization with a solution of CrPV IGR IRES – cNL-B96 RNA at 380 nM in 120 µL.

2. The switchBUILD program is loaded in the switchCONTROL software.

3. The vials filled with all solutions (water, passivation and regeneration solutions, auxiliary buffer, ligand and analyte) are disposed in the autosampler part of the device. Start the experiment.

3.4 switchSENSE® data analysis

1. The switchANALYSIS software is opened and datasets generated during the "Kinetics" step are loaded.

2. In the "Settings" window, all association and dissociation events are listed as successive blocks (one block corresponding to one concentration of 80S). If blanks have been done, drag association blank in each association blocks, and dissociation block in dissociation block.

3. To be treated, each block of association is dragged in the "Association" box and the dissociation block is dragged in the "Dissociation" box. Time windows are generated automatically for each curve of association and dissociation.

4. Results appeared in the "Results" window. Graphics and kinetic data are then available, in particular "Individual", "Average" and "Global" analysis.

5. Finally, a publication-quality image could be copied in the clipboard (Fig. 2). Raw datasets could also be exported in a format file (ASCII, Excel…) compatible with other software tools.

4. Notes

1. CrPV IGR IRES – cNLB96 oligonucleotide RNA sequence (CAACAAATATTAATACGACTCACTATAGCAAAAAUGUGAUCUUGCUUGUAAAU ACAAUUUUGAGAGGUUAAUAAAUUACAAGUAGUGCUAUUUUUGUAUUUAGGU UAGCUAUUUAGCUUUACGUUCCAGGAUGCCUAGUGGCAGCCCCACAAUAUCCA GGAAGCCCUCUCUGCGGUUUUUCAGAUUAGGUAGUCGAAAAACCUAAGAAAUU UACCUGCUACAUUUCAAGAUACCGAAGACGCCAAAAACAUCAGGAACUACAGG GUGCCCUACUUGCUCUCGGAGGUACUGUAACUAAUCAGCGUUCGAUGCUUCCG ACUAAUCAGCCAUAUCAGCUUACGACUA) is a T7 transcript, obtained from PCR products, and purified by phenol-chloroform extraction followed by a dialysis in Amicon concentrator against miliQ H_2O.

2. In the proximity sensing mode, a constant voltage (-0.1V in our conditions) is applied on the chip, maintaining the nanolever at a constant angle in the 1X Reaction Buffer. Any event affecting this angle and/or the distance of the fluorophore with the quenching surface of the biochip (protein binding, polymerization, dissociation) could lead to a signal interpretable for the experiment.

3. This automatized standard procedure (using a commercially available kit solution) is used to avoid any unspecific binding of analytes on the biosurface.

4. The time required for hybridization of the complementary nanolever on the DNA anchor on the chip is directly correlated to its concentration; this can be adjusted depending on the hybridization quality.

5. Association and dissociation time, as well as flow rate, depend on the predicted kinetic values given in the switchBUILD program. Consequently, volumes and concentrations of the analyte are also directly correlated to the considered kinetic parameters.

6. It is possible to insert a dissociation step after association for each concentration, leading to a consequent increase of the experiment duration.

7. This automatized standard procedure removes analytes and ligands from the surface and defines conditions suitable for chip storage.

Acknowledgments

Special thanks to Claire Batisse, who provides us the yeast strain for 80S purification. This strain was generously given by Yusupov lab, which was elaborated in the first place by Dinman lab. The authors would like to thank dynamic Biosensor for the encouraging collaboration. Finally, thank you to Philippe Dumas for his constant support, Yaser Hashem, Stefano Marzi and Angelita Simonetti for fruitful discussion.

Figures

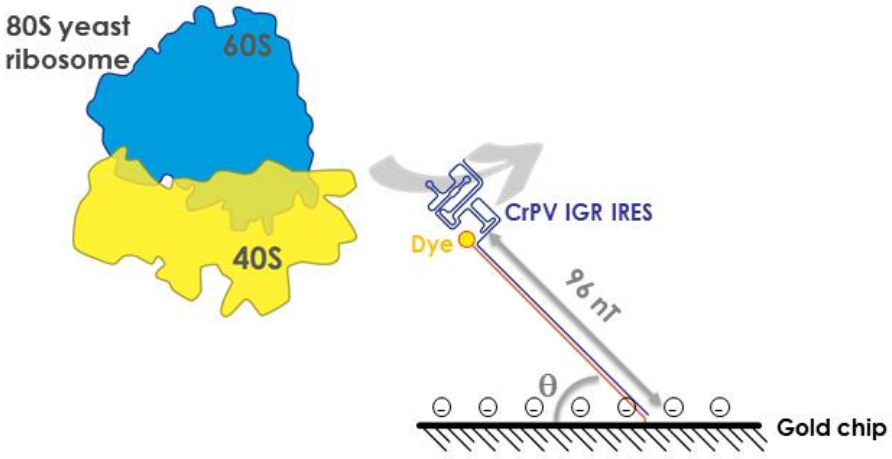

Fig. 1: Principle of switchSENSE® technology applied to the CrPV IGR IRES – ribosome system of interaction.

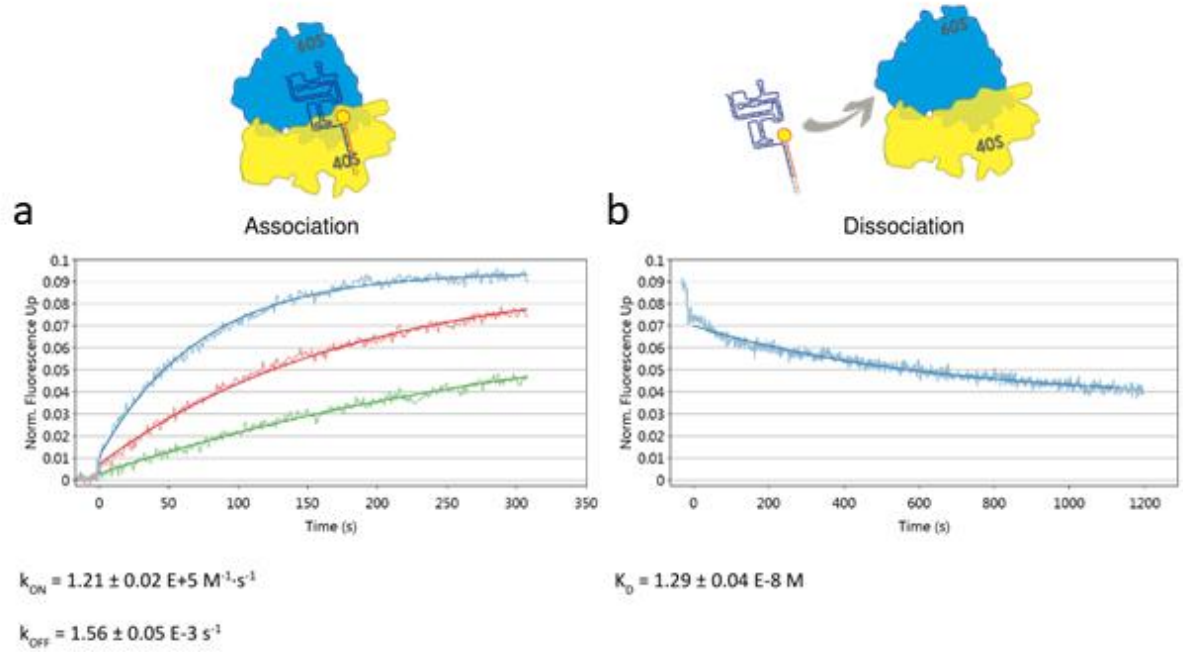

Fig. 2: CrPV IGR IRES binding kinetics on 80S yeast ribosome at 25 °C. Curves of association (a), for 3 concentrations of 80S (11, 33 and 100 nM), and dissociation (b), only for the higher concentration, presents the normalized fluorescence up as a function of time.

References

1. Balvay, L., Soto Rifo, R., Ricci, E.P., Decimo, D. & Ohlmann, T. Structural and functional diversity of viral IRESes. *Biochim Biophys Acta* **1789**, 542-57 (2009).
2. Kieft, J.S. Viral IRES RNA structures and ribosome interactions. *Trends Biochem Sci* **33**, 274-83 (2008).
3. Thompson, S.R. Tricks an IRES uses to enslave ribosomes. *Trends Microbiol* **20**, 558-66 (2012).
4. Filbin, M.E. & Kieft, J.S. Toward a structural understanding of IRES RNA function. *Curr Opin Struct Biol* **19**, 267-76 (2009).
5. Johnson, A.G., Grosely, R., Petrov, A.N. & Puglisi, J.D. Dynamics of IRES-mediated translation. *Philos Trans R Soc Lond B Biol Sci* **372**(2017).
6. Bugaud, O. et al. Kinetics of CrPV and HCV IRES-mediated eukaryotic translation using single-molecule fluorescence microscopy. *RNA* **23**, 1626-1635 (2017).
7. Petrov, A., Grosely, R., Chen, J., O'Leary, S.E. & Puglisi, J.D. Multiple Parallel Pathways of Translation Initiation on the CrPV IRES. *Mol Cell* **62**, 92-103 (2016).
8. Muhs, M. et al. Cryo-EM of ribosomal 80S complexes with termination factors reveals the translocated cricket paralysis virus IRES. *Mol Cell* **57**, 422-32 (2015).
9. Murray, J. et al. Structural characterization of ribosome recruitment and translocation by type IV IRES. *Elife* **5**(2016).
10. Kerr, C.H., Ma, Z.W., Jang, C.J., Thompson, S.R. & Jan, E. Molecular analysis of the factorless internal ribosome entry site in Cricket Paralysis virus infection. *Sci Rep* **6**, 37319 (2016).
11. Pestova, T.V., Lomakin, I.B. & Hellen, C.U. Position of the CrPV IRES on the 40S subunit and factor dependence of IRES/80S ribosome assembly. *EMBO Rep* **5**, 906-13 (2004).
12. Knezevic, J. et al. Quantitation of affinity, avidity, and binding kinetics of protein analytes with a dynamically switchable biosurface. *J Am Chem Soc* **134**, 15225-8 (2012).
13. Langer, A. et al. Protein analysis by time-resolved measurements with an electro-switchable DNA chip. *Nat Commun* **4**, 2099 (2013).
14. Rant, U. et al. Detection and size analysis of proteins with switchable DNA layers. *Nano Lett* **9**, 1290-5 (2009).
15. Kroener, F., Heerwig, A., Kaiser, W., Mertig, M. & Rant, U. Electrical Actuation of a DNA Origami Nanolever on an Electrode. *J Am Chem Soc* **139**, 16510-16513 (2017).
16. Clery, A., Sohier, T.J.M., Welte, T., Langer, A. & Allain, F.H.T. switchSENSE: A new technology to study protein-RNA interactions. *Methods* **118-119**, 137-145 (2017).
17. Ben-Shem, A. et al. The structure of the eukaryotic ribosome at 3.0 A resolution. *Science* **334**, 1524-9 (2011).

ANNEX 3

Supplementary figures

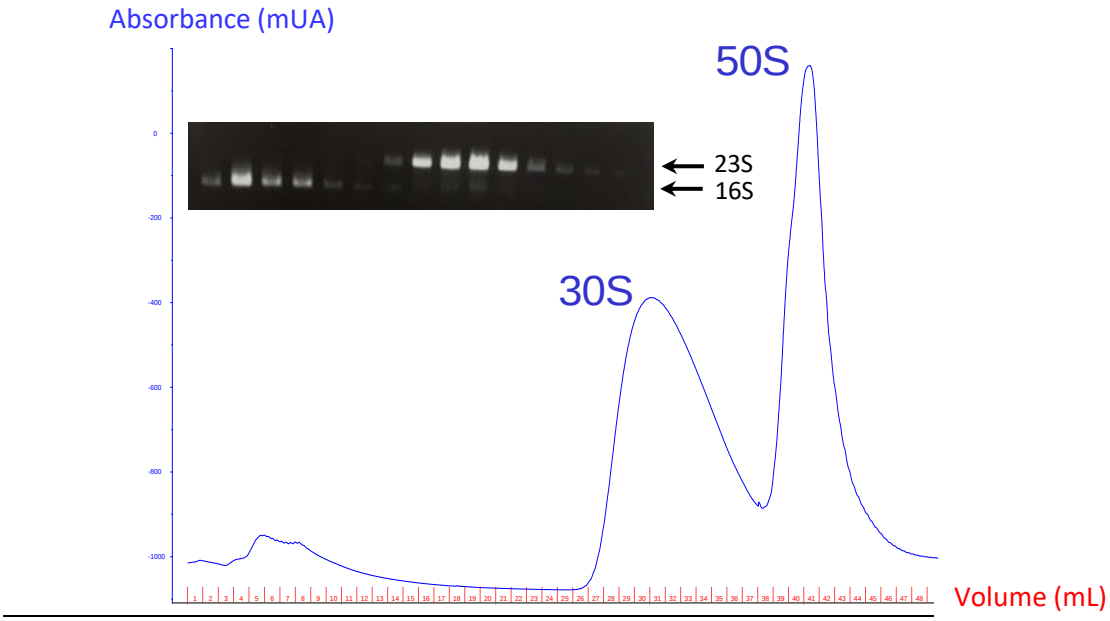

Figure S1: Dissociation of bacterial ribosomal subunits 30S and 50S from 70S ribosome.
After decreasing the $MgCl_2$ concentration using dialysis, the dissociated 70S is separated on a 10 % - 30 % sucrose gradient. Ribosomal subunits are then collected from the top using a Gradient Fractionator (Auto Densi-Flow Labconco) connected to an AKTA FPLC system (GE Healthcare). Subunits are detected thanks to absorbance (blue curve). Purity of fractions is assessed by visualization of 16S rRNA and 23S rRNA (dark arrows) on 1 % agarose gel, 0.5 µg.mL^{-1} EtBr.

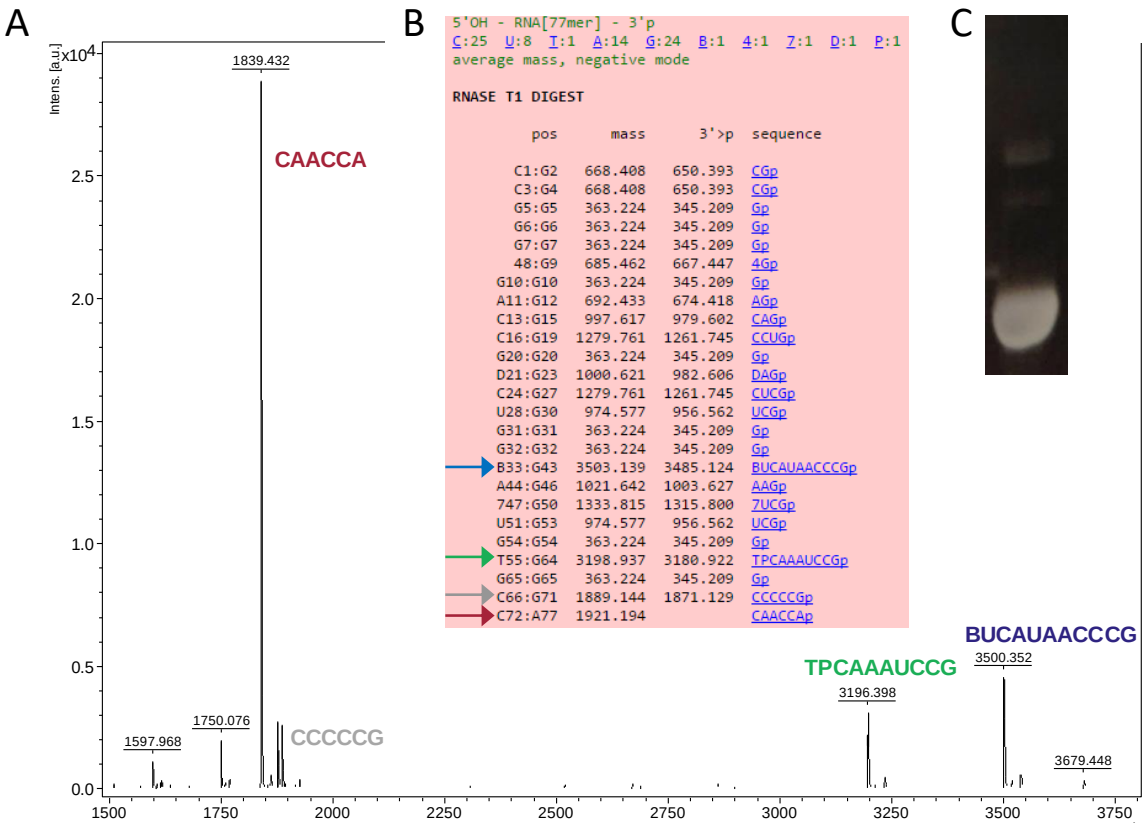

Figure S2: Identity validation of bacterial initiator transfer RNA, tRNA^{Meti}.
After several chromatography colums, the purity of tRNA^{Meti} is visualized on a denaturing 8 % acrylamide gel (C). Fragments of T1 RNAse digestion are predicted (http://mods.rna.albany.edu/masspec/Mongo-Oligo) and listed (B). Finally, after T1 digestion, the identity of the initiator tRNA^{Meti} is validated thanks MALDI-TOF analysis (A).

A

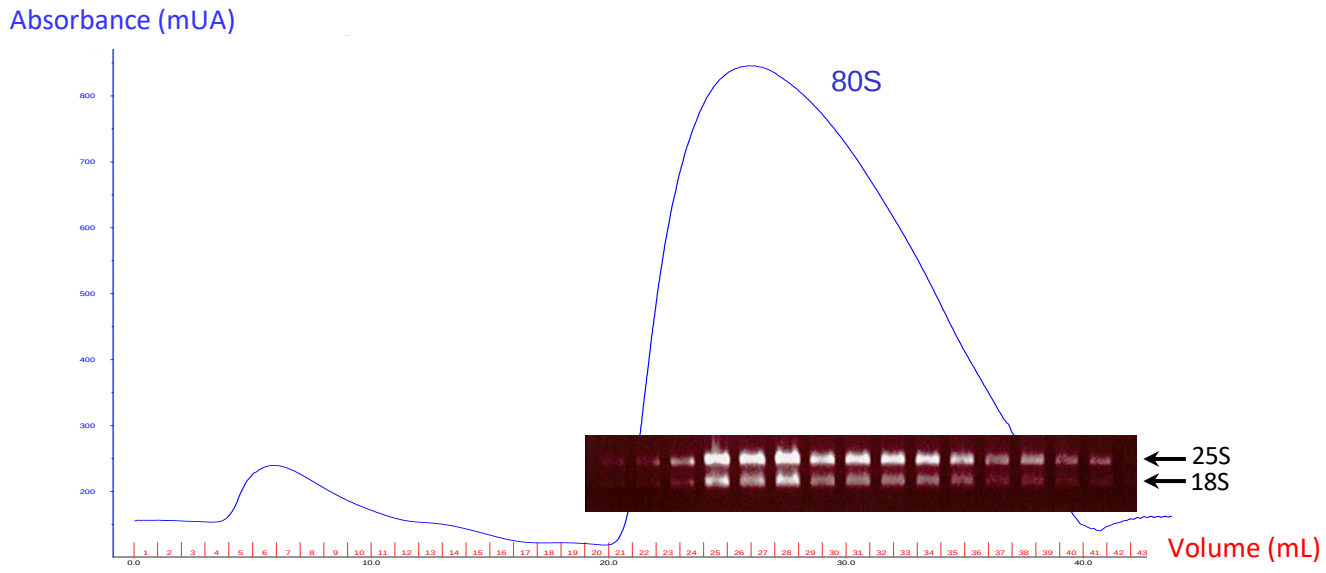

B

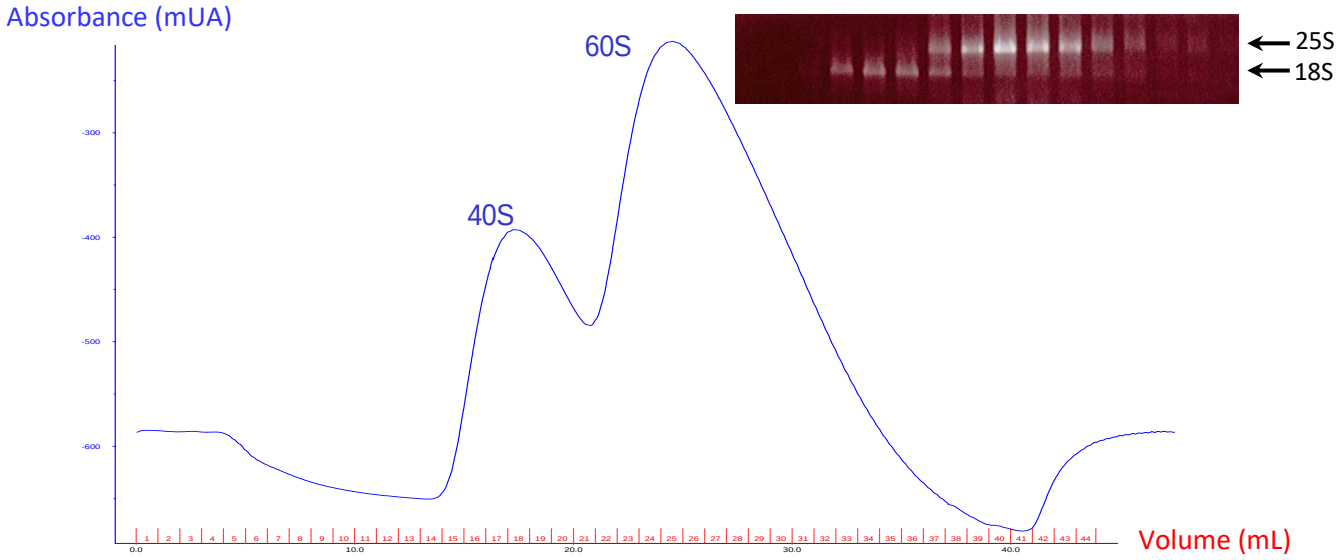

Figure S3: Purification and dissociation of yeast 80S ribosome.
80S are recovered using a 15 % - 30 % sucrose gradient while 40S and 60S are separated using a 10 % - 30 % sucrose gradient. 80S ribosomes (A) and ribosomal subunits (B) are collected from the top using a Gradient Fractionator (Auto Densi-Flow Labconco) connected to an AKTA FPLC system (GE Healthcare). Subunits are detected thanks to absorbance (blue curve). Purity of fractions is assessed by visualization of 18S rRNA and 25S rRNA (dark arrows) on 1 % agarose gel, 0.5 µg.mL^{-1} EtBr.

			Thermodynamics (ITC)					Kinetics (kinITC)			
Temperature	PrAMPs	Experiment	ΔH (kcal/mol)	-TΔS (kcal/mol)	ΔG (kcal/mol)	Kd (nM)	N	Kd (nM)	kon (M-1.s-1)	koff (s-1)	Chi2 test
15	Bac7	1	-13,8 ± 0,1	3,7	-10,1	21,8 ± 4,6	0,97				
		2	-14,4 ± 0,07	4,4	-10	26,6 ± 1,9	0,93	31,4 ± 9,1	1,232 ± 0,24*10^5	3,87± 0,74*10^-3	1,25
		Average	-14,1	4,05	-10,05	24,2	0,95				
		Ecart type	0,3	0,4	0,0	2,4	0,03				
	Metalnikowin	1	-9,6 ± 0,045	-0,3	-10	26,6 ± 1,9	0,78				
		2	-7,1 ± 0,04	-2,5	-9,6	39,1 ±	1				
		Average	-8,3	-1,5	-9,9	32,85	0,89				
		Ecart type	1,3	1,2	0,1	6,3	0,16				
	Pyrrhocoricin	1	-18,9 ± 0,2	8,6	-10,3	16,9 ± 2,2	0,96				
		2	-18,1 ± 0,1	8	-10,1	22,3 ± 0,2	0,63				
		3	-24,2 ± 0,1	8,7	-10,3	13,4 ± 0,03	0,45				
		4	-19 ± 0,2	13,9	-10,3	16,2 ± 1,3	0,92	10,6 ± 2,7	8,196 ± 1,3*10^4	8,66± 1,4*10^-4	15,4
		Average	-20,05	9,8	-10,25	17,2	0,74				
		Ecart type	2,5	2,1	0,1	2,6	0,24				
20	Bac7	1	-14,8 ± 0,2	4,3	-10,5	16,9 ±	0,94				
		2	-18,5 ± 0,1	8,1	-10,4	18,4 ± 1,9	0,97	16,3 ± 4,2	3,01 ± 0,59*10^5	4,92± 0,96*10^-3	1,74
		Average	-16,65	6,2	-10,45	17,65	0,955				
		Ecart type	1,9	1,9	0,0	0,8	0,02				
	Metalnikowin	1	-13,4 ± 0,04	3,6	-9,8	48,2 ± 1,7	0,75				
		2	-10,2 ± 0,03	0,09	-10,2	27 ± 1	0,89				
		Average	-11,8	1,845	-10	37,6	0,82				
		Ecart type	1,6	1,8	0,2	10,6	0,10				
	Pyrrhocoricin	1	-22,5 ± 0,1	12	-10,4	17,1 ± 1,1	1				
		2	-22 ± 0,1	11,7	-10,3	20,1 ± 0,7	0,83				
		3	-20,8 ± 0,1	10,6	-10,2	25,3 ± 0,5	0,62				
		4	-21,1 ± 0,15	10,5	-10,6	12,8 ± 2,2	0,96	2,1 ± 0,9	2,593 ± 0,75*10^5	5,52± 1,6*10^-4	10,6
		Average	-21,6	11,2	-10,375	18,83	0,8525				
		Ecart type	0,6	0,7	0,1	3,9	0,17				
25	Bac7		-20,8 ± 0,1	10,7	-10,1	40 ± 2,6	0,98	22,4 ± 4	2,074 ± 0,32*10^5	4,66± 0,71*10^-3	1,4
	Metalnikowin	1	-14,2 ± 0,06	4,4	-9,8	63,3 ± 1,5	0,94				
		2	-13,8 ± 0,065	3,9	-9,9	55,9 ± 3	0,94	42,5 ± 11,3	3,02 ± 1,95*10^5	1,28 ± 0,83*10^-2	0,4
		3	-19 ± 0,2	9	-10	51,5 ± 5,6	0,75	58,8 ± 10,9	1,51 ± 0,4*10^5	8,92 ± 2,37*10^-3	0,39
		4	-14,2 ± 0,1	3,8	-10,4	22,3 ± 1,7	0,87	63,8 ± 17,9	1,13 ± 0,37*10^5	7,19 ± 2,35*10^-3	0,61
		Average	-15,3	5,275	-10,025	48,25	0,875	55,03	1,88*10^5	9,6*10^-3	
		Ecart type	2,1	1,9	0,2	13	0,09	11,14	1*10^5	2,9*10^-3	
	Pyrrhocoricin	1	-31,1 ± 0,4	21,5	-9,6	88,8 ± 9,7	0,97				
		2	-28,7 ± 0,06	18,4	-10,3	26,1± 0,9	0,42	16,3 ± 4,5	1,88 ± 0,33*10^5	3,05 ± 0,54*10^-3	1,83
		3	-27,8 ± 0,1	16,9	-10,9	10,4 ± 0,9	0,83	4,6 ± 1,7	1,38 ± 0,33*10^5	6,39± 1,54*10^-4	0,82
		4	-25 ± 0,07	14,3	-10,8	13,1 ± 0,8	0,7				
		Average	-28,15	17,775	-10,4	34,6	0,73	10,45	1,63*10^5	1,85*10^-3	
		Ecart type	1,8	2,2	0,5	27,1	0,23	8,27	0,35*10^5	1,71*10^-3	
30	Bac7	1	-21,8 ± 0,2	11,9	-10	64,8 ± 7,2	1				
		2	-22,7 ± 0,2	12,6	-10,1	48,4 ± 3,8	0,88				
		3	-30,4 ± 0,3	20,8	-9,6	73,1 ± 15,8	0,75	32,6 ± 10,9	9,55 ± 2,6*10^4	3,12 ± 0,84*10^-3	0,62
		4	-21,4 ± 0,1	11,3	-10,1	49,6 ± 2,8	0,94	35,2 ± 6,3	1,07 ± 0,14*10^5	3,77± 0,48*10^-3	2,1
		5	-21,5 ± 1,7	11,5	-10	59 ± 1,1	0,62				
		6	-19,8 ± 0,1	10	-9,8	80,5 ± 1	0,68				
		7	-20,9 ± 0,2	10,9	-10	55,1 ± 0,8	0,73				
		8	-20,5 ± 0,1	10,6	-10	64,6 ± 3,5	0,91				
		Average	-22,33	12,45	-9,95	61,89	0,81	33,9	1,01*10^5	3,45*10^-3	
		Ecart type	2,0	2,1	0,1	8,90	0,14	1,84	0,08*10^5	0,46*10^-3	
	Metalnikowin	1	-15 ± 0,08	4,5	-10,5	28,9 ± 2,1	0,94				
		2	-16,8 ± 0,1	6,8	-10	60,3 ± 4,9	0,94				
		3	-15 ± 0,09	1,2	-10,7	19,9 ± 2	0,99				
		4	-19,7 ± 0,05	9,1	-10,6	24,1 ± 1	0,68	7,3 ± 5,3	3,61 ± 1,68*10^5	2,65± 1,23*10^-3	0,97
		5	-15,6 ± 1,3	5,4	-10,2	42,5 ± 1,2	0,86				
		6	-16,4 ± 0,07	5,4	-11	12,6 ± 0,96	0,93	33,5 ± 5,6	1,189 ± 0,19*10^5	3,98± 0,62*10^-3	4,33
		Average	-16,42	5,4	-10,5	31,38	0,89				
		Ecart type	1,2	1,7	0,3	13,30	0,11				
	Pyrrhocoricin	1	-31,6 ± 0,1	20,9	-10,7	19,9 ± 1,5	0,76				
		2	-26,7 ± 0,09	15,7	-11	11,6 ± 0,7	0,90				
		3	-27,7 ± 0,1	17,3	-10,4	33,7 ± 2	0,94				
		4	-29,1 ± 0,4	19,2	-9,9	78,3 ± 10,2	1				
		5	-28,7 ± 0,3	17,9	-10,3	36,7 ± 5,2	1				
		6	-31,3 ± 0,2	21,3	-10	61,8 ± 8	0,4				
		7	-30,5 ± 0,2	20,3	-10,2	42,7 ± 9	0,42				
		8	-27,5 ± 0,2	17	-10,5	26,7 ± 2,8	1				
		9	-36,9 ± 0,35	26,7	-10,2	45,7 ± 5,3	0,96				
		10	-30,4 ± 0,1	20,2	-10,3	39,4 ± 2,4	1				
		11	-30 ± 0,08	19,6	-10,4	31 ± 2,6	1				
		12	-33,8 ± 0,1	23,1	-10,6	21,2 ± 1	0,74				
		13	-30,1 ± 0,1	19,2	-10,9	14,3 ± 0,7	0,82				
		14	-24,8 ± 0,2	14,1	-10,7	19,4 ± 2,4	0,94				
		15	-29,4 ± 0,2	19	-10,4	32,5 ± 2,7	1				
		16	-32,3 ± 0,3	22	-10,2	42,8 ± 4,8	0,96	34,3 ± 4,5	9,06 ± 0,77*10^4	3,11± 0,26*10^-3	0,49
		17	-28,4 ± 0,45	18,3	-10,1	53,5 ± 9,7	1,13				
		18	-31,3 ± 0,1	21,1	-10,2	45,7 ± 2,4	0,93	31,3 ± 2,9	1,15 ± 0,98*10^5	3,61± 0,31*10^-3	0,9
		19	-33,2 ± 0,2	23	-10,2	47,6 ± 3,4	1	29,2 ± 2,5	1,13 ± 0,19*10^5	3,29± 0,54*10^-3	7,03
		20	-27 ± 0,2	17	-10	60,9 ± 4,4	0,88				
		21	-25,1 ± 0,1	14,6	-10,5	27,5 ± 1,9	0,82				
		22	-24,1 ± 0,2	13,4	-10,7	20,6 ± 1,8	0,98				
		23	-31,9 ± 0,4	22	-10	62 ± 6,5	0,94				
		24	-27,3 ± 0,4	17,2	-10,1	53,4 ± 3,4	1,1				
		25	-32,1 ± 0,2	22	-10,1	49,3 ± 3	0,99				
		26	-29,6 ± 0,3	19,4	-10,2	42,7 ± 4,7	0,99				
		27	-30,1 ± 0,2	19,7	-10,4	31,8 ± 2,4	1				
		28	-31,6 ± 0,3	21,5	-10,1	53,7 ± 6,2	1,1				
		29	-30,7 ± 0,1	20,1	-10,6	24 ± 1,9	1				
		Average	-29,77	19,41	-10,34	38,63	0,92	32,8	1,03*10^5	3,36*10^-3	
		Ecart type	2,2	2,2	0,2	13,80	0,17	2,1	0,2*10^5	0,4*10^-3	
	Lincomycin	1	6 ± 0,1	-13,6	-7,6	3140 ± 335	0,94				
		2	5,4 ± 0,1	-13,5	-8,1	1350 ± 106	1				
		Average	5,65	-13,55	-7,9	2245,00	0,97				
		Ecart type	0,35	0,1	0,4		0,04				
35	Bac7		-29,2 ± 0,25	19,6	-9,7	136 ± 8,6	0,88	109,3 ± 18,1	1,07 ± 0,18*10^5	1,17 ± 0,2*10^-2	0,54
	Metalnikowin	1	-15 ± 0,08	4,3	-10,7	25,2 ± 2,2	0,94				
		2	-23,9 ± 0,2	13,4	-10,5	34,2 ± 4,2	0,82				
		3	-20,7 ± 0,2	10,6	-10,1	65,3 ± 5,7	0,88	20,3 ± 6,1	4,82 ± 0,84*10^4	9,79± 1,7*10^-4	4,3
		Average	-19,87	9,43	-10,43	41,57	0,88				
		Ecart type	3,2	3,4	0,2	15,80	0,06				
	Pyrrhocoricin	1	-39,8 ± 0,2	29,5	-10,3	48,5 ± 3	0,84	38,7 ± 2,4	1,735 ± 0,12*10^5	6,71± 0,45*10^-3	0,99
		2	-31,3 ± 0,2	21,3	-10	78 ± 6,7	1				
		3	-34 ± 0,2	23,7	-10,3	47,3 ± 3,2	0,9				
		Average	-35,03	24,83	-10,20	57,93	0,91				
		Ecart type	3,2	3,1	0,1	13,40	0,08				

Table S1: Thermodynamic and kinetic data from ITC experiments used for PrAMP study.
All the experiments used for the analysis of binding of Bac 7, metalnikowin, pyrrhocoricin and lincomycin from several temperatures are listed. Thermodynamic analysis was done with PEAQ software from Malvern while kinetic analysis was done with kinITC from Affinimeter. Data shown in red are non-relevant for kinetic analysis because of the Chi2 test >> 1.

ITC at 30 °C							
Binding parameters			ΔH (kcal/mol)	-T?S (kcal/mol)	ΔG (kcal/mol)	Kd (nM)	N
Direct ITC	Erythromycin		-1,8 ± 0,015	-9,2	-11		0,8
	Azithromycin	1	-2,4 ± 0,015	-8,7	-11,1		0,7
		2	-2,6 ± 0,05	-11,4	-14		0,79
		Average	-2,5	-10,05	-12,55		0,745
		Ecart type	0,14	1,91	2,05		0,06
	Telithromycin	1	-0,34 ± 0,003	-11,7	-12,1		0,95
		2	-0,78 ± 0,01	-9,3	-10,1		1
		Average	-0,56	-10,5	-11,1		0,975
		Ecart type	0,31	1,70	1,41		0,04
	Josamycin		-5,8 ± 0,03	-6,4	-12,2		0,99
Bac7 displacement	Erythromycin		-0,1 ± 0,1	-12	-11,9	2,7 ± 0,14	0,91
	Azithromycin		-6 ± 0,2	-6,8	-12,8	0,6 ± 0,07	0,72
	Telithromycin	1	3,2 ± 0,45	-15	-11,8	2,8 ± 0,36	0,81
		2	-1,8 ± 0,4	-9,8	-11,6	4,2 ± 0,46	0,95
		3	-6,8 ± 0,2	-5,7	-12,5	1 ± 0,1	0,71
		Average	-1,8	-10,17	-11,97	2,67	0,82
		Ecart type	5,00	4,66	0,47	1,60	0,12
	Josamycin		-3,6 ± 0,2	-8,3	-11,9	2,7 ± 0,04	0,65
Pyrrhocoricin displacement	Erythromycin	1	-5,3 ± 0,6	-6,7	-12,1	2 ± 0,3	0,76
		2	-8,1 ± 0,2	-3,9	-12	2,5 ± 0,12	0,77
		3	-5,4 ± 0,3	-6,4	-11,8	3 ± 0,2	0,98
		4	-7,4 ± 0,4	-4,8	-12,2	1,9 ± 0,2	0,92
		5	-7,7 ± 0,3	-4	-12,2	3,7 ± 0,3	0,91
		Average	-6,78	-5,16	-12,06	2,62	0,868
		Ecart type	1,33	1,32	0,17	0,75	0,10
	Azithromycin	1	-2,7 ± 0,3	-10,4	-13,1	0,36 ± 0,03	0,78
		2	3,3 ± 0,6	-15,3	-12	2,1 ± 0,3	0,83
		3	-1,5 ± 0,2	-11,5	-13	0,44 ± 0,04	0,98
		Average	-0,3	-12,4	-12,7	0,97	0,86
		Ecart type	3,17	2,57	0,61	0,98	0,10
	Telithromycin	1	-7,2 ± 0,1	-5,5	-12,7	0,65 ± 0,04	0,95
		2	1,4 ± 0,7	-14,4	-13	0,4 ± 0,04	0,67
		3	-1 ± 0,2	-11,1	-12,1	1,8 ± 0,07	0,8
		4	-4 ± 0,25	-9	-13	0,4 ± 0,07	0,98
		Average	-2,7	-10	-12,7	0,81	0,85
		Ecart type	3,73	3,73	0,42	0,67	0,14
	Josamycin	1	-5,3 ± 0,35	-7,9	-13,2	0,3 ± 0,03	0,27
		2	-1,8 ± 5	-10,3	-12,1	1,95 ± 0,4	0,15
		Average	-3,55	-9,1	-12,65	1,1	0,21
		Ecart type	2,47	1,70	0,78	1,13	0,08
Lincomycin displacement	Pyrrhociricin	1	-31,9 ± 0,4	22	-10	62 ± 6,5	0,94
		2	-27,3 ± 0,4	17,2	-10,1	53,4 ± 3,4	1,1
		Average	-29,6	19,6	-10,05	57,7	1,02
		Ecart type	3,25	3,39	0,07	6,08	0,11

Table S2: Thermodynamic parameters and affinities of macrolides by direct ITC or competition experiments.

All the experiments for the analysis of binding of macrolides are listed for direct ITC and after displacement of Bac 7 or pyrrhocoricin at 30 °C.

			ITC							
			Thermodynamics					Kinetics (kinITC)		
Temperature	Ribosome	Experiment	ΔH (kcal/mol)	-T?S (kcal/mol)	ΔG (kcal/mol)	Kd (nM)	N	Kd (nM)	kon (M-1.s-1)	koff (s-1)
15	80S	1	-12,1 ± 0,15	2,8	-9,3	87,4 ± 10,6	1			
		2	-17,5 ± 0,1	8,1	-9,4	70,3 ± 4,9	0,95	89,5 ± 21,3	4,53 ± 0,86 *10^4	4,05 ± 0,77 *10^-3
		Average	14,8	5,5	-9,4	78,9	0,98			
		Ecart type	3,82	4,1	0,1	12,09	0,035			
	70S		-17,9 ± 0,2	9,1	-8,8	219 ± 12,6	1,03	241 ± 39	7,83 ± 3,4 *10^4	1,88 ± 0,83 *10^-2
20	80S	1	-23,7 ± 0,3	14,0	-9,7	59 ± 1,7	0,34			
		2	-18,8 ± 0,2	9,4	-9,4	89,5 ± 9,1	0,86	86,9 ± 23,6	1,38 ± 0,38 *10^5	1,12 ± 0,33 *10^-2
		Average	21,3	11,7	-9,6	74,3	0,6			
		Ecart type	3,46	3,25	0,21	21,57	0,37			
25	80S	1	-33,3 ± 0,3	23,3	-10,0	45,6 ± 4,3	1,1			
		2	-30,4 ± 0,25	20,4	-10,0	46 ± 4,6	0,76	49,8 ± 10,5	1,43 ± 0,3 *10^5	7,13 ± 1,52 *10^-3
		Average	-31,9	21,9	-10,0	45,8	0,93			
		Ecart type	2,05	2,05	0,00	0,28	0,24			
	40S		-37,6 ± 0,4	28,6	-9,0	253 ± 1,7	0,97			
30	80S	1	-19,3 ±	9,3	-10,0	58,4 ± 6,4	0,38			
		2	-42 ± 0,15	31,6	-10,4	30,8 ± 1,6	1	32,1 ± 4,4	4,08 ± 0,37 *10^4	1,31± 0,12 *10^-3
		3	-43,1 ± 0,2	32,9	-10,2	42,6 ± 1,9	1	11,9 ± 3,9	4,63 ± 1,7 *10^5	5,52 ± 2,1 *10^-3
		4	-36 ± 0,2	25,7	-10,3	36,7 ± 2,7	0,48	42,1 ± 13,4	6,14 ± 1,37 *10^4	2,58 ± 0,57 *10^-3
		5	-41,2 ± 0,4	31,3	-9,9	82,2 ± 7,4	0,31			
		Average	40,6	30,4	-10,2	50,1	0,63	22,00	2,5*10^5	3,42*10^-3
		Ecart type	3,15	3,19	0,22	20,7	0,34	14,28	2,99*10^5	2,98*10^-3
	40S		-39,6 ± 0,3	30,2	-9,4	184 ± 10	0,98	524 ± 126	3,54 ± 0,79 *10^4	1,85 ± 0,41 *10^-2
35	80S		-50,7 ± 0,6	40,1	-10,1	65 ± 6,6	0,25	24,4 ±12,5	1,50 ± 0,5 *10^5	3,65 ± 1,21 *10^-3

Table S3: Thermodynamic and kinetic data from ITC experiments used for ribosome-IRES interaction study.
All the experiments for the analysis of binding of the CrPV IGR IRES are listed for all the tested temperatures. Thermodynamic analysis was done with PEAQ software from Malvern while kinetic analysis was done with kinITC from Affinimeter. Data shown in red are non-relevant for kinetic analysis because of the Chi2 test >> 1.

			switchSENSE		
Temperature	Ribosome	Experiment	Kd (nM)	kon (M-1.s-1)	koff (s-1)
15	80S		103 ± 4	2,2 ± 0,03 *10^4	2,3 ± 0,08 *10^-3
20	80S	1	37,4 ± 4,5	4,11 ± 0,16 *10^4	1,54 ± 0,17 *10^-3
		2	104 ± 2	2,6 ± 0,03 *10^4	2,7 ± 0,05 *10^-3
		Average	70,7	3,35*10^4	2,12*10^-3
		Ecart type	47,09	0,11*10^4	0,82*10^-3
25	80S	1	12,9 ± 0,04	1,21 ± 0,03 *10^5	1,56 ± 0,05 *10^-3
		2	35,1 ± 0,1	3,1 ± 0,07 *10^5	1,1 ± 0,02 *10^-3
		3	7,6 ± 0,2	1,43 ± 0,03 *10^5	1,1 ± 0,01 *10^-3
		4	13,4 ± 0,04	1,34 ± 0,02 *10^5	1,8 ± 0,04 *10^-3
		5	11,3 ± 0,03	1,72 ± 0,03 *10^5	1,94 ± 0,03 *10^-3
		6	35,2 ± 3	4,65 ± 0,16 *10^4	1,64 ± 0,13 *10^-3
		Average	19,3	1,54*10^5	1,52*10^-3
		Ecart type	12,49	0,87*10^5	0,34*10^-3
	40S		158 ± 12	3,86 ± 0,17 *10^4	6,11 ± 0,38 *10^-3
	70S	1	969 ± 85	2,72 ± 0,15 *10^5	2,64 ± 0,18 *10^-1
		2	1100 ± 100	2,83 ± 0,26 *10^5	3,11 ± 0,18 *10^-1
		Average	1034	2,78*10^5	2,88*10^-1
		Ecart type	92,63	0,078*10^5	3,3*10^-1
30	80S	1	83,4 ± 7,4	3,25 ± 0,08 *10^4	2,71 ± 0,23 *10^-3
		2	8,8 ± 0,89	1,59 ± 0,05 *10^5	1,4 ± 0,13 *10^-3
		3	30,8 ± 1,8	6,74 ± 0,2 *10^4	2,07 ± 0,11 *10^-3
		Average	41	8,63*10^4	2,06*10^-3
		Ecart type	38,33	0,66*10^4	0,65*10^-3
	40S		111 ± 5	2,3 ± 0,08 *10^4	2,5 ± 0,08 *10^-3
35	80S	1	38,4 ± 2,2	3,47 ± 0,09 *10^4	1,33 ± 0,07 *10^-3
		2	23 ± 0,9	9,4 ± 0,21 *10^4	2,16 ± 0,07 *10^-3
		3	42 ± 0,9	6,9 ± 0,09 *10^4	2,9 ± 0,04 *10^-3
		Average	34,5	6,6*10^4	2,13*10^-3
		Ecart type	10,09	0,28*10^4	0,80*10^-3

Table S4: Kinetic data from switchSENSE experiments used for ribosome-IRES interaction study.
All the experiments for the analysis of binding of the CrPV IGR IRES are listed for all the tested temperatures.

BIBLIOGRAPHY

REFERENCES

Abdi, N.M., and Fredrick, K. (2005). Contribution of 16S rRNA nucleotides forming the 30S subunit A and P sites to translation in Escherichia coli. RNA N. Y. N *11*, 1624–1632.

Abeyrathne, P.D., Koh, C.S., Grant, T., Grigorieff, N., and Korostelev, A.A. (2016). Ensemble cryo-EM uncovers inchworm-like translocation of a viral IRES through the ribosome. ELife *5*.

Abraham, E.P., and Chain, E. (1988). An enzyme from bacteria able to destroy penicillin. 1940. Rev. Infect. Dis. *10*, 677–678.

Abrishami, V., Zaldívar-Peraza, A., de la Rosa-Trevín, J.M., Vargas, J., Otón, J., Marabini, R., Shkolnisky, Y., Carazo, J.M., and Sorzano, C.O.S. (2013). A pattern matching approach to the automatic selection of particles from low-contrast electron micrographs. Bioinforma. Oxf. Engl. *29*, 2460–2468.

Achenbach, J., and Nierhaus, K.H. (2015). The mechanics of ribosomal translocation. Biochimie *114*, 80–89.

Agerberth, B., Lee, J.Y., Bergman, T., Carlquist, M., Boman, H.G., Mutt, V., and Jörnvall, H. (1991). Amino acid sequence of PR-39. Isolation from pig intestine of a new member of the family of proline-arginine-rich antibacterial peptides. Eur. J. Biochem. *202*, 849–854.

Agrawal, R.K., Spahn, C.M.T., Penczek, P., Grassucci, R.A., Nierhaus, K.H., and Frank, J. (2000). Visualization of Trna Movements on the Escherichia coli 70s Ribosome during the Elongation Cycle. J. Cell Biol. *150*, 447–460.

Alanjary, M., Kronmiller, B., Adamek, M., Blin, K., Weber, T., Huson, D., Philmus, B., and Ziemert, N. (2017). The Antibiotic Resistant Target Seeker (ARTS), an exploration engine for antibiotic cluster prioritization and novel drug target discovery. Nucleic Acids Res. *45*, W42–W48.

Alekshun, M.N., and Levy, S.B. (2007). Molecular Mechanisms of Antibacterial Multidrug Resistance. Cell *128*, 1037–1050.

Amici, C., La Frazia, S., Brunelli, C., Balsamo, M., Angelini, M., and Santoro, M.G. (2015). Inhibition of viral protein translation by indomethacin in vesicular stomatitis virus infection: role of eIF2α kinase PKR. Cell. Microbiol. *17*, 1391–1404.

Andersson, D.I., and Hughes, D. (2011). Persistence of antibiotic resistance in bacterial populations. FEMS Microbiol. Rev. *35*, 901–911.

Andino, R., Rieckhof, G.E., and Baltimore, D. (1990). A functional ribonucleoprotein complex forms around the 5' end of poliovirus RNA. Cell *63*, 369–380.

Andino, R., Rieckhof, G.E., Achacoso, P.L., and Baltimore, D. (1993). Poliovirus RNA synthesis utilizes an RNP complex formed around the 5'-end of viral RNA. EMBO J. *12*, 3587–3598.

Andreev, D.E., Fernandez-Miragall, O., Ramajo, J., Dmitriev, S.E., Terenin, I.M., Martinez-Salas, E., and Shatsky, I.N. (2007). Differential factor requirement to assemble translation initiation complexes at the alternative start codons of foot-and-mouth disease virus RNA. RNA N. Y. N *13*, 1366–1374.

Appelt, K., Dijk, J., Reinhardt, R., Sanhuesa, S., White, S.W., Wilson, K.S., and Yonath, A. (1981). The crystallization of ribosomal proteins from the 50 S subunit of the Escherichia coli and Bacillus stearothermophilus ribosome. J. Biol. Chem. *256*, 11787–11790.

Arenz, S., and Wilson, D.N. (2016). Bacterial Protein Synthesis as a Target for Antibiotic Inhibition. Cold Spring Harb. Perspect. Med. *6*.

Arenz, S., Meydan, S., Starosta, A.L., Berninghausen, O., Beckmann, R., Vázquez-Laslop, N., and Wilson, D.N. (2014). Drug sensing by the ribosome induces translational arrest via active site perturbation. Mol. Cell *56*, 446–452.

Arenz, S., Juette, M.F., Graf, M., Nguyen, F., Huter, P., Polikanov, Y.S., Blanchard, S.C., and Wilson, D.N. (2016). Structures of the orthosomycin antibiotics avilamycin and evernimicin in complex with the bacterial 70S ribosome. Proc. Natl. Acad. Sci. U. S. A. *113*, 7527–7532.

Arévalo, M.A., Tejedor, F., Polo, F., and Ballesta, J.P. (1988). Protein components of the erythromycin binding site in bacterial ribosomes. J. Biol. Chem. *263*, 58–63.

Au, H.H.T., and Jan, E. (2012). Insights into factorless translational initiation by the tRNA-like pseudoknot domain of a viral IRES. PloS One *7*, e51477.

Au, H.H., Cornilescu, G., Mouzakis, K.D., Ren, Q., Burke, J.E., Lee, S., Butcher, S.E., and Jan, E. (2015). Global shape mimicry of tRNA within a viral internal ribosome entry site mediates translational reading frame selection. Proc. Natl. Acad. Sci. U. S. A. *112*, E6446-6455.

Aylett, C.H.S., Boehringer, D., Erzberger, J.P., Schaefer, T., and Ban, N. (2015). Structure of a yeast 40S-eIF1-eIF1A-eIF3-eIF3j initiation complex. Nat. Struct. Mol. Biol. *22*, 269–271.

Bagley, M.C., Dale, J.W., Merritt, E.A., and Xiong, X. (2005). Thiopeptide antibiotics. Chem. Rev. *105*, 685–714.

Baird, S.D., Lewis, S.M., Turcotte, M., and Holcik, M. (2007). A search for structurally similar cellular internal ribosome entry sites. Nucleic Acids Res. *35*, 4664–4677.

Ban, N., Nissen, P., Hansen, J., Moore, P.B., and Steitz, T.A. (2000). The complete atomic structure of the large ribosomal subunit at 2.4 A resolution. Science *289*, 905–920.

Bartesaghi, A., Merk, A., Banerjee, S., Matthies, D., Wu, X., Milne, J.L.S., and Subramaniam, S. (2015). 2.2 Å resolution cryo-EM structure of β-galactosidase in complex with a cell-permeant inhibitor. Science *348*, 1147–1151.

Barthélémy, P., Autissier, D., Gerbaud, G., and Courvalin, P. (1984). Enzymic hydrolysis of erythromycin by a strain of Escherichia coli. A new mechanism of resistance. J. Antibiot. (Tokyo) *37*, 1692–1696.

Baumann, S., Schoof, S., Bolten, M., Haering, C., Takagi, M., Shin-ya, K., and Arndt, H.-D. (2010). Molecular determinants of microbial resistance to thiopeptide antibiotics. J. Am. Chem. Soc. *132*, 6973–6981.

Bébéar, C., de Barbeyrac, B., Bébéar, C.M., Renaudin, H., and Allery, A. (1997). New developments in diagnostic and treatment of mycoplasma infections in humans. Wien. Klin. Wochenschr. *109*, 594–599.

Belardinelli, R., Sharma, H., Caliskan, N., Cunha, C.E., Peske, F., Wintermeyer, W., and Rodnina, M.V. (2016). Choreography of molecular movements during ribosome progression along mRNA. Nat. Struct. Mol. Biol. *23*, 342–348.

Belova, L., Tenson, T., Xiong, L., McNicholas, P.M., and Mankin, A.S. (2001). A novel site of antibiotic action in the ribosome: interaction of evernimicin with the large ribosomal subunit. Proc. Natl. Acad. Sci. U. S. A. *98*, 3726–3731.

Belsham, G.J. (2009). Divergent picornavirus IRES elements. Virus Res. *139*, 183–192.

Benincasa, M., Scocchi, M., Podda, E., Skerlavaj, B., Dolzani, L., and Gennaro, R. (2004). Antimicrobial activity of Bac7 fragments against drug-resistant clinical isolates. Peptides *25*, 2055–2061.

Ben-Shem, A., Jenner, L., Yusupova, G., and Yusupov, M. (2010). Crystal structure of the eukaryotic ribosome. Science *330*, 1203–1209.

Ben-Shem, A., Garreau de Loubresse, N., Melnikov, S., Jenner, L., Yusupova, G., and Yusupov, M. (2011). The structure of the eukaryotic ribosome at 3.0 Å resolution. Science *334*, 1524–1529.

Berisio, R., Harms, J., Schluenzen, F., Zarivach, R., Hansen, H.A.S., Fucini, P., and Yonath, A. (2003). Structural insight into the antibiotic action of telithromycin against resistant mutants. J. Bacteriol. *185*, 4276–4279.

Berthold, N., Czihal, P., Fritsche, S., Sauer, U., Schiffer, G., Knappe, D., Alber, G., and Hoffmann, R. (2013). Novel apidaecin 1b analogs with superior serum stabilities for treatment of infections by gram-negative pathogens. Antimicrob. Agents Chemother. *57*, 402–409.

Blaha, G., Burkhardt, N., and Nierhaus, K.H. (2002). Formation of 70S ribosomes: large activation energy is required for the adaptation of exclusively the small ribosomal subunit. Biophys. Chem. *96*, 153–161.

Blair, J.M.A., Webber, M.A., Baylay, A.J., Ogbolu, D.O., and Piddock, L.J.V. (2015). Molecular mechanisms of antibiotic resistance. Nat. Rev. Microbiol. *13*, 42–51.

von Böhlen, K., Makowski, I., Hansen, H.A., Bartels, H., Berkovitch-Yellin, Z., Zaytzev-Bashan, A., Meyer, S., Paulke, C., Franceschi, F., and Yonath, A. (1991). Characterization and preliminary attempts for derivatization of crystals of large ribosomal subunits from Haloarcula marismortui diffracting to 3 A resolution. J. Mol. Biol. *222*, 11–15.

Bommakanti, A.S., Lindahl, L., and Zengel, J.M. (2008). Mutation from guanine to adenine in 25S rRNA at the position equivalent to E. coli A2058 does not confer erythromycin sensitivity in Sacchromyces cerevisae. RNA N. Y. N *14*, 460–464.

Bonning, B.C., and Miller, W.A. (2010). Dicistroviruses. Annu. Rev. Entomol. *55*, 129–150.

Borovinskaya, M.A., Pai, R.D., Zhang, W., Schuwirth, B.S., Holton, J.M., Hirokawa, G., Kaji, H., Kaji, A., and Cate, J.H.D. (2007). Structural basis for aminoglycoside inhibition of bacterial ribosome recycling. Nat. Struct. Mol. Biol. *14*, 727–732.

Borovinskaya, M.A., Shoji, S., Fredrick, K., and Cate, J.H.D. (2008). Structural basis for hygromycin B inhibition of protein biosynthesis. RNA N. Y. N *14*, 1590–1599.

Böttger, E.C., Springer, B., Prammananan, T., Kidan, Y., and Sander, P. (2001). Structural basis for selectivity and toxicity of ribosomal antibiotics. EMBO Rep. *2*, 318–323.

Brandi, L., Marzi, S., Fabbretti, A., Fleischer, C., Hill, W.E., Gualerzi, C.O., and Stephen Lodmell, J. (2004). The translation initiation functions of IF2: targets for thiostrepton inhibition. J. Mol. Biol. *335*, 881–894.

Brandi, L., Maffioli, S., Donadio, S., Quaglia, F., Sette, M., Milón, P., Gualerzi, C.O., and Fabbretti, A. (2012). Structural and functional characterization of the bacterial translocation inhibitor GE82832. FEBS Lett. *586*, 3373–3378.

Brilot, A.F., Korostelev, A.A., Ermolenko, D.N., and Grigorieff, N. (2013). Structure of the ribosome with elongation factor G trapped in the pretranslocation state. Proc. Natl. Acad. Sci. U. S. A. *110*, 20994–20999.

Brodersen, D.E., Clemons, W.M., Carter, A.P., Morgan-Warren, R.J., Wimberly, B.T., and Ramakrishnan, V. (2000). The structural basis for the action of the antibiotics tetracycline, pactamycin, and hygromycin B on the 30S ribosomal subunit. Cell *103*, 1143–1154.

Brodersen, R., Bunch-Christensen, K., and Tybring, L. (1953). Antibiotic properties of picromycin. Acta Pharmacol. Toxicol. (Copenh.) *9*, 255–258.

Brown, E.D., and Wright, G.D. (2016). Antibacterial drug discovery in the resistance era. Nature *529*, 336–343.

Bugaud, O., Barbier, N., Chommy, H., Fiszman, N., Le Gall, A., Dulin, D., Saguy, M., Westbrook, N., Perronet, K., and Namy, O. (2017). Kinetics of CrPV and HCV IRES-mediated eukaryotic translation using single-molecule fluorescence microscopy. RNA N. Y. N *23*, 1626–1635.

Bulkley, D., Innis, C.A., Blaha, G., and Steitz, T.A. (2010). Revisiting the structures of several antibiotics bound to the bacterial ribosome. Proc. Natl. Acad. Sci. U. S. A. *107*, 17158–17163.

Bulkley, D., Johnson, F., and Steitz, T.A. (2012). The antibiotic thermorubin inhibits protein synthesis by binding to inter-subunit bridge B2a of the ribosome. J. Mol. Biol. *416*, 571–578.

Bulkley, D., Brandi, L., Polikanov, Y.S., Fabbretti, A., O'Connor, M., Gualerzi, C.O., and Steitz, T.A. (2014). The antibiotics dityromycin and GE82832 bind protein S12 and block EF-G-catalyzed translocation. Cell Rep. *6*, 357–365.

Burnouf, D., Ennifar, E., Guedich, S., Puffer, B., Hoffmann, G., Bec, G., Disdier, F., Baltzinger, M., and Dumas, P. (2012). kinITC: a new method for obtaining joint thermodynamic and kinetic data by isothermal titration calorimetry. J. Am. Chem. Soc. *134*, 559–565.

Bushell, M., and Sarnow, P. (2002). Hijacking the translation apparatus by RNA viruses. J. Cell Biol. *158*, 395–399.

C Y Woo, P., Lau, S., K Y Choi, G., Huang, Y., L L Teng, J., Tsoi, H.-W., Tse, H., Lung Yeung, M., Chan, K.-H., Jin, D.-Y., et al. (2011). Natural Occurrence and Characterization of Two Internal Ribosome Entry Site Elements in a Novel Virus, Canine Picodicistrovirus, in the Picornavirus-Like Superfamily. J. Virol. *86*, 2797–2808.

Canu, A., Malbruny, B., Coquemont, M., Davies, T.A., Appelbaum, P.C., and Leclercq, R. (2002). Diversity of ribosomal mutations conferring resistance to macrolides, clindamycin, streptogramin, and telithromycin in Streptococcus pneumoniae. Antimicrob. Agents Chemother. *46*, 125–131.

Cao, B., Zhao, C.-J., Yin, Y.-D., Zhao, F., Song, S.-F., Bai, L., Zhang, J.-Z., Liu, Y.-M., Zhang, Y.-Y., Wang, H., et al. (2010). High prevalence of macrolide resistance in Mycoplasma pneumoniae isolates from adult and adolescent patients with respiratory tract infection in China. Clin. Infect. Dis. Off. Publ. Infect. Dis. Soc. Am. *51*, 189–194.

Carrasco, L., Sanz, M.A., and González-Almela, E. (2018). The Regulation of Translation in Alphavirus-Infected Cells. Viruses *10*.

Carter, A.P., Clemons, W.M., Brodersen, D.E., Morgan-Warren, R.J., Wimberly, B.T., and Ramakrishnan, V. (2000). Functional insights from the structure of the 30S ribosomal subunit and its interactions with antibiotics. Nature *407*, 340–348.

Casteels, P., Ampe, C., Jacobs, F., Vaeck, M., and Tempst, P. (1989). Apidaecins: antibacterial peptides from honeybees. EMBO J. *8*, 2387–2391.

Casteels-Josson, K., Capaci, T., Casteels, P., and Tempst, P. (1993). Apidaecin multipeptide precursor structure: a putative mechanism for amplification of the insect antibacterial response. EMBO J. *12*, 1569–1578.

Cavalleri, B., Turconi, M., and Pallanza, R. (1985). Synthesis and antibacterial activity of some derivatives of the antibiotic thermorubin. J. Antibiot. (Tokyo) *38*, 1752–1760.

Chernysh, S., Cociancich, S., Briand, J.-P., Hetru, C., and Bulet, P. (1996). The inducible antibacterial peptides of the Hemipteran insect Palomena prasina: Identification of a unique family of prolinerich peptides and of a novel insect defensin. J. Insect Physiol. *42*, 81–89.

Chinali, G., Moureau, P., and Cocito, C.G. (1984). The action of virginiamycin M on the acceptor, donor, and catalytic sites of peptidyltransferase. J. Biol. Chem. *259*, 9563–9568.

Cociancich, S., Dupont, A., Hegy, G., Lanot, R., Holder, F., Hetru, C., Hoffmann, J.A., and Bulet, P. (1994). Novel inducible antibacterial peptides from a hemipteran insect, the sap-sucking bug Pyrrhocoris apterus. Biochem. J. *300 (Pt 2)*, 567–575.

Colussi, T.M., Costantino, D.A., Zhu, J., Donohue, J.P., Korostelev, A.A., Jaafar, Z.A., Plank, T.-D.M., Noller, H.F., and Kieft, J.S. (2015). Initiation of translation in bacteria by a structured eukaryotic IRES RNA. Nature *519*, 110–113.

Connor, J.H., and Lyles, D.S. (2005). Inhibition of host and viral translation during vesicular stomatitis virus infection. eIF2 is responsible for the inhibition of viral but not host translation. J. Biol. Chem. *280*, 13512–13519.

Cornish, P.V., Ermolenko, D.N., Noller, H.F., and Ha, T. (2008). Spontaneous intersubunit rotation in single ribosomes. Mol. Cell *30*, 578–588.

Costantino, D., and Kieft, J.S. (2005). A preformed compact ribosome-binding domain in the cricket paralysis-like virus IRES RNAs. RNA N. Y. N *11*, 332–343.

Costantino, D.A., Pfingsten, J.S., Rambo, R.P., and Kieft, J.S. (2008). tRNA-mRNA mimicry drives translation initiation from a viral IRES. Nat. Struct. Mol. Biol. *15*, 57–64.

Crick, F. (1970). Central dogma of molecular biology. Nature *227*, 561–563.

Davis, A.R., Gohara, D.W., and Yap, M.-N.F. (2014). Sequence selectivity of macrolide-induced translational attenuation. Proc. Natl. Acad. Sci. U. S. A. *111*, 15379–15384.

D'Costa, V.M., King, C.E., Kalan, L., Morar, M., Sung, W.W.L., Schwarz, C., Froese, D., Zazula, G., Calmels, F., Debruyne, R., et al. (2011). Antibiotic resistance is ancient. Nature *477*, 457–461.

Demeshkina, N., Jenner, L., Westhof, E., Yusupov, M., and Yusupova, G. (2012). A new understanding of the decoding principle on the ribosome. Nature *484*, 256–259.

Denis, A., Agouridas, C., Auger, J.M., Benedetti, Y., Bonnefoy, A., Bretin, F., Chantot, J.F., Dussarat, A., Fromentin, C., D'Ambrières, S.G., et al. (1999). Synthesis and antibacterial activity of HMR 3647 a new ketolide highly potent against erythromycin-resistant and susceptible pathogens. Bioorg. Med. Chem. Lett. *9*, 3075–3080.

Dever, T.E., and Green, R. (2012). The elongation, termination, and recycling phases of translation in eukaryotes. Cold Spring Harb. Perspect. Biol. *4*, a013706.

Dhote, V., Gupta, S., and Reynolds, K.A. (2008). An O-phosphotransferase catalyzes phosphorylation of hygromycin A in the antibiotic-producing organism Streptomyces hygroscopicus. Antimicrob. Agents Chemother. *52*, 3580–3588.

Di Giambattista, M., Engelborghs, Y., Nyssen, E., and Cocito, C. (1987). Kinetics of binding of macrolides, lincosamides, and synergimycins to ribosomes. J. Biol. Chem. *262*, 8591–8597.

Dinos, G.P. (2017). The macrolide antibiotic renaissance. Br. J. Pharmacol. *174*, 2967–2983.

Donadio, S., Staver, M.J., McAlpine, J.B., Swanson, S.J., and Katz, L. (1991). Modular organization of genes required for complex polyketide biosynthesis. Science *252*, 675–679.

Donia, M.S., and Fischbach, M.A. (2015). HUMAN MICROBIOTA. Small molecules from the human microbiota. Science *349*, 1254766.

Donia, M.S., Cimermancic, P., Schulze, C.J., Wieland Brown, L.C., Martin, J., Mitreva, M., Clardy, J., Linington, R.G., and Fischbach, M.A. (2014). A systematic analysis of biosynthetic gene clusters in the human microbiome reveals a common family of antibiotics. Cell *158*, 1402–1414.

Doucet-Populaire, F., Capobianco, J.O., Zakula, D., Jarlier, V., and Goldman, R.C. (1998). Molecular basis of clarithromycin activity against Mycobacterium avium and Mycobacterium smegmatis. J. Antimicrob. Chemother. *41*, 179–187.

Douthwaite, S. (2001). Structure-activity relationships of ketolides vs. macrolides. Clin. Microbiol. Infect. Off. Publ. Eur. Soc. Clin. Microbiol. Infect. Dis. *7 Suppl 3*, 11–17.

Dumas, P., Ennifar, E., Da Veiga, C., Bec, G., Palau, W., Di Primo, C., Piñeiro, A., Sabin, J., Muñoz, E., and Rial, J. (2016). Extending ITC to Kinetics with kinITC. Methods Enzymol. *567*, 157–180.

Dunkle, J.A., Xiong, L., Mankin, A.S., and Cate, J.H.D. (2010). Structures of the Escherichia coli ribosome with antibiotics bound near the peptidyl transferase center explain spectra of drug action. Proc. Natl. Acad. Sci. U. S. A. *107*, 17152–17157.

Dunkle, J.A., Wang, L., Feldman, M.B., Pulk, A., Chen, V.B., Kapral, G.J., Noeske, J., Richardson, J.S., Blanchard, S.C., and Cate, J.H.D. (2011). Structures of the bacterial ribosome in classical and hybrid states of tRNA binding. Science *332*, 981–984.

Duval, M., Korepanov, A., Fuchsbauer, O., Fechter, P., Haller, A., Fabbretti, A., Choulier, L., Micura, R., Klaholz, B.P., Romby, P., et al. (2013). Escherichia coli ribosomal protein S1 unfolds structured mRNAs onto the ribosome for active translation initiation. PLoS Biol. *11*, e1001731.

Etchison, D., Milburn, S.C., Edery, I., Sonenberg, N., and Hershey, J.W. (1982). Inhibition of HeLa cell protein synthesis following poliovirus infection correlates with the proteolysis of a 220,000-dalton polypeptide associated with eucaryotic initiation factor 3 and a cap binding protein complex. J. Biol. Chem. *257*, 14806–14810.

Faccone, D., Andres, P., Galas, M., Tokumoto, M., Rosato, A., and Corso, A. (2005). Emergence of a Streptococcus pneumoniae clinical isolate highly resistant to telithromycin and fluoroquinolones. J. Clin. Microbiol. *43*, 5800–5803.

Fajardo, A., Martínez-Martín, N., Mercadillo, M., Galán, J.C., Ghysels, B., Matthijs, S., Cornelis, P., Wiehlmann, L., Tümmler, B., Baquero, F., et al. (2008). The neglected intrinsic resistome of bacterial pathogens. PloS One *3*, e1619.

Farrell, D.J., Douthwaite, S., Morrissey, I., Bakker, S., Poehlsgaard, J., Jakobsen, L., and Felmingham, D. (2003). Macrolide resistance by ribosomal mutation in clinical isolates of Streptococcus pneumoniae from the PROTEKT 1999-2000 study. Antimicrob. Agents Chemother. *47*, 1777–1783.

Farrell, D.J., Morrissey, I., Bakker, S., Buckridge, S., and Felmingham, D. (2004). In vitro activities of telithromycin, linezolid, and quinupristin-dalfopristin against Streptococcus pneumoniae with macrolide resistance due to ribosomal mutations. Antimicrob. Agents Chemother. *48*, 3169–3171.

Farrell, D.J., Mendes, R.E., and Jones, R.N. (2015). Antimicrobial activity of solithromycin against serotyped macrolide-resistant Streptococcus pneumoniae isolates collected from U.S. medical centers in 2012. Antimicrob. Agents Chemother. *59*, 2432–2434.

Fechter, P., Chevalier, C., Yusupova, G., Yusupov, M., Romby, P., and Marzi, S. (2009). Ribosomal initiation complexes probed by toeprinting and effect of trans-acting translational regulators in bacteria. Methods Mol. Biol. Clifton NJ *540*, 247–263.

Fernández, I.S., Bai, X.-C., Murshudov, G., Scheres, S.H.W., and Ramakrishnan, V. (2014). Initiation of translation by cricket paralysis virus IRES requires its translocation in the ribosome. Cell *157*, 823–831.

Fernández-Miragall, O., Ramos, R., Ramajo, J., and Martínez-Salas, E. (2006). Evidence of reciprocal tertiary interactions between conserved motifs involved in organizing RNA structure essential for internal initiation of translation. RNA N. Y. N *12*, 223–234.

Filbin, M.E., and Kieft, J.S. (2009). Toward a structural understanding of IRES RNA function. Curr. Opin. Struct. Biol. *19*, 267–276.

Fitzpatrick, A.W.P., Llabrés, S., Neuberger, A., Blaza, J.N., Bai, X.-C., Okada, U., Murakami, S., van Veen, H.W., Zachariae, U., Scheres, S.H.W., et al. (2017). Structure of the MacAB-TolC ABC-type tripartite multidrug efflux pump. Nat. Microbiol. *2*, 17070.

Flather, D., and Semler, B.L. (2015). Picornaviruses and nuclear functions: targeting a cellular compartment distinct from the replication site of a positive-strand RNA virus. Front. Microbiol. *6*, 594.

Florin, T., Maracci, C., Graf, M., Karki, P., Klepacki, D., Berninghausen, O., Beckmann, R., Vázquez-Laslop, N., Wilson, D.N., Rodnina, M.V., et al. (2017). An antimicrobial peptide that inhibits translation by trapping release factors on the ribosome. Nat. Struct. Mol. Biol. *24*, 752–757.

Fong, D.H., Burk, D.L., Blanchet, J., Yan, A.Y., and Berghuis, A.M. (2017). Structural Basis for Kinase-Mediated Macrolide Antibiotic Resistance. Struct. Lond. Engl. 1993 *25*, 750-761.e5.

Franceschi, F., and Duffy, E.M. (2006). Structure-based drug design meets the ribosome. Biochem. Pharmacol. *71*, 1016–1025.

Franceschi, F., Kanyo, Z., Sherer, E.C., and Sutcliffe, J. (2004). Macrolide resistance from the ribosome perspective. Curr. Drug Targets Infect. Disord. *4*, 177–191.

Frank, J., Zhu, J., Penczek, P., Li, Y., Srivastava, S., Verschoor, A., Radermacher, M., Grassucci, R., Lata, R.K., and Agrawal, R.K. (1995). A model of protein synthesis based on cryo-electron microscopy of the E. coli ribosome. Nature *376*, 441–444.

Fros, J.J., and Pijlman, G.P. (2016). Alphavirus Infection: Host Cell Shut-Off and Inhibition of Antiviral Responses. Viruses *8*.

Fyfe, C., Grossman, T.H., Kerstein, K., and Sutcliffe, J. (2016). Resistance to Macrolide Antibiotics in Public Health Pathogens. Cold Spring Harb. Perspect. Med. *6*.

Gagnon, M.G., Roy, R.N., Lomakin, I.B., Florin, T., Mankin, A.S., and Steitz, T.A. (2016). Structures of proline-rich peptides bound to the ribosome reveal a common mechanism of protein synthesis inhibition. Nucleic Acids Res. *44*, 2439–2450.

Gao, W., Li, Q., Zhu, R., and Jin, J. (2016). La Autoantigen Induces Ribosome Binding Protein 1 (RRBP1) Expression through Internal Ribosome Entry Site (IRES)-Mediated Translation during Cellular Stress Condition. Int. J. Mol. Sci. *17*.

Garrey, J.L., Lee, Y.-Y., Au, H.H.T., Bushell, M., and Jan, E. (2010). Host and viral translational mechanisms during cricket paralysis virus infection. J. Virol. *84*, 1124–1138.

Garza-Ramos, G., Xiong, L., Zhong, P., and Mankin, A. (2001). Binding site of macrolide antibiotics on the ribosome: new resistance mutation identifies a specific interaction of ketolides with rRNA. J. Bacteriol. *183*, 6898–6907.

Geissmann, T.A., and Touati, D. (2004). Hfq, a new chaperoning role: binding to messenger RNA determines access for small RNA regulator. EMBO J. *23*, 396–405.

Gennaro, R., Skerlavaj, B., and Romeo, D. (1989). Purification, composition, and activity of two bactenecins, antibacterial peptides of bovine neutrophils. Infect. Immun. *57*, 3142–3146.

Gingras, A.C., Svitkin, Y., Belsham, G.J., Pause, A., and Sonenberg, N. (1996). Activation of the translational suppressor 4E-BP1 following infection with encephalomyocarditis virus and poliovirus. Proc. Natl. Acad. Sci. U. S. A. *93*, 5578–5583.

Girard, A.E., Girard, D., English, A.R., Gootz, T.D., Cimochowski, C.R., Faiella, J.A., Haskell, S.L., and Retsema, J.A. (1987). Pharmacokinetic and in vivo studies with azithromycin (CP-62,993), a new macrolide with an extended half-life and excellent tissue distribution. Antimicrob. Agents Chemother. *31*, 1948–1954.

Giuliodori, A.M., Spurio, R., Milón, P., and Fabbretti, A. (2018). Antibiotics Targeting the 30S Ribosomal Subunit: A Lesson from Nature to Find and Develop New Drugs. Curr. Top. Med. Chem. *18*, 2080–2096.

Golkar, T., Zieliński, M., and Berghuis, A.M. (2018). Look and Outlook on Enzyme-Mediated Macrolide Resistance. Front. Microbiol. *9*, 1942.

Gomez-Lorenzo, M.G., Spahn, C.M., Agrawal, R.K., Grassucci, R.A., Penczek, P., Chakraburtty, K., Ballesta, J.P., Lavandera, J.L., Garcia-Bustos, J.F., and Frank, J. (2000). Three-dimensional cryo-electron microscopy localization of EF2 in the Saccharomyces cerevisiae 80S ribosome at 17.5 A resolution. EMBO J. *19*, 2710–2718.

Gonzalez, R.L., Chu, S., and Puglisi, J.D. (2007). Thiostrepton inhibition of tRNA delivery to the ribosome. RNA N. Y. N *13*, 2091–2097.

Goyal, A., Belardinelli, R., Maracci, C., Milón, P., and Rodnina, M.V. (2015). Directional transition from initiation to elongation in bacterial translation. Nucleic Acids Res. *43*, 10700–10712.

Gradi, A., Svitkin, Y.V., Imataka, H., and Sonenberg, N. (1998). Proteolysis of human eukaryotic translation initiation factor eIF4GII, but not eIF4GI, coincides with the shutoff of host protein synthesis after poliovirus infection. Proc. Natl. Acad. Sci. U. S. A. *95*, 11089–11094.

Graf, M., and Wilson, D.N. (2019). Intracellular Antimicrobial Peptides Targeting the Protein Synthesis Machinery. Adv. Exp. Med. Biol. *1117*, 73–89.

Graf, M., Mardirossian, M., Nguyen, F., Seefeldt, A.C., Guichard, G., Scocchi, M., Innis, C.A., and Wilson, D.N. (2017). Proline-rich antimicrobial peptides targeting protein synthesis. Nat. Prod. Rep. *34*, 702–711.

Gross, L., Vicens, Q., Einhorn, E., Noireterre, A., Schaeffer, L., Kuhn, L., Imler, J.-L., Eriani, G., Meignin, C., and Martin, F. (2017). The IRES5'UTR of the dicistrovirus cricket paralysis virus is a type III IRES containing an essential pseudoknot structure. Nucleic Acids Res. *45*, 8993–9004.

Gryczan, T.J., Grandi, G., Hahn, J., Grandi, R., and Dubnau, D. (1980). Conformational alteration of mRNA structure and the posttranscriptional regulation of erythromycin-induced drug resistance. Nucleic Acids Res. *8*, 6081–6097.

Gualtieri, M., Aumelas, A., and Thaler, J.-O. (2009). Identification of a new antimicrobial lysine-rich cyclolipopeptide family from *Xenorhabdus nematophila*. J. Antibiot. (Tokyo) *62*, 295–302.

Hammerschlag, M.R., Roblin, P.M., and Bébéar, C.M. (2001). Activity of telithromycin, a new ketolide antibacterial, against atypical and intracellular respiratory tract pathogens. J. Antimicrob. Chemother. *48 Suppl T1*, 25–31.

Hansen, J.L., Moore, P.B., and Steitz, T.A. (2003). Structures of five antibiotics bound at the peptidyl transferase center of the large ribosomal subunit. J. Mol. Biol. *330*, 1061–1075.

Harms, J., Schluenzen, F., Zarivach, R., Bashan, A., Gat, S., Agmon, I., Bartels, H., Franceschi, F., and Yonath, A. (2001). High resolution structure of the large ribosomal subunit from a mesophilic eubacterium. Cell *107*, 679–688.

Harms, J.M., Schlünzen, F., Fucini, P., Bartels, H., and Yonath, A. (2004). Alterations at the peptidyl transferase centre of the ribosome induced by the synergistic action of the streptogramins dalfopristin and quinupristin. BMC Biol. *2*, 4.

Hayashi, K., Nakashima, R., Sakurai, K., Kitagawa, K., Yamasaki, S., Nishino, K., and Yamaguchi, A. (2016). AcrB-AcrA Fusion Proteins That Act as Multidrug Efflux Transporters. J. Bacteriol. *198*, 332–342.

Hellen, C.U.T. (2009). IRES-induced conformational changes in the ribosome and the mechanism of translation initiation by internal ribosomal entry. Biochim. Biophys. Acta *1789*, 558–570.

Hertz, M.I., and Thompson, S.R. (2011). Mechanism of translation initiation by Dicistroviridae IGR IRESs. Virology *411*, 355–361.

Hoffman, M.A., and Palmenberg, A.C. (1995). Mutational analysis of the J-K stem-loop region of the encephalomyocarditis virus IRES. J. Virol. *69*, 4399–4406.

Horinouchi, S., and Weisblum, B. (1980). Posttranscriptional modification of mRNA conformation: mechanism that regulates erythromycin-induced resistance. Proc. Natl. Acad. Sci. U. S. A. *77*, 7079–7083.

Hue, K.K., and Bechhofer, D.H. (1992). Regulation of the macrolide-lincosamide-streptogramin B resistance gene ermD. J. Bacteriol. *174*, 5860–5868.

Imai, S., Kumar, P., Hellen, C.U.T., D'Souza, V.M., and Wagner, G. (2016). An accurately preorganized IRES RNA structure enables eIF4G capture for initiation of viral translation. Nat. Struct. Mol. Biol. *23*, 859–864.

Ippolito, J.A., Kanyo, Z.F., Wang, D., Franceschi, F.J., Moore, P.B., Steitz, T.A., and Duffy, E.M. (2008). Crystal structure of the oxazolidinone antibiotic linezolid bound to the 50S ribosomal subunit. J. Med. Chem. *51*, 3353–3356.

Jaafar, Z.A., and Kieft, J.S. (2019). Viral RNA structure-based strategies to manipulate translation. Nat. Rev. Microbiol. *17*, 110–123.

Jackson, R.J. (2005). Alternative mechanisms of initiating translation of mammalian mRNAs. Biochem. Soc. Trans. *33*, 1231–1241.

Jan, E., and Sarnow, P. (2002). Factorless ribosome assembly on the internal ribosome entry site of cricket paralysis virus. J. Mol. Biol. *324*, 889–902.

Jang, C.J., and Jan, E. (2010). Modular domains of the Dicistroviridae intergenic internal ribosome entry site. RNA N. Y. N *16*, 1182–1195.

Jang, S.K., Kräusslich, H.G., Nicklin, M.J., Duke, G.M., Palmenberg, A.C., and Wimmer, E. (1988). A segment of the 5' nontranslated region of encephalomyocarditis virus RNA directs internal entry of ribosomes during in vitro translation. J. Virol. *62*, 2636–2643.

Jang, S.K., Pestova, T.V., Hellen, C.U., Witherell, G.W., and Wimmer, E. (1990). Cap-independent translation of picornavirus RNAs: structure and function of the internal ribosomal entry site. Enzyme *44*, 292–309.

Jenner, L., Starosta, A.L., Terry, D.S., Mikolajka, A., Filonava, L., Yusupov, M., Blanchard, S.C., Wilson, D.N., and Yusupova, G. (2013). Structural basis for potent inhibitory activity of the antibiotic tigecycline during protein synthesis. Proc. Natl. Acad. Sci. U. S. A. *110*, 3812–3816.

Jensen, J.S., Fernandes, P., and Unemo, M. (2014). In vitro activity of the new fluoroketolide solithromycin (CEM-101) against macrolide-resistant and -susceptible Mycoplasma genitalium strains. Antimicrob. Agents Chemother. *58*, 3151–3156.

Jobe, A., Liu, Z., Gutierrez-Vargas, C., and Frank, J. (2019). New Insights into Ribosome Structure and Function. Cold Spring Harb. Perspect. Biol. *11*.

Johnson, A.G., Grosely, R., Petrov, A.N., and Puglisi, J.D. (2017). Dynamics of IRES-mediated translation. Philos. Trans. R. Soc. B Biol. Sci. *372*.

Jonić, S., Sorzano, C.O.S., Cottevieille, M., Larquet, E., and Boisset, N. (2007). A novel method for improvement of visualization of power spectra for sorting cryo-electron micrographs and their local areas. J. Struct. Biol. *157*, 156–167.

Jopling, C.L., Yi, M., Lancaster, A.M., Lemon, S.M., and Sarnow, P. (2005). Modulation of hepatitis C virus RNA abundance by a liver-specific MicroRNA. Science *309*, 1577–1581.

Just-Baringo, X., Albericio, F., and Álvarez, M. (2014). Thiopeptide antibiotics: retrospective and recent advances. Mar. Drugs *12*, 317–351.

Kafasla, P., Morgner, N., Pöyry, T.A.A., Curry, S., Robinson, C.V., and Jackson, R.J. (2009). Polypyrimidine tract binding protein stabilizes the encephalomyocarditis virus IRES structure via binding multiple sites in a unique orientation. Mol. Cell *34*, 556–568.

Kafasla, P., Morgner, N., Robinson, C.V., and Jackson, R.J. (2010). Polypyrimidine tract-binding protein stimulates the poliovirus IRES by modulating eIF4G binding. EMBO J. *29*, 3710–3722.

Kannan, K., Vázquez-Laslop, N., and Mankin, A.S. (2012). Selective protein synthesis by ribosomes with a drug-obstructed exit tunnel. Cell *151*, 508–520.

Kannan, K., Kanabar, P., Schryer, D., Florin, T., Oh, E., Bahroos, N., Tenson, T., Weissman, J.S., and Mankin, A.S. (2014). The general mode of translation inhibition by macrolide antibiotics. Proc. Natl. Acad. Sci. U. S. A. *111*, 15958–15963.

Karijolich, J., and Yu, Y.-T. (2014). Therapeutic suppression of premature termination codons: mechanisms and clinical considerations (review). Int. J. Mol. Med. *34*, 355–362.

Kastner, B., Stöffler-Meilicke, M., and Stöffler, G. (1981). Arrangement of the subunits in the ribosome of Escherichia coli: demonstration by immunoelectron microscopy. Proc. Natl. Acad. Sci. U. S. A. *78*, 6652–6656.

Katz, L., Brown, D., Boris, K., and Tuan, J. (1987). Expression of the macrolide-lincosamide-streptogramin-B-resistance methylase gene, ermE, from Streptomyces erythraeus in Escherichia coli results in N6-monomethylation and N6,N6-dimethylation of ribosomal RNA. Gene *55*, 319–325.

Khatter, H., Myasnikov, A.G., Mastio, L., Billas, I.M.L., Birck, C., Stella, S., and Klaholz, B.P. (2014). Purification, characterization and crystallization of the human 80S ribosome. Nucleic Acids Res. *42*, e49.

Khawaja, A., Vopalensky, V., and Pospisek, M. (2015). Understanding the potential of hepatitis C virus internal ribosome entry site domains to modulate translation initiation via their structure and function. Wiley Interdiscip. Rev. RNA *6*, 211–224.

Khong, A., Bonderoff, J.M., Spriggs, R.V., Tammpere, E., Kerr, C.H., Jackson, T.J., Willis, A.E., and Jan, E. (2016). Temporal Regulation of Distinct Internal Ribosome Entry Sites of the Dicistroviridae Cricket Paralysis Virus. Viruses *8*.

Kieft, J.S. (2008). Viral IRES RNA structures and ribosome interactions. Trends Biochem. Sci. *33*, 274–283.

Kim, Y.-H., Cha, C.-J., and Cerniglia, C.E. (2002). Purification and characterization of an erythromycin esterase from an erythromycin-resistant Pseudomonas sp. FEMS Microbiol. Lett. *210*, 239–244.

King, H.A., Cobbold, L.C., and Willis, A.E. (2010). The role of IRES trans-acting factors in regulating translation initiation. Biochem. Soc. Trans. *38*, 1581–1586.

Kolupaeva, V.G., Pestova, T.V., Hellen, C.U., and Shatsky, I.N. (1998). Translation eukaryotic initiation factor 4G recognizes a specific structural element within the internal ribosome entry site of encephalomyocarditis virus RNA. J. Biol. Chem. *273*, 18599–18604.

Komar, A.A., and Hatzoglou, M. (2011). Cellular IRES-mediated translation: the war of ITAFs in pathophysiological states. Cell Cycle Georget. Tex *10*, 229–240.

Komar, A.A., and Hatzoglou, M. (2015). Exploring Internal Ribosome Entry Sites as Therapeutic Targets. Front. Oncol. *5*, 233.

Korostelev, A.A. (2011). Structural aspects of translation termination on the ribosome. RNA N. Y. N *17*, 1409–1421.

Kozak, M. (1999). Initiation of translation in prokaryotes and eukaryotes. Gene *234*, 187–208.

Krizsan, A., Volke, D., Weinert, S., Sträter, N., Knappe, D., and Hoffmann, R. (2014). Insect-derived proline-rich antimicrobial peptides kill bacteria by inhibiting bacterial protein translation at the 70S ribosome. Angew. Chem. Int. Ed Engl. *53*, 12236–12239.

Krizsan, A., Knappe, D., and Hoffmann, R. (2015). Influence of the yjiL-mdtM Gene Cluster on the Antibacterial Activity of Proline-Rich Antimicrobial Peptides Overcoming Escherichia coli Resistance Induced by the Missing SbmA Transporter System. Antimicrob. Agents Chemother. *59*, 5992–5998.

Krokidis, M., Bougas, A., Stavropoulou, M., Kalpaxis, D., and Dinos, G.P. (2016). The slow dissociation rate of K-1602 contributes to the enhanced inhibitory activity of this novel alkyl-aryl-bearing fluoroketolide. J. Enzyme Inhib. Med. Chem. *31*, 276–282.

Krupkin, M., Wekselman, I., Matzov, D., Eyal, Z., Diskin Posner, Y., Rozenberg, H., Zimmerman, E., Bashan, A., and Yonath, A. (2016). Avilamycin and evernimicin induce structural changes in rProteins uL16 and CTC that enhance the inhibition of A-site tRNA binding. Proc. Natl. Acad. Sci. U. S. A. *113*, E6796–E6805.

Lacerda, R., Menezes, J., and Romão, L. (2017). More than just scanning: the importance of cap-independent mRNA translation initiation for cellular stress response and cancer. Cell. Mol. Life Sci. CMLS *74*, 1659–1680.

LaMarre, J., Mendes, R.E., Szal, T., Schwarz, S., Jones, R.N., and Mankin, A.S. (2013). The genetic environment of the cfr gene and the presence of other mechanisms account for the very high linezolid resistance of Staphylococcus epidermidis isolate 426-3147L. Antimicrob. Agents Chemother. *57*, 1173–1179.

Lamphear, B.J., Yan, R., Yang, F., Waters, D., Liebig, H.D., Klump, H., Kuechler, E., Skern, T., and Rhoads, R.E. (1993). Mapping the cleavage site in protein synthesis initiation factor eIF-4 gamma of the 2A proteases from human Coxsackievirus and rhinovirus. J. Biol. Chem. *268*, 19200–19203.

Lamphear, B.J., Kirchweger, R., Skern, T., and Rhoads, R.E. (1995). Mapping of functional domains in eukaryotic protein synthesis initiation factor 4G (eIF4G) with picornaviral proteases. Implications for cap-dependent and cap-independent translational initiation. J. Biol. Chem. *270*, 21975–21983.

Landry, D.M., Hertz, M.I., and Thompson, S.R. (2009). RPS25 is essential for translation initiation by the Dicistroviridae and hepatitis C viral IRESs. Genes Dev. *23*, 2753–2764.

Leach, K.L., Swaney, S.M., Colca, J.R., McDonald, W.G., Blinn, J.R., Thomasco, L.M., Gadwood, R.C., Shinabarger, D., Xiong, L., and Mankin, A.S. (2007). The site of action of oxazolidinone antibiotics in living bacteria and in human mitochondria. Mol. Cell *26*, 393–402.

Leach, K.L., Brickner, S.J., Noe, M.C., and Miller, P.F. (2011). Linezolid, the first oxazolidinone antibacterial agent. Ann. N. Y. Acad. Sci. *1222*, 49–54.

Lee, K.-M., Chen, C.-J., and Shih, S.-R. (2017). Regulation Mechanisms of Viral IRES-Driven Translation. Trends Microbiol. *25*, 546–561.

Li, S., Cheng, X., Zhou, Y., and Xi, Z. (2011). Sparsomycin-linezolid conjugates can promote ribosomal translocation. Chembiochem Eur. J. Chem. Biol. *12*, 2801–2806.

Liang, J.-H., and Han, X. (2013). Structure-activity relationships and mechanism of action of macrolides derived from erythromycin as antibacterial agents. Curr. Top. Med. Chem. *13*, 3131–3164.

Lin, J., Gagnon, M.G., Bulkley, D., and Steitz, T.A. (2015). Conformational changes of elongation factor G on the ribosome during tRNA translocation. Cell *160*, 219–227.

Lin, J., Zhou, D., Steitz, T.A., Polikanov, Y.S., and Gagnon, M.G. (2018). Ribosome-Targeting Antibiotics: Modes of Action, Mechanisms of Resistance, and Implications for Drug Design. Annu. Rev. Biochem. *87*, 451–478.

Livingstone, J.R., Spolar, R.S., and Record, M.T. (1991). Contribution to the thermodynamics of protein folding from the reduction in water-accessible nonpolar surface area. Biochemistry *30*, 4237–4244.

Llácer, J.L., Hussain, T., Marler, L., Aitken, C.E., Thakur, A., Lorsch, J.R., Hinnebusch, A.G., and Ramakrishnan, V. (2015). Conformational Differences between Open and Closed States of the Eukaryotic Translation Initiation Complex. Mol. Cell *59*, 399–412.

Long, K.S., Poehlsgaard, J., Kehrenberg, C., Schwarz, S., and Vester, B. (2006). The Cfr rRNA methyltransferase confers resistance to Phenicols, Lincosamides, Oxazolidinones, Pleuromutilins, and Streptogramin A antibiotics. Antimicrob. Agents Chemother. *50*, 2500–2505.

López de Quinto, S., and Martínez-Salas, E. (1997). Conserved structural motifs located in distal loops of aphthovirus internal ribosome entry site domain 3 are required for internal initiation of translation. J. Virol. *71*, 4171–4175.

López de Quinto, S., and Martínez-Salas, E. (1999). Involvement of the aphthovirus RNA region located between the two functional AUGs in start codon selection. Virology *255*, 324–336.

López de Quinto, S., Lafuente, E., and Martínez-Salas, E. (2001). IRES interaction with translation initiation factors: functional characterization of novel RNA contacts with eIF3, eIF4B, and eIF4GII. RNA N. Y. N *7*, 1213–1226.

López-Alonso, J.P., Fabbretti, A., Kaminishi, T., Iturrioz, I., Brandi, L., Gil-Carton, D., Gualerzi, C.O., Fucini, P., and Connell, S.R. (2017). Structure of a 30S pre-initiation complex stalled by GE81112 reveals structural parallels in bacterial and eukaryotic protein synthesis initiation pathways. Nucleic Acids Res. *45*, 2179–2187.

Lovmar, M., Tenson, T., and Ehrenberg, M. (2004). Kinetics of macrolide action: the josamycin and erythromycin cases. J. Biol. Chem. *279*, 53506–53515.

Lovmar, M., Nilsson, K., Vimberg, V., Tenson, T., Nervall, M., and Ehrenberg, M. (2006). The molecular mechanism of peptide-mediated erythromycin resistance. J. Biol. Chem. *281*, 6742–6750.

Lovmar, M., Nilsson, K., Lukk, E., Vimberg, V., Tenson, T., and Ehrenberg, M. (2009). Erythromycin resistance by L4/L22 mutations and resistance masking by drug efflux pump deficiency. EMBO J. *28*, 736–744.

Lozano, G., and Martínez-Salas, E. (2015). Structural insights into viral IRES-dependent translation mechanisms. Curr. Opin. Virol. *12*, 113–120.

Lozano, G., Fernandez, N., and Martinez-Salas, E. (2016). Modeling Three-Dimensional Structural Motifs of Viral IRES. J. Mol. Biol. *428*, 767–776.

Lukavsky, P.J., Kim, I., Otto, G.A., and Puglisi, J.D. (2003). Structure of HCV IRES domain II determined by NMR. Nat. Struct. Biol. *10*, 1033–1038.

Mailliot, J., and Martin, F. (2018). Viral internal ribosomal entry sites: four classes for one goal. Wiley Interdiscip. Rev. RNA *9*.

Malnou, C.E., Pöyry, T.A.A., Jackson, R.J., and Kean, K.M. (2002). Poliovirus internal ribosome entry segment structure alterations that specifically affect function in neuronal cells: molecular genetic analysis. J. Virol. *76*, 10617–10626.

Mardirossian, M., Grzela, R., Giglione, C., Meinnel, T., Gennaro, R., Mergaert, P., and Scocchi, M. (2014). The host antimicrobial peptide Bac71-35 binds to bacterial ribosomal proteins and inhibits protein synthesis. Chem. Biol. *21*, 1639–1647.

Mardirossian, M., Pérébaskine, N., Benincasa, M., Gambato, S., Hofmann, S., Huter, P., Müller, C., Hilpert, K., Innis, C.A., Tossi, A., et al. (2018). The Dolphin Proline-Rich Antimicrobial Peptide Tur1A Inhibits Protein Synthesis by Targeting the Bacterial Ribosome. Cell Chem. Biol. *25*, 530-539.e7.

Marks, J., Kannan, K., Roncase, E.J., Klepacki, D., Kefi, A., Orelle, C., Vázquez-Laslop, N., and Mankin, A.S. (2016). Context-specific inhibition of translation by ribosomal antibiotics targeting the peptidyl transferase center. Proc. Natl. Acad. Sci. U. S. A. *113*, 12150–12155.

Martin, F., Barends, S., Jaeger, S., Schaeffer, L., Prongidi-Fix, L., and Eriani, G. (2011). Cap-assisted internal initiation of translation of histone H4. Mol. Cell *41*, 197–209.

Martínez-Salas, E., Francisco-Velilla, R., Fernandez-Chamorro, J., Lozano, G., and Diaz-Toledano, R. (2015). Picornavirus IRES elements: RNA structure and host protein interactions. Virus Res. *206*, 62–73.

Martinez-Salas, E., Francisco-Velilla, R., Fernandez-Chamorro, J., and Embarek, A.M. (2018). Insights into Structural and Mechanistic Features of Viral IRES Elements. Front. Microbiol. *8*.

Mast, Y., and Wohlleben, W. (2014). Streptogramins - two are better than one! Int. J. Med. Microbiol. IJMM *304*, 44–50.

Mattiuzzo, M., Bandiera, A., Gennaro, R., Benincasa, M., Pacor, S., Antcheva, N., and Scocchi, M. (2007). Role of the Escherichia coli SbmA in the antimicrobial activity of proline-rich peptides. Mol. Microbiol. *66*, 151–163.

Matzov, D., Eyal, Z., Benhamou, R.I., Shalev-Benami, M., Halfon, Y., Krupkin, M., Zimmerman, E., Rozenberg, H., Bashan, A., Fridman, M., et al. (2017). Structural insights of lincosamides targeting the ribosome of Staphylococcus aureus. Nucleic Acids Res. *45*, 10284–10292.

McCann, C.M., Christgen, B., Roberts, J.A., Su, J.-Q., Arnold, K.E., Gray, N.D., Zhu, Y.-G., and Graham, D.W. (2019). Understanding drivers of antibiotic resistance genes in High Arctic soil ecosystems. Environ. Int. *125*, 497–504.

McClary, B., Zinshteyn, B., Meyer, M., Jouanneau, M., Pellegrino, S., Yusupova, G., Schuller, A., Reyes, J.C.P., Lu, J., Guo, Z., et al. (2017). Inhibition of Eukaryotic Translation by the Antitumor Natural Product Agelastatin A. Cell Chem. Biol. *24*, 605-613.e5.

McCormack, J.C., Yuan, X., Yingling, Y.G., Kasprzak, W., Zamora, R.E., Shapiro, B.A., and Simon, A.E. (2008). Structural domains within the 3' untranslated region of Turnip crinkle virus. J. Virol. *82*, 8706–8720.

Mcguire, J.M., Bunch, R.L., Anderson, R.C., Boaz, H.E., Flynn, E.H., Powell, H.M., and Smith, J.W. (1952). [Ilotycin, a new antibiotic]. Schweiz. Med. Wochenschr. *82*, 1064–1065.

McInerney, G.M., Kedersha, N.L., Kaufman, R.J., Anderson, P., and Liljeström, P. (2005). Importance of eIF2alpha phosphorylation and stress granule assembly in alphavirus translation regulation. Mol. Biol. Cell *16*, 3753–3763.

Melnikov, S., Ben-Shem, A., Garreau de Loubresse, N., Jenner, L., Yusupova, G., and Yusupov, M. (2012). One core, two shells: bacterial and eukaryotic ribosomes. Nat. Struct. Mol. Biol. *19*, 560–567.

Metelev, M., Osterman, I.A., Ghilarov, D., Khabibullina, N.F., Yakimov, A., Shabalin, K., Utkina, I., Travin, D.Y., Komarova, E.S., Serebryakova, M., et al. (2017). Klebsazolicin inhibits 70S ribosome by obstructing the peptide exit tunnel. Nat. Chem. Biol. *13*, 1129–1136.

Mikolajka, A., Liu, H., Chen, Y., Starosta, A.L., Márquez, V., Ivanova, M., Cooperman, B.S., and Wilson, D.N. (2011). Differential effects of thiopeptide and orthosomycin antibiotics on translational GTPases. Chem. Biol. *18*, 589–600.

Milon, P., Konevega, A.L., Peske, F., Fabbretti, A., Gualerzi, C.O., and Rodnina, M.V. (2007). Transient kinetics, fluorescence, and FRET in studies of initiation of translation in bacteria. Methods Enzymol. *430*, 1–30.

Miras, M., Miller, W.A., Truniger, V., and Aranda, M.A. (2017). Non-canonical Translation in Plant RNA Viruses. Front. Plant Sci. *8*, 494.

Mokrejs, M., Masek, T., Vopálensky, V., Hlubucek, P., Delbos, P., and Pospísek, M. (2010). IRESite--a tool for the examination of viral and cellular internal ribosome entry sites. Nucleic Acids Res. *38*, D131-136.

Monro, R.E. (1967). Catalysis of peptide bond formation by 50 S ribosomal subunits from Escherichia coli. J. Mol. Biol. *26*, 147–151.

Monshupanee, T., Johansen, S.K., Dahlberg, A.E., and Douthwaite, S. (2012). Capreomycin susceptibility is increased by TlyA-directed 2'-O-methylation on both ribosomal subunits. Mol. Microbiol. *85*, 1194–1203.

Moore, I.F., Hughes, D.W., and Wright, G.D. (2005). Tigecycline is modified by the flavin-dependent monooxygenase TetX. Biochemistry *44*, 11829–11835.

Morar, M., Pengelly, K., Koteva, K., and Wright, G.D. (2012). Mechanism and diversity of the erythromycin esterase family of enzymes. Biochemistry *51*, 1740–1751.

Mosenkis, J., Daniels-McQueen, S., Janovec, S., Duncan, R., Hershey, J.W., Grifo, J.A., Merrick, W.C., and Thach, R.E. (1985). Shutoff of host translation by encephalomyocarditis virus infection does not involve cleavage of the eucaryotic initiation factor 4F polypeptide that accompanies poliovirus infection. J. Virol. *54*, 643–645.

Mosher, R.H., Camp, D.J., Yang, K., Brown, M.P., Shaw, W.V., and Vining, L.C. (1995). Inactivation of chloramphenicol by O-phosphorylation. A novel resistance mechanism in Streptomyces venezuelae ISP5230, a chloramphenicol producer. J. Biol. Chem. *270*, 27000–27006.

Muñoz, E., Sabín, J., Rial, J., Pérez, D., Ennifar, E., Dumas, P., and Piñeiro, Á. (2019). Thermodynamic and Kinetic Analysis of Isothermal Titration Calorimetry Experiments by Using KinITC in AFFINImeter. Methods Mol. Biol. Clifton NJ *1964*, 225–239.

Murray, J., Savva, C.G., Shin, B.-S., Dever, T.E., Ramakrishnan, V., and Fernández, I.S. (2016). Structural characterization of ribosome recruitment and translocation by type IV IRES. ELife *5*.

Nakashima, N., and Uchiumi, T. (2009). Functional analysis of structural motifs in dicistroviruses. Virus Res. *139*, 137–147.

Nguyen, F., Starosta, A.L., Arenz, S., Sohmen, D., Dönhöfer, A., and Wilson, D.N. (2014). Tetracycline antibiotics and resistance mechanisms. Biol. Chem. *395*, 559–575.

Nicholson, B.L., and White, K.A. (2011). 3' Cap-independent translation enhancers of positive-strand RNA plant viruses. Curr. Opin. Virol. *1*, 373–380.

Nicholson, B.L., Wu, B., Chevtchenko, I., and White, K.A. (2010). Tombusvirus recruitment of host translational machinery via the 3' UTR. RNA N. Y. N *16*, 1402–1419.

Niepmann, M. (2013). Hepatitis C virus RNA translation. Curr. Top. Microbiol. Immunol. *369*, 143–166.

Nissen, P., Hansen, J., Ban, N., Moore, P.B., and Steitz, T.A. (2000). The structural basis of ribosome activity in peptide bond synthesis. Science *289*, 920–930.

Noeske, J., Huang, J., Olivier, N.B., Giacobbe, R.A., Zambrowski, M., and Cate, J.H.D. (2014). Synergy of streptogramin antibiotics occurs independently of their effects on translation. Antimicrob. Agents Chemother. *58*, 5269–5279.

Noller, H.F., Lancaster, L., Mohan, S., and Zhou, J. (2017). Ribosome structural dynamics in translocation: yet another functional role for ribosomal RNA. Q. Rev. Biophys. *50*, e12.

Nudelman, I., Rebibo-Sabbah, A., Cherniavsky, M., Belakhov, V., Hainrichson, M., Chen, F., Schacht, J., Pilch, D.S., Ben-Yosef, T., and Baasov, T. (2009). Development of novel aminoglycoside (NB54) with reduced toxicity and enhanced suppression of disease-causing premature stop mutations. J. Med. Chem. *52*, 2836–2845.

Nunez-Samudio, V., and Chesneau, O. (2013). Functional interplay between the ATP binding cassette Msr(D) protein and the membrane facilitator superfamily Mef(E) transporter for macrolide resistance in Escherichia coli. Res. Microbiol. *164*, 226–235.

Odom, O.W., Picking, W.D., Tsalkova, T., and Hardesty, B. (1991). The synthesis of polyphenylalanine on ribosomes to which erythromycin is bound. Eur. J. Biochem. *198*, 713–722.

Ogle, J.M., Brodersen, D.E., Clemons, W.M., Tarry, M.J., Carter, A.P., and Ramakrishnan, V. (2001). Recognition of cognate transfer RNA by the 30S ribosomal subunit. Science *292*, 897–902.

Olson, M.W., Ruzin, A., Feyfant, E., Rush, T.S., O'Connell, J., and Bradford, P.A. (2006). Functional, biophysical, and structural bases for antibacterial activity of tigecycline. Antimicrob. Agents Chemother. *50*, 2156–2166.

Omura, S., Morimoto, S., Nagate, T., Adachi, T., and Kohno, Y. (1992). [Research and development of clarithromycin]. Yakugaku Zasshi *112*, 593–614.

Osterman, I.A., Khabibullina, N.F., Komarova, E.S., Kasatsky, P., Kartsev, V.G., Bogdanov, A.A., Dontsova, O.A., Konevega, A.L., Sergiev, P.V., and Polikanov, Y.S. (2017). Madumycin II inhibits peptide bond formation by forcing the peptidyl transferase center into an inactive state. Nucleic Acids Res. *45*, 7507–7514.

Otaka, T., and Kaji, A. (1975). Release of (oligo) peptidyl-tRNA from ribosomes by erythromycin A. Proc. Natl. Acad. Sci. U. S. A. *72*, 2649–2652.

Otvos, L., O, I., Rogers, M.E., Consolvo, P.J., Condie, B.A., Lovas, S., Bulet, P., and Blaszczyk-Thurin, M. (2000). Interaction between heat shock proteins and antimicrobial peptides. Biochemistry *39*, 14150–14159.

Pantel, L., Florin, T., Dobosz-Bartoszek, M., Racine, E., Sarciaux, M., Serri, M., Houard, J., Campagne, J.-M., de Figueiredo, R.M., Midrier, C., et al. (2018). Odilorhabdins, Antibacterial Agents that Cause Miscoding by Binding at a New Ribosomal Site. Mol. Cell *70*, 83-94.e7.

Pelletier, J., and Sonenberg, N. (1988). Internal initiation of translation of eukaryotic mRNA directed by a sequence derived from poliovirus RNA. Nature *334*, 320–325.

Perry, J.A., Westman, E.L., and Wright, G.D. (2014). The antibiotic resistome: what's new? Curr. Opin. Microbiol. *21*, 45–50.

Pestova, T.V., and Hellen, C.U.T. (2003). Translation elongation after assembly of ribosomes on the Cricket paralysis virus internal ribosomal entry site without initiation factors or initiator tRNA. Genes Dev. *17*, 181–186.

Pestova, T.V., Hellen, C.U., and Shatsky, I.N. (1996). Canonical eukaryotic initiation factors determine initiation of translation by internal ribosomal entry. Mol. Cell. Biol. *16*, 6859–6869.

Pestova, T.V., Lomakin, I.B., and Hellen, C.U.T. (2004). Position of the CrPV IRES on the 40S subunit and factor dependence of IRES/80S ribosome assembly. EMBO Rep. *5*, 906–913.

Petrov, A., Grosely, R., Chen, J., O'Leary, S.E., and Puglisi, J.D. (2016a). Multiple Parallel Pathways of Translation Initiation on the CrPV IRES. Mol. Cell *62*, 92–103.

Petrov, A., Grosely, R., Chen, J., O'Leary, S.E., and Puglisi, J.D. (2016b). Multiple parallel pathways of translation initiation on the CrPV IRES. Mol. Cell *62*, 92–103.

Piddock, L.J.V. (2006). Multidrug-resistance efflux pumps - not just for resistance. Nat. Rev. Microbiol. *4*, 629–636.

Pihlajamäki, M., Kataja, J., Seppälä, H., Elliot, J., Leinonen, M., Huovinen, P., and Jalava, J. (2002). Ribosomal mutations in Streptococcus pneumoniae clinical isolates. Antimicrob. Agents Chemother. *46*, 654–658.

Pilipenko, E.V., Gmyl, A.P., Maslova, S.V., Svitkin, Y.V., Sinyakov, A.N., and Agol, V.I. (1992). Prokaryotic-like cis elements in the cap-independent internal initiation of translation on picornavirus RNA. Cell *68*, 119–131.

Piñeiro, Á., Muñoz, E., Sabín, J., Costas, M., Bastos, M., Velázquez-Campoy, A., Garrido, P.F., Dumas, P., Ennifar, E., García-Río, L., et al. (2019). AFFINImeter: A software to analyze molecular recognition processes from experimental data. Anal. Biochem. *577*, 117–134.

Pioletti, M., Schlünzen, F., Harms, J., Zarivach, R., Glühmann, M., Avila, H., Bashan, A., Bartels, H., Auerbach, T., Jacobi, C., et al. (2001). Crystal structures of complexes of the small ribosomal subunit with tetracycline, edeine and IF3. EMBO J. *20*, 1829–1839.

Podda, E., Benincasa, M., Pacor, S., Micali, F., Mattiuzzo, M., Gennaro, R., and Scocchi, M. (2006). Dual mode of action of Bac7, a proline-rich antibacterial peptide. Biochim. Biophys. Acta *1760*, 1732–1740.

Poehlsgaard, J., and Douthwaite, S. (2003). Macrolide antibiotic interaction and resistance on the bacterial ribosome. Curr. Opin. Investig. Drugs Lond. Engl. 2000 *4*, 140–148.

Poehlsgaard, J., and Douthwaite, S. (2005). The bacterial ribosome as a target for antibiotics. Nat. Rev. Microbiol. *3*, 870–881.

Pokrovskaya, V., and Baasov, T. (2010). Dual-acting hybrid antibiotics: a promising strategy to combat bacterial resistance. Expert Opin. Drug Discov. *5*, 883–902.

Polikanov, Y.S., Szal, T., Jiang, F., Gupta, P., Matsuda, R., Shiozuka, M., Steitz, T.A., Vázquez-Laslop, N., and Mankin, A.S. (2014a). Negamycin interferes with decoding and translocation by simultaneous interaction with rRNA and tRNA. Mol. Cell *56*, 541–550.

Polikanov, Y.S., Osterman, I.A., Szal, T., Tashlitsky, V.N., Serebryakova, M.V., Kusochek, P., Bulkley, D., Malanicheva, I.A., Efimenko, T.A., Efremenkova, O.V., et al. (2014b). Amicoumacin a inhibits translation by stabilizing mRNA interaction with the ribosome. Mol. Cell *56*, 531–540.

Polikanov, Y.S., Steitz, T.A., and Innis, C.A. (2014c). A proton wire to couple aminoacyl-tRNA accommodation and peptide-bond formation on the ribosome. Nat. Struct. Mol. Biol. *21*, 787–793.

Polikanov, Y.S., Aleksashin, N.A., Beckert, B., and Wilson, D.N. (2018). The Mechanisms of Action of Ribosome-Targeting Peptide Antibiotics. Front. Mol. Biosci. *5*, 48.

Prokhorova, I., Altman, R.B., Djumagulov, M., Shrestha, J.P., Urzhumtsev, A., Ferguson, A., Chang, C.-W.T., Yusupov, M., Blanchard, S.C., and Yusupova, G. (2017). Aminoglycoside interactions and impacts on the eukaryotic ribosome. Proc. Natl. Acad. Sci. U. S. A. *114*, E10899–E10908.

Prokhorova, I.V., Akulich, K.A., Makeeva, D.S., Osterman, I.A., Skvortsov, D.A., Sergiev, P.V., Dontsova, O.A., Yusupova, G., Yusupov, M.M., and Dmitriev, S.E. (2016). Amicoumacin A induces cancer cell death by targeting the eukaryotic ribosome. Sci. Rep. *6*, 27720.

Prunier, A.-L., Trong, H.N., Tande, D., Segond, C., and Leclercq, R. (2005). Mutation of L4 ribosomal protein conferring unusual macrolide resistance in two independent clinical isolates of Staphylococcus aureus. Microb. Drug Resist. Larchmt. N *11*, 18–20.

Pulk, A., Maiväli, U., and Remme, J. (2006). Identification of nucleotides in E. coli 16S rRNA essential for ribosome subunit association. RNA N. Y. N *12*, 790–796.

Rajesh, T., Sung, C., Kim, H., Song, E., Park, H.-Y., Jeon, J.-M., Yoo, D., Kim, H.J., Kim, Y.H., Choi, K.-Y., et al. (2013). Phosphorylation of chloramphenicol by a recombinant protein Yhr2 from Streptomyces avermitilis MA4680. Bioorg. Med. Chem. Lett. *23*, 3614–3619.

Ramakrishnan, V. (2002). Ribosome Structure and the Mechanism of Translation. Cell *108*, 557–572.

Ramu, H., Mankin, A., and Vazquez-Laslop, N. (2009). Programmed drug-dependent ribosome stalling. Mol. Microbiol. *71*, 811–824.

Ratje, A.H., Loerke, J., Mikolajka, A., Brünner, M., Hildebrand, P.W., Starosta, A.L., Dönhöfer, A., Connell, S.R., Fucini, P., Mielke, T., et al. (2010). Head swivel on the ribosome facilitates translocation by means of intra-subunit tRNA hybrid sites. Nature *468*, 713–716.

Ren, Q., Au, H.H.T., Wang, Q.S., Lee, S., and Jan, E. (2014). Structural determinants of an internal ribosome entry site that direct translational reading frame selection. Nucleic Acids Res. *42*, 9366–9382.

Retsema, J., Girard, A., Schelkly, W., Manousos, M., Anderson, M., Bright, G., Borovoy, R., Brennan, L., and Mason, R. (1987). Spectrum and mode of action of azithromycin (CP-62,993), a new 15-membered-ring macrolide with improved potency against gram-negative organisms. Antimicrob. Agents Chemother. *31*, 1939–1947.

Rheinberger, H.J., Sternbach, H., and Nierhaus, K.H. (1981). Three tRNA binding sites on Escherichia coli ribosomes. Proc. Natl. Acad. Sci. U. S. A. *78*, 5310–5314.

Roberts, M.C. (2008). Update on macrolide-lincosamide-streptogramin, ketolide, and oxazolidinone resistance genes. FEMS Microbiol. Lett. *282*, 147–159.

Roberts, M.C., Sutcliffe, J., Courvalin, P., Jensen, L.B., Rood, J., and Seppala, H. (1999). Nomenclature for macrolide and macrolide-lincosamide-streptogramin B resistance determinants. Antimicrob. Agents Chemother. *43*, 2823–2830.

Rodnina, M.V., Savelsbergh, A., Matassova, N.B., Katunin, V.I., Semenkov, Y.P., and Wintermeyer, W. (1999). Thiostrepton inhibits the turnover but not the GTPase of elongation factor G on the ribosome. Proc. Natl. Acad. Sci. U. S. A. *96*, 9586–9590.

Roy, R.N., Lomakin, I.B., Gagnon, M.G., and Steitz, T.A. (2015). The mechanism of inhibition of protein synthesis by the proline-rich peptide oncocin. Nat. Struct. Mol. Biol. *22*, 466–469.

Ruehle, M.D., Zhang, H., Sheridan, R.M., Mitra, S., Chen, Y., Gonzalez, R.L., Cooperman, B.S., and Kieft, J.S. (2015). A dynamic RNA loop in an IRES affects multiple steps of elongation factor-mediated translation initiation. ELife *4*.

Sagan, S.M., Chahal, J., and Sarnow, P. (2015). cis-Acting RNA elements in the hepatitis C virus RNA genome. Virus Res. *206*, 90–98.

Sarciaux, M., Pantel, L., Midrier, C., Serri, M., Gerber, C., Marcia de Figueiredo, R., Campagne, J.-M., Villain-Guillot, P., Gualtieri, M., and Racine, E. (2018). Total Synthesis and Structure-Activity Relationships Study of Odilorhabdins, a New Class of Peptides Showing Potent Antibacterial Activity. J. Med. Chem. *61*, 7814–7826.

Sasaki, J., and Nakashima, N. (1999). Translation Initiation at the CUU Codon Is Mediated by the Internal Ribosome Entry Site of an Insect Picorna-Like Virus In Vitro. J. Virol. *73*, 1219–1226.

Schaffrath, R., Abdel-Fattah, W., Klassen, R., and Stark, M.J.R. (2014). The diphthamide modification pathway from Saccharomyces cerevisiae--revisited. Mol. Microbiol. *94*, 1213–1226.

Schenckbecher, E., Meyer, B., and Ennifar, E. (2019). ITC Studies of Ribosome/Antibiotics Interactions. Methods Mol. Biol. Clifton NJ *1964*, 89–98.

Scheres, S.H.W. (2012). RELION: implementation of a Bayesian approach to cryo-EM structure determination. J. Struct. Biol. *180*, 519–530.

Schlünzen, F., Zarivach, R., Harms, J., Bashan, A., Tocilj, A., Albrecht, R., Yonath, A., and Franceschi, F. (2001). Structural basis for the interaction of antibiotics with the peptidyl transferase centre in eubacteria. Nature *413*, 814–821.

Schmeing, T.M., and Ramakrishnan, V. (2009). What recent ribosome structures have revealed about the mechanism of translation. Nature *461*, 1234–1242.

Schmeing, T.M., Huang, K.S., Strobel, S.A., and Steitz, T.A. (2005). An induced-fit mechanism to promote peptide bond formation and exclude hydrolysis of peptidyl-tRNA. Nature *438*, 520–524.

Schüler, M., Connell, S.R., Lescoute, A., Giesebrecht, J., Dabrowski, M., Schroeer, B., Mielke, T., Penczek, P.A., Westhof, E., and Spahn, C.M.T. (2006). Structure of the ribosome-bound cricket paralysis virus IRES RNA. Nat. Struct. Mol. Biol. *13*, 1092–1096.

Schuster, S., Vavra, M., and Kern, W.V. (2019). Efflux-mediated resistance to new oxazolidinones and pleuromutilin derivatives in Escherichia coli with class specificities in the RND-type drug transport pathways. Antimicrob. Agents Chemother.

Schuwirth, B.S., Borovinskaya, M.A., Hau, C.W., Zhang, W., Vila-Sanjurjo, A., Holton, J.M., and Cate, J.H.D. (2005). Structures of the bacterial ribosome at 3.5 A resolution. Science *310*, 827–834.

Schuwirth, B.S., Day, J.M., Hau, C.W., Janssen, G.R., Dahlberg, A.E., Cate, J.H.D., and Vila-Sanjurjo, A. (2006). Structural analysis of kasugamycin inhibition of translation. Nat. Struct. Mol. Biol. *13*, 879–886.

Scocchi, M., Tossi, A., and Gennaro, R. (2011). Proline-rich antimicrobial peptides: converging to a non-lytic mechanism of action. Cell. Mol. Life Sci. CMLS *68*, 2317–2330.

Scotti, P.D., Hoefakker, P., and Dearing, S. (1996). The production of cricket paralysis virus in suspension cultures of insect cell lines. J. Invertebr. Pathol. *68*, 109–112.

Seefeldt, A.C., Graf, M., Pérébaskine, N., Nguyen, F., Arenz, S., Mardirossian, M., Scocchi, M., Wilson, D.N., and Innis, C.A. (2016). Structure of the mammalian antimicrobial peptide Bac7(1-16) bound within the exit tunnel of a bacterial ribosome. Nucleic Acids Res. *44*, 2429–2438.

Seiple, I.B., Zhang, Z., Jakubec, P., Langlois-Mercier, A., Wright, P.M., Hog, D.T., Yabu, K., Allu, S.R., Fukuzaki, T., Carlsen, P.N., et al. (2016). A platform for the discovery of new macrolide antibiotics. Nature *533*, 338–345.

Selmer, M., Dunham, C.M., Murphy, F.V., Weixlbaumer, A., Petry, S., Kelley, A.C., Weir, J.R., and Ramakrishnan, V. (2006). Structure of the 70S ribosome complexed with mRNA and tRNA. Science *313*, 1935–1942.

Shakya, T., and Wright, G.D. (2010). Nucleotide selectivity of antibiotic kinases. Antimicrob. Agents Chemother. *54*, 1909–1913.

Sharkey, L.K.R., Edwards, T.A., and O'Neill, A.J. (2016). ABC-F Proteins Mediate Antibiotic Resistance through Ribosomal Protection. MBio *7*, e01975.

Shatsky, I.N., Dmitriev, S.E., Terenin, I.M., and Andreev, D.E. (2010). Cap- and IRES-independent scanning mechanism of translation initiation as an alternative to the concept of cellular IRESs. Mol. Cells *30*, 285–293.

Skerlavaj, B., Romeo, D., and Gennaro, R. (1990). Rapid membrane permeabilization and inhibition of vital functions of gram-negative bacteria by bactenecins. Infect. Immun. *58*, 3724–3730.

Song, Y., Mugavero, J., Stauft, C.B., and Wimmer, E. (2019). Dengue and Zika Virus 5′ Untranslated Regions Harbor Internal Ribosomal Entry Site Functions. MBio *10*.

Sothiselvam, S., Liu, B., Han, W., Ramu, H., Klepacki, D., Atkinson, G.C., Brauer, A., Remm, M., Tenson, T., Schulten, K., et al. (2014). Macrolide antibiotics allosterically predispose the ribosome for translation arrest. Proc. Natl. Acad. Sci. U. S. A. *111*, 9804–9809.

Sothiselvam, S., Neuner, S., Rigger, L., Klepacki, D., Micura, R., Vázquez-Laslop, N., and Mankin, A.S. (2016). Binding of Macrolide Antibiotics Leads to Ribosomal Selection against Specific Substrates Based on Their Charge and Size. Cell Rep. *16*, 1789–1799.

Spahn, C.M.T., Jan, E., Mulder, A., Grassucci, R.A., Sarnow, P., and Frank, J. (2004). Cryo-EM visualization of a viral internal ribosome entry site bound to human ribosomes: the IRES functions as an RNA-based translation factor. Cell *118*, 465–475.

Spížek, J., and Řezanka, T. (2017). Lincosamides: Chemical structure, biosynthesis, mechanism of action, resistance, and applications. Biochem. Pharmacol. *133*, 20–28.

Spolar, R.S., Ha, J.H., and Record, M.T. (1989). Hydrophobic effect in protein folding and other noncovalent processes involving proteins. Proc. Natl. Acad. Sci. U. S. A. *86*, 8382–8385.

Stanley, R.E., Blaha, G., Grodzicki, R.L., Strickler, M.D., and Steitz, T.A. (2010). The structures of the anti-tuberculosis antibiotics viomycin and capreomycin bound to the 70S ribosome. Nat. Struct. Mol. Biol. *17*, 289–293.

Stark, H., Mueller, F., Orlova, E.V., Schatz, M., Dube, P., Erdemir, T., Zemlin, F., Brimacombe, R., and van Heel, M. (1995). The 70S Escherichia coli ribosome at 23 A resolution: fitting the ribosomal RNA. Struct. Lond. Engl. 1993 *3*, 815–821.

Starosta, A.L., Karpenko, V.V., Shishkina, A.V., Mikolajka, A., Sumbatyan, N.V., Schluenzen, F., Korshunova, G.A., Bogdanov, A.A., and Wilson, D.N. (2010). Interplay between the ribosomal tunnel, nascent chain, and macrolides influences drug inhibition. Chem. Biol. *17*, 504–514.

Stensvåg, K., Haug, T., Sperstad, S.V., Rekdal, O., Indrevoll, B., and Styrvold, O.B. (2008). Arasin 1, a proline-arginine-rich antimicrobial peptide isolated from the spider crab, Hyas araneus. Dev. Comp. Immunol. *32*, 275–285.

Stupina, V.A., Meskauskas, A., McCormack, J.C., Yingling, Y.G., Shapiro, B.A., Dinman, J.D., and Simon, A.E. (2008). The 3′ proximal translational enhancer of Turnip crinkle virus binds to 60S ribosomal subunits. RNA N. Y. N *14*, 2379–2393.

Suhren, O. (1951). [First clinical experience with pikromycin, a new antibiotic from actinomyces in therapy of pyoderma]. Med. Klin. *46*, 722–723.

Svetlov, M.S., Vázquez-Laslop, N., and Mankin, A.S. (2017). Kinetics of drug-ribosome interactions defines the cidality of macrolide antibiotics. Proc. Natl. Acad. Sci. U. S. A. *114*, 13673–13678.

Svetlov, M.S., Plessa, E., Chen, C.-W., Bougas, A., Krokidis, M.G., Dinos, G.P., and Polikanov, Y.S. (2019). High-resolution crystal structures of ribosome-bound chloramphenicol and erythromycin provide the ultimate basis for their competition. RNA N. Y. N *25*, 600–606.

Svidritskiy, E., and Korostelev, A.A. (2018). Mechanism of Inhibition of Translation Termination by Blasticidin S. J. Mol. Biol. *430*, 591–593.

Svidritskiy, E., Ling, C., Ermolenko, D.N., and Korostelev, A.A. (2013). Blasticidin S inhibits translation by trapping deformed tRNA on the ribosome. Proc. Natl. Acad. Sci. U. S. A. *110*, 12283–12288.

Sweeney, T.R., Abaeva, I.S., Pestova, T.V., and Hellen, C.U.T. (2014). The mechanism of translation initiation on Type 1 picornavirus IRESs. EMBO J. *33*, 76–92.

Tait-Kamradt, A., Davies, T., Appelbaum, P.C., Depardieu, F., Courvalin, P., Petitpas, J., Wondrack, L., Walker, A., Jacobs, M.R., and Sutcliffe, J. (2000a). Two new mechanisms of macrolide resistance in clinical strains of Streptococcus pneumoniae from Eastern Europe and North America. Antimicrob. Agents Chemother. *44*, 3395–3401.

Tait-Kamradt, A., Davies, T., Cronan, M., Jacobs, M.R., Appelbaum, P.C., and Sutcliffe, J. (2000b). Mutations in 23S rRNA and ribosomal protein L4 account for resistance in pneumococcal strains selected in vitro by macrolide passage. Antimicrob. Agents Chemother. *44*, 2118–2125.

Tellinghuisen, J. (2005). Optimizing experimental parameters in isothermal titration calorimetry. J. Phys. Chem. B *109*, 20027–20035.

Tenson, T., Xiong, L., Kloss, P., and Mankin, A.S. (1997). Erythromycin resistance peptides selected from random peptide libraries. J. Biol. Chem. *272*, 17425–17430.

Tenson, T., Lovmar, M., and Ehrenberg, M. (2003). The mechanism of action of macrolides, lincosamides and streptogramin B reveals the nascent peptide exit path in the ribosome. J. Mol. Biol. *330*, 1005–1014.

Thom, G., and Prescott, C.D. (1997). The selection in vivo and characterization of an RNA recognition motif for spectinomycin. Bioorg. Med. Chem. *5*, 1081–1086.

Thompson, J., Pratt, C.A., and Dahlberg, A.E. (2004). Effects of a number of classes of 50S inhibitors on stop codon readthrough during protein synthesis. Antimicrob. Agents Chemother. *48*, 4889–4891.

Thompson, S.R., Gulyas, K.D., and Sarnow, P. (2001). Internal initiation in Saccharomyces cerevisiae mediated by an initiator tRNA/eIF2-independent internal ribosome entry site element. Proc. Natl. Acad. Sci. U. S. A. *98*, 12972–12977.

Toyoda, H., Franco, D., Fujita, K., Paul, A.V., and Wimmer, E. (2007). Replication of poliovirus requires binding of the poly(rC) binding protein to the cloverleaf as well as to the adjacent C-rich spacer sequence between the cloverleaf and the internal ribosomal entry site. J. Virol. *81*, 10017–10028.

Trakhanov, S., Yusupov, M., Shirokov, V., Garber, M., Mitschler, A., Ruff, M., Thierry, J.C., and Moras, D. (1989). Preliminary X-ray investigation of 70 S ribosome crystals from Thermus thermophilus. J. Mol. Biol. *209*, 327–328.

Trono, D., Andino, R., and Baltimore, D. (1988). An RNA sequence of hundreds of nucleotides at the 5′ end of poliovirus RNA is involved in allowing viral protein synthesis. J. Virol. *62*, 2291–2299.

Tu, D., Blaha, G., Moore, P.B., and Steitz, T.A. (2005). Structures of MLSBK antibiotics bound to mutated large ribosomal subunits provide a structural explanation for resistance. Cell *121*, 257–270.

Vaklavas, C., Meng, Z., Choi, H., Grizzle, W.E., Zinn, K.R., and Blume, S.W. (2015). Small molecule inhibitors of IRES-mediated translation. Cancer Biol. Ther. *16*, 1471–1485.

Vaklavas, C., Blume, S.W., and Grizzle, W.E. (2017). Translational Dysregulation in Cancer: Molecular Insights and Potential Clinical Applications in Biomarker Development. Front. Oncol. *7*.

Vázquez-Laslop, N., and Mankin, A.S. (2018). How Macrolide Antibiotics Work. Trends Biochem. Sci. *43*, 668–684.

Vazquez-Laslop, N., Thum, C., and Mankin, A.S. (2008). Molecular mechanism of drug-dependent ribosome stalling. Mol. Cell *30*, 190–202.

Vázquez-Laslop, N., Klepacki, D., Mulhearn, D.C., Ramu, H., Krasnykh, O., Franzblau, S., and Mankin, A.S. (2011). Role of antibiotic ligand in nascent peptide-dependent ribosome stalling. Proc. Natl. Acad. Sci. U. S. A. *108*, 10496–10501.

Ventoso, I., Sanz, M.A., Molina, S., Berlanga, J.J., Carrasco, L., and Esteban, M. (2006). Translational resistance of late alphavirus mRNA to eIF2α phosphorylation: a strategy to overcome the antiviral effect of protein kinase PKR. Genes Dev. *20*, 87–100.

Vester, B., and Douthwaite, S. (2001). Macrolide resistance conferred by base substitutions in 23S rRNA. Antimicrob. Agents Chemother. *45*, 1–12.

Vilches, C., Hernandez, C., Mendez, C., and Salas, J.A. (1992). Role of glycosylation and deglycosylation in biosynthesis of and resistance to oleandomycin in the producer organism, Streptomyces antibioticus. J. Bacteriol. *174*, 161–165.

Volkers, G., Palm, G.J., Weiss, M.S., Wright, G.D., and Hinrichs, W. (2011). Structural basis for a new tetracycline resistance mechanism relying on the TetX monooxygenase. FEBS Lett. *585*, 1061–1066.

Walter, J.D., Hunter, M., Cobb, M., Traeger, G., and Spiegel, P.C. (2012). Thiostrepton inhibits stable 70S ribosome binding and ribosome-dependent GTPase activation of elongation factor G and elongation factor 4. Nucleic Acids Res. *40*, 360–370.

Wang, L., Pulk, A., Wasserman, M.R., Feldman, M.B., Altman, R.B., Cate, J.H.D., and Blanchard, S.C. (2012). Allosteric control of the ribosome by small-molecule antibiotics. Nat. Struct. Mol. Biol. *19*, 957–963.

Watson, J.D. (1964). THE SYNTHESIS OF PROTEINS UPON RIBOSOMES. Bull. Soc. Chim. Biol. (Paris) *46*, 1399–1425.

Weisblum, B. (1995). Insights into erythromycin action from studies of its activity as inducer of resistance. Antimicrob. Agents Chemother. *39*, 797–805.

Wilson, D.N. (2009). The A-Z of bacterial translation inhibitors. Crit. Rev. Biochem. Mol. Biol. *44*, 393–433.

Wilson, D.N. (2014). Ribosome-targeting antibiotics and mechanisms of bacterial resistance. Nat. Rev. Microbiol. *12*, 35–48.

Wilson, D.N. (2016). The ABC of Ribosome-Related Antibiotic Resistance. MBio *7*.

Wilson, D.N., Schluenzen, F., Harms, J.M., Starosta, A.L., Connell, S.R., and Fucini, P. (2008). The oxazolidinone antibiotics perturb the ribosomal peptidyl-transferase center and effect tRNA positioning. Proc. Natl. Acad. Sci. U. S. A. *105*, 13339–13344.

Wilson, J.E., Powell, M.J., Hoover, S.E., and Sarnow, P. (2000). Naturally occurring dicistronic cricket paralysis virus RNA is regulated by two internal ribosome entry sites. Mol. Cell. Biol. *20*, 4990–4999.

Wimberly, B.T., Brodersen, D.E., Clemons, W.M., Morgan-Warren, R.J., Carter, A.P., Vonrhein, C., Hartsch, T., and Ramakrishnan, V. (2000). Structure of the 30S ribosomal subunit. Nature *407*, 327–339.

Wiseman, T., Williston, S., Brandts, J.F., and Lin, L.N. (1989). Rapid measurement of binding constants and heats of binding using a new titration calorimeter. Anal. Biochem. *179*, 131–137.

Wondrack, L., Massa, M., Yang, B.V., and Sutcliffe, J. (1996). Clinical strain of Staphylococcus aureus inactivates and causes efflux of macrolides. Antimicrob. Agents Chemother. *40*, 992–998.

Wright, G.D. (2005). Bacterial resistance to antibiotics: enzymatic degradation and modification. Adv. Drug Deliv. Rev. *57*, 1451–1470.

Wu, Y.J., and Su, W.G. (2001). Recent developments on ketolides and macrolides. Curr. Med. Chem. *8*, 1727–1758.

Yoshizawa, S., Fourmy, D., and Puglisi, J.D. (1999). Recognition of the codon-anticodon helix by ribosomal RNA. Science *285*, 1722–1725.

Yusupov, M.M., Garber, M.B., Vasiliev, V.D., and Spirin, A.S. (1991). Thermus thermophilus ribosomes for crystallographic studies. Biochimie *73*, 887–897.

Yusupov, M.M., Yusupova, G.Z., Baucom, A., Lieberman, K., Earnest, T.N., Cate, J.H., and Noller, H.F. (2001). Crystal structure of the ribosome at 5.5 A resolution. Science *292*, 883–896.

Yusupova, G., Yusupov, M., Spirin, A., Ebel, J.P., Moras, D., Ehresmann, C., and Ehresmann, B. (1991). Formation and crystallization of Thermus thermophilus 70S ribosome/tRNA complexes. FEBS Lett. *290*, 69–72.

Zanetti, M., Litteri, L., Gennaro, R., Horstmann, H., and Romeo, D. (1990). Bactenecins, defense polypeptides of bovine neutrophils, are generated from precursor molecules stored in the large granules. J. Cell Biol. *111*, 1363–1371.

Zasloff, M. (2002). Antimicrobial peptides of multicellular organisms. Nature *415*, 389–395.

Zhu, J., Korostelev, A., Costantino, D.A., Donohue, J.P., Noller, H.F., and Kieft, J.S. (2011). Crystal structures of complexes containing domains from two viral internal ribosome entry site (IRES) RNAs bound to the 70S ribosome. Proc. Natl. Acad. Sci. U. S. A. *108*, 1839–1844.

Zipperer, A., Konnerth, M.C., Laux, C., Berscheid, A., Janek, D., Weidenmaier, C., Burian, M., Schilling, N.A., Slavetinsky, C., Marschal, M., et al. (2016). Human commensals producing a novel antibiotic impair pathogen colonization. Nature *535*, 511–516.

Zivanov, J., Nakane, T., and Scheres, S.H.W. (2019). A Bayesian approach to beam-induced motion correction in cryo-EM single-particle analysis. IUCrJ *6*, 5–17.

Emma SCHENCKBECHER

Etude thermodynamique de la synthèse protéique et d'antibiotiques ciblant le ribosome

Résumé

Le ribosome est une machine biomoléculaire primordiale pour la survie de tout organisme du fait de son rôle central au sein de la synthèse protéique. La caractérisation des interactions avec ses nombreux partenaires est un élément crucial pour mieux comprendre les mécanismes de la traduction et de son inhibition chez les eucaryotes et procaryotes.

Cette inhibition est d'ailleurs une stratégie utilisée par beaucoup d'antibiotiques ciblant le ribosome pour lutter contre les infections bactériennes. La compréhension de leur mode d'action est devenue une priorité mondiale pour faire face au problème de la résistance bactérienne. Chez les eucaryotes, une autre stratégie est employée par les virus pour bloquer et s'approprier la machinerie traductionnelle de l'hôte grâce à des structures d'ARN non codant (IRES) capables de recruter directement le ribosome.

Bien que largement caractérisés, peu de données thermodynamiques et cinétiques sont disponibles concernant ces deux systèmes d'interaction avec le ribosome. Mon projet a pour vocation d'utiliser des approches biophysiques innovantes afin de compléter les études sur les interactions du ribosome d'*E. coli* avec les macrolides, et du ribosome de *S. cerevisiae* avec l'IRES intergénique du CrPV.

Mots clés : ribosome, thermodynamique, cinétique, antibiotique, macrolides, IRES intergénique

Summary

The ribosome is a biomolecular machine essential for the survival of any organism due to its central role in protein synthesis. The characterization of its interactions with its many partners is a crucial element in better understanding the mechanisms of translation and inhibition in eukaryotes and prokaryotes.

Inhibition of translation is a strategy used by many ribosome-targeting antibiotics to fight bacterial infections. Understanding their mode of action has become a global priority in addressing the problem of bacterial resistance. In eukaryotes, another strategy is used by viruses to block and appropriate the host's translational machinery through non-coding RNA structures (IRES) capable of directly recruiting the ribosome.

Although widely characterized, few thermodynamic and kinetic data are available for these two ribosome interaction systems. My project is intended to use innovative biophysical approaches in order to provide an original view of the interactions of the *E. coli* ribosome with macrolides, and of the *S. cerevisiae* ribosome with the intergenic IRES of the CrPV.

Keywords: ribosome, thermodynamics, kinetics, antibiotics, macrolides, intergenic IRES